



HAL
open science

Multi-parametric quantitative magnetic resonance imaging of collagen : methodological contributions to the assessment of myocardial fibrosis

William Alberto Romero Ramírez

► **To cite this version:**

William Alberto Romero Ramírez. Multi-parametric quantitative magnetic resonance imaging of collagen : methodological contributions to the assessment of myocardial fibrosis. Human health and pathology. Université Claude Bernard - Lyon I, 2022. English. NNT : 2022LYO10209 . tel-04343113

HAL Id: tel-04343113

<https://theses.hal.science/tel-04343113>

Submitted on 13 Dec 2023

HAL is a multi-disciplinary open access archive for the deposit and dissemination of scientific research documents, whether they are published or not. The documents may come from teaching and research institutions in France or abroad, or from public or private research centers.

L'archive ouverte pluridisciplinaire **HAL**, est destinée au dépôt et à la diffusion de documents scientifiques de niveau recherche, publiés ou non, émanant des établissements d'enseignement et de recherche français ou étrangers, des laboratoires publics ou privés.



THESE de DOCTORAT DE L'UNIVERSITE CLAUDE BERNARD LYON 1

**Ecole Doctorale N° 205
Interdisciplinaire Sciences Santé**

Discipline : Innovation Technologique pour le Biomédical

Soutenue publiquement le 09/12/2022, par :
William A. ROMERO R.

Multi-parametric quantitative magnetic resonance imaging of collagen: methodological contributions to the assessment of myocardial fibrosis

Devant le jury composé de :

Mewton, Nathan Professeur des Universités - Praticien Hospitalier, Université Lyon 1, U1060 - CARMEN	Président
Quesson, Bruno Directeur de Recherche, CNRS Bordeaux, U1045 - CRCTB	Rapporteur
Vallée, Jean-Paul Professeur Associé, Université de Genève Suisse Département de radiologie et informatique médicale	Rapporteur
Beaumont, Marine Ingénieure de recherche hospitalier, CHRU Nancy	Examinatrice
Rapacchi, Stanislas Chercheur associé, Aix-Marseille Université, UMR 7339 - CRMBM	Examinateur
Ratiney, Hélène Chargée de Recherche, CNRS Lyon, UMR 5220 - CREATIS	Examinatrice
Viallon, Magalie Physicienne médicale HDR, CHU de Saint-Étienne, UMR 5220 - CREATIS	Directrice de thèse
Croisille, Pierre Professeur des Universités - Praticien Hospitalier, Université Jean Monnet Saint-Étienne, UMR 5220 - CREATIS	Co-directeur de thèse
Troalen, Thomas Ingénieur, Siemens Healthcare SAS	Invité

Abstract

In most of the cardiovascular diseases an increase in collagen has been observed, through the apparition of a myocardial infarct scar or the development of fibrosis during and after cardiac remodelling (structural change of the tissue). Consequently, collagen stands out as a very valuable biomarker to provide information on the development of cardiac diseases.

The current clinical standard MRI (Magnetic Resonance Imaging) technique to assess myocardial fibrosis is T1-Mapping. However, even if T1 imaging is a non-invasive technique, the use of a contrast agent is often necessary to highlight the fibrotic tissue enough for clinical diagnosis, which entails secondary effects to health. Moreover, T1-mapping provides a measure of the Extra Cellular Volume (ECV), which does not allow for a precise quantification of collagen. Previous studies have shown that quantitative imaging of collagen in the myocardium could be obtained without the use of a contrast agent (on small animals) by using Ultra-short TE (UTE) imaging sequences for imaging components with short- T_2^* such as collagen. In addition, in vitro experiments have been reported in order to validate a bi-component model with an oscillation term for short- T_2^* component due to the resonance frequency of collagen at 7T and 3T; these studies showed a correct quantification short- T_2^* on aqueous solutions with concentration of collagen above 10%.

This thesis documents the methodological building blocks for a quantitative imaging of collagen components towards clinical application in myocardial fibrosis assessment. In vitro experiments on aqueous solutions have been performed to understand the required conditions for measuring collagen short- T_2^* . When the concentration of collagen is below 10%, the UTE gradient echo sequence is not able to correctly capture the short- T_2^* from collagen components which leads to wrong estimation of parameters by the numerical methods for model fitting. The results of these in vitro experiments confirm that a reliable measurement of collagen on a clinical scanner (3T) by detecting the short- T_2^* is restricted to a set of constraints such as collagen concentration and Signal-to-Noise Ratio (SNR) that can hardly be achieved on in vivo scans.

Nevertheless, T_2^* is not the only quantitative MR measure for differentiating collagen deposition and healthy tissue in the myocardium. Imaging experiments were conducted to evaluate the feasibility of MRI parameters such as magnetic susceptibility, diffusion and $T_1\rho$ relaxation, to provide a specific contrast to different collagen concentrations. The results provide convincing evidence that apparent diffusion coefficient (ADC) is the parameter that guarantees the most precise differentiation of collagen concentrations in aqueous solutions. A multi-parametric approach allows to define an MRI signature based on magnetic susceptibility, diffusion and $T_1\rho$ parameters which might be useful to identify different clusters related to different types of fibrosis (diffuse, reactive, infiltrative, focal). A multi-parametric approach would enable a better understanding of MRI biomarkers in the assessment of myocardial fibrosis, specially the quantification of collagen in the cardiac tissue.

Résumé

Une augmentation de collagène a pu être observée dans la plupart des maladies cardiovasculaires, à travers l'apparition d'une cicatrice d'infarctus sur le myocarde ou le développement d'une fibrose avant ou après le remodelage cardiaque (un changement structural du tissu cardiaque). Par conséquent, le collagène semble être un biomarqueur très utile pour obtenir des informations sur le développement des maladies cardiaques.

La technique standard d'IRM (Imagerie par Résonance Magnétique) pour évaluer la présence de fibrose myocardique est actuellement le T_1 mapping. Néanmoins, même si l'imagerie T_1 est une technique non-invasive, il est souvent nécessaire d'avoir recours à un agent de contraste pour pouvoir rendre davantage visible le tissu fibrotique afin d'effectuer un diagnostic clinique, ce qui entraîne des effets secondaires bien documentés. Par ailleurs, le T_1 mapping génère une mesure de volume extracellulaire (ECV), ce qui ne permet pas de quantifier précisément le collagène. Des études précédentes ont montré qu'il était possible d'obtenir (sur des petits animaux) une imagerie quantitative du collagène dans le myocarde sans utiliser d'agent de contraste, en ayant recours à des séquences d'imagerie TE ultra court (Ultra-short echo time) pour des composants avec un T_2^* court comme le collagène. De plus, des expériences in vitro ont été effectuées pour valider un modèle à deux composantes avec un terme d'oscillation pour des composants à T_2^* court, en raison de la fréquence de résonance du collagène à 7T et 3T. Ces études révèlent une quantification de T_2^* court juste sur des solutions hydrolysées avec des concentrations de collagène supérieures à 10%.

Cette thèse présente les fondements méthodologiques pour une imagerie quantitative de composants du collagène en vue d'une application clinique pour évaluer la fibrose du myocarde. Des expériences in vitro ont été réalisées sur des solutions hydrolysées pour identifier les conditions requises pour mesurer le T_2^* court du collagène. Lorsque la concentration de collagène est inférieure à 10%, la séquence UTE ne permet pas de saisir le T_2^* court des composants de collagène, ce qui conduit à une interprétation erronée des paramètres via les méthodes numériques d'ajustement de courbes. Les résultats de ces expériences in vitro confirment qu'une mesure fiable du collagène sur un scanner clinique (3T) en détectant le T_2^* court est limitée par un ensemble de contraintes telles que la concentration de collagène et le rapport signal sur bruit (SNR), ce qui peut difficilement être obtenu par des scans in vivo.

Néanmoins, le T_2^* court n'est pas la seule mesure quantitative de résonance magnétique pour différencier les dépôts de collagène des tissus sains dans le myocarde. Des expériences d'imagerie ont été réalisées pour évaluer la faisabilité de paramètres IRM tels que la susceptibilité magnétique, la diffusion et la relaxation de $T_1\rho$ pour pouvoir obtenir un contraste spécifique à différentes concentrations de collagène. Les résultats prouvent que le coefficient de diffusion apparent (ADC) est le paramètre qui permet la différenciation la plus précise des concentrations de collagène dans les solutions hydrolysées. Une approche multi-paramétrique permet de définir une signature IRM fondée sur la susceptibilité magnétique,

la diffusion et les paramètres $T_1\rho$ qui pourraient être utiles pour identifier différents clusters liés à différents types de fibrose (diffuse, réactive, infiltrative, focale). Une approche multi-paramétrique offrirait donc une meilleure compréhension des biomarqueurs IRM dans l'évaluation de la fibrose myocardique, et en particulier de la quantification du collagène dans le tissu cardiaque.

Acknowledgements

First and foremost, I must express my gratitude to Magalie Viallon and Pierre Croisille, who introduced me to the fascinating world of Cardiac MRI. You have played an immense role in my professional development. Thank you for setting me on this path.

This work would never have been made if it was not supported by SIEMENS Healthcare France. My thanks to Dr. Thomas Troalen, Matthieu Lepetit Coiffe and Christian Bert.

To Dr. Stanislas Rapacchi, our prime collaborator from the Centre for Magnetic Resonance in Biology and Medicine (Marseille), and Dr. Frank Kober, thank you for your patient advice and encouragement under challenging circumstances.

Dr. Alain Guignandon and Sylvie Peyroche from the research group SAINBIOSE (St. Etienne); I will remember, with gratitude, your enthusiasm in pursuing the right formula (fibrillar collagen matrices) for my experiments.

My thanks to Team 5 at CREATIS, especially to Dr. Hélène Ratiney, for an ongoing active role analysing and discussing my experimental results. To Dr. Benjamin Leporq, who generously shared his computational methods for QSM. Also, to Dr. Sébastien Valette who gave me access to the computer needed to process the experiments and to Pierre Ferrier for configuring the computers to meet my requirements.

To Dr. Irvin Teh and Dr. Jürgen Schneider from the Special Interest Group in Cardiac Diffusion (Society for Cardiovascular Magnetic Resonance) for enabling me to test new tools and infrastructure technologies within the multi-centre research project.

These acknowledgments would not be complete without thanking Dr. Arthur Coste for taking the time to answer my questions every day at 8 A.M. My heartfelt thanks also go to Dr. Jabrane Karkouri for educating me on the basics of MR spectroscopy. To Dr. Carlos Bula and Dr. Javier Gonzalez who verified some numerical methods.

I must add a note of special thanks to Agathe Henssien, Dr. Alfredo Morales and Dennis Heaphy. In addition to providing practical assistance every step of this academic journey, you have sustained me with your love, humor and friendship over these past five years.

I especially want to thank Maciej and Sylvie Orkisz who were so instrumental in getting me over the finish line.

Finally, hugs and gratitude to my Colombian and French family for the love and support you have provided me on this journey. With laughter, my favorite foods and songs, as well as tears, you have seen me through some of the lowest points in my life and in too many ways to count, made this important step in my life possible. Thank you.

List of publications

Romero R, W. A., Viallon M. et al., “*CMRSegTools: an open-source software enabling reproducible research in segmentation of acute myocardial infarct in CMR images*”, PloS one 17.9 (2022): e0274491.

Teh, I., Romero R, W. A., et al., “*Validation of cardiac diffusion tensor imaging sequences: A multicentre test–retest phantom study*”, NMR in Biomedicine 35.6 (2022): e4685. <https://doi.org/10.1002/nbm.4685>

Romero R, W. A. et al., “*Exploring DTI Benchmark Databases Through Visual Analytics*”, Computational Diffusion MRI, Springer, Cham, 2021. 291-301.
<https://doi.org/10.1007/978-3-030-73018-523>

Moulin K., Viallon M., Romero W., et al., “*MRI of reperfused acute myocardial infarction edema: ADC quantification versus T1 and T2 mapping*”, Radiology 295.3 (2020): 542-549. <https://doi.org/10.1148/radiol.2020192186>

Teh I., Romero W., et al., “*Multi-centre evaluation of diffusion tensor imaging (dti) in anisotropic phantom: Towards validation of cardiac dti sequences*”, in SCMR 23rd Annual Scientific Sessions, 2020.

Teh I., Romero W., et al., “*Reproducibility of diffusion tensor imaging (DTI) on 12 clinical scanners: Towards validation of cardiac dti sequences*”, in ISMRM 2020. Available: <https://archive.ismrm.org/2020/2055.html>

Romero R, W. A., et al., “*CMRDiffTools: A Processing and Analysis Tool for Cardiac Diffusion MR images*”, in ISMRM 2018.
Available: <https://cds.ismrm.org/protected/18MProceedings/PDFfiles/4778.html>

List of application software

CMRSegTools: an open-source application software designed for the segmentation and quantification of myocardial infarct lesion enabling full access to state-of-the-art segmentation methods and parameters, easy integration of new algorithms and standardised results sharing. The source code has been released under the CeCILL licence (September 2022) and it is available on Github: <https://github.com/OpenCardiacMRIsoftware/CMRSegTools>

CMRDiffTools: an OsiriX/Horos plug-in for simplifying and streamlining the processing and analysis tasks of Cardiac Diffusion MR images. This tool empowers research scientist with workflows for post-processing and quality control.

CMRDiffMonitor: a visual analytics application for longitudinal monitoring the stability of MR systems. Based on data acquired on an isotropic phantom, the application enables MR scientists to verify protocol compliance, identify anomalies and compare the outcomes with similar imaging systems from different sites. Available on the [The Human Heart Project](#) research ecosystem.

Table of Contents

1	Introduction	1
1.1	Motivation	1
1.2	Objectives	2
1.3	Overview	2
2	Background	3
2.1	Magnetic Resonance Imaging	3
2.1.1	Physics	3
2.1.2	Imaging	4
2.1.3	Radial 3D k-Space sampling	5
2.1.4	Compressed Sensing	5
2.1.5	Ultrashort echo time (UTE) imaging sequence and short- T_2^* quantification	6
2.1.6	Quantitative susceptibility mapping	8
2.1.7	$T_1\rho$ relaxation	10
2.1.8	Diffusion Tensor Imaging (DTI)	10
2.2	Myocardial Fibrosis	11
2.3	Clinical MRI standard for assessing myocardial fibrosis: T_1 -Mapping	12
3	Materials and methods for in vitro UTE MR collagen signal studies	15
3.1	Collagen/Gelatin fibrillar matrices	15
3.1.1	Materials and methods	17
3.1.1.1	Aqueous solutions of collagen type I and III	17
3.1.1.2	Collagen/Gelatin fibrillar matrices of collagen type I	17
3.1.1.3	Non-Localised spectroscopy	17
3.1.1.4	Polarised light microscopy	17
3.1.2	Results	18
3.1.3	Discussion	23
3.1.4	Conclusion	23
3.2	Accelerated multi-echo radial 3D imaging sequence and compressed sensing reconstruction	23
3.2.1	Materials and methods	23
3.2.1.1	Golden-Angle radial 3D k-Space sampling	23
3.2.1.2	Imaging sequence implementation	27
3.2.1.3	Data acquisition	28
3.2.1.4	Compressed sensing-based reconstruction	29
3.2.1.5	Data analysis	33
3.2.2	Results	33
3.2.3	Discussion	36

3.2.4	Conclusion	37
4	Reliability and validity of MR collagen signal: an in vitro validation study using collagen/gelatin matrices	38
4.1	Materials and methods	39
4.1.1	Collagen Phantom	39
4.1.2	Noise propagation analysis by Monte Carlo simulations	40
4.1.3	Multivariate De-noising using Wavelets and PCA	42
4.1.4	Data acquisition	42
4.1.5	Image reconstruction	44
4.1.6	Data analysis	44
4.2	Results	45
4.2.1	Noise floor estimation	50
4.2.2	De-noising parameters	51
4.2.3	Compressed sensing reconstruction	51
4.2.4	Collagen quantification	53
4.3	Discussion	57
4.4	Conclusion	61
5	Multi-parametric quantitative MRI characterisation of collagen	62
5.1	Materials and methods	62
5.1.1	Collagen phantoms	62
5.1.2	Data acquisition	63
5.1.3	Data analysis	64
5.2	Results	65
5.3	Discussion	70
5.4	Conclusion	70
6	Diffusion Tensor Imaging: post-processing workflow, imaging sequences benchmarking and clinical transfer	72
6.1	Imaging sequences benchmarking	72
6.1.1	Materials and methods	73
6.1.1.1	Phantom preparation	73
6.1.1.2	Data acquisition	74
6.1.1.3	Data management, post-processing and analysis	74
6.1.2	Results	76
6.1.3	Discussion	78
6.1.4	Conclusion	79
6.2	Preliminary analysis of the correlation between ADC and age in healthy volunteers	79
6.2.1	Materials and methods	80
6.2.2	Patient population	80
6.2.2.1	Data acquisition	80
6.2.2.2	Data analysis	80
6.2.3	Results	81
6.2.4	Discussion	86
6.2.5	Conclusion	87
7	Conclusions	88

List of Tables

3.1	Percentage of collagen concentration across tubes.	17
3.2	Imaging parameters.	28
3.3	Trajectory rotation parameters across scans.	29
3.4	Regularisation parameters.	31
3.5	k-Space data schemes.	32
3.6	Image reconstruction and computing requirements.	33
4.1	Imaging parameters.	43
4.2	Trajectory rotation parameters across scans.	44
4.3	Summary of the parameter estimation across tubes 1, 2, and 3.	56
4.4	Absolute percentage error in parameter estimation with sub-sampled images (Slice A).	57
4.5	Absolute percentage error in parameter estimation with sub-sampled images (Slice B).	57
5.1	Imaging parameters.	64
6.1	Imaging parameters.	80
6.2	Correlation of ADC with age.	86

List of Figures

2.1	Magnetisation and relaxation.	4
2.2	Radial sampling scheme.	5
2.3	MR magnitude signal from short- T_2^* (collagen) vs signal from cardiac muscle T_2^*	6
2.4	Radial UTE 3D sequence diagram.	7
2.5	Comparison of bi-component models.	8
2.6	Susceptibility spectrum.	9
2.7	$T_{1\rho}$ relaxation.	10
2.8	Pulsed Gradient Spin Echo (PGSE).	11
2.9	Etiopathology of Myocardial Fibrosis.	12
2.10	T_1 -mapping in the heart based on Modified Look-Locker Inversion Recovery (MOLLI).	13
2.11	Different types of fibrosis and T_1 maps.	14
3.1	Structural organisation of collagen.	16
3.2	Collagen/Gelatin fibrillar dense matrices prepared with a fixed concentration of collagen.	19
3.3	Collagen/Gelatin fibrillar matrices.	20
3.4	Microscopy photographs on the collagen/gelatin fibrillar dense phase.	21
3.5	MR Spectra from collagen solutions.	22
3.6	k-Space trajectory rotation.	25
3.7	Distribution of the projection's angles in k-Space.	26
3.8	Comparison of radial 3D k-Space trajectories.	26
3.9	Sequence diagram of the default radial 3D trajectory.	27
3.10	Sequence diagram of the implemented Golden-Angle radial 3D trajectory.	27
3.11	Special card on the graphical user interface.	28
3.12	Image reconstruction workflow.	30
3.13	Assessment of magnitude images at 0.05 ms.	34
3.14	Assessment of magnitude images at 2.20 ms.	35
3.15	Assessment of magnitude images at 10 ms.	36
4.1	Phantom design.	40
4.2	Model fitting of simulated MR signal.	45
4.3	Model fitting of simulated MR signal.	46
4.4	Selection of echo times	46
4.5	Histograms of the parameter estimation after 3300 iterations.	47
4.6	Probability density histograms of the parameter estimation after 3300 iterations.	48

List of Figures

4.7	Histograms of the parameter estimation and probability density after 3300 iterations.	49
4.8	Signal intensity variation as a function of the collagen signal fraction. . . .	50
4.9	Wavelet decomposition of the MR signal from magnitude images on tube 1 (2 g/L).	51
4.10	Image reconstruction assessment on slice A.	52
4.11	Image reconstruction assessment on slice B.	53
4.12	MR signals and parameter estimation from collagen/gelatin matrices (tubes 1, 2 and 3).	54
4.13	MR signals and parameter estimation from collagen/gelatin matrices (tubes 4, 5 and 6).	55
4.14	Parameter estimation with 10 TE.	56
4.15	ROI-based signal intensity reported in [3] on fibrotic tissue.	58
4.16	Model fitting by using a bi-component model with no oscillation term for short- T_2^*	59
4.17	Noise floor on short-axis magnitude images (FLASH 2D with dark blood pulse).	60
4.18	Noise floor on short-axis magnitude images (FLASH 2D).	60
5.1	Tubes layout within collagen phantoms.	63
5.2	Exemplar T_1 , T_2 and $T_{1\rho}$ parametric maps - Collagen powder (type I and III)/Water.	66
5.3	Exemplar ADC, FA and magnetic susceptibility (χ) parametric maps - Collagen powder (type I and III)/Water.	67
5.4	Exemplar T_1 , T_2 and $T_{1\rho}$ parametric maps - Collagen (type I)/Gelatin fibrillar matrices.	68
5.5	Exemplar ADC, FA and magnetic susceptibility (χ) parametric maps - Collagen (type I)/Gelatin fibrillar matrices.	69
5.6	MRI parametric z -score maps.	70
6.1	Isotropic Phantom, ROI and DAI maps.	73
6.2	Data management and data processing.	74
6.3	Post-Processing workflow.	75
6.4	Graphical User Interface (GUI) of CMRDiffMonitor.	76
6.5	Average MD across ROI as a function of PVP concentration.	77
6.6	Bland-Altman plots of MD and FA across two scans.	78
6.7	Image quality assessment.	82
6.8	Image quality assessment impact on the Helix Angle map.	83
6.9	Image quality assessment impact on the ADC map.	83
6.10	ADC values in the myocardium across age.	84
6.11	ADC mean values across age by segment on the left ventricle.	85

Chapter 1

Introduction

Magnetic Resonance Imaging (MRI) has emerged as one of the fundamental clinical diagnosis tools for cardiovascular diseases. Cardiac MRI enables not only imaging cardiac anatomy, it also enables to perform functional analysis such as left ventricular (LV) ejection fraction and myocardial wall thickening with cine imaging. In addition, quantitative parameters estimation (mapping) allows to characterise specific components in the myocardial tissue such as fibrosis.

Myocardial fibrosis is defined as a significant increase in the collagen volume fraction (CVF) of myocardial tissue [1]. Deposition of collagen affects in particular the interstitial and perivascular space, leading to a reduction of myocardial and arterial compliance and ultimately impaired diastolic function. Abnormal collagen deposition is observed in most of the cardiac diseases through the apparition of a myocardial infarct scar or the development of fibrosis during and after a structural change of the tissue (cardiac remodelling). Consequently, considerable research attention has been directed toward to fibrosis quantification by measuring the extracellular volume fraction (ECV) to assess changes in the extracellular matrix (extracellular space) between fibrotic and healthy tissue. The clinical standard to assess myocardial fibrosis requires a contrast agent (gadolinium, Gd) to highlight extracellular space on T1 pre-Gd/post-Gd images, and hematocrit measurement in order to calculate ECV. However, it does not allow for a quantification of collagen which is the main component of the fibrotic tissue.

The direct collagen quantification on the myocardium without the use of a contrast agent has been explored in few pre-clinical studies using ultra-short echo time (UTE) sequences for imaging components with short- T_2^* such as collagen [2], [3]. In addition, a bi-component model with an oscillation term for short- T_2^* components due to the resonance frequency of collagen has been validated on in vitro experiments at 7T and 3T [4], [5]. To translate this technique into clinical practice (cardiovascular imaging), some major challenges need to be addressed such as the sub-sampling strategies and compressed sensing-based image reconstruction.

1.1 Motivation

Even if T_1 imaging is a non-invasive technique, the use of a contrast agent is often necessary to highlight the fibrotic tissue enough for clinical diagnosis, which entails secondary effects that are widely documented in [6]–[8]. Therefore, there is a need for a non-invasive technique, which does not involve any contrast agent. Current studies suggest the potential of MRI parameters such as magnetic susceptibility, diffusion and $T_1\rho$ resonance for assessing

myocardial fibrosis by a direct quantification of collagen.

These ideas lead to the following question: which MRI protocol could be designed to obtain a reliable quantitative imaging of the myocardium focused on the characterisation of myocardial fibrosis in humans? And what are the best parameters for assessing myocardial fibrosis?

1.2 Objectives

The objective of this thesis is to describe the required MRI parameters and their constraints for assessing myocardial fibrosis. This includes:

1. develop an single-echo / multi-echo ultra-short TE radial 3D acquisition sequence with sub-sampling parameters,
2. develop a compressed sensing-based image reconstruction workflow,
3. implement computational methods for multi-parametric quantitative analysis,
4. design an experimental framework for the assessment of imaging sequences focused on collagen quantification, and
5. translate computational methods to reliable computer-based tools for clinical practice and research.

1.3 Overview

The remainder of this document is structured as follows:

Chapter 2: Background. This introductory chapter provides important contextual information regarding the basics of MRI, clinical background and current research directions in the assessment of myocardial fibrosis.

Chapter 3: Materials and methods for in vitro UTE MR collagen signal studies. This chapter introduces the key components of the imaging experiments: 1 Collagen/Gelatin fibrillar matrices. 2 A UTE 3D imaging sequence based on a Golden-Angle k-Space sampling. 3 Compressed sensing-based reconstruction.

Chapter 4: Reliability and validity of MR collagen signal: an in vitro validation study using collagen/gelatin matrices In this chapter, numerical experiment are used to study the optimal sampling points of the UTE MR collagen signal for a reliable quantification with a sub-sampled acquisition. Therefore, in vitro imaging experiments were conducted in order to evaluate sub-samplig strategies, compressed sensing-based reconstruction and parameter estimation methods.

Chapter 5: Multi-parametric quantitative MRI characterisation of collagen. This chapter presents a comparative analysis of different parameters for the collagen quantification: magnetic susceptibility, diffusion and $T_1\rho$ relaxation.

Chapter 6: Diffusion Tensor Imaging: post-processing workflow, imaging sequences benchmarking and clinical transfer. This chapter describes the development and evaluation of computer software designed to enhance research and clinical practice focused on DTI post-processing, visualisation and analysis.

Chapter 2

Background

This chapter provides an overview of the basic concepts in the assessment of myocardial fibrosis by magnetic resonance imaging (MRI) techniques which are the theoretical framework of this thesis. The first section introduces the basics of MRI including: Ultra-short echo time (UTE) and short- T_2^* quantification, Compressed Sensing (CS), Quantitative Susceptibility Mapping (QSM), $T_1\rho$ relaxation and Diffusion Tensor Imaging (DTI). The second section provides the clinical context regarding myocardial fibrosis followed by a description of the current clinical MRI standard for the assessment of myocardial fibrosis.

2.1 Magnetic Resonance Imaging

Magnetic resonance imaging is a non-invasive medical imaging technique that allows the creation of images of tissues inside the human body. This technique is based on the spin properties of the atoms and their behaviour under external external magnetic fields. This section explains the physics behind MRI followed by the basics of image reconstruction techniques.

2.1.1 Physics

Nuclear spins submitted to a magnetic field B_0 produce a net magnetisation moment parallel to B_0 (alignment in the direction of B_0 or z -direction) and spins precess at a well-defined frequency. This frequency known as *Larmor* frequency is defined by

$$\omega_0 = \gamma B_0 \tag{2.1}$$

where γ corresponds to the gyro-magnetic ratio, a unique constant for each atom.

By applying a radio frequency (RF) pulse in the transverse direction the spin alignment (magnetisation vector) is rotated (excited) away from the equilibrium (z -direction) while precessing about the Z -axis. After the RF excitation pulse the longitudinal component of the magnetisation returns to its thermal equilibrium state while the transverse component decays away (Figure 2.1) [9].

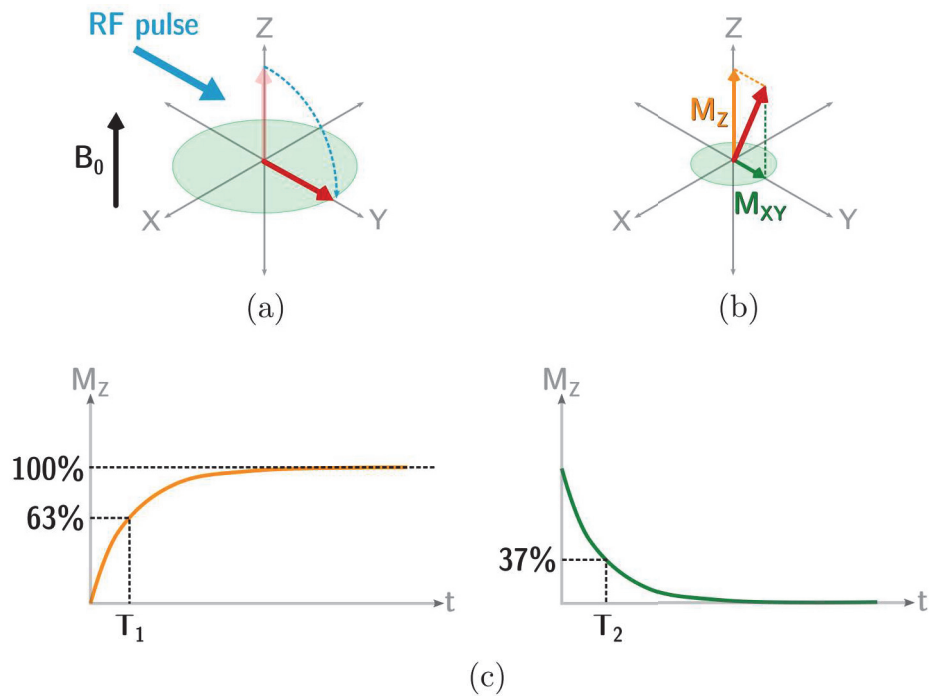


Figure 2.1: Magnetisation and relaxation. (a) Nuclear spins submitted to a magnetic field B_0 and RF pulse in the transverse direction; (b) M_z and M_{xy} magnetisation after suppressing RF pulse; (c) T_1 and T_2 relaxation times.

The behaviour of the longitudinal and transverse components of the magnetisation is described by

$$\frac{dM_z}{dt} = -\frac{M_z - M_0}{T_1} \quad (2.2)$$

$$\frac{dM_{xy}}{dt} = -\frac{M_{xy}}{T_2} \quad (2.3)$$

The solutions to these differential equations, assuming $M_z(0) = 0$ and $M_{xy}(0) = M_0$ (after a 90° RF excitation) are

$$M_z(t) = M_0 \left(1 - e^{-\frac{t}{T_1}}\right) \quad (2.4)$$

$$M_{xy}(t) = e^{-\frac{t}{T_2}} \quad (2.5)$$

where T_1 is the longitudinal relaxation (spin-lattice relaxation) time and T_2 is the transverse relaxation (spin-spin relaxation) time.

2.1.2 Imaging

The signal $S(t) \in \mathbb{C}$ acquired at time t is described by

$$S(t) = \int_r M_{xy}(\vec{r}, t) e^{-i2\pi k(t)^T r} dr + w(t) \quad (2.6)$$

where $M_{xy}(r, t)$ is the transverse component of the magnetisation; $k(t)$ is the k-Space (spatial encoding) and $k(t)^T$ denotes the transpose operation, and $w(t)$ corresponds to white Gaussian noise.

2.1.3 Radial 3D k-Space sampling

Introduced by Lauterbur in 1973 [10], a radial acquisition samples k-space following a trajectory defined by radial spokes rather than a rectilinear grid. The term projection refers to the radial spokes, views or rays. In the 3D space, a projection is defined by the polar and azimuthal angles over the ranges $0 \leq \theta < \pi$ and $0 \leq \phi < 2\pi$ respectively as presented in Figure 2.2.

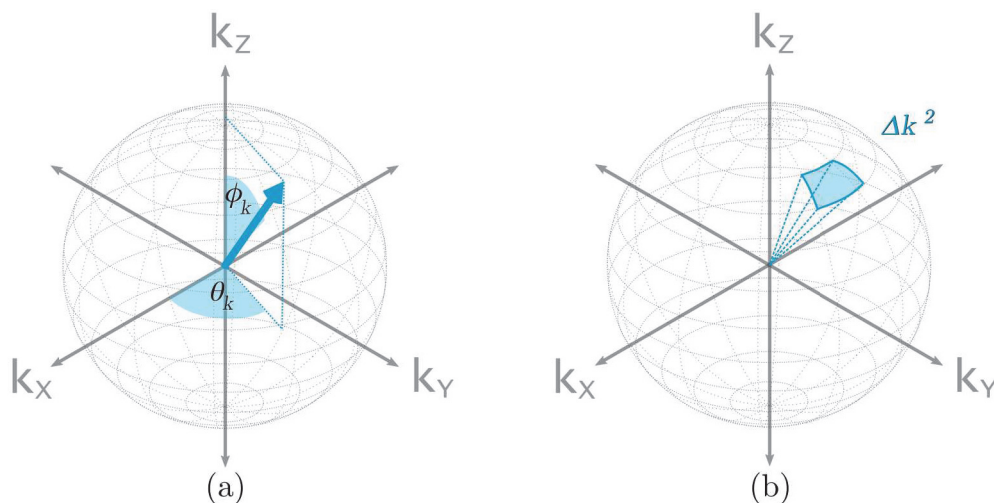


Figure 2.2: Radial sampling scheme. (a) Polar and azimuthal angles. (b) Sampling area on the sphere's surface covered by the radial sampling pattern. Illustration adapted from [11].

2.1.4 Compressed Sensing

One of the key tasks in signal and image processing is to recover a signal from an incomplete set of measurements. In mathematical terms, this recovering task can be formulated as:

$$y = Ax \quad (2.7)$$

where $x \in \mathbb{C}^N$ is the object (signal) to recover, $y \in \mathbb{C}^m$ is the vector of measured data (signal samples) and $A \in \mathbb{C}^{m \times N}$ models the linear measurement (information) process. To recover the vector $x \in \mathbb{C}^N$, it is necessary to solve the above linear system. Classical linear algebra states clearly that if the number of measurements m are less than the length of the signal N , the linear system is undetermined and there is not a single solution (there is at least one). Consequently, is not possible to recover the object x if $m < N$. To overcome this limitation ($m < N$), compressing sensing relies on the assumption of the sparsity of the vector x , which means that most of its components are zero. By reducing the matrix A to the nonzero elements the system of linear equations becomes over-determined and can be solved [12]. Now, the solution relies on a combinatorial optimisation problem in which the objective is to minimise the norm (l_0 , l_1 or l_2) of the vector x , in mathematical terms (i.e. l_0 -minimisation.)

$$\text{minimise } \|x\|_0 \text{ subject to } y = Ax \quad (2.8)$$

In the field of MRI, the main assumption is that the image has a sparse representation in some domain. Lustig et al. in [13] have shown that MR images have a sparse representation by using the discrete cosine transform (DCT) and wavelet transform. Therefore, the image reconstruction of MRI images involves the solution of the problem

$$\text{minimise } \|R(m)\|_1 \text{ subject to } \|\mathcal{F}_u m - y\|_2 < \varepsilon \quad (2.9)$$

where R is the sparsifying transform function, m is the image to recover, \mathcal{F}_u the Fourier transform and y the MR measured data. Minimisation of $\|R(m)\|_1$ (l_1 -norm) guarantee sparsity and $\|\mathcal{F}_u m - y\|_2$ imposes data consistency, using ε as a fidelity control parameter [13].

Overall, the compressed sensing-based reconstruction algorithm relies on the solution to the following combinatorial optimisation problem:

$$x = \arg \max_x \|Ax - y\|_2^2 + \sum_k \lambda_k R_k(x) \quad (2.10)$$

where x is the image and y the k-Space data. The sensing (or encoding) matrix A includes the gridding operation, fourier transform and coil sensitivity. The sparsity transforms are denoted by R_k and λ_k is the corresponding regularisation parameter.

2.1.5 Ultrashort echo time (UTE) imaging sequence and short- T_2^* quantification

Ultra-short TE (UTE) sequences have been developed to address the difficulty of imaging organs with short- T_2^* components. Collagen-related components in the tissue have a short transversal relaxation (T_2 and T_2^*). Figure 2.3 illustrates the difference between the MR signal from collagen (short- T_2^*) and cardiac muscle (long- T_2^*). Acquisitions over 6 ms will only reflect the signal contribution from muscular structures. In contrast acquisitions under 0.15 ms will include the contribution of collagen components [2].

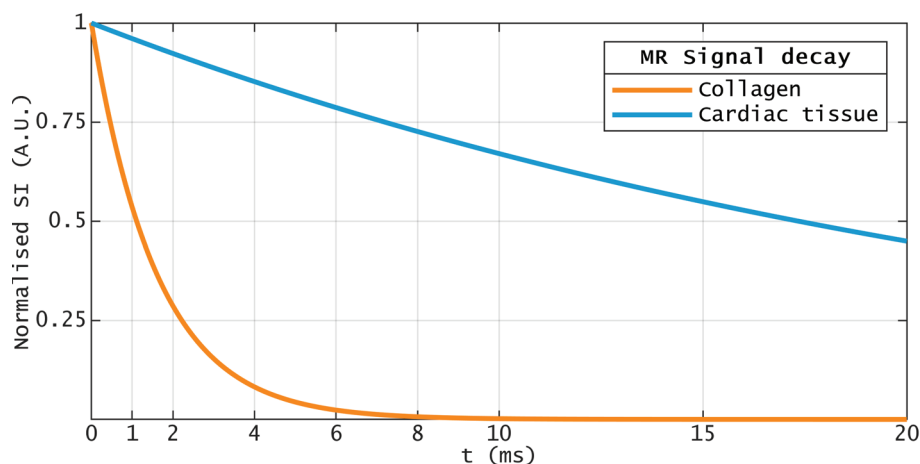


Figure 2.3: MR magnitude signal from short- T_2^* (collagen) vs signal from cardiac muscle T_2^* . Collagen short- $T_2^* = 1.6$ ms at 3T [5] and cardiac muscle $T_2^* = 25$ ms at 3T [14]. Illustration adapted from [2].

The MR signal of short- T_2^* components have a fast decay and consequently, little signal (or nothing at all) is detectable by the readout time of conventional MRI sequences in a clinical setting. UTE sequences were designed and implemented to overcome that issue [15], [16]. Consequently, data is acquired starting from zero gradient, following the ramp up to the plateau (Analogue-to-digital Converter, ADC) in order to reduce the echo time (Figure 2.4).

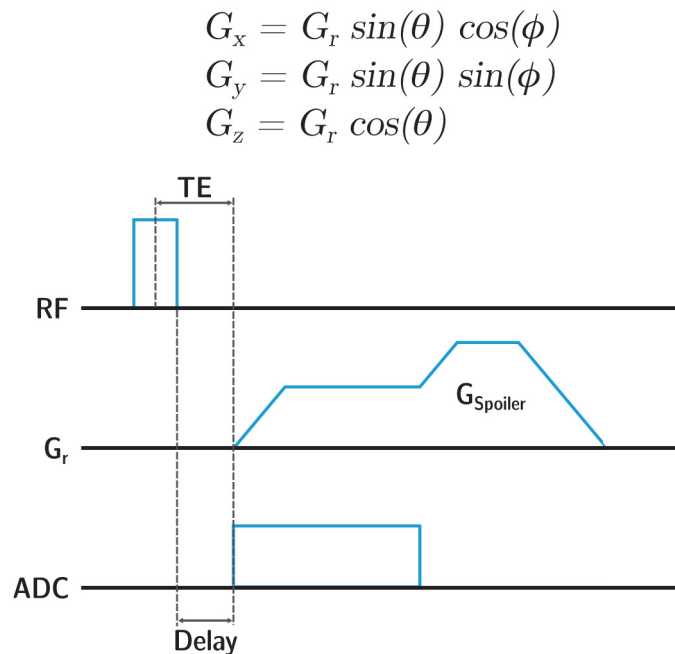


Figure 2.4: Radial UTE 3D sequence diagram. Image adapted from [17].

The UTE MR signal from short- T_2^* components is quantified by estimating the parameters of a signal decay model. The MR signal decay in terms of short- and long- T_2^* components, is given by the equation

$$S(t) = S_{0,c} e^{\frac{-t}{T_{2,c}^*}} + S_{0,l} e^{\frac{-t}{T_{2,l}^*}} \quad (2.11)$$

where $S_{0,c}$, and $T_{2,c}^*$ describe the initial signal intensity and transversal decay of protons in the collagen molecule respectively; and $S_{0,l}$ and $T_{2,l}^*$ the initial signal intensity and transversal decay of the long components. Performing a non-localised spectroscopy at 7T of a hydrolysed solution with 50% collagen concentration, Siu et al estimated the f_c at 1.06 ± 0.02 kHz, which corresponds to a chemical shift of -3.56 ± 0.07 ppm relative to water [4]. Including the resonance frequency f_c which describes the collagen component, the bi-component model with an oscillation term is

$$S(t) = S_{0,c} e^{i2\pi f_c t} e^{\frac{-t}{T_{2,c}^*}} + S_{0,l} e^{\frac{-t}{T_{2,l}^*}} \quad (2.12)$$

the equation can be written as

$$S(t) = S_{0,c} e^{t\left(i\omega_c - \frac{1}{T_{2,c}^*}\right)} + S_{0,l} e^{\frac{-t}{T_{2,l}^*}} \quad (2.13)$$

by developing the product of exponentials in the first term of the Equation 2.12

$$e^{i2\pi f_c t} \times e^{\frac{-t}{T_{2,c}^*}} = e^{i2\pi f_c t - \frac{t}{T_{2,c}^*}}$$

factorising t in the exponent as

$$i2\pi f_c t - \frac{t}{T_{2s}} = t \left(i2\pi f_c - \frac{1}{T_{2,c}^*} \right)$$

and using angular frequency

$$\frac{\omega_c}{2\pi} = f_c$$

Consequently, the magnitude of the signal is described by

$$|S(t)| = \left| S_{0,c} e^{t \left(i2\pi f_c - \frac{1}{T_{2,c}^*} \right)} + S_{0,l} e^{\frac{-t}{T_{2,l}^*}} \right| \quad (2.14)$$

The difference between the MR signal decay models (with and without oscillation term) is presented in Figure 2.5 as well as the contribution from short- T_2^* components to the signal.

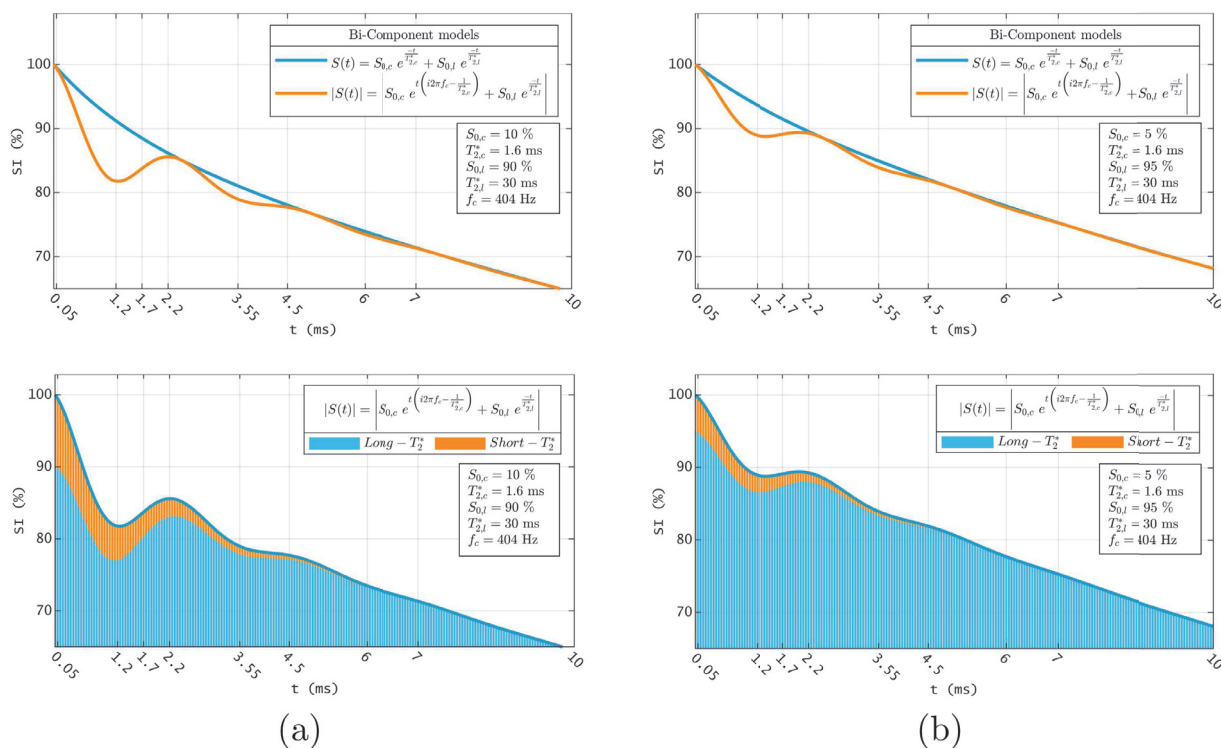


Figure 2.5: Comparison of bi-component models (top row) and MR UTE signal distribution within the bi-component model with an oscillation term (bottom row). (a) Signal from aqueous solution with 20% of collagen concentration (in mass percent); (b) Signal from aqueous solution with 10% of collagen concentration. Parameters from [5].

2.1.6 Quantitative susceptibility mapping

The magnetic susceptibility χ is defined as a dimensionless tissue property which reflects the magnetisation M gained inside an external magnetic field B_0 .

$$\chi = \frac{M}{B_0} \quad (2.15)$$

Magnetic susceptibility is categorised as paramagnetic ($\chi > 0$) meaning that the components in the tissue align with the magnetic field; or diamagnetic ($\chi < 0$) in which components align in the opposite direction of the field (Figure 2.6). For instance, commonly paramagnetic component in the human body is Iron [18], [19] and a diamagnetic component is calcium [20], [21].

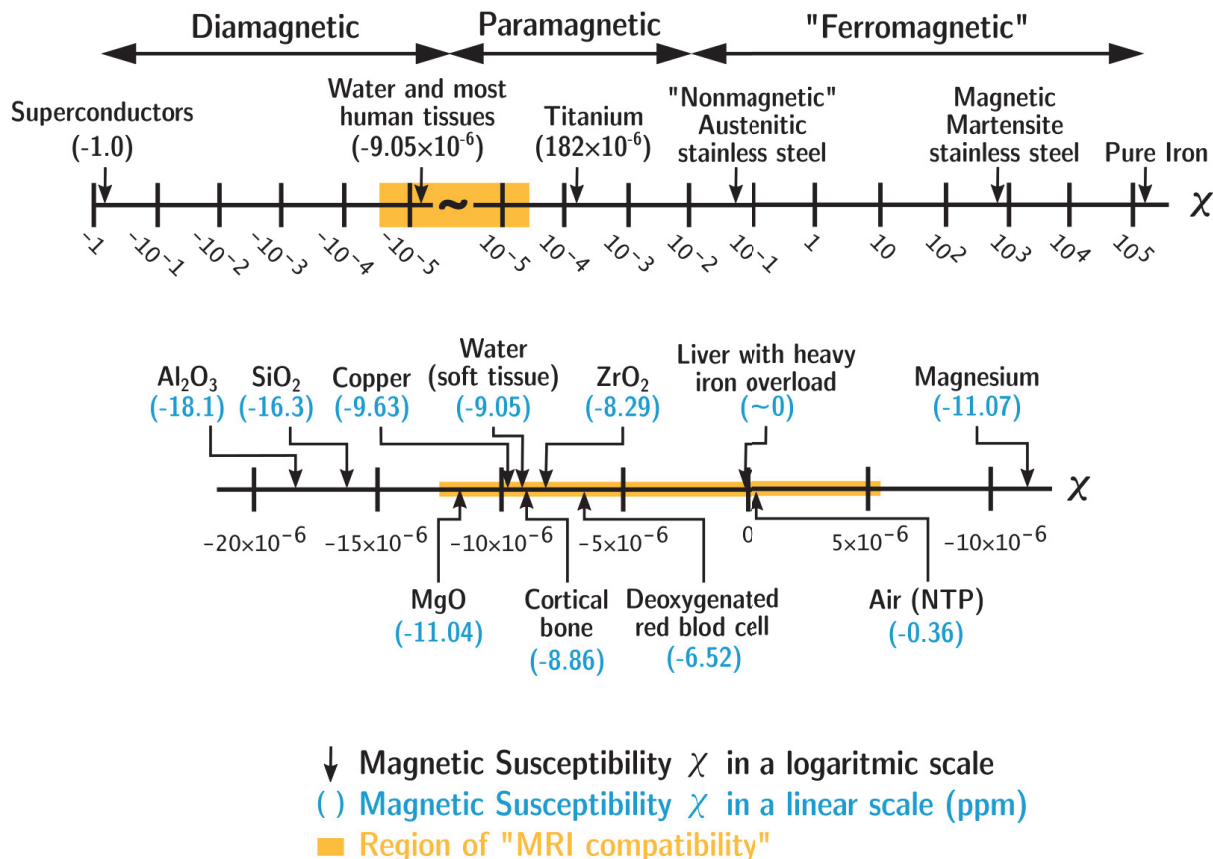


Figure 2.6: Susceptibility spectrum. Illustration reproduced from [18].

The field variation $\Delta B(\vec{r})$ induced by $\chi(\vec{r})$ is defined by the convolution

$$\Delta B(\vec{r}) = B_0 \cdot d(\vec{r}) * \chi(\vec{r}) \quad (2.16)$$

where B_0 corresponds to the main magnetic field and $d(\vec{r})$ is the point-dipole (field of a unit magnetic dipole) defined by

$$d(\vec{r}) = \frac{1}{4\pi} \cdot \frac{3 \cos^2(\theta) - 1}{|\vec{r}|^3} = \mathcal{F}^{-1} \left\{ \frac{1}{3} - \frac{k_z^2}{|\vec{k}|^2} \right\} \quad (2.17)$$

where \vec{r} and \vec{k} are vectors (spherical polar coordinates) in the image space and k-Space respectively; r the radial distance and θ the polar angle, and \mathcal{F}^{-1} denotes the inverse Fourier transform [22]. From Equation 2.16 the B_0 inhomogeneity map (magnetic field variations) is derived as a function of the susceptibility distribution. To calculate the susceptibility map from the magnetic field map, the inverse calculation must be performed.

2.1.7 $T_{1\rho}$ relaxation

$T_{1\rho}$ describes the decay of magnetisation along the transverse direction, which means, $T_{1\rho}$ is the relaxation along the RF field of the pulse (Figure 2.7).

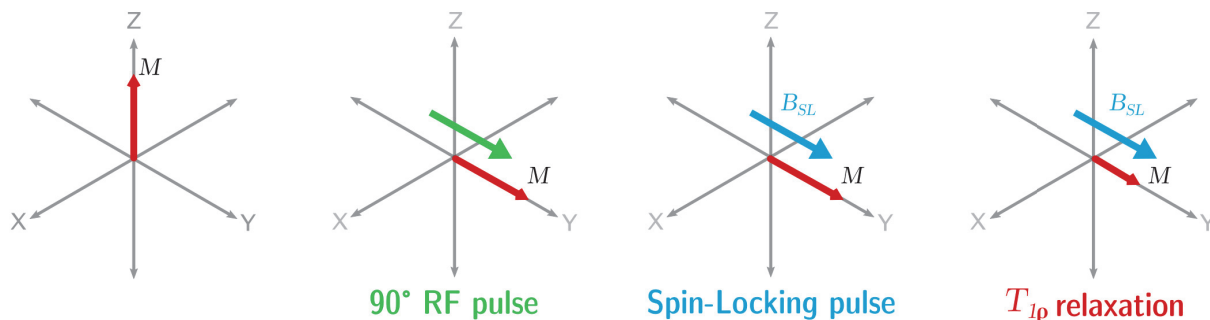


Figure 2.7: $T_{1\rho}$ relaxation.

In this sequence, a first 90° RF pulse is applied to rotate M_0 to the transverse plane, then a spin-lock pulse (B_{SL}) for a period of time (spin-lock length, TSL) is applied followed by a final short pulse rotating the magnetisation back to the longitudinal direction. $T_{1\rho}$ is measured as the decay time of the locked magnetisation during TSL to 0. $T_{1\rho}$ is dependant on the T1 and T2 of the tissue, but changing the amplitude of the spin locking pulse can also select for different properties within the tissue (e.g. slow motion in the lattice such as proteins) [23]. The $T_{1\rho}$ map is calculated by a pixel-wise model fitting to a mono-exponential decay model

$$S(t) = S_0 e^{-\frac{t}{T_{1\rho}}} \quad (2.18)$$

2.1.8 Diffusion Tensor Imaging (DTI)

Diffusion MRI measures the Brownian motion of water molecules in biological tissues. The diffusion coefficient D to describe the mean square displacement of the diffusing water molecules per unit time in three dimensions is defined by

$$D = \frac{\langle r^2 \rangle}{6t} \quad (2.19)$$

where r is the particle or spin displacement over the time t in which diffusion is being quantified [24], [25].

The diffusion of water in the human body is restricted by biological structures such as cells, membranes, vessels, etc. Therefore, orientation of anisotropic structures (i.e fibres in the cardiac tissue) can be inferred by measuring diffusion.

The Larmor frequency of spins submitted to a magnetic field B_0 depends on the proton gyro-magnetic ratio (γ) and the pulsed field gradient (\vec{g}). Therefore, the transverse magnetisation is described by the Bloch-Torrey equation

$$\frac{\partial M(\vec{r}, t)}{\partial t} = -i\gamma \vec{g} \cdot \vec{r} - \frac{M(\vec{r}, t)}{T_2} + D\nabla^2 M(\vec{r}, t) - V \cdot \nabla M(\vec{r}, t) \quad (2.20)$$

where \vec{r} are the nuclear spin coordinates, D is the diffusion coefficient, V is flow and T_2 corresponds to the relaxation time [25].

The baseline pulse sequence to sensitise the MR signal to diffusion is presented in Figure 2.8 [26] including diffusion gradients G_1 and G_2 . After the RF-pulse, spins are in phase; therefore spins are dephased by G_1 , and then inverted by a second RF-pulse; finally spins are rephased by G_2 . If diffusion occurs in the direction of the diffusion gradients G_1 and G_2 , the spins are incompletely rephased. The phase dispersion causes a signal loss which is proportional to the degree of random motion [25].

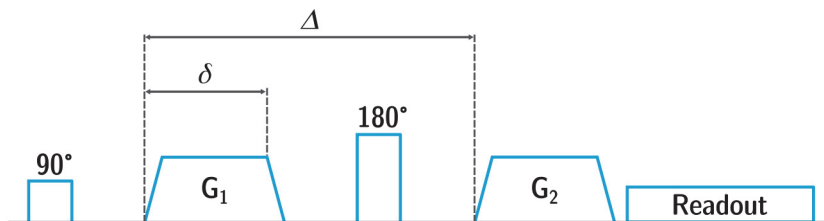


Figure 2.8: Pulsed Gradient Spin Echo (PGSE). The duration of a single gradient is denoted by δ , while Δ corresponds to the time between the onset of G_1 and G_2 gradients.

The signal decrease due to the PGSE sequence is described by

$$S(b) = S_0 e^{-bD} \quad (2.21)$$

where D is the apparent diffusion coefficient (ADC) and b is given by

$$b = \gamma^2 G^2 \delta^2 \left(\Delta - \frac{\delta}{3} \right) \quad (2.22)$$

where γ is the gyro-magnetic ratio, G is the diffusion sensitising gradient magnitude, δ is the gradient duration and Δ corresponds to the time between the onset of first and second gradient.

Diffusion Tensor Imaging (DTI) would require the acquisition of diffusion weighted images in at least 6 non-collinear directions. Diffusion is pixel-wise approximated with a second order tensor enabling the calculation of different diffusion properties such as mean diffusivity (MD) and fractional anisotropy (FA) as follows

$$MD(D) = \frac{\lambda_1 + \lambda_2 + \lambda_3}{3} \quad (2.23)$$

$$FA(D) = \sqrt{\frac{(\lambda_1 - \lambda_2)^2 + (\lambda_1 - \lambda_3)^2 + (\lambda_2 - \lambda_3)^2}{2(\lambda_1^2 + \lambda_2^2 + \lambda_3^2)}} \quad (2.24)$$

where λ_k is the k -th eigenvector of tensor D [27], [28].

2.2 Myocardial Fibrosis

Myocardial fibrosis can be defined as a “significant increase in the collagen volume fraction” (CVF) of myocardial tissue [1]. In the ageing heart, the thickening of the collagen-based mesh (increase of collagen deposition in the extracellular matrix, ECM) is a normal process [29], [30]. This progressive fibrosis can be observed as well in various organs. In the myocardium, the deposition of collagen affects in particular the interstitial and perivascular space, leading to a reduction of myocardial and arterial compliance and ultimately impaired

diastolic function (Figure 2.9). However, a collagen deposition is observed in most of the cardiac diseases, hence the interest for myocardial fibrosis detection for clinical diagnosis and treatment of these diseases. It has also been detected in cases of hypertension, diabetes and valvular disorders, offering an insight as to other potential factors leading to heart failure. It has to be pointed out though that myocardial fibrosis is both a cause and a consequence of heart failure [1], [29], [31], [32]. Collagen distribution varies depending on the pathology, affecting localised areas of the tissue or being diffuse in the myocardium.

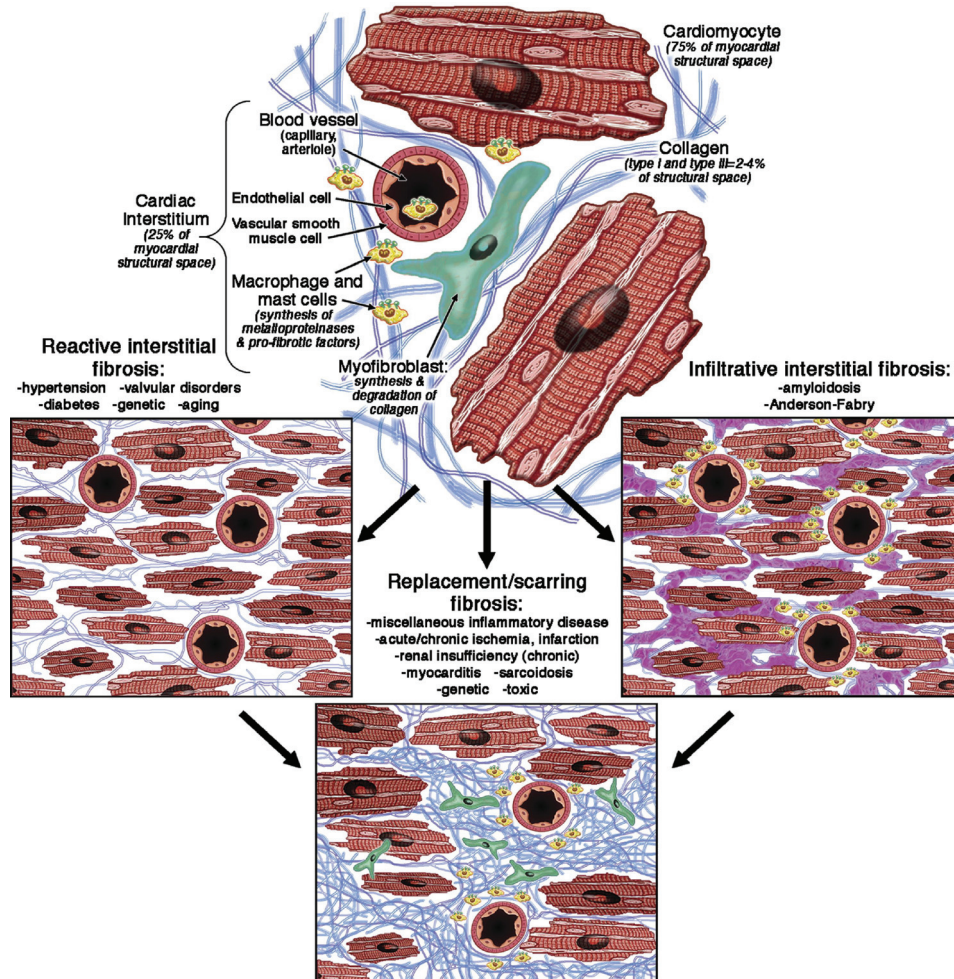


Figure 2.9: Etiophysiology of Myocardial Fibrosis. The development of myocardial fibrosis involves each cellular component of the myocardial tissue. Myocardial fibroblasts have a key role in the production of extracellular matrix, including collagen, under the influence of various factors such as renin-angiotensin system, myocyte apoptosis, pro-inflammatory cytokines, reactive oxygen species, etc. Figure reproduced from [1].

2.3 Clinical MRI standard for assessing myocardial fibrosis: T_1 -Mapping

As defined in Section 2.1.1, T_1 registers the course of recovery of longitudinal magnetisation and represents the time when this recovery has reached 63% of its original state (Figure 2.4, Equation 2.4). Relaxation time depends on the molecular environment of the water molecules present in each tissue, which makes it possible to characterise each tissue and

variations in the same tissue depending on its state (fibrosis or inflammation for instance). These variations can be enhanced using Gadolinium Contrast Agents (GCA). As there are differences in wash-in and wash-out kinetics of fibrotic and normal tissues, the contrast agents remain longer in fibrotic tissues than in healthy ones. These agents shorten the relaxation time (T_1), leading to a change in signal intensity between zones of high gadolinium concentration and normal myocardial tissue, allowing the detection of abnormal ECM concentration or a scar following recovery from a heart infarction, etc. [1], [33].

T_1 -mapping consist in a pixel-wise curve fitting based on images acquired at different time points of the recovery curve (Figure 2.10). Consequently, the pixel-map of T_1 is an estimation of the relaxation time parameter based on a signal model [11]. T_1 -mapping can be performed without GCA (native T_1 /pre-Gd) or with some (post-contrast T_1 /post-Gd). In most cases of disease, native T_1 values increase while post-contrast T_1 values decrease. Both provide measurement of intra and extracellular space but also allow for the calculation of the Extra Cellular Volume (ECV) with post-contrast T_1 by identifying the influence of accumulated GCA in the ECM [33], [34].

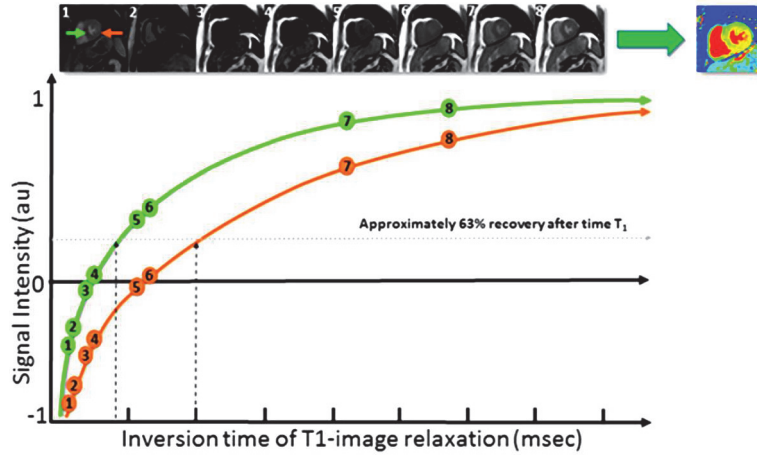


Figure 2.10: T_1 -mapping in the heart based on Modified Look-Locker Inversion Recovery (MOLLI). Illustration reproduced from [34].

The T_1 relaxation rate is defined as $R = \frac{1}{T_1}$; the change in relaxation rate between pre and post contrast can be expressed as

$$\Delta R = \frac{1}{T_{1\text{post}}} - \frac{1}{T_{1\text{pre}}} \quad (2.25)$$

therefore, the ECV fraction is defined by

$$ECV = \frac{\frac{1}{T_{1\text{myo post}}} - \frac{1}{T_{1\text{myo pre}}}}{\frac{1}{T_{1\text{blood post}}} - \frac{1}{T_{1\text{blood pre}}}} \times (1 - \text{hematocrit}) \quad (2.26)$$

In other words, the ECV fraction is defined as the relation of the contrast agent concentration in the extracellular space to the blood [35].

Late Gadolinium Enhancement relies on regional segregation of tissue characteristics to generate the imaging contrast. As it is grounded on differential degrees of spatial accumulation, regional differences within the myocardium need to be sharp for the GCAs to provide meaningful and accurate information (Figure 2.11). It is thus not operable in the case of a diffuse pathology affecting the myocardium in a uniform way, such as diffuse myocardial inflammation, fibrosis or hypertrophy. Early stages of certain diseases such as

non-ischemic cardiomyopathies, which are characterised by a combination of various diffuse interstitial processes, cannot be detected via LGE [33]. This might delay diagnosis and prognosis, though LGE proves to be very reliable at advanced disease stages.

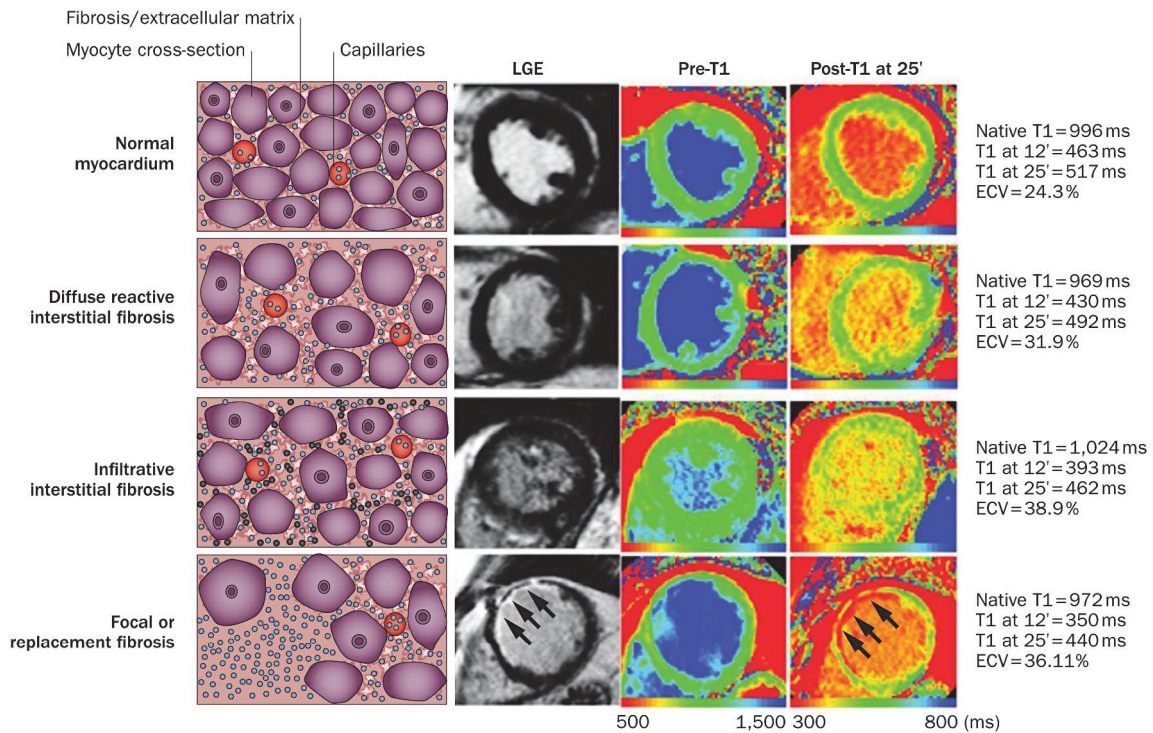


Figure 2.11: Different types of fibrosis and maps after contrast administration and post-contrast T_1 mapping (performed 25 min after agent administration). Depending on the nature of fibrosis (interstitial or replacement), the gadolinium retained highlights different patterns of collagen deposition. On the right, gadolinium molecules appear in blue, cellular infiltrates in grey circles and arrows show an ischaemic myocardial scar. Figure reproduced from [31].

As T_1 -Mapping allows the successful detection and assessment of significant depositions in the ECM, it has become the regular procedure and has been reviewed extensively and standardised for clinical use in [36].

Chapter 3

Materials and methods for in vitro UTE MR collagen signal studies

This chapter details the development made in order to define an experimental setup for the assessment of the MR signal from short- T_2^* components. It focuses specifically on the preparation of collagen/gelatin fibrillar matrices, the implementation of an accelerated UTE radial 3D imaging sequence and the development of a workflow for image reconstruction based on compressed sensing.

The development of the collagen/gelatin fibrillar matrices draw on a one-year collaboration with Dr. Alain Guignandon and Sylvie Peyroche from the research group SAINBIOSE: SAnité INgénérie BIOlogie St-Étienne (UMR INSERM 1059, St. Étienne, France).

3.1 Collagen/Gelatin fibrillar matrices

Published in vitro studies [4], [5], [37] have worked on aqueous solution (collagen type I and III powder diluted in demineralised water). These solutions do not correspond to the fibrillar structure of collagen in the human body [38]–[40]. Fibrillar collagen is the most abundant protein of the cardiac ECM composed of 80% of collagen type I and 10% of collagen type III [41].

Major fibrillar collagens are types I, II and III, and minor fibrillar collagens correspond to types V and XI. The common structural motif across collagen proteins is the triple helix structure, forming elongated fibril structures with a distinct 640–670 Å band periodicity (14 Å diameter and about 3000 Å length, Figure 3.1). The triple helix is formed by a repetitive pattern of an amino acid sequence: *glycine-Xaa-Yaa*, where *Xaa* and *Yaa* are often proline and hydroxyproline. Fibrillar collagen have a clear structural role of mechanical support and dimensional stability in biological structures [42].

This section details the preparations for making collagen/gelatin fibrillar dense matrices. The starting point for this study was to examine the MR spectra of aqueous solutions (collagen type I and III, no fibrillar structure) following the methodology published by Siu et al. [4]. Consequently, MR spectroscopy was used to validate the chemical shift of collagen in the fibrillar samples (collagen type I). In addition, the fibrillar organisation was assessed by cryosection of the dense phase of collagen, picosirus staining and polarised light observation.

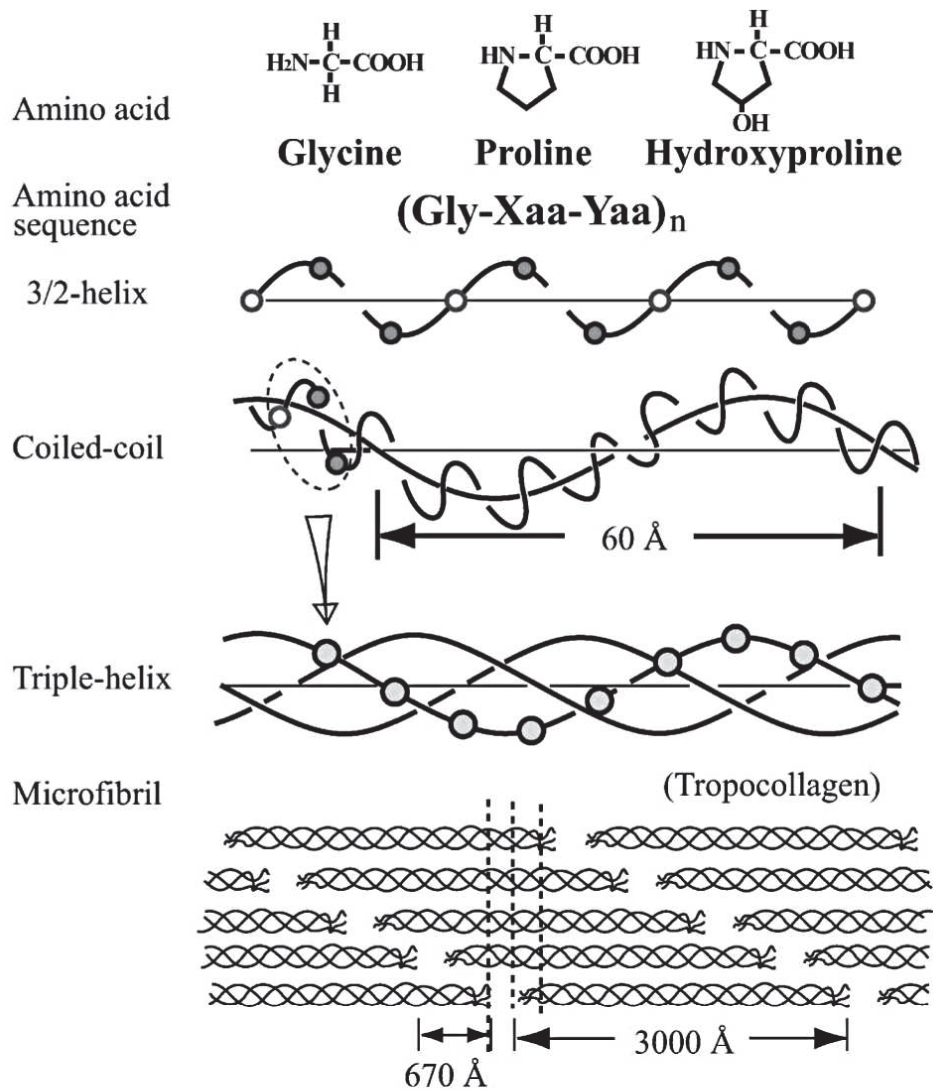


Figure 3.1: Structural organisation of collagen. The triple helix is formed by a repetitive pattern of an amino acid sequence: *glycine-Xaa-Yaa*, where *Xaa* and *Yaa* are often proline and hydroxyproline. Figure reproduced from [43].

3.1.1 Materials and methods

Experiments were conducted using a 3T MRI scanner (MAGNETOM Prisma, Siemens, Erlangen, Germany).

3.1.1.1 Aqueous solutions of collagen type I and III

Collagen solutions were prepared by dissolving collagen powder (NeoCell Super Collagen Type I and III Powder, NeoCell, Irvine, California, USA) in demineralised water. A second set of solutions were prepared including 2.5% of Agar. Collagen concentrations are described in table 3.1.

Collagen solution (percentage of mass)	Collagen powder/Water (g/50 mL)	Agar (g/50 mL)
40%	20	1.25
30%	15	1.25
20%	10	1.25
10%	5	1.25
5%	2.5	1.25

Table 3.1: Percentage of collagen concentration across tubes for the first set of solutions.

3.1.1.2 Collagen/Gelatin fibrillar matrices of collagen type I

Collagen/gelatin diluted solutions were obtained by mixing pure collagen (tail-rat Coll1 3 mg/mL, Institut Jacques Boy) and gelatin (Sigma-Aldrich, ref. G2625, 300 g bloom) prepared separately. The gelatin concentration was fixed to 10% for collagen concentrations ranging from 0.025 g/L to 2 g/L. 45ml of collagen/gelatin mix was prepared in cell culture medium and neutralised with *NaOH* to initiate collagen fibrillogenesis and densification of the matrices. Tubes were gently agitated to homogeneously distribute collagen solutions. Fibrillogenesis is done at 37 °C, 5% CO_2 in an incubator overnight.

3.1.1.3 Non-Localised spectroscopy

Non-localized spectroscopy (NSPECT) was performed on different collagen solutions (sequential acquisitions, 1 scan per solution) using a single element loop coil (RAPID Biomed, Wursburg, Germany). Relevant acquisition parameters: vector size = 512, TE=0.15 ms, TR=2000 ms, and Bandwidth=5000 Hz.

3.1.1.4 Polarised light microscopy

Fibrillary organisation of the dense phase of collagen was assessed by cryosection of the gel, picosirus staining and polarized light observation.

3.1.2 Results

After fibrillogenesis was completed, two phases were observed. One containing pure gelatin (no fibrillary organisation under polarised light) and one containing a dense fibrillary/porous matrix composed of collagen and gelatin (fibrillary phase). The densification process by adding gelatin solution was tested ([44], [45]) to increase fibrillar density without removing water of the mixture. The gelatin concentration was fixed to 10% based on previous trials (Figure 3.2) in which concentrations ranging from 1% to 20% were assessed. Figure 3.3 shows the final collagen/gelatin fibrillar matrices.

Representative microscopy photographs on the collagen/gelatin fibrillar dense phase are presented in Figure 3.4.

The Figure 3.5 presents the MR spectra across the different collagen-based solutions. The dominant peak of the collagen macromolecule was observed between -2.6 and -4.0 ppm as reported by [4], [37], [46].

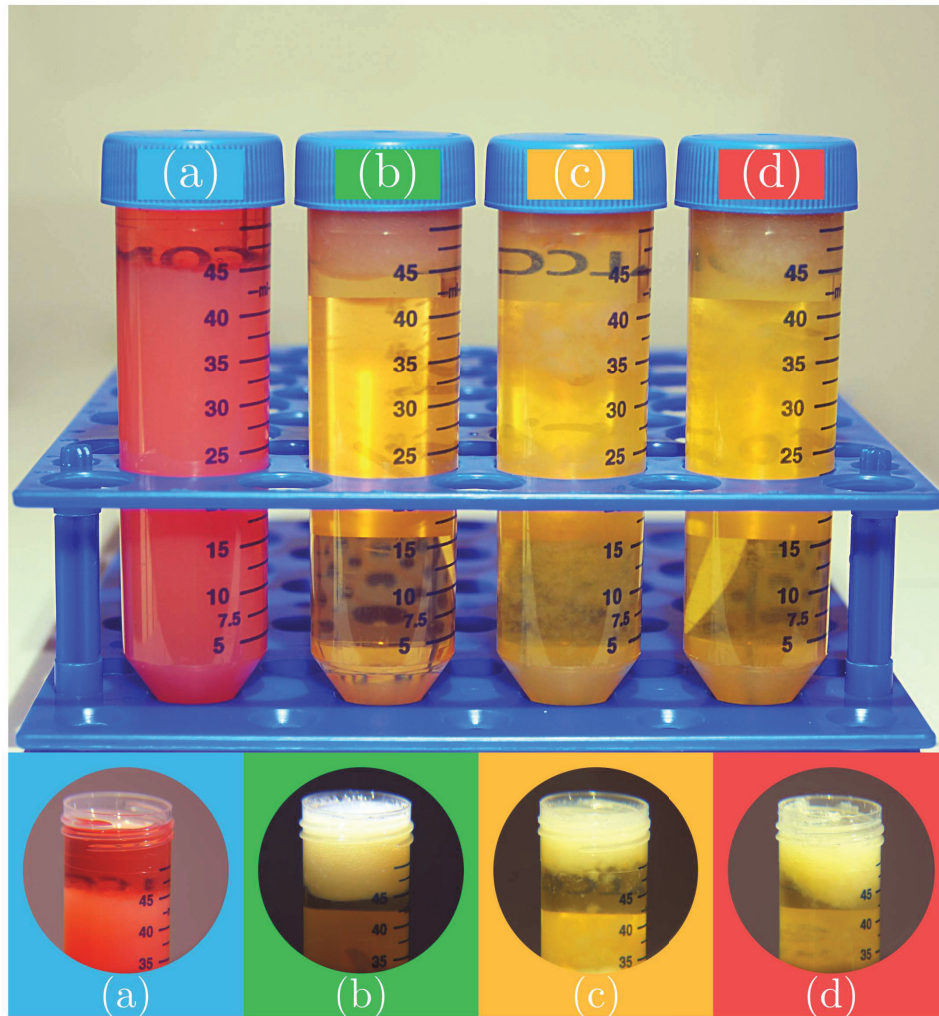


Figure 3.2: Collagen/Gelatin fibrillar dense matrices prepared with a fixed concentration of collagen. The collagen dense phase rises in the tube because of the higher gelatin density. (a) Collagen gel (10 mL) diluted in a concentrated medium; collagen/gelatin solutions prepared with: (b) 1%, (c) 5% and (d) 10% of gelatin.

Collagen/Gelatin fibrillar matrices

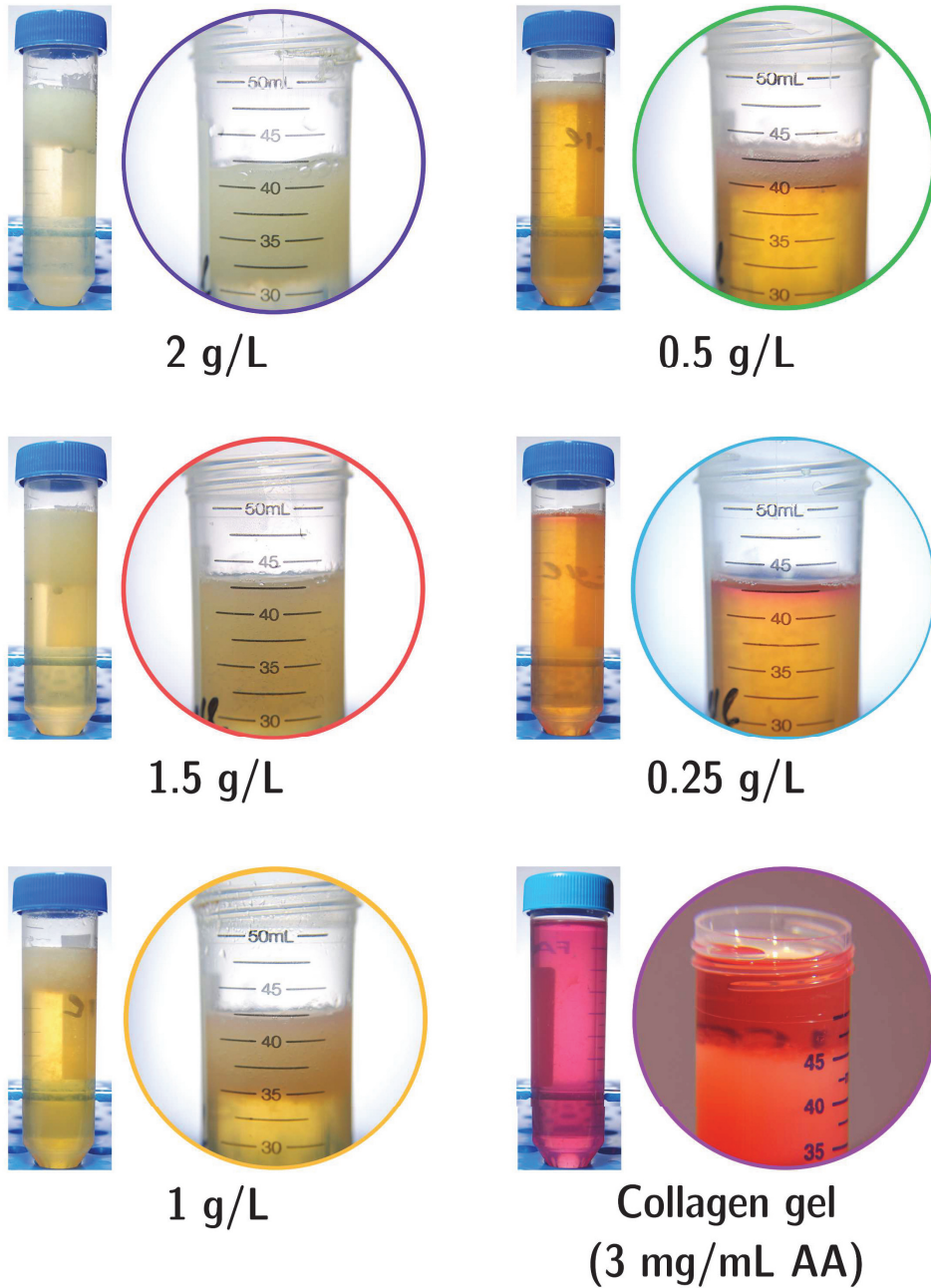


Figure 3.3: Collagen/Gelatin fibrillar matrices. The collagen type I concentrations used in the initial solution are ranging from 0.25 g/L to 2 g/L.

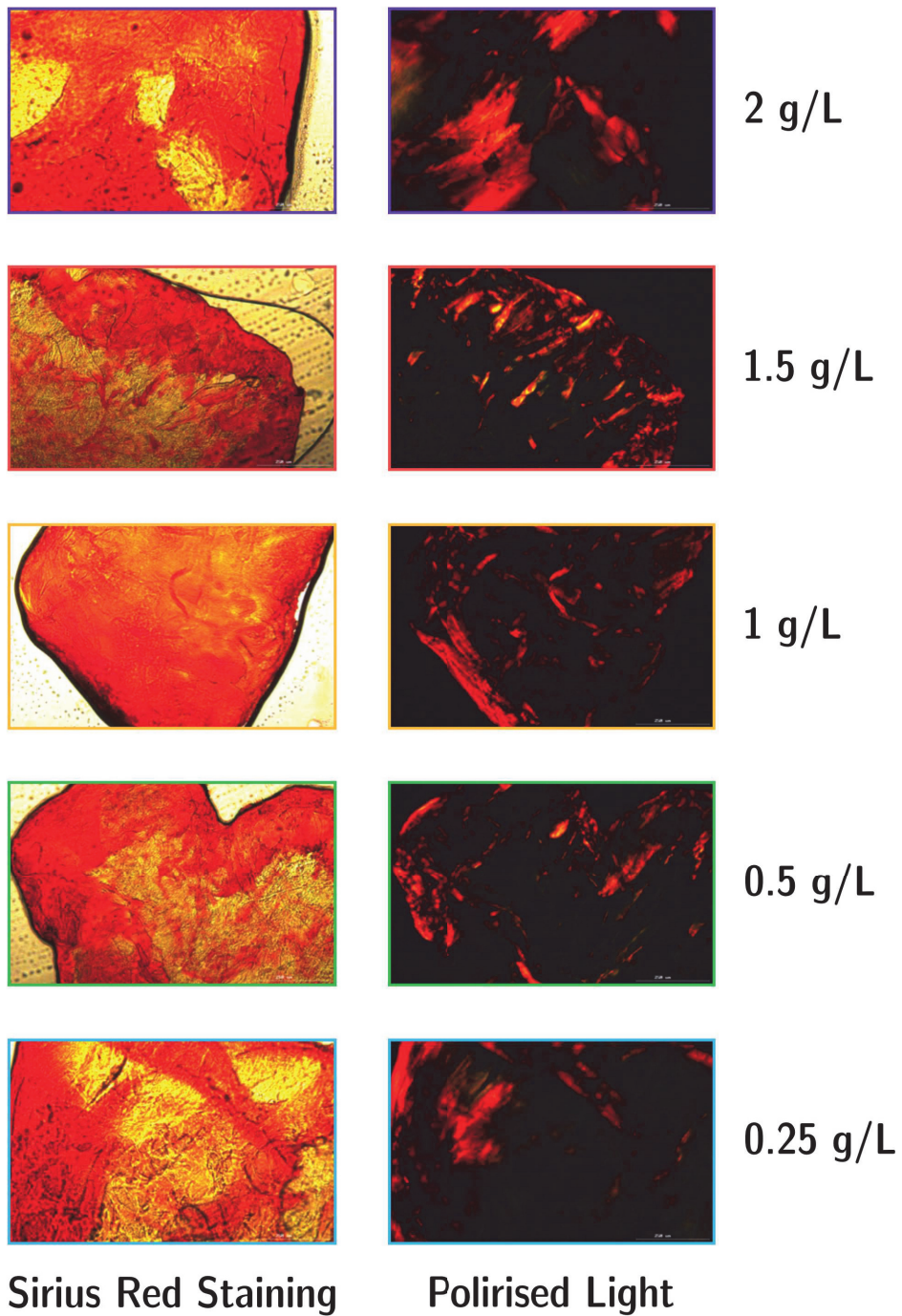


Figure 3.4: Microscopy photographs on the collagen/gelatin fibrillar dense phase from each solution.

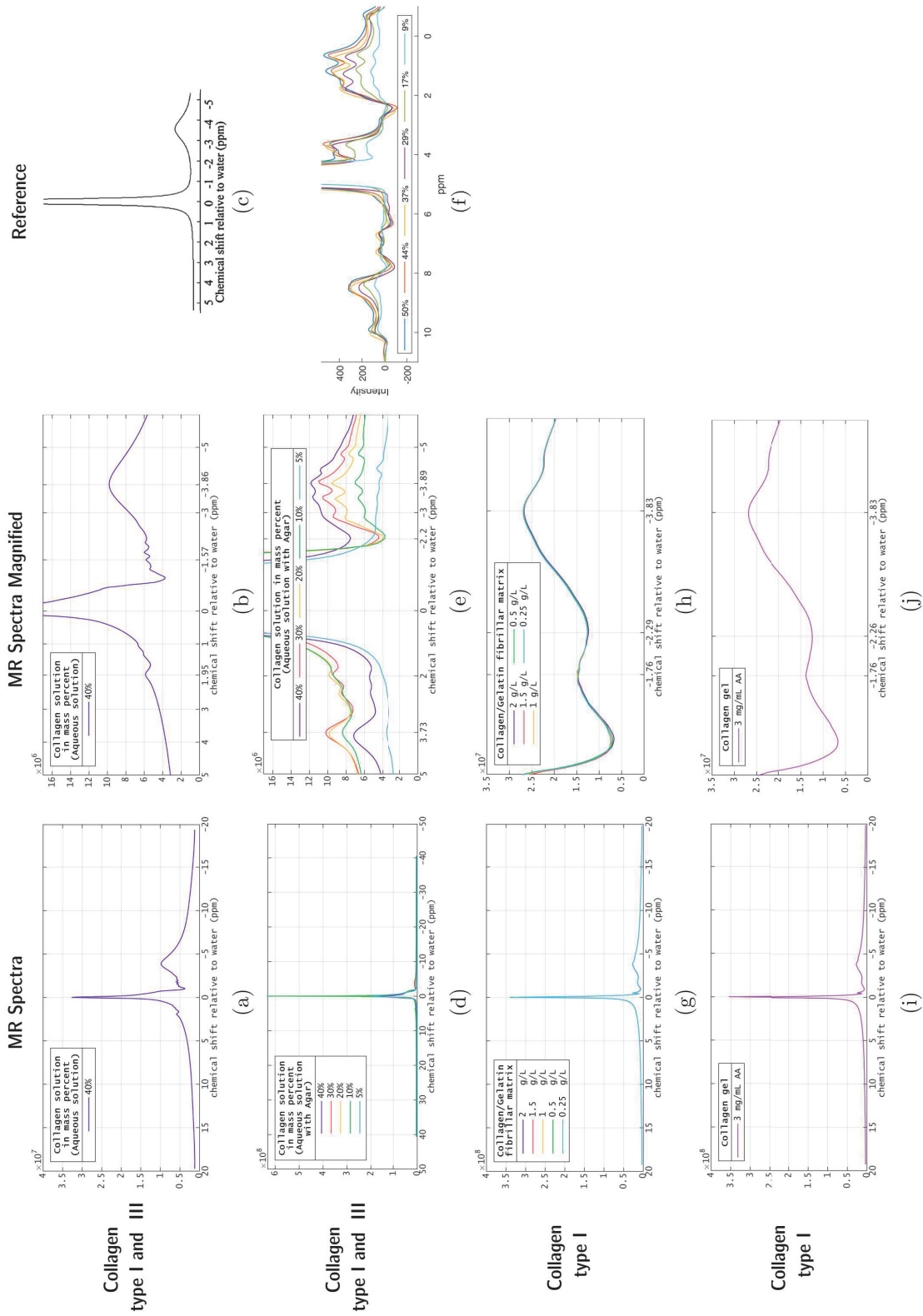


Figure 3.5: MR Spectra from collagen solutions. (a) and (b) Spectra of the 40% aqueous solution; (c) collagen spectra, reproduced from Figure 2 in [16]; (d) and (e) spectra of collagen solutions (concentrations ranging from 5% to 40%) with Agar; (f) collagen spectra, reproduced from Figure 2 in [16]; (g) and (h) spectra of collagen/gelatin fibrillar dense (i) and (j) spectra from collagen gel (3 mg/mL acetic acid).

3.1.3 Discussion

Previous imaging experiments were performed in order to assess and define the preparation of collagen/gelatin fibrillar matrices. The process was challenging and that has limited the number of successful trials, a limitation for a statistical analysis and validation (repeatability of matrices with the same collagen density) . In addition, as fibrillogenesis is the result of a random reaction generating a dense fibrillary/porous matrix (composed of collagen and gelatin), the collagen concentration (in mass percent) is unknown. This study reports the collagen concentration in terms of g/L of collagen type I used to induce fibrillogenesis. Consequently, the preparation of samples with a well-known final collagen concentration is a limitation of the presented technique.

The chemical shift of -3.8 ± 0.4 for the different collagen samples (aqueous solutions and fibrillar matrices) was close to the values reported by Kflak-Hachulska et al. (-3.2 ppm [46]), Siu et al. (-3.56 ppm [4]). The spectra profile from aqueous solutions with Agar are close with the 11 peaks model presented by Fischer et al. [37]. Accurate characterisation of the MR spectra is out of the scope of this study. MR spectra was used as an assessment measure in the preparation of collagen/gelatin fibrillar matrices. The difference between the reported chemical shifts and the estimation in this study may be explained by the nature of the baseline collagen used in the solutions: powdered type I collagen from bovine Achilles tendon [46], powdered type I and III collagen from bovine hide [4].

3.1.4 Conclusion

In vitro MR spectroscopy experiments were conducted in order to define the preparation of collagen/gelatin fibrillar dense solutions made of collagen type I which corresponds to a 0.25 of the collagen I / collagen III ratio in early post-myocardial infarction [47]. Fibrillar organisation was assessed by cryosection of the dense phase of collagen, picosirus staining and polarised light observation.

3.2 Accelerated multi-echo radial 3D imaging sequence and compressed sensing reconstruction

The baseline for the sequence development is the Siemens BEAT module. This module includes a ECG-triggered imaging sequence with a radial 3D sampling scheme enabling UTE acquisitions. Image reconstruction is handled by Non-Cartesian ICE program on the scanner [48]. The objective was to implement a UTE radial 3D acquisition sequence with sub-sampling parameters including an image reconstruction workflow based on parallel imaging and compressed sensing.

3.2.1 Materials and methods

3.2.1.1 Golden-Angle radial 3D k-Space sampling

The default 3D radial trajectory (DT) in the Siemens BEAT sequence follows a spiral path on the surface of a sphere (uniformly distributed points) as described in [49].

The polar θ and azimuthal ϕ angles for the k -th projection are calculated by

$$\theta_k = \arccos(h_k), h_k = -1 + \frac{2(k-1)}{N_p-1}, 1 \leq k \leq N_p \quad (3.1)$$

$$\phi_k = \left(\phi_{k-1} + \frac{3.6}{\sqrt{N_p}} \times \frac{1}{\sqrt{1-h_k^2}} \right) \times \text{mod}(2\pi), 2 \leq k \leq N_p - 1, \phi_1 = \phi_{N_p} = 0$$

where N_p is the total number of projections.

To introduce an incoherent sampling method, a 3D radial sampling scheme based on the Golden Angle (GA) as described in [50] was implemented in the BEAT sequence. The polar θ and azimuthal ϕ angles for the k -th projection are calculated by

$$\theta_k = \arccos(\text{mod}(k \psi_2, 1)) \quad (3.2)$$

$$\phi_k = 2\pi \cdot \text{mod}(k \psi_1, 1) \quad (3.3)$$

where the multidimensional golden means are $\psi_1 = 0.4656$ and $\psi_2 = 0.6823$.

One of the key aspects in the optimisation of a compressed sensing strategy is the transform sparsity along time dimension. Consequently, in addition to the GA-based trajectory, a GA-based rotation in time, based on [51], has been included in order to increase the sparsity acquired signal. The k-Space was sampled with the radial 3D GA trajectory. The rotation angle for the j -th scan was calculated by the equation

$$\alpha_j = \left((j-1) \times \frac{\pi}{N_p} \times \frac{\sqrt{5}-1}{2} \right) \times \text{mod}(\pi, N_p) \quad (3.4)$$

where j is the rotation index and the number of projections is defined as

$$N_p = \frac{\text{Projections per echo}}{\text{Temporal resolution}} \quad (3.5)$$

The N_p must include a resolution factor in order to better exploit k-Space sampling across different scans (temporal resolution). Therefore, polar and azimuthal angles for the k -th projection are rotated by α_j

$$\theta_{k,j} = \theta_k + \alpha_j \quad (3.6)$$

$$\phi_{k,j} = \phi_k + \alpha_j \quad (3.7)$$

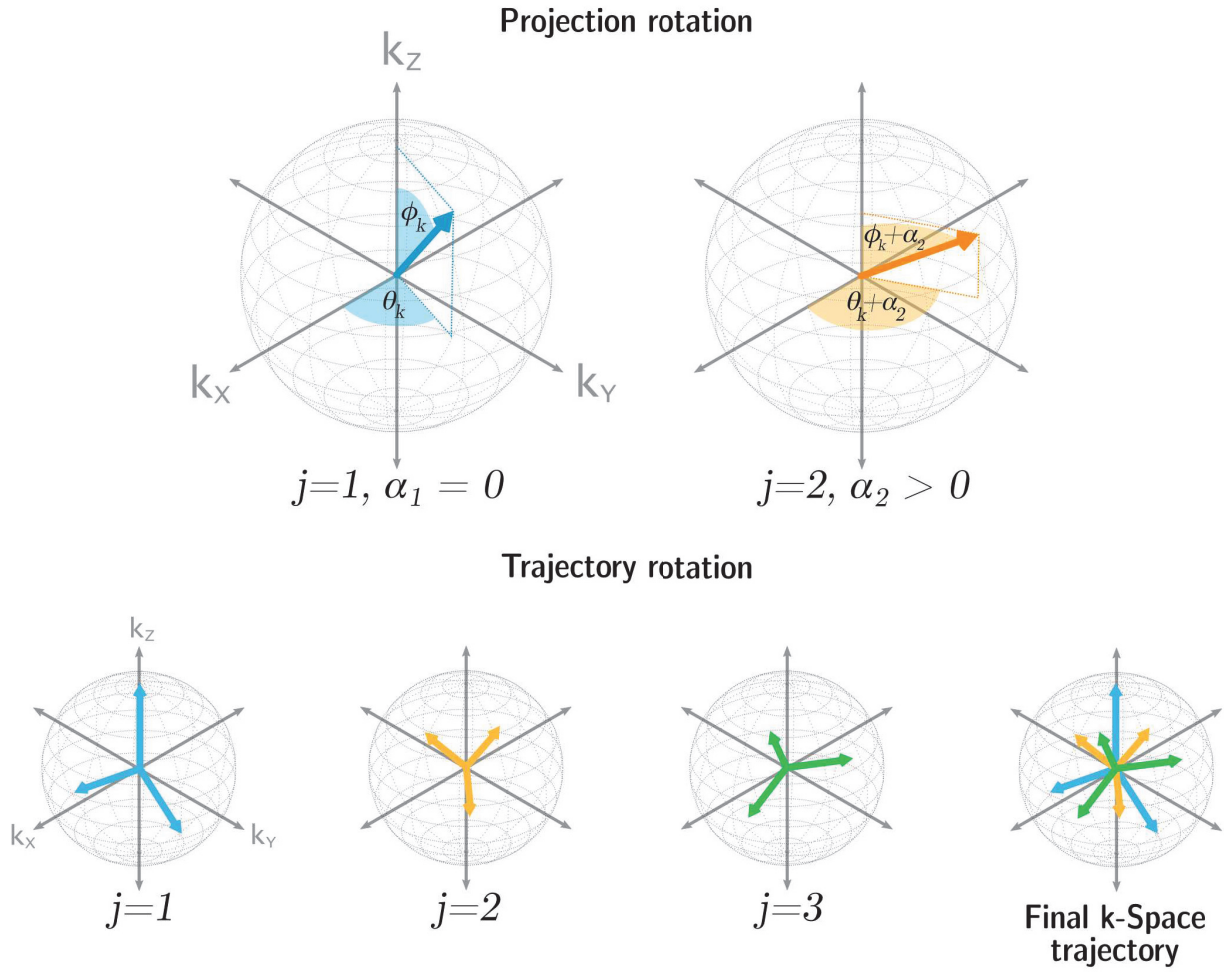


Figure 3.6: k-Space trajectory rotation. A single projection is rotated by α_i (Equation 3.6) across different temporal points j (scans).

To illustrate most clearly, for 6 consecutive scans (i.e. $TE = \{0.05, 0.6, 1.2, 2.2, 6.0, 10\}$ ms) with 72 projections, temporal resolution 6, $N_p = \frac{72}{6}$. The first scan is performed with the baseline trajectory $\alpha_1 = 0$; for the second scan, the trajectory is rotated by the angle α_2 .

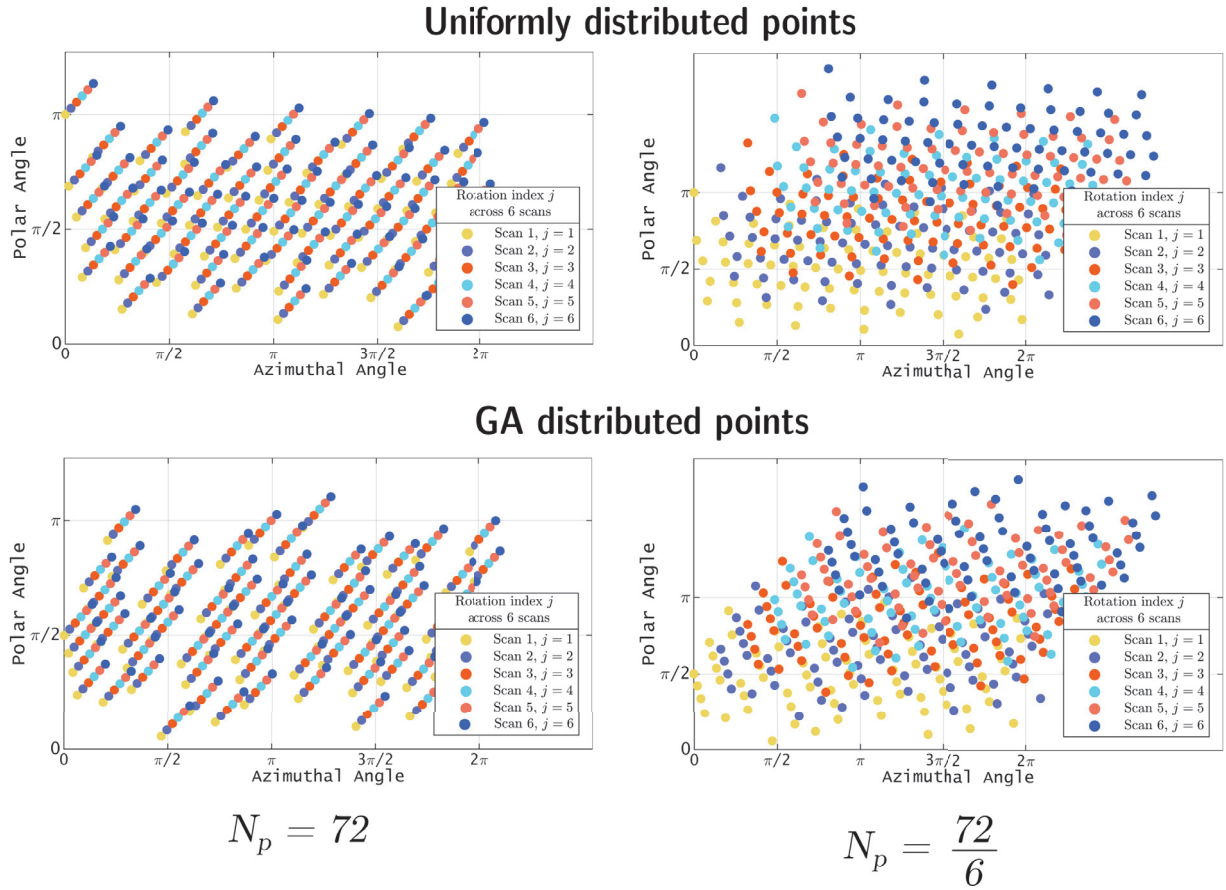


Figure 3.7: Distribution of the projection's angles in k-Space. If N_p in Equation 3.4 is equal to the number of projections per scan, the trajectory does not rotate enough (across scans) as if $N_p = \frac{\text{Projections per echo}}{\text{Temporal resolution}}$. This translates to a better signal sampling. Trajectory calculated for 72 projections. GA: Golden Angle.

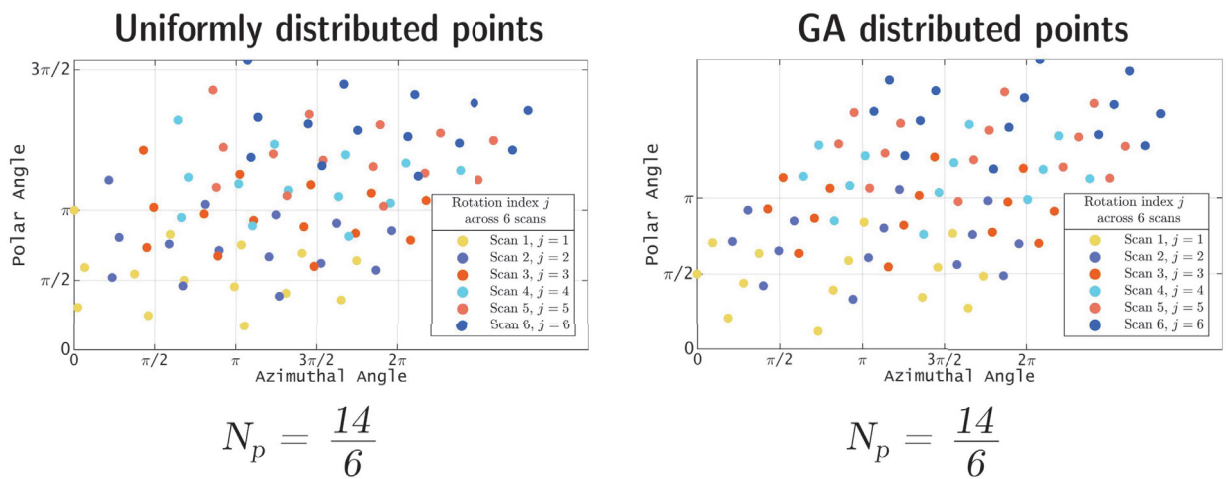


Figure 3.8: Comparison of radial 3D k-Space trajectories. GA trajectory provides more heterogeneity (no overlapping points) than a trajectory based on uniformly distributed points.

3.2.1.2 Imaging sequence implementation

The sampling strategy described in the previous section was implemented on the Siemens' integrated development environment for applications software (IDEA) in C++ programming language. The sequence diagrams of the default radial 3D trajectory and the GA implementation are presented in figures 3.9 and 3.10 respectively.

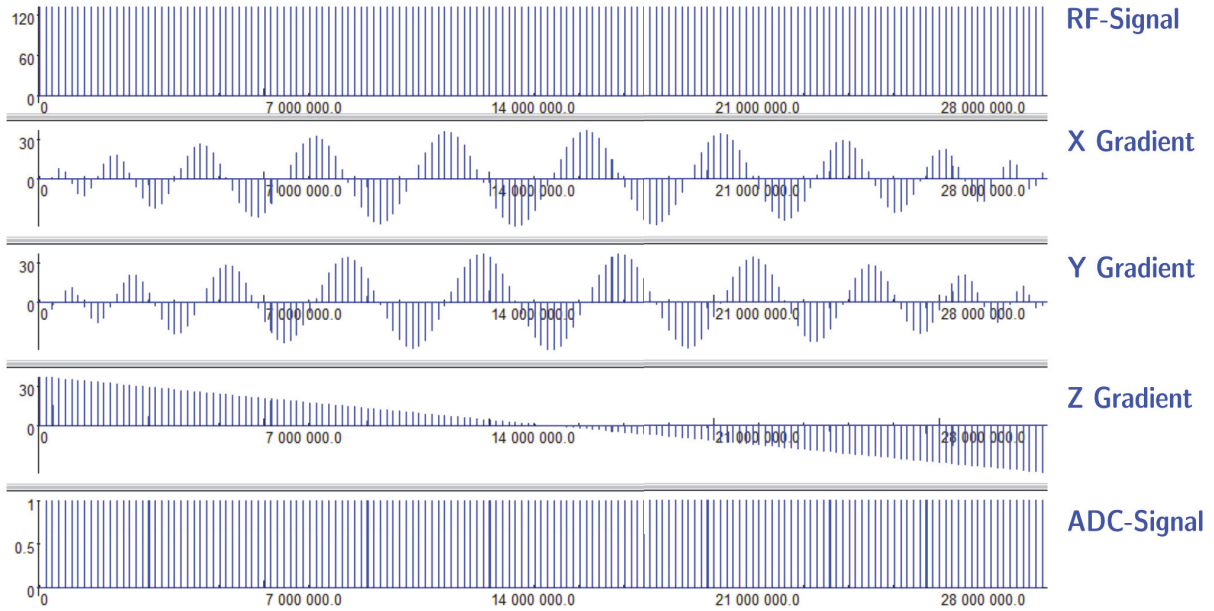


Figure 3.9: Sequence diagram of the default radial 3D trajectory. Screenshot of the Siemens IDEA simulation environment. Simulation performed with 126 projections.

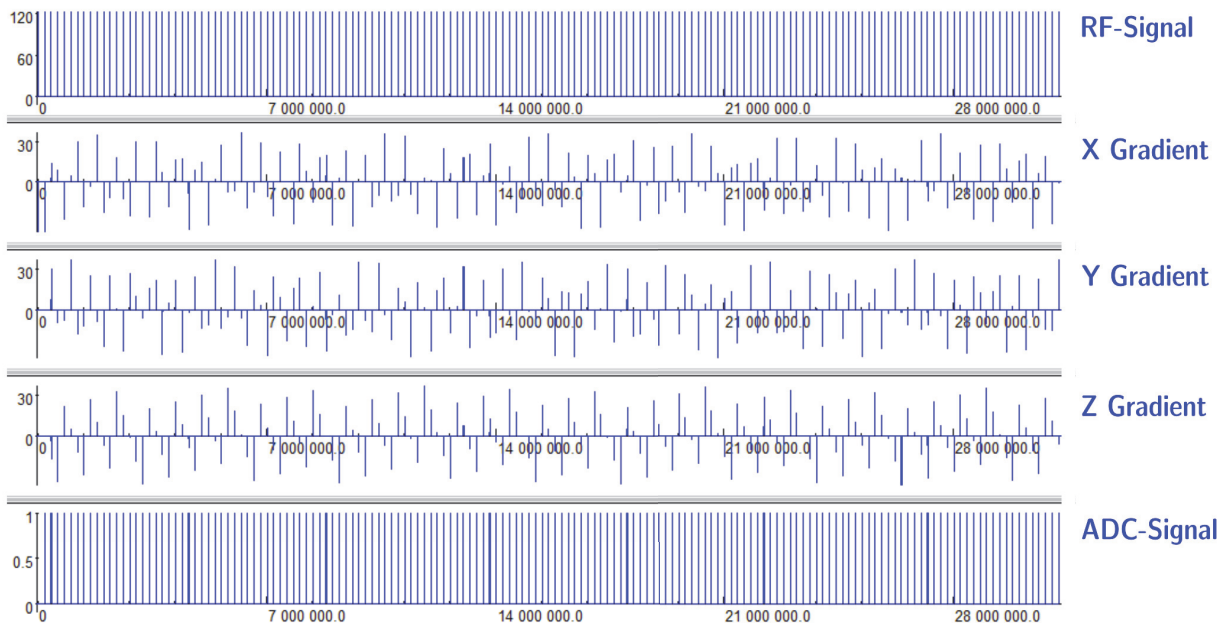


Figure 3.10: Sequence diagram of the implemented Golden-Angle radial 3D trajectory. Screenshot of the Siemens IDEA simulation environment. Simulation performed with 126 projections.

The graphical user interface (imaging sequence special card) displays the configurable parameters *Rotation index* (Equation 3.4) and *Temporal Resolution* (Equation 3.5) as presented in Figure 3.11.

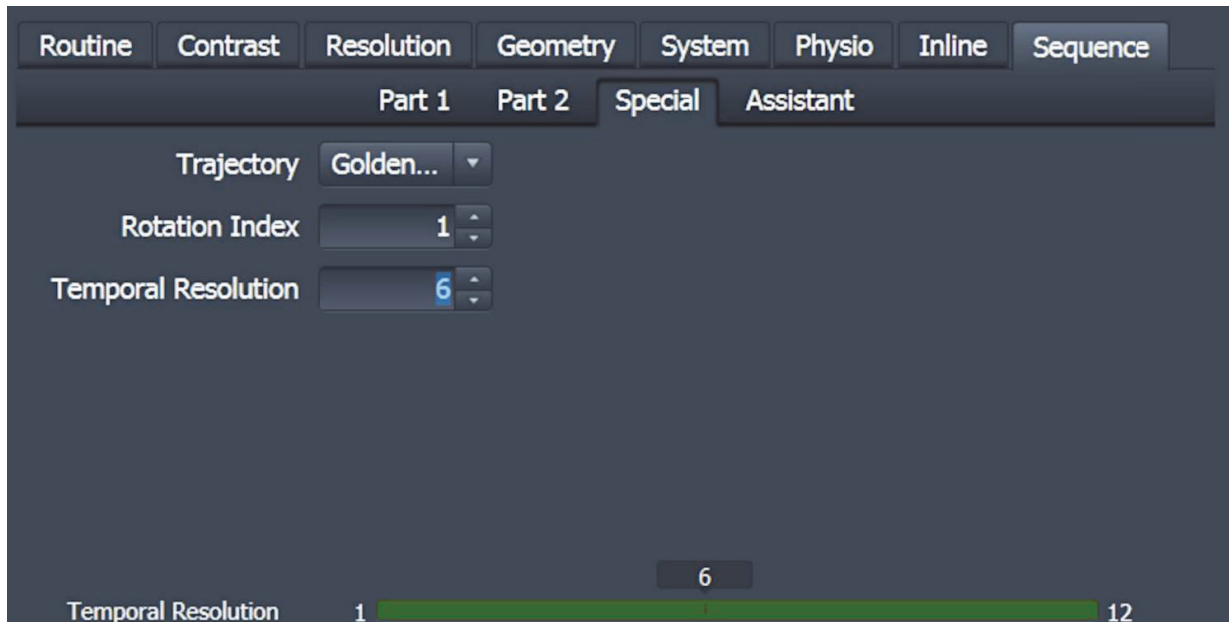


Figure 3.11: Special card on the graphical user interface for setting trajectory rotation parameters: rotation index j (Equation 3.4) and temporal resolution (Equation 3.5).

3.2.1.3 Data acquisition

In vivo experiments were conducted using a 3T MRI scanner (MAGNETOM Prisma, Siemens, Erlangen, Germany) with an 18 channels cardiac phased-array coil combined with appropriate elements of the spin array coils, as used in clinical practice. Each scan was ECG-triggered during a breath-hold of 24 s. Imaging parameters are summarised in Table 3.2. The parameters for the trajectory rotation across scans are presented in Table 3.3.

Parameter	Description
k-Space trajectory	Golden-Angle
TR (<i>ms</i>)	456
TE (<i>ms</i>)	0.05, 1.2, 1.7, 2.2, 3.55, 4.5, 6.0, 8.0, 10
FOV (<i>mm</i>)	400
Image matrix	208x208
Pixel resolution (<i>mm</i> ³)	1.9
Flip angle (<i>deg</i>)	15
Bandwidth (<i>Hz/pixel</i>)	728
Projections per scan	1040
Samples per projection	208
Acquisition time per scan (<i>s</i>)	24 (single breath-hold)

Table 3.2: Imaging parameters.

Echo time index	Echo time (ms)	Scan index	Projections per scan	Trajectory	Rotation index	Temporal resolution
1	0.05	1	1040	GA	1	3
		2	1040	GA	2	3
		3	1040	GA	3	3
2	0.6	4	1040	GA	1	3
		5	1040	GA	2	3
		6	1040	GA	3	3
3	1.2	7	1040	GA	1	3
		8	1040	GA	2	3
		9	1040	GA	3	3
4	1.7	10	1040	GA	1	3
		11	1040	GA	2	3
		12	1040	GA	3	3
5	2.2	13	1040	GA	1	3
		14	1040	GA	2	3
		15	1040	GA	3	3
6	3.55	16	1040	GA	1	3
		17	1040	GA	2	3
		18	1040	GA	3	3
7	4.5	19	1040	GA	1	3
		20	1040	GA	2	3
		21	1040	GA	3	3
8	6.0	22	1040	GA	1	3
		23	1040	GA	2	3
		24	1040	GA	3	3
9	8.0	25	1040	GA	1	3
		26	1040	GA	2	3
		27	1040	GA	3	3
10	10	28	1040	GA	1	3
		29	1040	GA	2	3
		30	1040	GA	3	3

Table 3.3: Trajectory rotation parameters across scans. Rotation index j (Equation 3.4) and temporal resolution (Equation 3.5). GA: Golden Angle.

3.2.1.4 Compressed sensing-based reconstruction

As presented in Section 2.1.4, the CS-Based reconstruction algorithm relies on the solution to the following combinatorial optimisation problem

$$x = \arg \max_x \|Ax - y\|_2^2 + \sum_k \lambda_k R_k(x) \quad (3.8)$$

where x is the image and y the k-Space data. The sensing (or encoding) matrix A includes the gridding operation, Fourier transform and coil sensitivity. The sparsity trans-

forms are denoted by R_k and λ_k is the corresponding regularisation parameter. In this study, the models used for image reconstruction were defined as

$$x = \arg \max_x \|Ax - y\|_2^2 + \lambda_1 TV_{xyz}(x) + \lambda_2 \Psi_{xyz}(x) \quad (3.9)$$

$$x = \arg \max_x \|Ax - y\|_2^2 + \lambda_1 TV_{xyz}(x) + \lambda_2 \Psi_{xyz}(x) + \lambda_3 \Psi_{xyzt}(x) + \lambda_4 TV_t(x) \quad (3.10)$$

where TV_{xyz} and Ψ_{xyz} are the Total Variation (TV) and the L1-Wavelet sparsity transforms in the spatial dimension respectively; Ψ_{xyzt} the joint L1-Wavelet and TV_t , the sparsity transform in the temporal dimension.

The image reconstruction workflow was implemented on BART [52]–[54] (Figure 3.12). Coil compression was performed (from 30 to 15 receiver coils) using Singular Value Decomposition (SVD) with a block size of 16. Sensitivity maps were calculated with an Adaptive Method with an eigenvalue cut-off of 0.54 over a calibration region of radius 24. Sensitivity maps calculation includes soft-SENSE [55] and intensity correction. Regularisation parameters were defined experimentally as λ_1 , λ_2 , λ_3 and λ_4 as presented in Table 3.4.

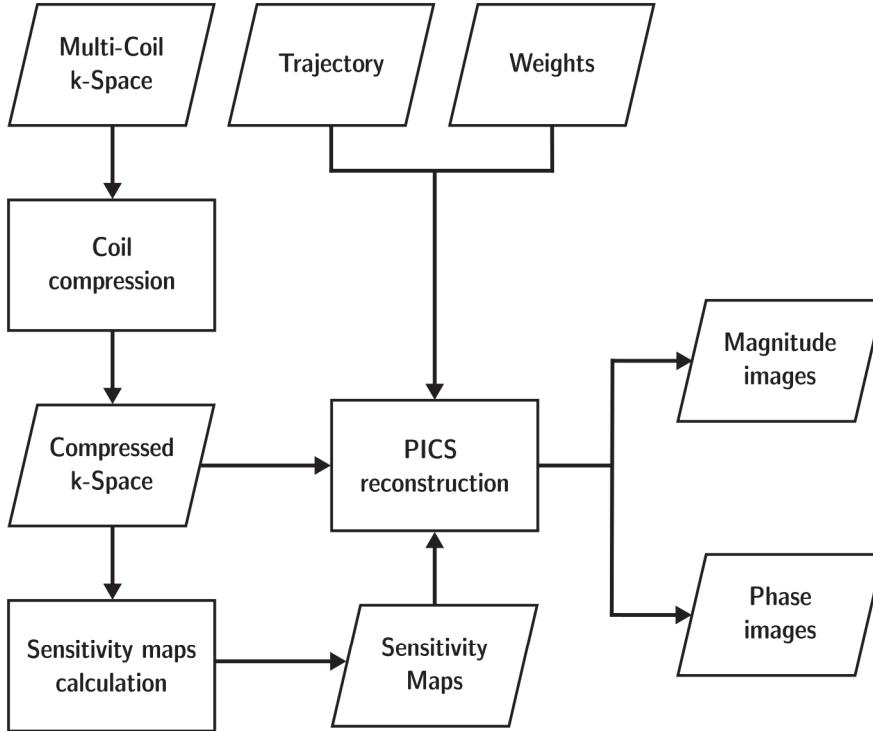


Figure 3.12: Image reconstruction workflow. PICS: Parallel Imaging and Compressed Sensing.

Sparsity transform	Regularisation parameter	Model 1 value	Model 2 value
TV_{xyz}	λ_1	0.057	0.057
Ψ_{xyz}	λ_2	0.033	0.033
Ψ_{xyzt}	λ_3	-	0.033
TV_t	λ_4	-	0.027

Table 3.4: Regularisation parameters. Model 1 corresponds to Equation 3.9 and Model 2 corresponds to Equation 3.10.

For the purpose of this study, the k-Space data were assembled according to the schemes defined in Table 3.5. In k-Space scheme A, the k-Space is composed of 3120 projections per echo time (100% k-Space data), whereas scheme B and C have 2080 ($\sim 66\%$ k-Space data) and 1040 ($\sim 33\%$ k-Space data) projections respectively. These schemes have the same k-Space trajectory for each echo time. In k-Space scheme D, the k-Space trajectory is not the same across echo times (rotation scheme presented in Table 3.3) and is composed of $\sim 33\%$ of the acquired k-Space data. Therefore, different number of projections and different trajectories per echo time were used to assess the impact of the trajectory rotation across echo times. In this direction, the image reconstruction was performed using spatio-temporal sparsity (Model 2, Equation 3.9) and spatial sparsity (Model 1, Equation 3.9) as defined in Table 3.6. Image reconstruction was performed on a computer cluster of 32 cores, Intel(R) Xeon(R) Gold 6226R, 2.90GHz; required RAM memory is specified in Table 3.6.

k-Space scheme	Echo time	k-Space data (Scan indices)	Projections per echo time
A	0.05	(1,2,3)	3120
	0.6	(4,5,6)	3120
	1.2	(7,8,9)	3120
	1.7	(10,11,12)	3120
	2.2	(13, 14, 15)	3120
	3.55	(16, 17, 18)	3120
	4.5	(19, 20, 21)	3120
	6	(22, 23, 24)	3120
	8	(25, 26, 27)	3120
	10	(28, 29, 30)	3120
B	0.05	(1,2)	2080
	0.6	(4,5)	2080
	1.2	(7,8)	2080
	1.7	(10,11)	2080
	2.2	(13, 14)	2080
	3.55	(16, 17)	2080
	4.5	(19, 20)	2080
	6	(22, 23)	2080
	8	(25, 26)	2080
	10	(28, 29)	2080
C	0.05	(1)	1040
	0.6	(4)	1040
	1.2	(7)	1040
	1.7	(10)	1040
	2.2	(13)	1040
	3.55	(16)	1040
	4.5	(19)	1040
	6	(22)	1040
	8	(25)	1040
	10	(28)	1040
D	0.05	(1)	1040
	0.6	(5)	1040
	1.2	(9)	1040
	1.7	(10)	1040
	2.2	(14)	1040
	3.55	(18)	1040
	4.5	(19)	1040
	6	(23)	1040
	8	(27)	1040
	10	(28)	1040

Table 3.5: k-Space data schemes. Data scheme A includes 3120 projections per echo time acquired in 3 scans. The trajectory rotation across scans is specified in Table 3.3, meaning that in k-Space scheme A the k-Space trajectory is the same for all echo times. In comparison, scheme D includes 1040 projections per echo time in which the k-Space trajectory was rotated across echo times according to Table 3.3.

k-Space scheme	Reconstruction model	Cores	Memory (GB)	Threads
A	1	32	64	16
A	2	32	240	16
B	1	32	64	16
C	1	32	64	16
C	2	32	192	16
D	2	32	192	16

Table 3.6: Image reconstruction and computing requirements. GB: Gigabytes.

3.2.1.5 Data analysis

Image quality metrics (IQM) were calculated on reconstructed magnitude images in order to quantify the impact of the trajectory rotation and image reconstruction models. The mean-squared error (MSE) was calculated as

$$MSE = \frac{1}{mn} \sum_{i=1}^m \sum_{j=1}^n (x_{i,j} - y_{i,j})^2 \quad (3.11)$$

where m is the number of rows and n the number of columns in the images; $x_{i,j}$ and $y_{i,j}$ the pixel values (signal intensity) of the images x and y .

As the mean-squared error depends strongly on the image intensity scaling, and there can be signal differences on magnitude images due to k-Space sub-sampling, the peak signal-to-noise ratio (PSNR) was calculated as

$$PSNR(x, y) = -10 \log_{10} \frac{MSE}{S^2} \quad (3.12)$$

where S is the maximum pixel value. Finally, for measuring structural image quality, the structural similarity (SSIM) index was calculated as

$$SSIM(x, y) = \frac{(2\mu_x\mu_y + C_1) + (2\sigma_{xy} + C_2)}{(\mu_x^2 + \mu_y^2 + C_1)(\sigma_x^2 + \sigma_y^2 + C_2)} \quad (3.13)$$

where μ_x and μ_y are the pixel sample mean of x and y respectively; σ_x^2 the variance of x ; σ_y^2 the variance of y ; σ_{xy} the covariance of x and y ; $c_1 = (k_1L)^2$ and $c_2 = (k_2L)^2$ two stabilisation variables with constants k_1 and k_2 [56].

3.2.2 Results

The magnitude images reconstructed with the k-Space scheme A and models 1 and 2 (A1 and A2 respectively) were used as the reference images for image quality assessment. A1 and A2 used 100% of the k-Space data. The magnitude images assessed were C2 and D2 which used $\sim 33\%$ k-Space data, representing a sub-sampled k-Space. C2 had the same k-Space trajectory for each echo time, reconstructed with Model 2 (including temporal dimension) whereas D2 the trajectory was rotated as specified in Table 3.3. Results with k-Space scheme B were excluded from figures as there is not a significant difference regarding IQM.

Representative magnitude images reconstructed using k-Space schemes A, C, and D at 0.05 ms are presented in Figure 3.13. D2 ($\sim 33\%$ k-Space data, trajectory rotated across echo times and spatio-temporal reconstruction model) reveal a high similitude to reference

images. Structural similarity is 10% higher than C2 compared with A2. The peak signal-to-noise ratio is almost the same as A2. The row and column profiles provide a quick overview of the amount of detail across images (sharpness). The row profile exhibits a similar signal intensity shape in all images. However, the column profile shows a difference in C2 which explains the lower value in structural similarity compared to D2.

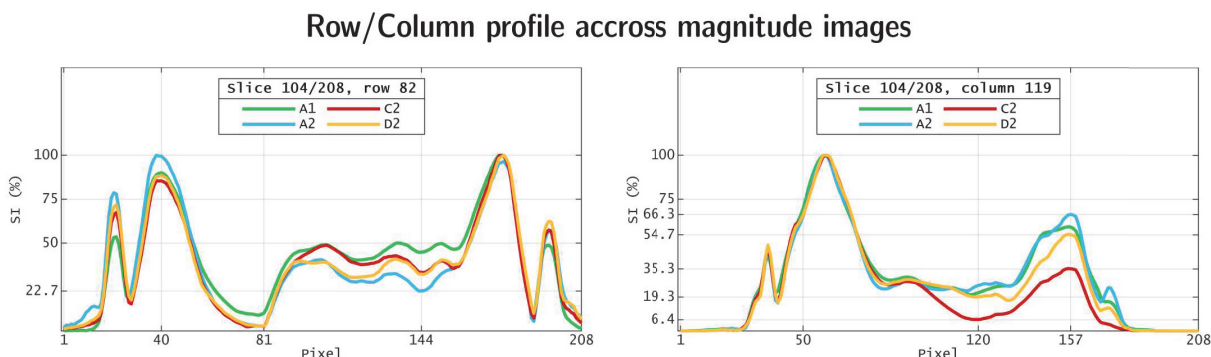
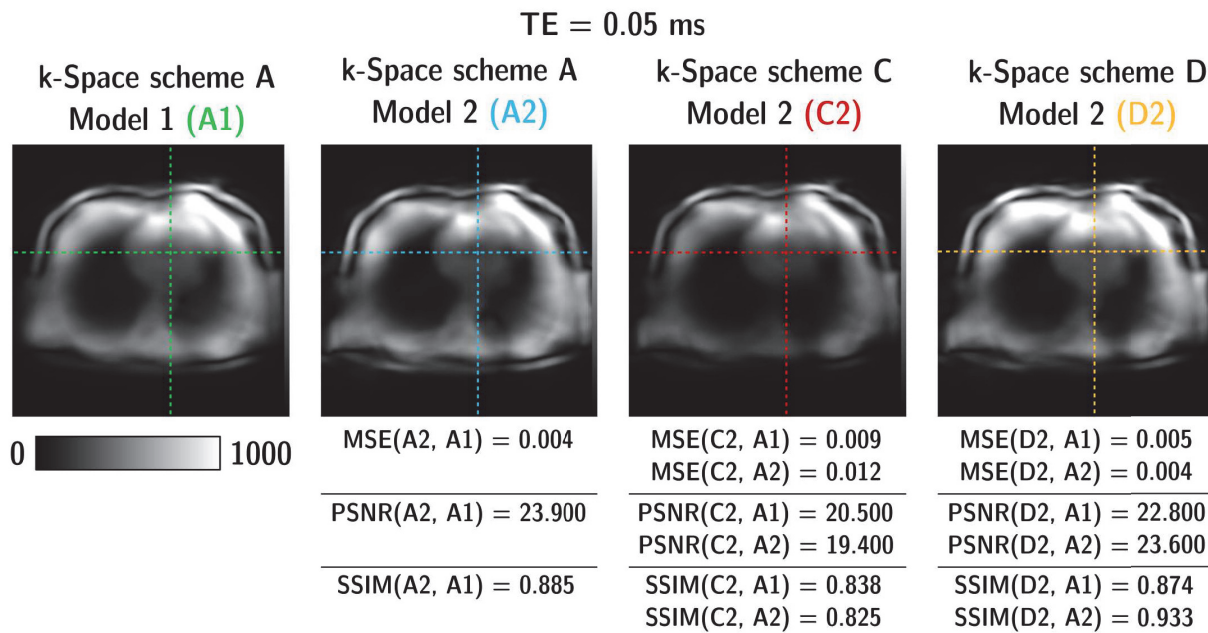
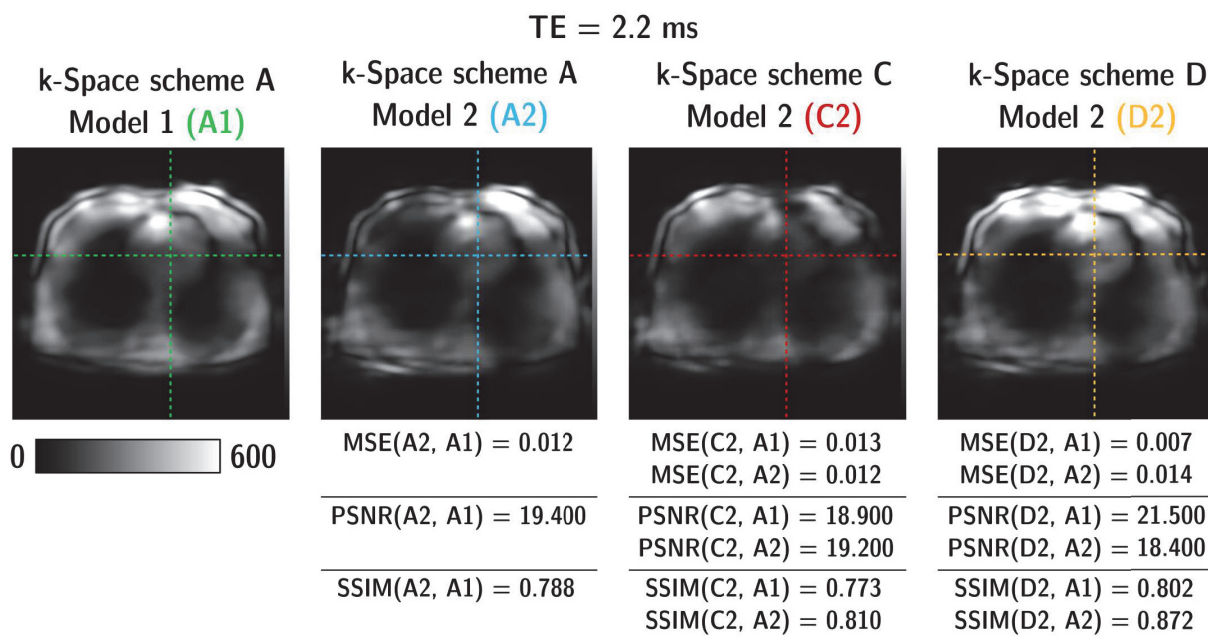


Figure 3.13: Assessment of magnitude images at 0.05 ms. D2 SSIM is 10% higher than C2 compared with A2; and the PSNR ratio is almost the same as A2. The row and column profiles provide a quick overview of the amount of detail across images (sharpness). MSE: mean-squared error; PSNR: peak signal-to-noise; SSIM: structural similarity index measure.

Representative magnitude images reconstructed using k-Space schemes A, C, and D at 2.2 ms are presented in Figure 3.14. In this case, there are no significant differences in IQM. However, row and column profiles of C2 present noticeable differences. For instance, in the row profile at pixel 155, C2 is losing sharpness. There is a clear local minimum which corresponds to the external border of the heart with at least 25% of difference in signal intensity from the previous local maximum. This pattern is present in A1, A2, and D2.

Representative magnitude images reconstructed using k-Space schemes A, C, and D at 10 ms are presented in Figure 3.15. Similar to images at 2.2 ms, there are no significant differences in IQM. Nevertheless, the magnitude image reconstructed with Model 1 (with-

out considering temporal dimension) exhibits a noticeable difference regarding A2, C2 and D2. The row and column profiles from A1 present different patterns, which explains the lower value in structural similarity compared to A2, C2, D2 (almost 30%).



Row/Column profile across magnitude images

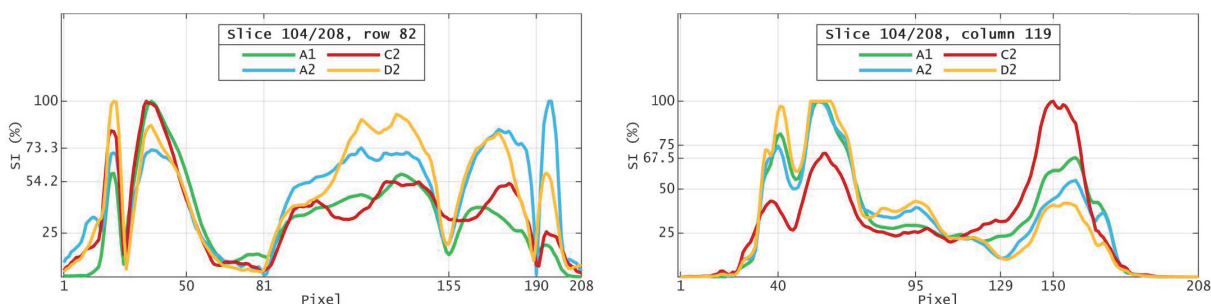


Figure 3.14: Assessment of magnitude images at 2.20 ms. There are no significant differences in IQM. There is a clear local minimum which corresponds to the external border of the heart with at least 25% of difference in signal intensity from previous local maximum. This pattern is present in A1, A2, and D2. MSE: mean-squared error; PSNR: peak signal-to-noise; SSIM: structural similarity index measure.

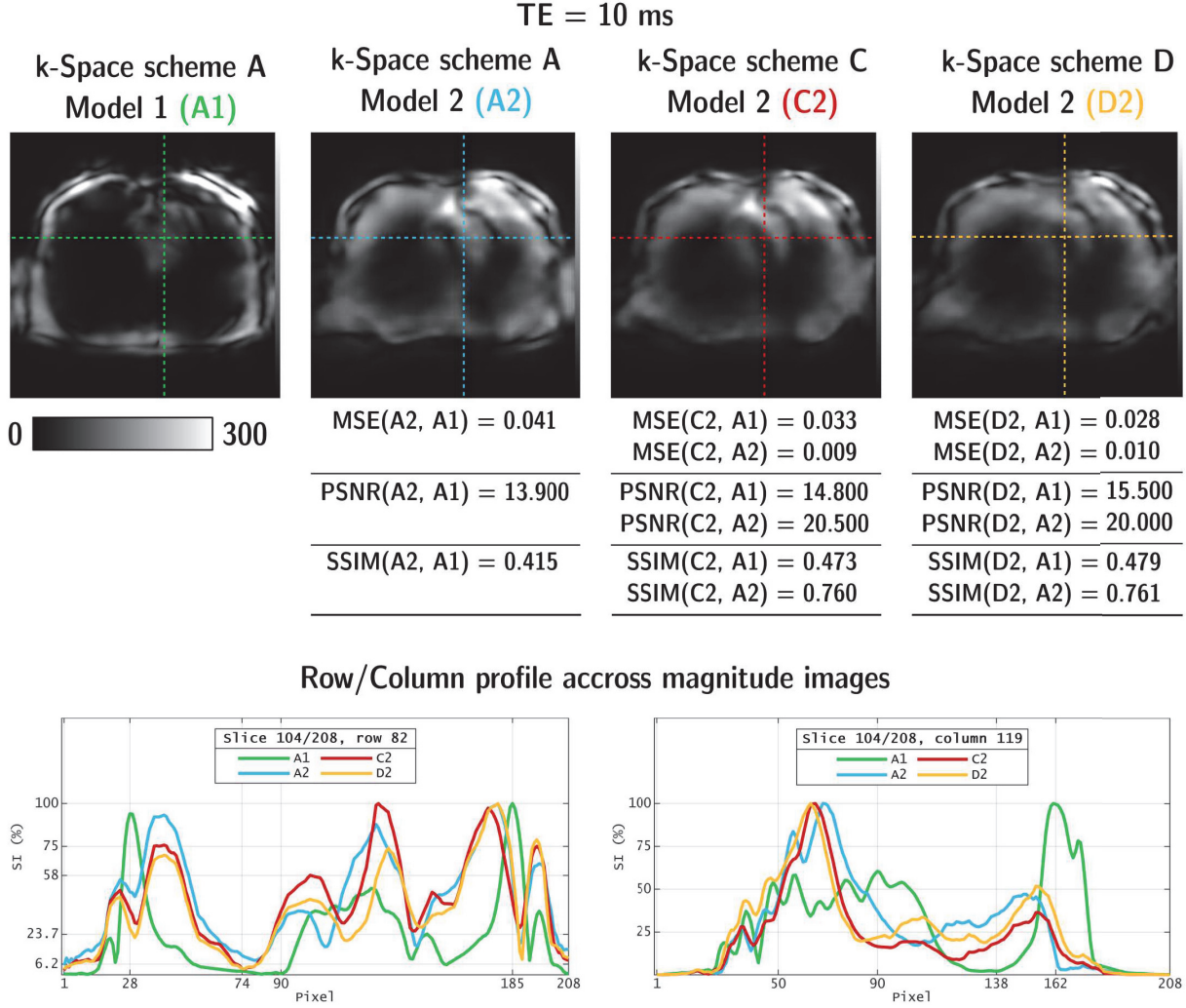


Figure 3.15: Assessment of magnitude images at 10 ms. The magnitude image reconstructed with A1 (without considering temporal dimension) exhibits a noticeable difference regarding A2, C2 and D2. This can be verified on the row and column profiles, which explains the lower value in structural similarity compared to A2, C2 and D2. MSE: mean-squared error; PSNR: peak signal-to-noise; SSIM: structural similarity index measure.

3.2.3 Discussion

Nowadays, the GA radial 3D sampling techniques are the backbone of cardiac imaging sequences. A clear example is the Golden Angle Radial Sparse Parallel MRI (GRASP) and the self-gating extension XD-GRASP [57], [58], a multidimensional compressed sensing technique which is able to exploit sparsity on cardiac and respiratory dimensions. Another examples of cardiac MRI applications includes T_1 and T_2 mapping [59], myocardial perfusion imaging [60], and evaluation of left ventricular diastolic dysfunction [61], amongst others.

In this work, a full 3D rotation of the k-Space trajectory was defined in order to exploit temporal sparsity across different echo times acquired in multiple scans. The rotation is based on the GA rotation angle used in 2D stack-of-stars [51] with a modification to define the space discretisation according to the number of projections per echo time and the numbers of scans (Equation 3.5).

The rotation strategy can be used to sample the k-Space of a single echo time with

multiple breath-hold scans. In this study, a k-Space trajectory composed of 3120 projections was acquired in 3 breath-hold scans. Each scan acquired 1040 projections in which the baseline trajectory of the first scan was rotated across the following two scans. Following this strategy, 10 echo times were acquired in 30 scans. The objective was to have a reference k-Space (3120 projections, 100% k-Space data) to evaluate the image reconstruction of a sub-sampled k-Space (1040 projections $\sim 33\%$, k-Space data). Moreover, two reconstruction models were used: the model 1 (Equation 3.9) considering spatial sparse representations: $TV_{xyz}(x)$ and $\Psi_{xyz}(x)$; and model 2 (Equation 3.10) spatio-temporal sparse representations: $\Psi_{xyzt}(x)$ and $TV_t(x)$.

To fulfil the Nyquist criterion for a radial 3D k-space (half-projection/radial out scheme) [62] it would require 135918 projections ($N_p = 208^2 \times \pi$). In this imaging experiment, only the 2.30% (3120 projections) and 0.77% (1040 projections) of the required k-Space data were acquired. The selection criterion of these imaging parameters was defined by the number of projections acquired in a breath-hold of ~ 24 s.

Bearing in mind that images were reconstructed with only 0.77% of the optimal signal sampling, the results provide evidence in favour of trajectory rotation during k-Space acquisition and spatio-temporal sparse representations for the reconstruction model. In the best scenario, in which the highest possible MR signal intensity is acquired (TE = 0.05 ms), the reconstructed image from sub-sampled k-Space ($\sim 33\%$) and trajectory rotation, has a 10% more structural similarity to the reference image (100% k-Space) than the reconstructed image from sub-sampled k-Space with no rotation; as well as 3 dB more in peak signal-to-noise ratio. The reconstruction based on spatio-temporal regularisation (model 2) was more robust. When the acquired MR signal was low (TE = 10 ms), the sharpness of the image is not affected as noticed on the row and column profiles.

This work is not considered as a detailed analysis about radial 3D sub-sampling or CS-based reconstruction. The objectives were to deploy a GA-based R3D imaging sequence and calibrate the acquisition and reconstruction parameters: rotation scheme, sensitivity maps estimation, CS model and regularisation parameters values.

3.2.4 Conclusion

An accelerated radial 3D imaging sequence was implemented on the Siemens integrated development environment for applications software (IDEA). The custom sequence provides a configurable parameters in order to exploit sparsity in temporal dimension (across different sequential scans). In addition, an image reconstruction workflow based on parallel imaging and compressed sensing was implemented using the Berkeley advanced reconstruction toolbox [52]–[54].

Chapter 4

Reliability and validity of MR collagen signal: an in vitro validation study using collagen/gelatin matrices

Previous ex vivo studies on small animals have shown that quantitative imaging of myocardial fibrosis could be obtained without the use of a contrast agent by using Ultra-short TE (UTE) imaging sequences for imaging components with short- T_2^* such as collagen ($T_2^* < 2$ ms) [2], [3]. In addition, published studies have reported experimental data (in vitro and ex vivo) to validate a bi-component model with an oscillation term for short- T_2^* component due to the resonance frequency of collagen [4], [5], [37], [46], [63]. Nevertheless, some major challenges need to be addressed prior using this imaging technique [63] in clinical routine.

The first challenge is to define an in vitro experimental setup based on solutions that better model MR properties of the fibrotic tissue. Published in vitro studies [4], [5], [37] have worked on aqueous solutions (collagen type I and III powder diluted in demineralised water) and this constraint has been discussed as a major limitation because these solutions do not correspond to the fibril structure of collagen in the human body [38]–[40]. This leads to the second challenge, which corresponds to the model used for the short- T_2^* estimation. The correlation between a bi-component model with an oscillation term for the collagen component and MR measurements has only been demonstrated on in vitro studies (aqueous solutions, no fibrillar structure). Ex vivo studies have used a non-oscillatory term in the model used for estimating the short- T_2^* from collagen components [3], [39], [40]. As the quantification of collagen concentration relies on the parameter estimation related to the fast signal decay, the model selection indeed impacts quantification accuracy.

Finally, current cardiac imaging sequences rely on compressed sensing (CS) techniques in order to reconstruct reliable diagnostic images from selected data from the acquired signal during free-breathing scans or signal data below the Nyquist criterion in a breath-hold scan [13], [64]–[67]. In the studies mentioned above, the reported scanning times are not feasible in clinical practice, directing attention toward CS-based implementations. The third challenge concerns the signal sub-sampling and reconstruction model. The characteristic decay (oscillation) of the MR collagen signal must be clear in order to set the right acceleration strategy [12], [68]. The MR collagen signal can be lost due to the sub-sampling scheme or can be attenuated due to the regularisation in the CS-based reconstruction. Consequently, the acceleration strategy must guarantee the integrity of the MR collagen signal especially if the signal has a characteristic oscillation due to the resonance frequency of collagen.

The starting point for this study was to examine the MR collagen signal on aqueous so-

lutions (collagen type I and III, no fibrillar structure) following the methodology published by Siu et al. [4]. In addition, scans were ECG-triggered simulating a 24s breath-hold, which means reducing the number of 3D radial projections below the Nyquist criterion within the k-space sampling scheme. The next stage included numerical simulations in order to select the echo times that guarantees a reliable estimation of the short- T_2^* from collagen. In this numerical analysis, a noise floor was identified such that the MR collagen signal is preserved within the intrinsic noise of images, setting the boundaries of reliability in MR measurements and quantifying the short- T_2^* at 3T. Finally, based on these results, the MR collagen signal was examined on stabilised fibrillar collagen I [44], [45] to investigate the validity of the model used on aqueous solutions.

This study sought to establish the conditions for a reliable quantification of the short- T_2^* which must be considered in developing and fine-tuning of custom imaging sequences developed by research groups in Cardiac MRI.

4.1 Materials and methods

Experiments were conducted using a 3T MRI scanner (MAGNETOM Prisma, Siemens, Erlangen, Germany) with an 18 channels cardiac phased-array coil combined with appropriate elements of the spin array coils, as used routinely in patients.

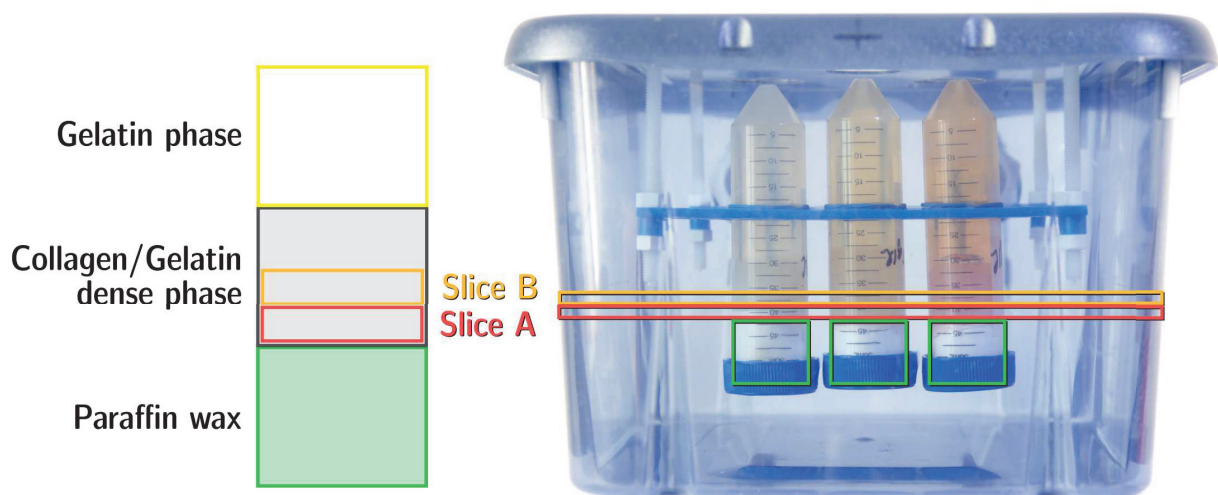
4.1.1 Collagen Phantom

The phantom comprised 5 × 50 ml Falcon tubes filled with collagen/gelatin matrices and one tube of Collagen gel (10 mL, diluted in a concentrated medium) as described in Section 3.1.1.2. To avoid air susceptibility artefacts and optimise magnetic field experimental MR conditions, tubes were filled with paraffin wax preparation as presented in Figure 4.1. The tubes were immersed in a water bath and scanned at 22° C.

As described in Section 3.1.1.2, the reported values of collagen concentration correspond to those used in the initial solution for inducing fibrillogenesis. The final concentration of collagen concentration (in mass percent) is unknown. There was no previous knowledge or MR measurements to rely as a ground truth measurement for short- T_2^* components.



(a)



(b)

Figure 4.1: Phantom design. (a) Photograph of phantom prior to filling with water; (b) composition of the tubes and selected slices for measurements.

4.1.2 Noise propagation analysis by Monte Carlo simulations

The MR signal decay on magnitude images was calculated using the following equation

$$S(t) = \left| S_{0,c} e^{t \left(i2\pi f_c - \frac{1}{T_{2,c}^*} \right)} + S_{0,l} e^{\frac{-t}{T_{2,l}^*}} \right| + \varepsilon(0, \sigma(t)) \quad (4.1)$$

where $\varepsilon(0, \sigma)$ models Gaussian noise with 0 mean μ and standard deviation $\sigma(t)$ that varies according to the following time ranges

$$\sigma(t) = \begin{cases} \sigma = 1 & 0.05 \leq t < 1.2 \\ \sigma = 2 & 1.2 \leq t < 6 \\ \sigma = 3 & \text{Otherwise} \end{cases} \quad (4.2)$$

in order to model the signal intensity loss observed on in vitro MR measurements. Monte Carlo simulations were implemented in order to assess the parameter estimation across different set of TE. In one iteration of the simulation:

1. 25 MR signals were calculated with 200 TE ($0.05 \leq TE \leq 10\text{ms}$; the first $TE = 0.05$ ms, $\Delta TE = 0.05$ ms) with Equation 4.1, in order to emulate p signals (pixel across TE) in a ROI.
2. The mean value and standard deviation of the signal ($\mu_p \pm \sigma_p$) are calculated, emulating the mean \pm standard deviation in a ROI of p pixels. This is the *raw reference signal*.
3. The parameters $S_{0,c}$, $T_{2,c}^*$, $S_{0,l}$ and $T_{2,l}^*$ are estimated by model fitting (Equation 2.14) the *raw reference signal* using non-linear optimisation methods (Levenberg-Marquardt and trust-region-reflective).
4. The *raw reference signal* is filtered by a wavelet PCA multivariate de-noising method [69] using p signals. The outcome of this step is the *de-noised reference signal*.
5. The parameters $S_{0,c}$, $T_{2,c}^*$, $S_{0,l}$ and $T_{2,l}^*$ are estimated by model fitting (Equation 2.14) the *de-noised reference signal* using non-linear optimisation methods (Levenberg-Marquardt and trust-region-reflective).
6. A group of 10 TE are selected. At this step, the mean value and standard deviation ($\mu_p \pm \sigma_p$) are known from step 2. This is the *raw target signal*.
7. The parameters $S_{0,c}$, $T_{2,c}^*$, $S_{0,l}$ and $T_{2,l}^*$ are estimated by model fitting the *raw target signal*.
8. The *raw target signal* is filtered by a wavelet PCA multivariate de-noising method. The outcome of this step is the *de-noised target signal*.
9. The parameters $S_{0,c}$, $T_{2,c}^*$, $S_{0,l}$ and $T_{2,l}^*$ are estimated by model fitting the *de-noised target signal*.
10. The relative error of parameter estimation is calculated between the *reference* and the *target* outcomes from steps 3, 5, 7 and 9.
11. Parameter values from steps 3, 5, 7 and 9 are stored as well as the relative error.

This process was repeated until the stabilisation of the probability density function (PDF) calculated from the histograms of each parameter. The PDF stabilises when there is no significant change of the estimated μ and σ in the following iteration. The signal generation, model fitting and PDF estimation methods were implemented on MATLAB R2020b (The MathWorks Inc.).

4.1.3 Multivariate De-noising using Wavelets and PCA

The short- T_2^* MR signal decay $S(t)$ on magnitude images acquired at $t = \{TE_1, TE_2, TE_3, \dots, TE_n\}$ can be represented by

$$X(t) = f(t) + \varepsilon(t) \quad (4.3)$$

where $X(t)$ is the observed signal, $f(t)$ the signal to be recovered and $\varepsilon(t)$ is a centred Gaussian white noise of unknown variance σ^2 . Inside a region of interest (ROI) of size p (pixels), each signal is consider for $1 \leq i \leq p$ and it is represented as

$$X^i(t) = f^i(t) + \varepsilon^i(t) \quad (4.4)$$

where $f^i \in L^2$. The covariance matrix Σ_ε , supposed to be positive, captures the stochastic link between the signals (components) of $X(t)$.

The wavelet PCA multivariate de-noising method is as follows [69]:

1. Perform the wavelet transform at level J of each column of X , producing matrices D_j and A_j which includes the detail coefficients at level 1 to J of the p signals and the approximation coefficients respectively;
2. Define $\hat{\Sigma}_\varepsilon$ estimator by the Minimum Covariance Determinant (MCD) method in order to select details in D_j with a thresholding strategy;
3. Perform the PCA of the matrix A_j and select the appropriate number p_{J+1} of principal components;
4. Reconstruct a de-noised matrix \hat{X} , from the simplified detail and approximation matrices, by inverting the wavelet transform;

In this study, the MATLAB implementation of the wavelet multivariate de-noising method (*wmulden* function, MATLAB Wavelet Toolbox R2020b, The MathWorks Inc.) was used. The relevant parameters were Wavelet *coif4*, level 4, selection of the number of principal components by Kaiser's rule. Moreover, the non-linear least squares methods (Levenberg-Marquardt and trust region reflective) from MATLAB were used.

4.1.4 Data acquisition

Phantom scans were performed using single-echo UTE Radial 3D sequences. All acquisitions were ECG-triggered with a simulated heart rate = 60 beats per minute (RR interval 1000 ms). Imaging parameters are summarised in Table 4.1.

Parameter	Single-Echo default R3D	Single-Echo custom GA R3D
k-Space trajectory	Uniform angle distribution, radial 3D	Golden-Angle, radial 3D
TR (<i>ms</i>)	456	456
TE (<i>ms</i>)	1 st TE = 0.05 / $\Delta TE = 0.05$ / $0.05 \leq TE \leq 5.95$ 1 st TE = 6 / $\Delta TE = 0.5$ / $6 \leq TE \leq 10$	10 TE (Table 4.2)
FOV (<i>mm</i>)	400	400
Image matrix	208x208	208x208
Pixel resolution (<i>mm</i> ³)	1.9	1.9
Flip angle (<i>deg</i>)	15	15
Bandwidth (<i>Hz/pixel</i>)	728	728
Projections	6240	3120
Samples per projection	208	208
Acquisition time	2 min 40 s per scan	1 min 20 s per scan

Table 4.1: Imaging parameters. The echo times and rotation parameters for the custom GA R3D are specified in Table 4.2

As presented in Section 4.2.4, the k-space sampling scheme in the product UTE R3D imaging sequence was calculated using Equation 3.1. The k-space trajectory of the custom GA R3D imaging sequence was calculated using Equation 3.2. This trajectory was rotated across scans according to Equation 3.6.

Echo time (ms)	Scan index	Projections per scan	Trajectory	Rotation index	Temporal resolution
0.05	1	6240	GA	1	10
	2	3120			
0.6	3	6240	GA	2	10
	4	3120			
1.2	5	6240	GA	3	10
	6	3120			
1.7	7	6240	GA	4	10
	8	3120			
2.2	9	6240	GA	5	10
	10	3120			
3.55	11	6240	GA	6	10
	12	3120			
4.5	13	6240	GA	7	10
	14	3120			
6	15	6240	GA	8	10
	16	3120			
8	17	6240	GA	9	10
	18	3120			
10	19	6240	GA	10	10
	20	3120			

Table 4.2: Trajectory rotation parameters across scans. Rotation index j (Equation 3.4) and temporal resolution (Equation 3.5). GA: Golden Angle.

4.1.5 Image reconstruction

Magnitude images from the UTE R3D imaging sequences were reconstructed using the scanner reconstruction software. Magnitude images from custom UTE GA R3D were reconstructed by a CS-Based workflow implemented on BART [52] using the model presented in Equation 3.10. Coil compression was performed (from 30 to 15 receiver coils) using Singular Value Decomposition (SVD) with a block size of 16. Sensitivity maps were calculated with an Adaptive Method with an eigenvalue cut-off of 0.54 over a calibration region of radius 24. Sensitivity maps calculation includes soft-SENSE [55] and intensity correction. Regularisation parameters were defined experimentally as λ_1 , λ_2 , λ_3 and λ_4 as presented in Table 3.4. Image reconstruction was performed on a computer cluster of 32 cores, Intel(R) Xeon(R) Gold 6226R, 2.90GHz; required RAM memory is specified in Table 3.6.

4.1.6 Data analysis

Regions of interest (ROI) were outlined on the magnitude images from UTE R3D scans within the Horos DICOM viewer [70]. The ROIs mean value and standard deviation in all tubes were reported. The parameters $S_{0,c}$, $T_{2,c}^*$, $S_{0,l}$ and $T_{2,l}^*$ are estimated by model

fitting (Equation 2.14) the signal sampled with a high temporal resolution (128 TE) and low temporal resolution (10 TE).

4.2 Results

According to the bi-component model with an oscillation term for short- T_2^* , the signal contribution from collagen short- T_2^* ends at 6 ms (Figure 2.5). In order to have a good sampling of the oscillation, TE selection included between 6 and 8 out of 10 TE below 6 ms minimising errors from numerical methods for model fitting (non-linear least squares). The Figures 4.2 (*reference signal*) and 4.2 (*target signal*) illustrates the simulation results from one iteration. The SI profile is well reproduced by the TE selection: local minimum about 1.2 ms and local maximum about 2.2 ms. Local minimum and maximum variations across different f_c are illustrated in Figure 4.4. The *raw reference signal* and the *de-noised reference signal* do not exhibit a significant difference which means that at this level of resolution, the parameters estimation is similar.

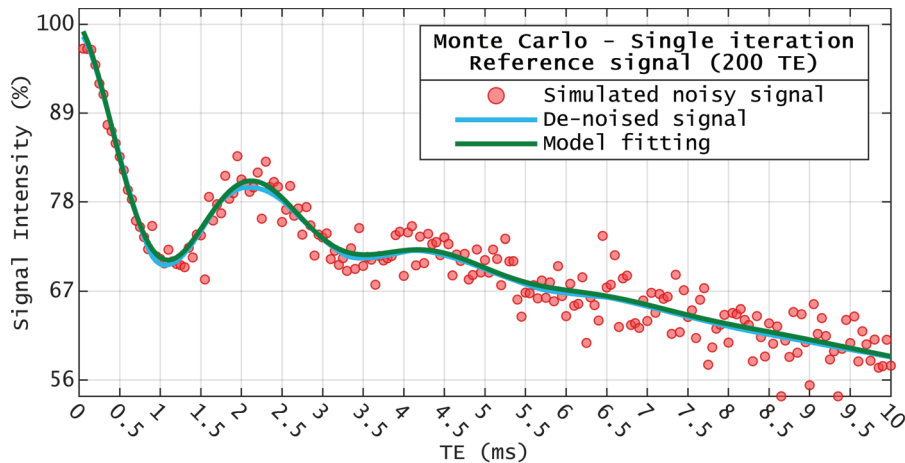


Figure 4.2: Model fitting of simulated MR signal. Simulated MR signal on magnitude images calculated using 200 TE (red dots); signal after wavelet PCA multivariate denoising (light green) and best model fit (dark green). The SI was calculated with $f_c = 438$ Hz, $S_{0,c} = 18$, $T_{2,c}^* = 1.5$ ms, $S_{0,l} = 82$ and $T_{2,l}^* = 30$ ms.

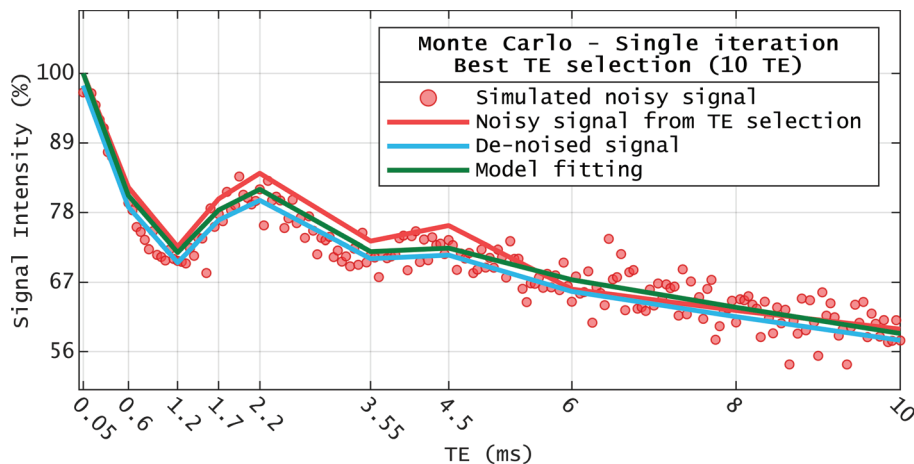


Figure 4.3: Model fitting of simulated SI. Signal from TE selection (red line), signal after de-noising (light green) and best model fit (dark green). The SI was calculated with $f_c = 438$ Hz, $S_{0,c} = 18$, $T_{2,c}^* = 1.5$ ms, $S_{0,l} = 82$ and $T_{2,l}^* = 30$ ms.

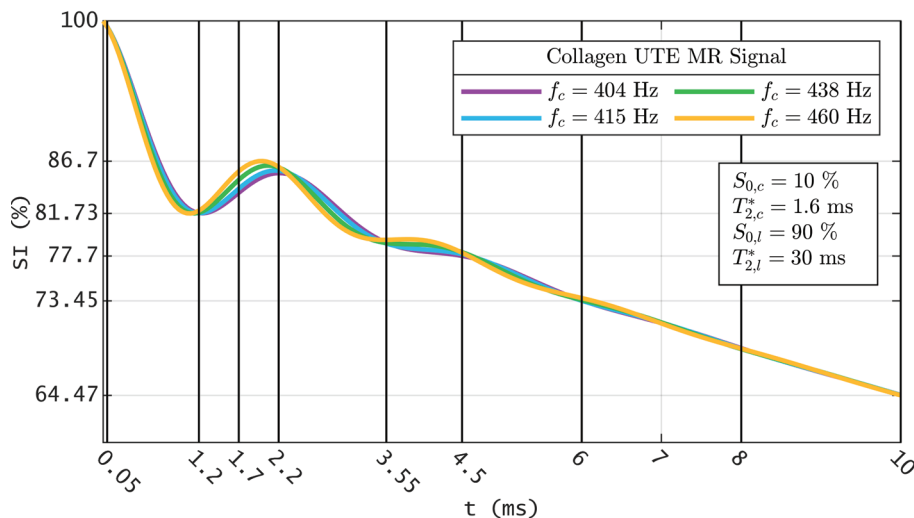


Figure 4.4: Selection of echo times. Local minimum and maximum variations across different f_c .

The outcomes of the parameter estimation from simulations can be observed in Figure 4.5, where the agreement between the ground truth and TE selection histograms improved when the de-noising step was included before the model fitting step. In addition, the relative error in parameter estimation is presented in Figure 4.6. This figure illustrates the reduction of the probability of error estimating parameters with the TE selection. For instance, in the case of $T_{2,c}^*$ estimation, the relative error in the parameter estimation has a lower bound of 22% with a probability of incidence below 0.02. Under this criteria the selected echo times for parameter estimation where $TE = \{0.05, 0.6, 1.2, 1.7, 2.2, 3.55, 4.5, 6.0, 8.0, 10\}$ ms. The difference in the parameter estimation between random and best TE is presented in Figure 4.7.

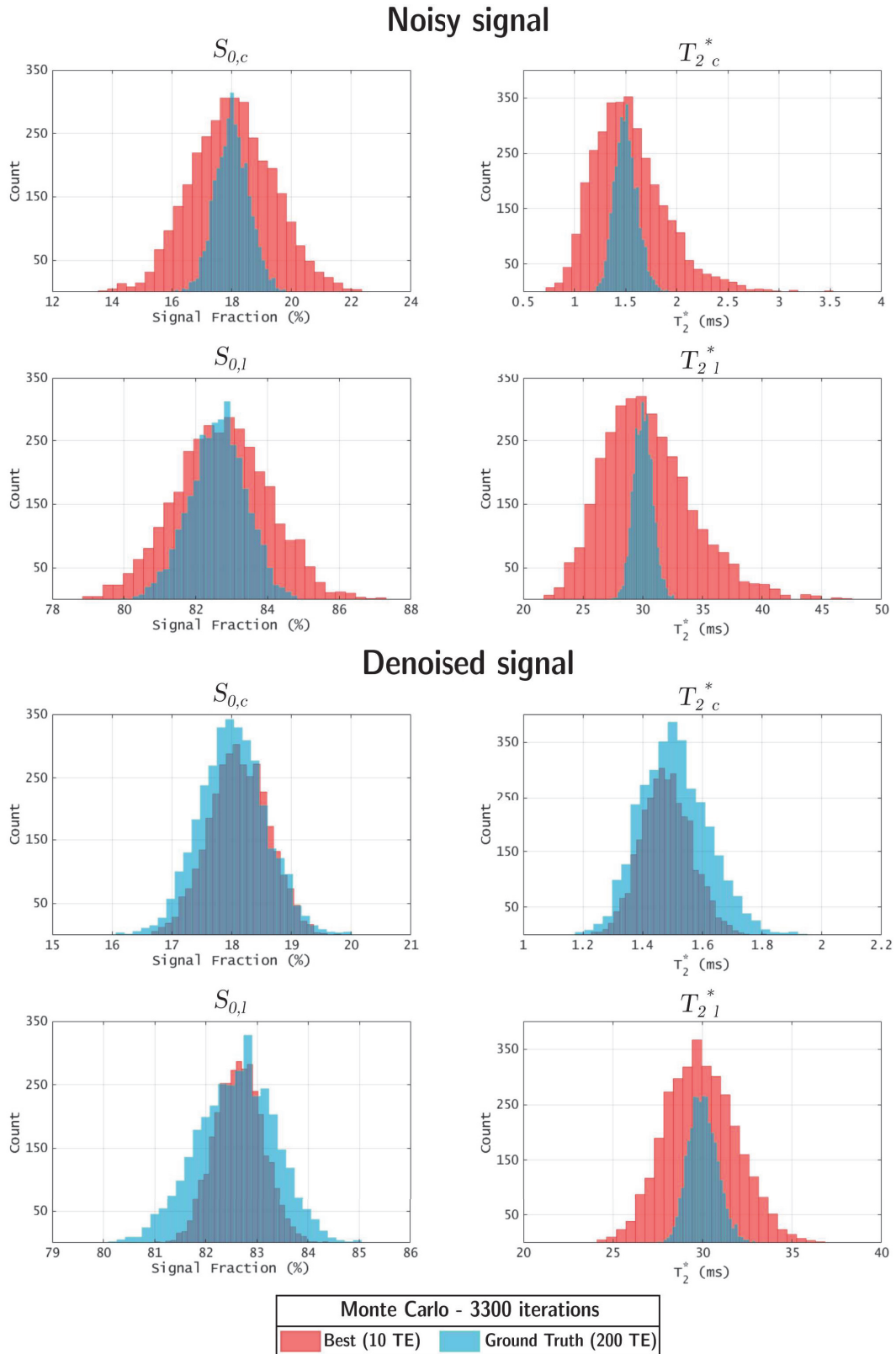


Figure 4.5: Histograms of the parameter estimation after 3300 iterations. The ground truth histograms (blue) were calculated for each parameter ($S_{0,c}$, $T_{2,c}^*$, $S_{0,l}$, and $T_{2,l}^*$) using 200 TE (reference signal). The target histograms (red) were calculated using the best TE selection (10 TE). Monte Carlo simulations were performed without filtering the signal from the TE selection (wavelet PCA multivariate de-noising) in order to assess the impact of de-noising.

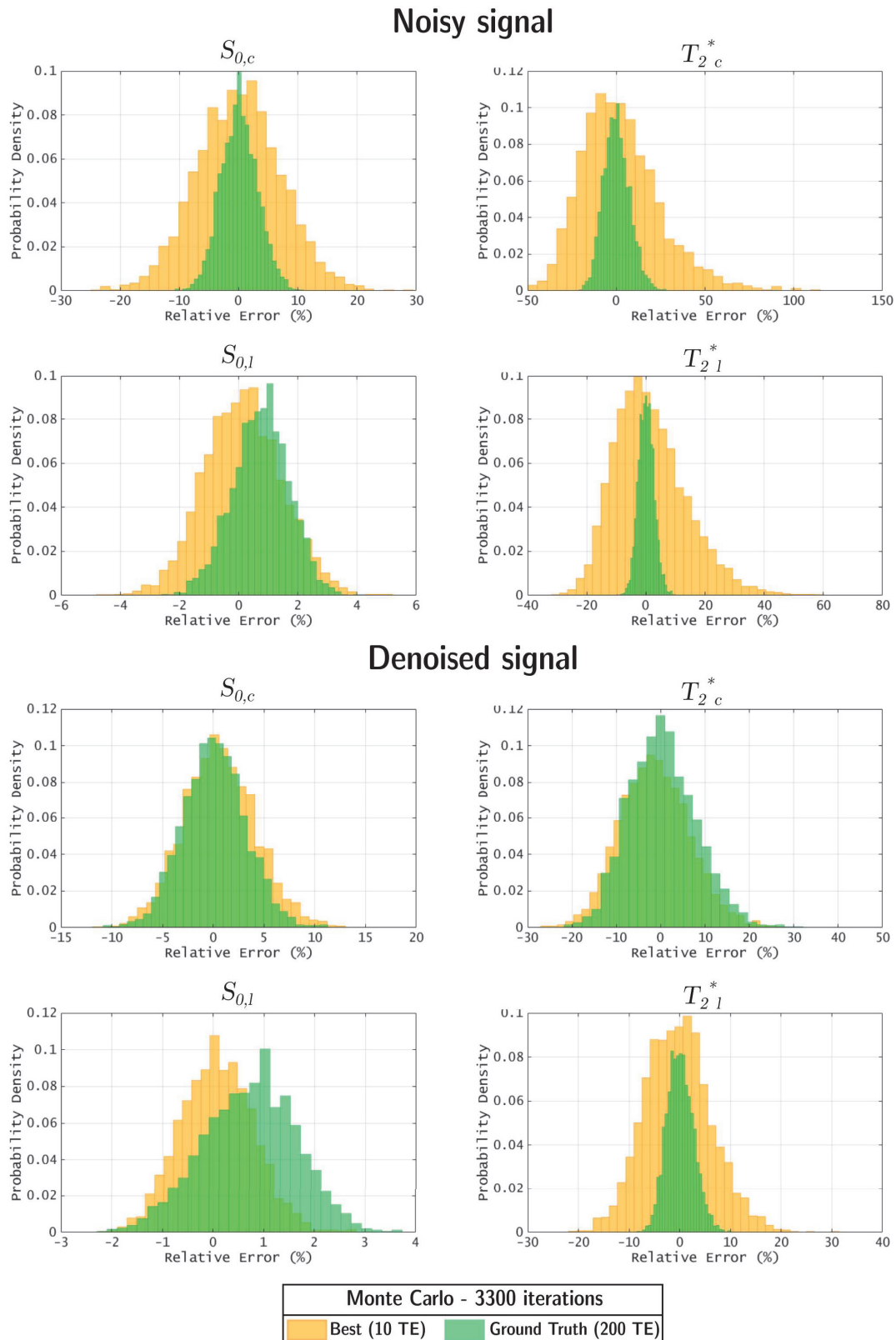


Figure 4.6: Probability density histograms of the parameter estimation after 3300 iterations. The ground truth histograms (green) show the relative error between the baseline values used for generating 200 noisy samples (reference signal), and the estimated values using the simulated signal. The assessment histogram (orange) is the relative error between the parameter estimation using 200 (reference signal) and 10 TE (selection). Monte Carlo simulations were performed without filtering the signal from the TE selection (wavelet PCA multivariate de-noising) in order to assess the impact of de-noising.

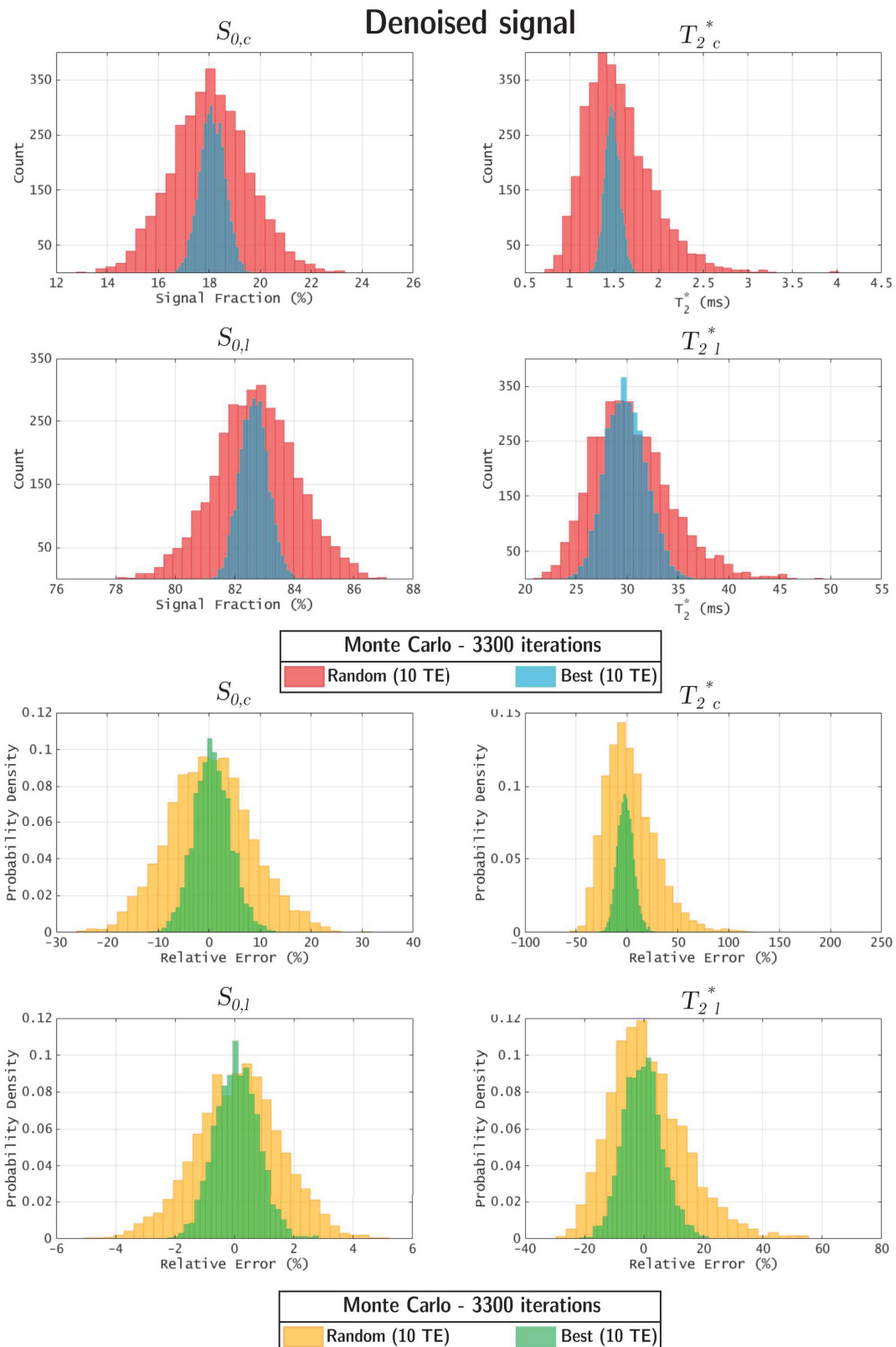


Figure 4.7: Histograms of the parameter estimation and probability density after 3300 iterations.

4.2.1 Noise floor estimation

In vitro studies [4], [5], [63] have reported a linear correlation between the Collagen Signal Fraction (CSF) and the collagen concentration of the imaged solution. Figure 4.8 illustrates the significance of the collagen concentration to signal intensity (SI) evolution. Assuming f_c between 415 and 460 Hz, the magnitude of the signal is characterised by a local minimum of SI between 1.13 and 1.28 ms; and a local maximum of SI between 1.89 and 2.03 ms. Therefore, a negative signal difference above 1% could be measured for CSF superior of 8.14%. On magnitude images, within a region of interest (ROI) with a mean value μ and standard deviation σ , the percentage of SI difference is given by

$$\Delta S = \left(\frac{2(\mu_{TE1} - \mu_{TE2})}{\mu_{TE2} + \mu_{TE1}} \right) \times 100 \quad (4.5)$$

where echo times (TE) are defined in the intervals $TE_1 \in [1.13, 1.28]$ ms and $TE_2 \in [1.89, 2.03]$ ms. The accuracy of the MR measurement will depend on the noise. Consequently, the measured signal (μ_{TE}) should not be less than the noise floor (NF)

$$NF = \left(\frac{\sqrt{2}\sqrt{\sigma_{TE1}^2 - \sigma_{TE2}^2}}{\mu_{TE2} + \mu_{TE1}} \right) \times 100 \quad (4.6)$$

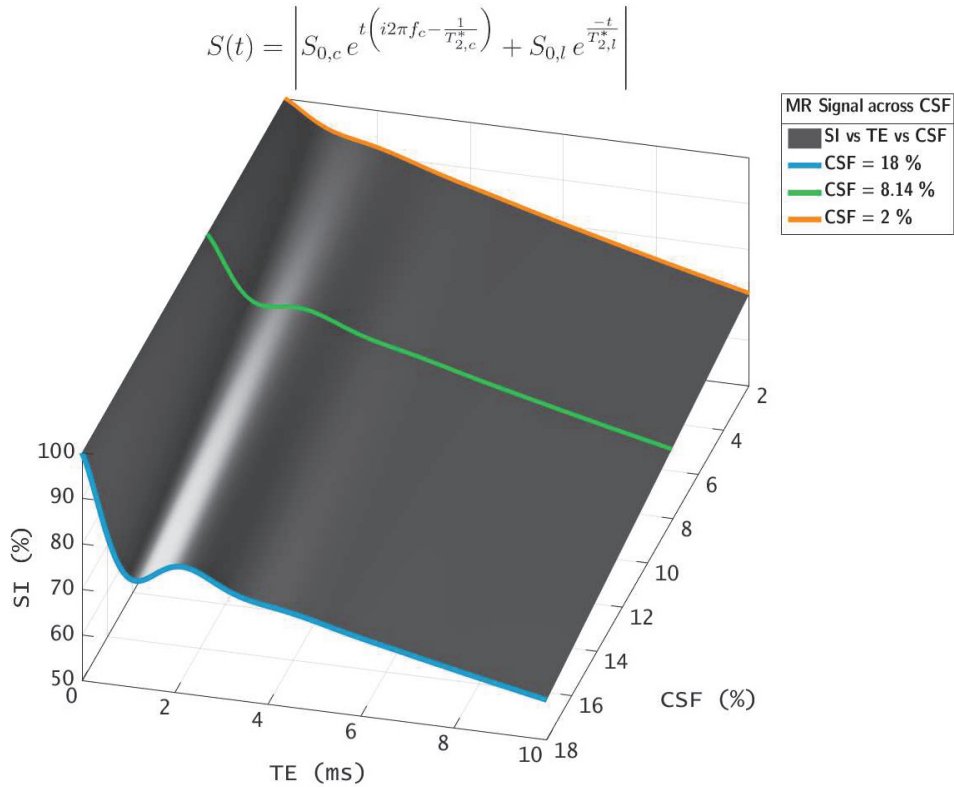


Figure 4.8: Signal intensity variation as a function of the collagen signal fraction calculated with Equation 2.14. The surface shows a significant positive gradient (white surface distribution) between 1.0 and 2.4 ms and the attenuation due to the decrease of the collagen signal fraction. The SI decay was calculated with $f_c = 438$ Hz, $S_{0,c} = CSF_i$, $T_{2,c}^* = 1.0$ ms, $S_{0,l} = 100 - CSF_i$ and $T_{2,l}^* = 30$ ms.

4.2.2 De-noising parameters

The wavelet PCA multivariate de-noising parameters were selected based on an analysis of MR signals from collagen/gelatin matrices. The Coiflet-4 (coif4) mother wavelet with 4 decomposition levels was selected as presented in Figure 4.9.

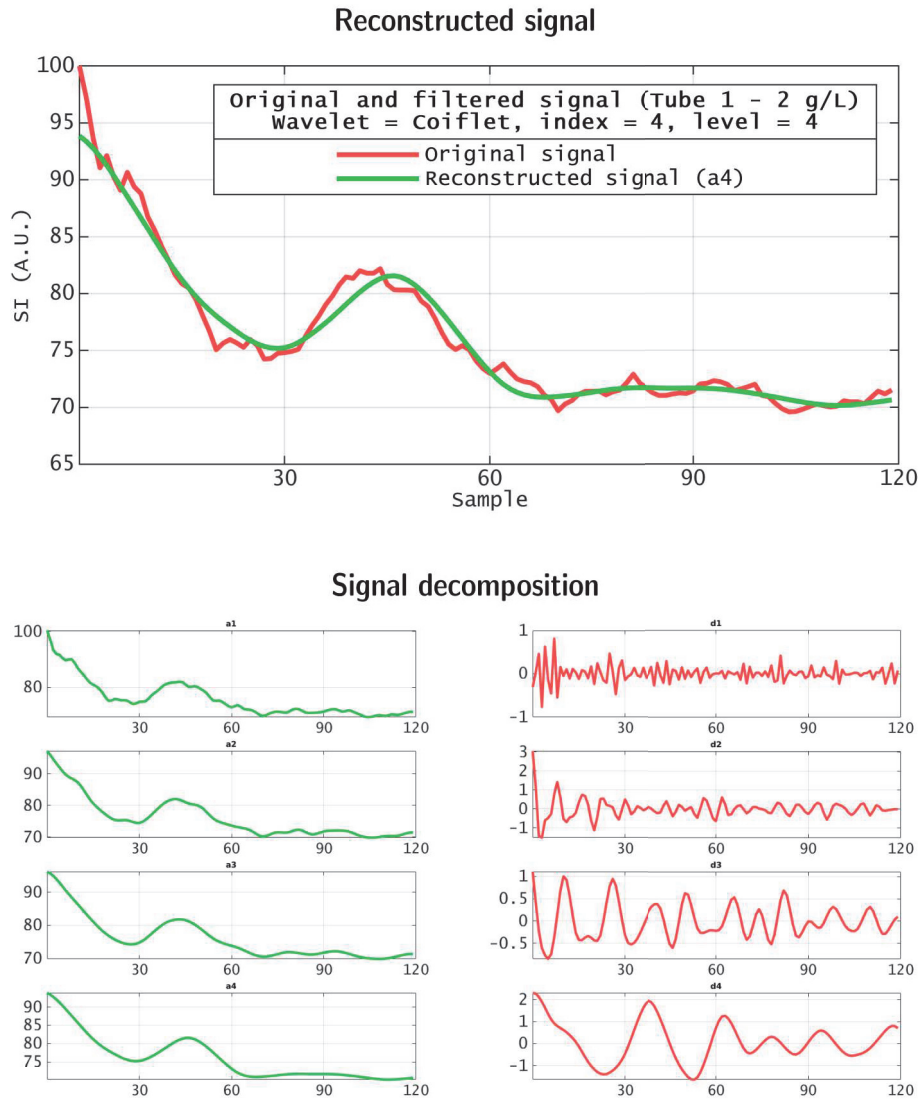


Figure 4.9: Wavelet decomposition of the MR signal from magnitude images on tube 1 (2 g/L). $S = a_4 + d_4 + d_3 + d_2 + d_1$.

4.2.3 Compressed sensing reconstruction

Representative magnitude images reconstructed on the slices for MR signal measurement and collagen quantification are presented in Figures 4.10 and 4.11. The optimal k-Space sampling requires 135918 projections. In this experiment, the k-Space composed of 6240 projections corresponds to the 4.59% of the optimal sampling, and the k-Space composed of 3120 projections corresponds to the 2.30%. Consequently the sub-sampling ratios are 0.0459 and 0.0230 respectively. The image reconstructed from the 6240 projections k-Space was used as a reference to assess the images reconstructed from sub-sampled k-Space. Row profiles show a good agreement.

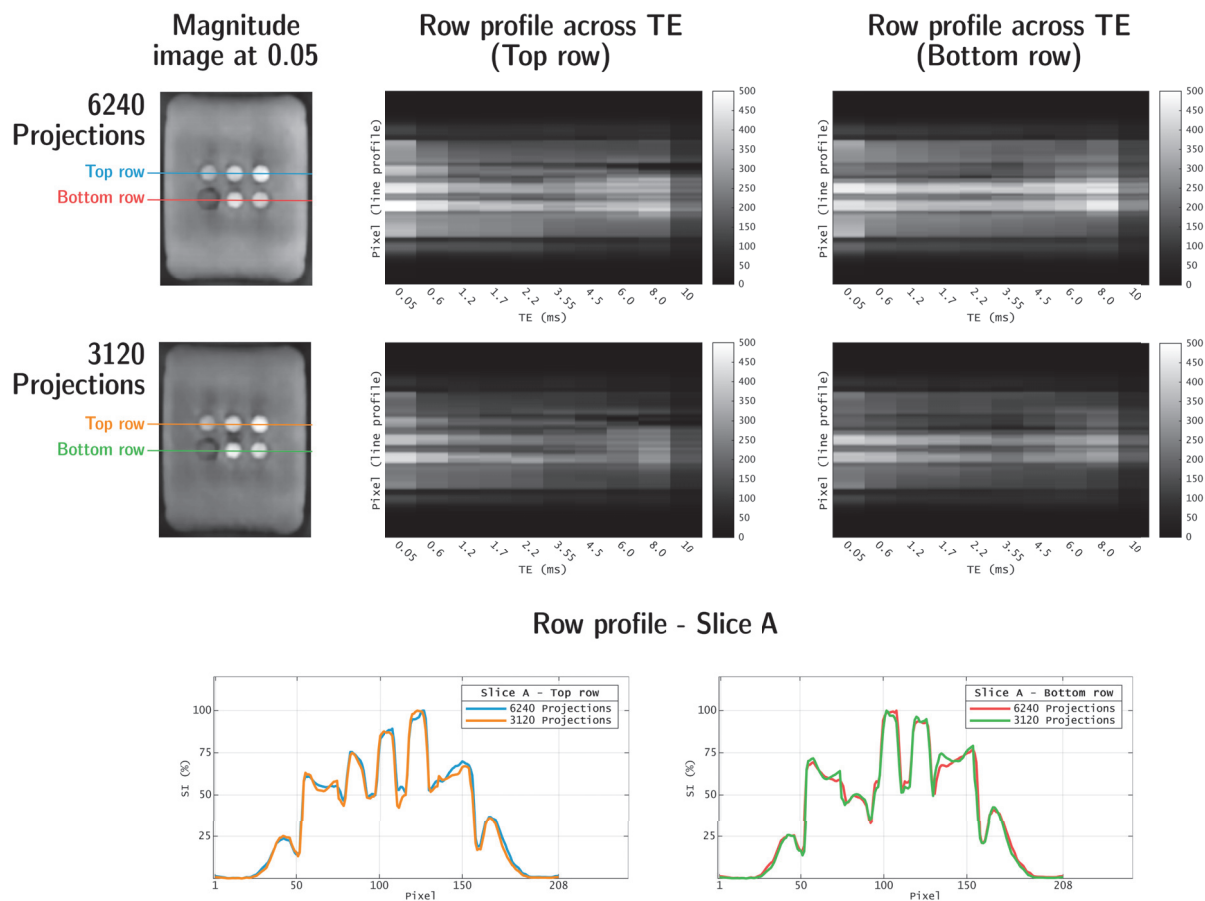


Figure 4.10: Image reconstruction assessment on slice A (defined in Figure 4.1). Image reconstructed with a k-Space composed of 3120 projections (target image, 2.30% of the optimal k-Space sampling) using as a reference an image reconstructed with the 4.59% of the optimal k-Space sampling (6240 projections). The row profiles outline the signal intensity of the pixels along an image’s row, as well as along echo times.

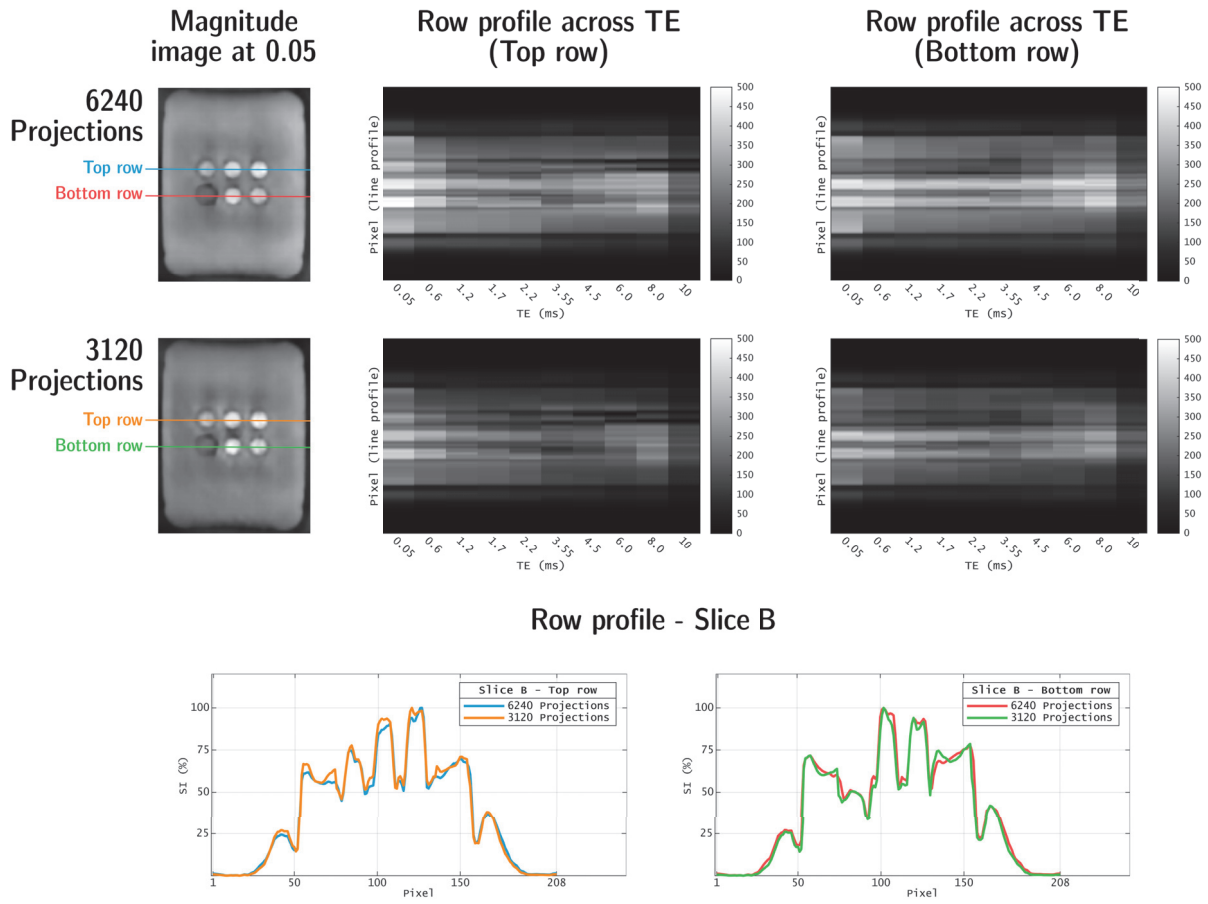


Figure 4.11: Image reconstruction assessment on slice B (defined in Figure 4.1). Image reconstructed with a k-Space composed of 3120 projections (target image, 2.30% of the optimal k-Space sampling) using as a reference an image reconstructed with the 4.59% of the optimal k-Space sampling (6240 projections). The row profiles outline the signal intensity of the pixels along an image’s row, as well as along echo times.

4.2.4 Collagen quantification

MR signals from collagen/gelatin matrices are presented in Figure 4.12 for tubes 1 (2 g/L), 2 (1.5 g/L) and 3 (1 g/L). As shown in Table 4.3 a significant difference in ΔS : (Equation 4.5) was observed across tubes 1, 2, and 3. The opposite is true for tubes 4 (0.5 g/L) , 5 (0.25 g/L) and 6 (No fibrillar matrix) as presented in Figure 4.13, the MR signal from short- T_2^* is very low which limits quantification.

Estimated Short- T_2^* between 1.19 ms and 1.71 is in agreement with previous previous studies [4], [5]. A summary of parameter estimation is presented in Table 4.3.

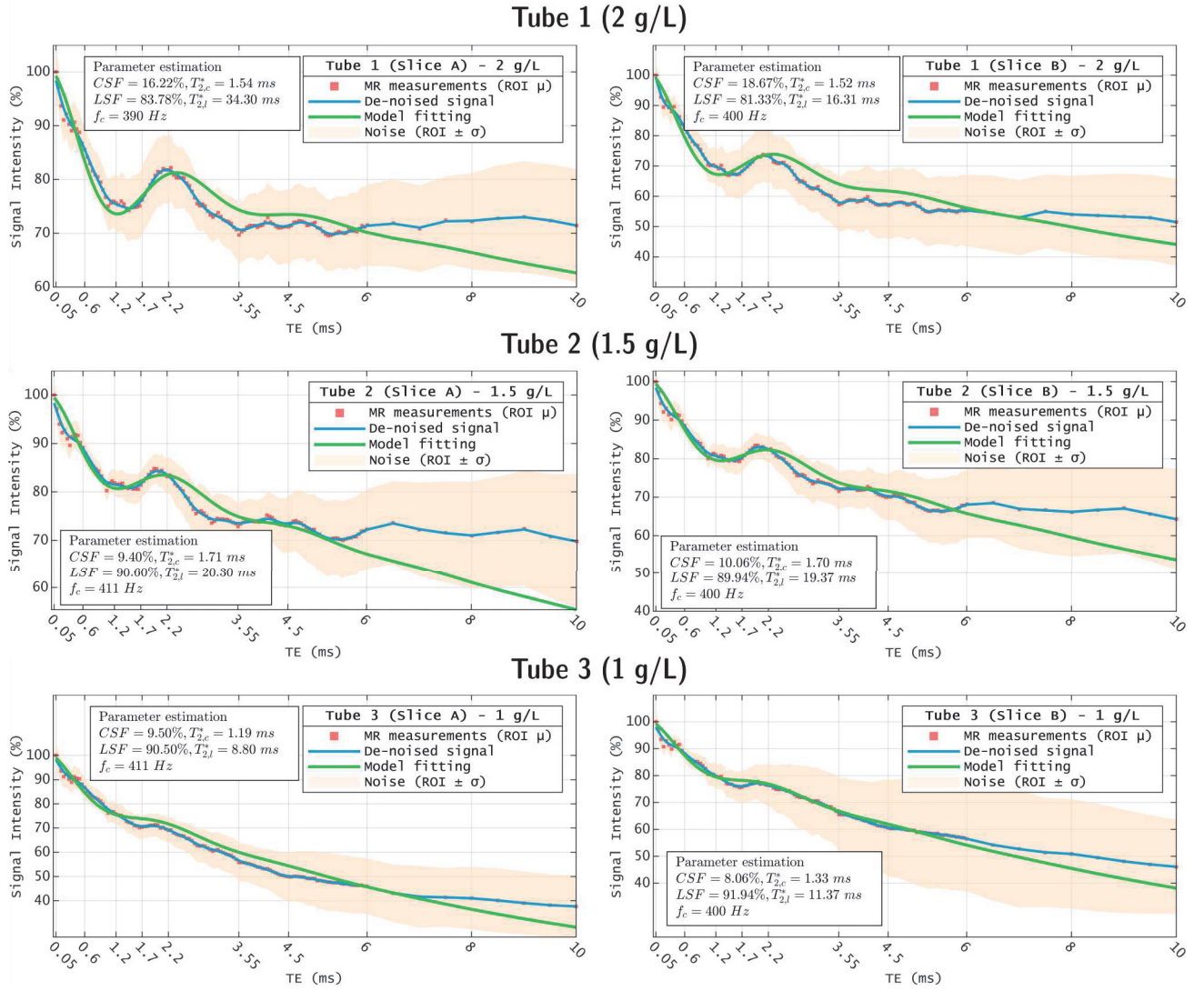


Figure 4.12: MR signals and parameter estimation from collagen/gelatin matrices in tubes 1, 2 and 3. The model fitting algorithm (trust region reflective) was constrained to be in the trust regions (closed interval) $S_{0,l} : [80, 95]$, $S_{c,l} : [5, 18]$, $T_{2,c}^* : [0.5, 2]$ and $T_{2,l}^* : [5, 35]$. $CSF = \frac{S_{0,c}}{S_{0,c} + S_{0,l}} \times 100$, $LSF = 100 - CSF$. CSF: Collagen Signal Fraction; LSF: Long Signal Fraction.

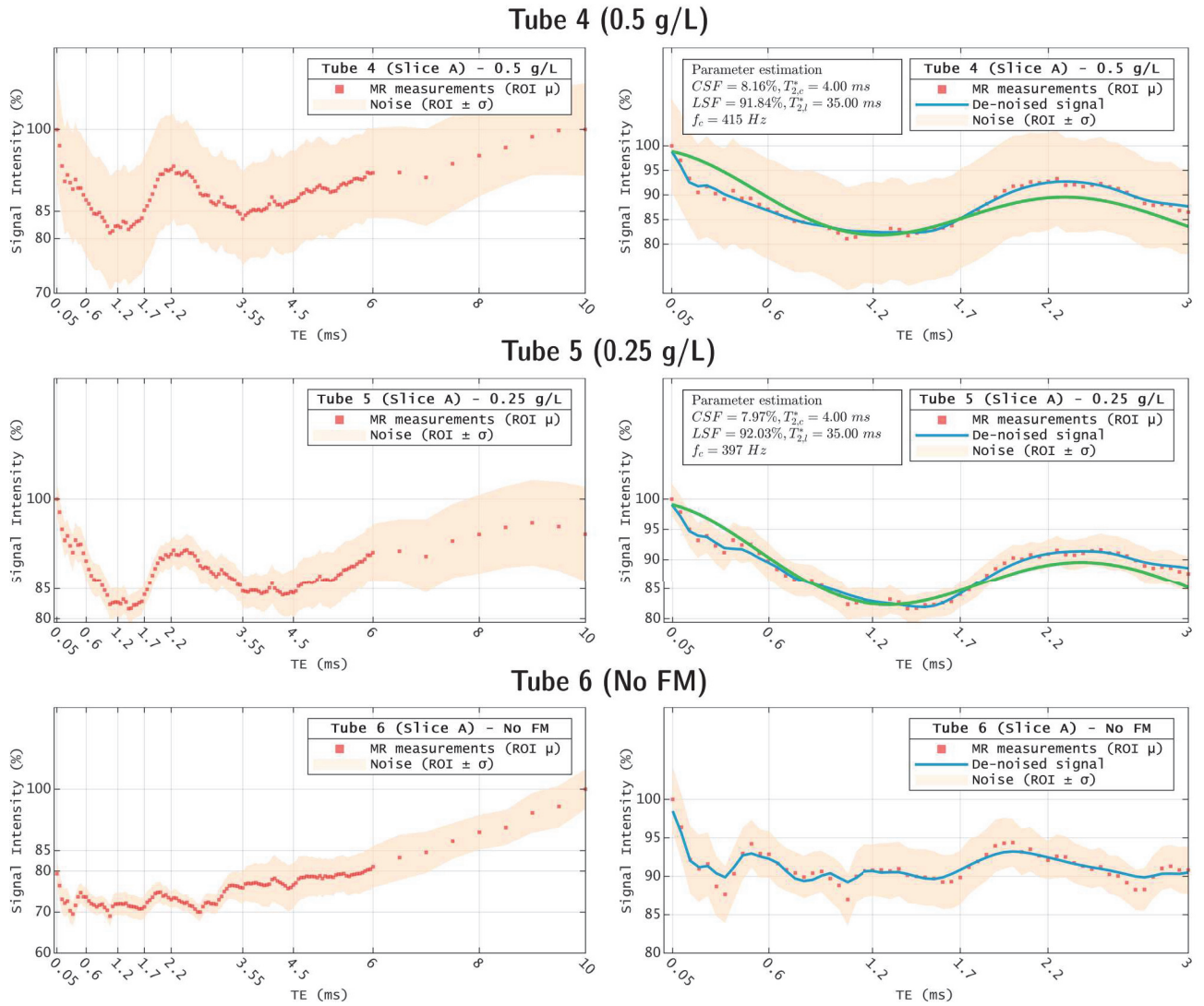


Figure 4.13: MR signals from collagen/gelatin matrices in tubes 4, 5 and 6. The left column presents the entire MR signal while the right column shows the signal up to 3 ms. Signals from tubes 4 and 5 exhibit a very low amplitude oscillation (right column). The model fitting algorithm (trust region reflective) was constrained to be in the trust regions (closed interval) $S_{0,l} : [80, 95]$, $S_{c,l} : [5, 18]$, $T_{2,c}^* : [0.5, 4]$ and $T_{2,l}^* : [5, 35]$. $CSF = \frac{S_{0,c}}{S_{0,c} + S_{0,l}} \times 100$, $LSF = 100 - CSF$. CSF: Collagen Signal Fraction; LSF: Long Signal Fraction.

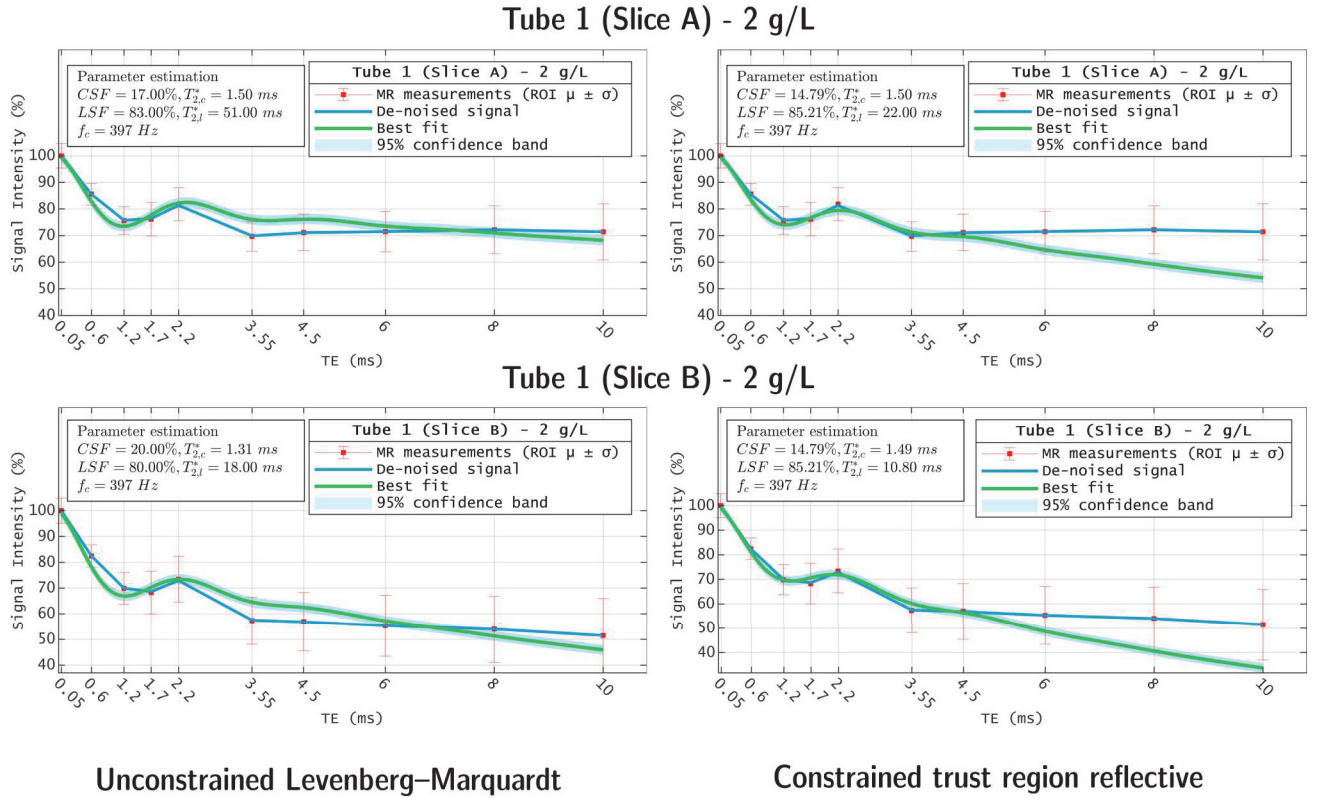


Figure 4.14: Parameter estimation with 10 TE. The left column presents the results using Levenberg-Marquardt algorithm and the right column the results using trust region reflective algorithm, constrained to be in the trust regions (closed interval) $S_{0,l} : [80, 95]$, $S_{c,l} : [5, 18]$, $T_{2,c}^* : [0.5, 4]$ and $T_{2,l}^* : [5, 35]$. $CSF = \frac{S_{0,c}}{S_{0,c} + S_{0,l}} \times 100$, $LSF = 100 - CSF$. The relative error in the short- T_2^* estimation is about 3%. CSF: Collagen Signal Fraction; LSF: Long Signal Fraction.

Tube index	Temporal resolution	Trajectory and Sub-sampling ratio	Slice	CSF (%)	$T_{2,c}^*$ (ms)	LSF (%)	$T_{2,l}^*$ (ms)	ΔS (%)	NF (%)
1	128	Default	A	16.22	1.54	83.78	34.30	-8.29	3.01
		0.0459	B	18.67	1.52	81.33	16.31	-5.98	6.2
2	128	Default	A	9.40	1.71	90.60	20.30	-1.94	2.14
		0.0459	B	10.06	1.71	89.94	19.37	-2.19	1.4
3	128	Default	A	9.50	1.19	9.50	8.80	8.66	2.73
		0.0459	B	8.06	1.33	91.94	11.37	3.97	5.66

Table 4.3: Summary of the parameter estimation across tubes 1, 2, and 3. These are the ground truth values for assessing parameter estimation with 10 TE. CSF: Collagen Signal Fraction; LSF: Long Signal Fraction. ΔS : Signal intensity difference (Equation 4.5) and NF : Noise Floor (Equation 4.6)

The percentage error in parameter estimation on sub-sampled images, specifically the images reconstructed from the k-Space acquired with a GA trajectory with temporal rotation (sub-sampling ratio 0.0230), is in the range of 5 to 10% (Tables 4.4 and 4.5). The

short- T_2^* is about 0.14 ms below the ground truth. A possible reason for this is that regularisation parameters were tuned for in vivo imaging in Section (Table 3.4). A strong regularisation reduces the amplitude (oscillation between [1, 2.4] ms) of the signal (which explains low T_2^*) even when the signal is stronger than the noise. However, these results are close to the parameter estimation on images with higher sub-sampling ratio (0.0459).

Description	Tube index	Slice	Temporal resolution	Trajectory and sub-sampling ratio	CSF (%)	$T_{2,c}^*$ (ms)	LSF (%)	$T_{2,l}^*$ (ms)
Reference Signal	1	A	128	Default 0.0459	16.22	1.54	83.78	34.30
Target Signal	1	A	10	Default 0.0459	17.00	1.50	83	51
				Error (%)	4.80	2.59	0.93	48.68
Target signal	1	A	10	$GA(\alpha_j)$ 0.0230	14.37	1.46	85.62	25.05
				Error (%)	11.40	5.19	2.19	26.96

Table 4.4: Absolute percentage error in parameter estimation with sub-sampled images (Slice A). Temporal sub-sampling, from 128 to 10 TE; spatial sub-sampling from 6240 to 3120 projections per TE. CSF: Collagen Signal Fraction; LSF: Long Signal Fraction. $GA(\alpha_j)$: Golden Angle trajectory with temporal rotation α_j

Description	Tube index	Slice	Temporal resolution	Trajectory and sub-sampling ratio	CSF (%)	$T_{2,c}^*$ (ms)	LSF (%)	$T_{2,l}^*$ (ms)
Reference Signal	1	B	128	Default 0.0459	18.67	1.52	81.33	16.31
Target Signal	1	B	10	Default 0.0459	20	1.31	80	18
				Error (%)	7.12	13.81	1.63	10.36
Target signal	1	B	10	$GA(\alpha_j)$ 0.0230	16.33	1.38	83.67	12.14
				Error (%)	0.67	9.21	2.87	25.56

Table 4.5: Absolute percentage error in parameter estimation with sub-sampled images (Slice B). Temporal sub-sampling, from 128 to 10 TE; spatial sub-sampling from 6240 to 3120 projections per TE. CSF: Collagen Signal Fraction; LSF: Long Signal Fraction. $GA(\alpha_j)$: Golden Angle trajectory with temporal rotation α_j

4.3 Discussion

In this study, the short- T_2^* from collagen was quantified based on:

1. collagen/gelatin fibrillar matrices of collagen type I which corresponds to a 0.25 of the collagen I / collagen III ratio in early post-myocardial infarction [47];

Discussion

2. an accelerated UTE GA R3D imaging sequence compatible with a clinical setting at 3T (sub-sampling ratios: 0.0459 and 0.0230, Section 4.2.3);
3. a set of specific TE, selected by Monte Carlo simulations;
4. a wavelet PCA multivariate de-noising method, and
5. model fitting with non-linear least squares methods.

As in previous studies [4], [5], the results of this analysis measured short- $T_2^* < 2$ ms.

Siu et al. [4] established the bi-component model with an oscillation term for short- T_2^* at 7T (UTE radial 3D), and this was reproduced by Araujo et al. [5] at 3T (UTE radial 2D). Both studies performed the measurements on aqueous solutions (diluted collagen powder), which has been discussed as an experimental limitation because these solutions lack the fibrillar structure (Figure 3.1) of collagen observed in fibrosis [38]–[40].

The model with an oscillation term for short- T_2^* has not been used on published experiments such as in [3], [40]. One possible reason for the non-utilisation of this model might be that the oscillation is lost within the intrinsic noise of images. Van Nierop et al. [3] reported ROI-based signal intensity curves of ex vivo and in vivo MR measurements from fibrotic tissue (mice hearts at 9.4 T) in which the ex vivo signals exhibit an oscillation that is not visible within in vivo signals (Figure 4.15).

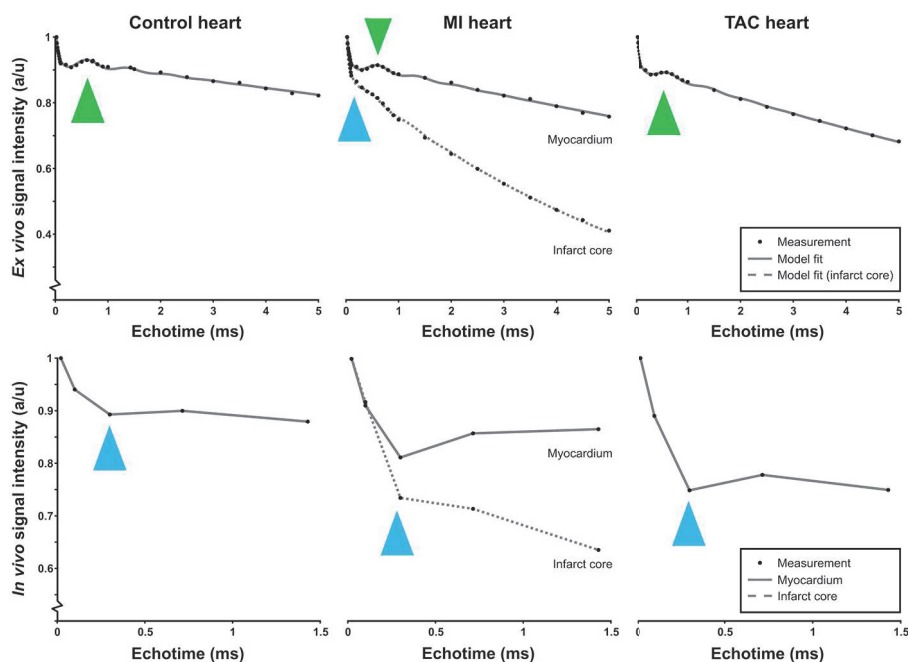


Figure 4.15: ROI-based signal intensity reported in [3] on fibrotic tissue. Green arrows highlight the signal oscillation and blue arrows highlight the slope change due to the characteristic first local minimum of the signal oscillation. Figure adapted from [3].

This difference can be explained by the higher temporal resolution of the ex vivo experiments (34 vs 5 TE) and the selection of the 5 TEs for the in vivo scans (not reported in the publication). In both cases (ex vivo and in vivo), the slope of the curve changes significantly and the signal decay becomes slow around the local minimum of the oscillation as highlighted in Figure 4.15. Moreover, the model used by Van Nierop et al. [3] was

$$SI = \left| I_{fast} e^{\frac{-TE}{T_{fast}^*}} + I_{slow} e^{\frac{-TE}{T_{slow}^*}} + I_{lipid} e^{\frac{-TE}{T_{lipid}^*} + i(\omega TE + \phi)} \right| \quad (4.7)$$

in which, according to the authors "the T_2^* signal decay curves were adequately described by two exponentially decreasing and one oscillating decaying lipid component" [3].

The fast slope change in the signal is also observed in other publications about short- T_2^* [71]. Using the echo times and parameters presented in [71], it is possible to calculate a signal with Equation 2.13 (bi-component and oscillation for short- T_2^*) and make a curve fitting based on a bi-component model without oscillation term with Equation 2.11 as presented in Figure 4.16.

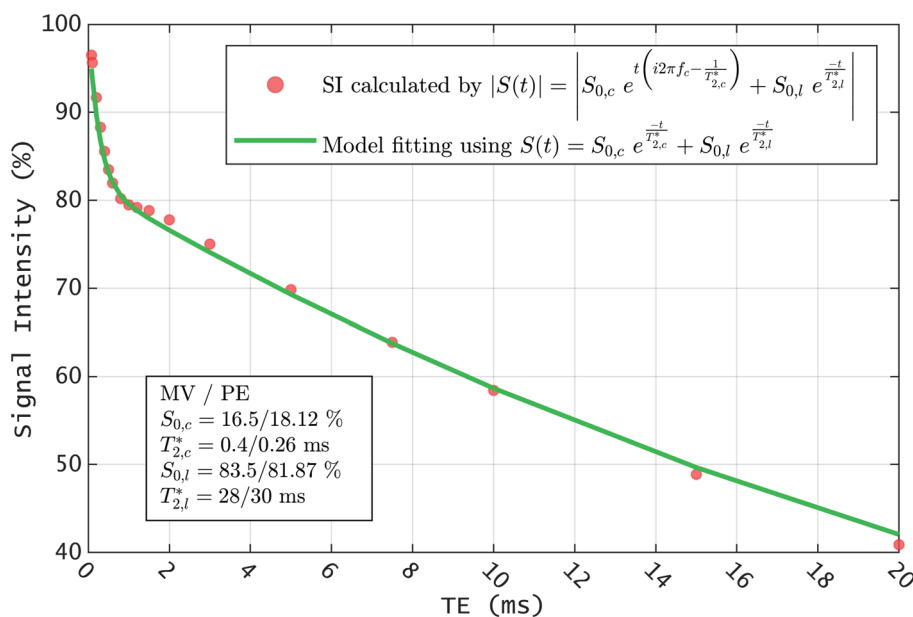


Figure 4.16: Model fitting by using a bi-component model with no oscillation term for short- T_2^* . MR signal calculated using Equation 2.14 (red dots) and model fitting using Equation 2.11 (green curve). MV: model values reported in [71]; PE: parameter estimation.

These are a clear examples of amplitude loss due to the selection of TE for MR measurements and SNR.

Published results [4], [5], [37] showed a strong association between the signal intensity and collagen concentration (in mass percent) on aqueous solutions. This correlation was used to derive the SI lower bound (Noise Floor, Equation 4.6) required to measure the amplitude of the oscillation. The noise floor, defined as the SI difference between the local minimum and maximum in the TE range (1, 2.4) ms, is a key feature of the bi-component model with an oscillation term for short- T_2^* due to the resonance frequency of collagen at 3T. The results yield insights into the conditions to detect the UTE MR collagen signal in which a 20% concentration of collagen (in mass percent) is required; below 10% SI oscillation is lost in the intrinsic noise of images. A theoretical threshold can be defined in a range between 8.14% to 9% when $\Delta S > 0$.

Exemplar short-axis magnitude images (T_2^* -weighted) are presented in Figures 4.17 and 4.18 with corresponding statistics (mean \pm SD) per segment. In general, the normalised difference in SI is negative as predicted by the collagen oscillatory model (Equation 2.12); however, this difference is below the noise floor required to use an oscillatory model for short- T_2^* quantification.

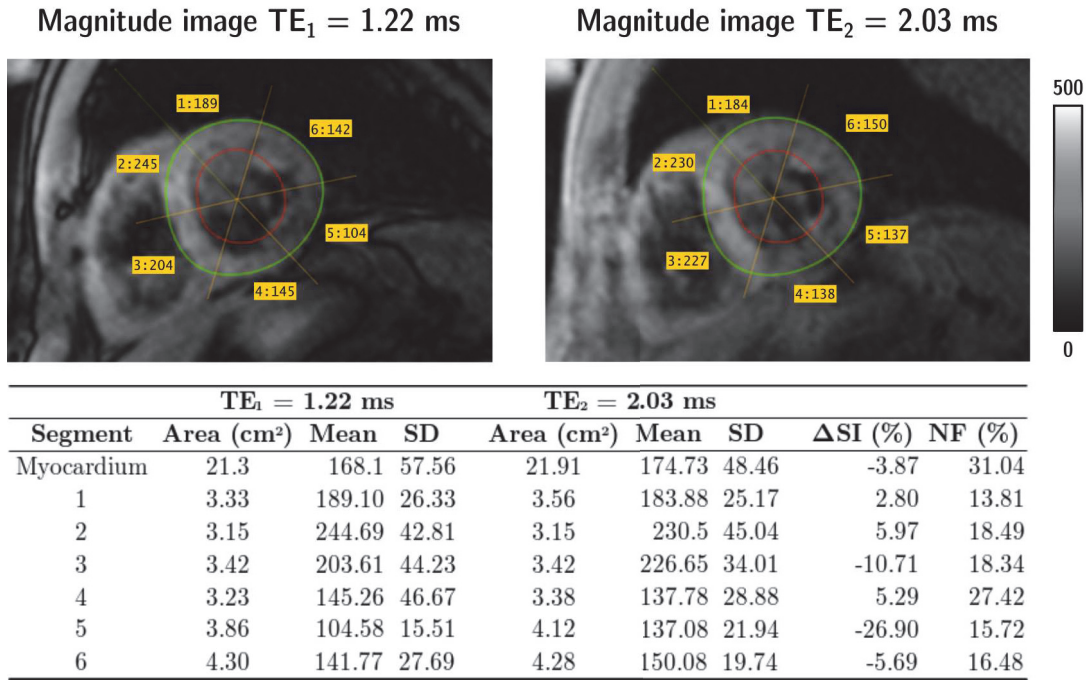


Figure 4.17: Noise floor on short-axis magnitude images (FLASH 2D with dark blood pulse). The normalised difference in SI is negative as predicted by the collagen oscillatory model (Equation 2.12). This difference is nevertheless below the noise floor required to use an oscillatory model for short- T_2^* quantification. SD: Standard deviation; SI: Signal intensity; NF: Noise floor.

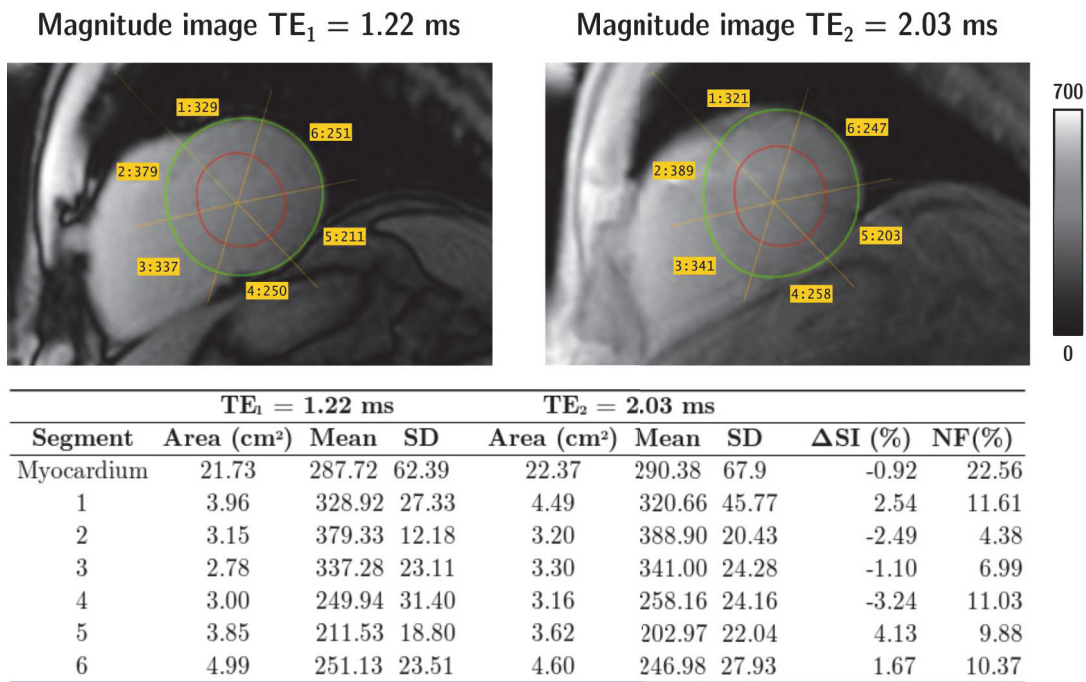


Figure 4.18: Noise floor on short-axis magnitude images (FLASH 2D). The normalised difference in SI is negative as predicted by the collagen oscillatory model (Equation 2.12). This difference is nevertheless below the noise floor required to use an oscillatory model for short- T_2^* quantification. SD: Standard deviation; SI: Signal intensity; NF: Noise floor.

Conclusion

Most of the MRI de-noising methods are based on a kernel-based convolution assuming statistical distribution for modelling noise in the image. These methods usually exploit the spatial domain using oriented or non-local neighbourhoods [72], and by enhancing the image quality, the accuracy in relaxometry measurements is improved [73]. As the quantification of collagen concentration relies on the short- T_2^* estimation from an oscillatory signal, the Wavelet PCA multivariate de-noising enables the identification of the underlying oscillation in the temporal domain, improving the response of model fitting algorithms.

Approximately 2 - 6.5% of the myocardium is collagen in a healthy adult heart [74], [75]. The volume fraction of fibrosis in diffuse myocardial fibrosis may range between 15% to 31% [75], [76] within hypertrophic cardiomyopathy. This provides a reliable range for the utilisation of a bi-component model with an oscillation term for short- T_2^* for parameter estimation.

In addition, previous studies have overlooked the challenges associated with cardiac imaging. Setting apart motion-induced issues, the clinical translation to cardiac applications is limited by the long scanning time required (Siu et al. about 11h 3D scan [4], Araujo et al. about 17 min for a single slice [5]). Despite the fact that using a static phantom prevents a true assessment of the heart conditions (impact of motion in the UTE MR collagen signal), this is an important first step for assessing the implementation of compressed sensing techniques enabling cardiac application in-vivo. Future studies will have to continue to explore further develop a free-breathing ECG-triggered acquisitions.

4.4 Conclusion

In this study, numerical methods and experimental data (on aqueous solutions) were used to: (1) assess and select a set of TE that guaranteed a reliable estimation of the short- T_2^* from collagen, and (2) derive the SI lower bound (noise floor) to maintain a correct parameter estimation. In vitro MRI experiments were conducted using fibrillary collagen/gelatin dense solution and an accelerated UTE GA R3D sequence compatible with a clinical setting at 3T. Experimental data provide convincing evidence demonstrating that MRI (3T) able to capture the collagen (type I) oscillation from a fibrillary structure when the collagen concentration (in mass percent) is above 10%.

Chapter 5

Multi-parametric quantitative MRI characterisation of collagen

T_2^* is not the only quantitative MR measure for differentiating collagen deposition and healthy tissue in the myocardium. QSM has emerged as a useful technique for medical assessment based on the paramagnetic and diamagnetic properties of biological tissues [77]–[79]. In recent years, several studies have investigated tissue magnetic susceptibility as a reliable biomarker in clinical applications specially in brain imaging and neurological conditions [21], [80], [81]. However, few studies have investigated clinical applications of QSM in Cardiac MRI [82], [83]. Moreover, an increased interest in $T_{1\rho}$ has emerged lately. Several studies have investigated the feasibility of $T_{1\rho}$ imaging technique and quantification methods to detect fibrosis [84]–[86]. With the same interest, Diffusion Tensor Imaging (DTI) has been used to assess diffuse fibrosis in failing hearts with an histological validation [87] as well as on patients with hypertrophic cardiomyopathy [88]. Consequently, DWI parameters (apparent diffusion coefficient, fractional anisotropy, mean diffusivity, etc.) can be used as reliable markers of fibrosis.

The purpose of this study is to assess the achievable level of contrast for different collagen concentrations by different MRI parameters such as $T_{1\rho}$, ADC, FA, B_0 , and χ .

5.1 Materials and methods

Experiments were conducted using a 3T MRI scanner (MAGNETOM Prisma, Siemens, Erlangen, Germany) with an 18 channels cardiac phased-array coil combined with appropriate elements of the spin array coils, as used in clinical practice.

5.1.1 Collagen phantoms

The first phantom comprised five collagen solutions that were prepared by dissolving collagen powder (Collagen Type I and III) in demineralised water as described in Section 3.1.1.1. Collagen concentrations are described in Table 3.1 and tubes were arranged as presented in Figure 5.1.

The second phantom comprised 5 × 50 ml Falcon tubes filled with collagen/gelatin matrices and one tube of Collagen gel (10 mL, diluted in a concentrated medium) as described in section 3.1.1.2. To avoid air susceptibility artefacts and optimise magnetic field experimental MR conditions, tubes were filled with a paraffin wax preparation as presented in Figure 4.1. The tubes were immersed in a water bath and scanned at 22°.

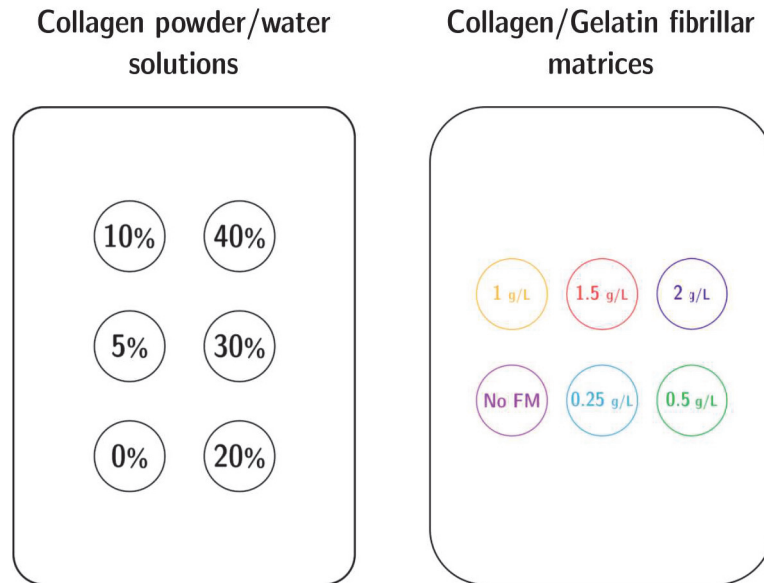


Figure 5.1: Tubes layout in the phantom according to collagen concentration (Table 3.1) in aqueous solutions (left). Tubes layout in the phantom according to collagen concentration used in the initial solution for inducing fibrillogenesis as described in Section 3.1.1.2 (right). Colours correspond to photographs presented in figure 3.3.

5.1.2 Data acquisition

Clinical standard cardiac imaging sequences for T_1 -, T_2 -, T_2^* -mapping were used as well as diffusion and $T_{1\rho}$; imaging parameters are summarised in Table 5.1. All acquisitions were ECG-triggered with a simulated heart rate = 60 beats per minute (RR interval 1000 ms).

	T1-Mapping	T2-Maping	QSM	Diffusion	$T_{1\rho}$
Sequence	MOLLI 4(1)3(1)2 / 5(3)3	FLASH2D	GAR3D	SE-EPI	GRE
TR (<i>ms</i>)	360.56 / 280.56	207.39	207.39	900	252.61
TE (<i>ms</i>)	1.12	1.32	1.2, 2.4, 3.6, 4.8, 6.0, 7.2	85	1.19
FOV <i>mm</i> ²	306x360	288x360	400x400x400	240x300	306x360
Image matrix	256x144	192x116	208x208x208	128x104	256x144
Pixel resolution (<i>mm</i> ²)	1.4	1.8	1.92	2.34	1.4
Slice thickness (<i>mm</i>)	8	8	1.92	8	8
Flip angle (<i>deg</i>)	35	12	15	90	41
Bandwidth (<i>Hz/pixel</i>)	1085	1185	728	2055	890
Number of projections			3120		
Diffusion gradient directions				6	
b_1 (<i>Hz</i>)					500 2, 10, 18,
TSL					26, 34, 42, 50

Table 5.1: Imaging parameters.

Magnitude images from FLASH 2D, custom DTI, $T_{1\rho}$ -weighted sequences were reconstructed using the scanner reconstruction software as well as the corresponding T_2 , ADC, FA and $T_{1\rho}$ maps. Magnitude and phase images from UTE GA R3D were reconstructed by a custom Compressed Sensing-Based workflow implemented on BART [52]–[54]. Magnetic susceptibility maps (B_0 and χ) were calculated on MATLAB R2020b. Regions of interest (ROI) were outlined on $T_{1\rho}$, ADC, FA, B_0 and χ maps. The ROI mean value across tubes was normalised to zero mean and unit standard deviation (Z score) in order to easily compare in the same scale different parameter measurements across collagen concentrations.

5.1.3 Data analysis

Regions of interest (ROI) were outlined on $T_{1\rho}$, ADC, FA, B_0 and χ maps. The ROI mean value μ_i across tubes was normalised to zero mean and unit standard deviation

$$z = \frac{\mu_i - \mu_{ALL}}{\sigma_{ALL}} \quad (5.1)$$

where μ_{ALL} is the average of the mean values across tubes and σ_{ALL} its standard deviation. z -score enables the comparison of the different MR parameters measurements in the same scale across collagen concentrations. Regions of interest (ROI) were outlined on parametric maps within the Horos DICOM viewer [70].

5.2 Results

Representative T_1 , T_2 , $T_{1\rho}$ parametric maps are presented in figures 5.2 and 5.4 for the collagen powder (type I and III) / water and collagen (type I)/gelatin fibrillar matrices phantoms respectively. Moreover, ADC, FA and magnetic susceptibility (χ) parametric maps are presented in figures 5.3 and 5.5.

T_1 , T_2 , decrease with increasing collagen. This results are in agreement with Winkler et al. [89]. Similarly, $T_{1\rho}$ and ADC measurements decrease with increasing collagen concentration. FA measurements increase with increasing collagen concentration.

Comparative $z - Score$ maps are shown in figure 5.6. The figure presents the best case in which the z -score is equally dispersed across the entire range from -1.85σ to 2.4σ . The ADC parameter is the closest one to the best decreasing case, generating specific contrast for aqueous solutions as well as collagen/gelatin fibrillar matrices. Completely different behaviour in the case of $T_{1\rho}$, the difference is not significant to create high contrast across collagen concentrations.

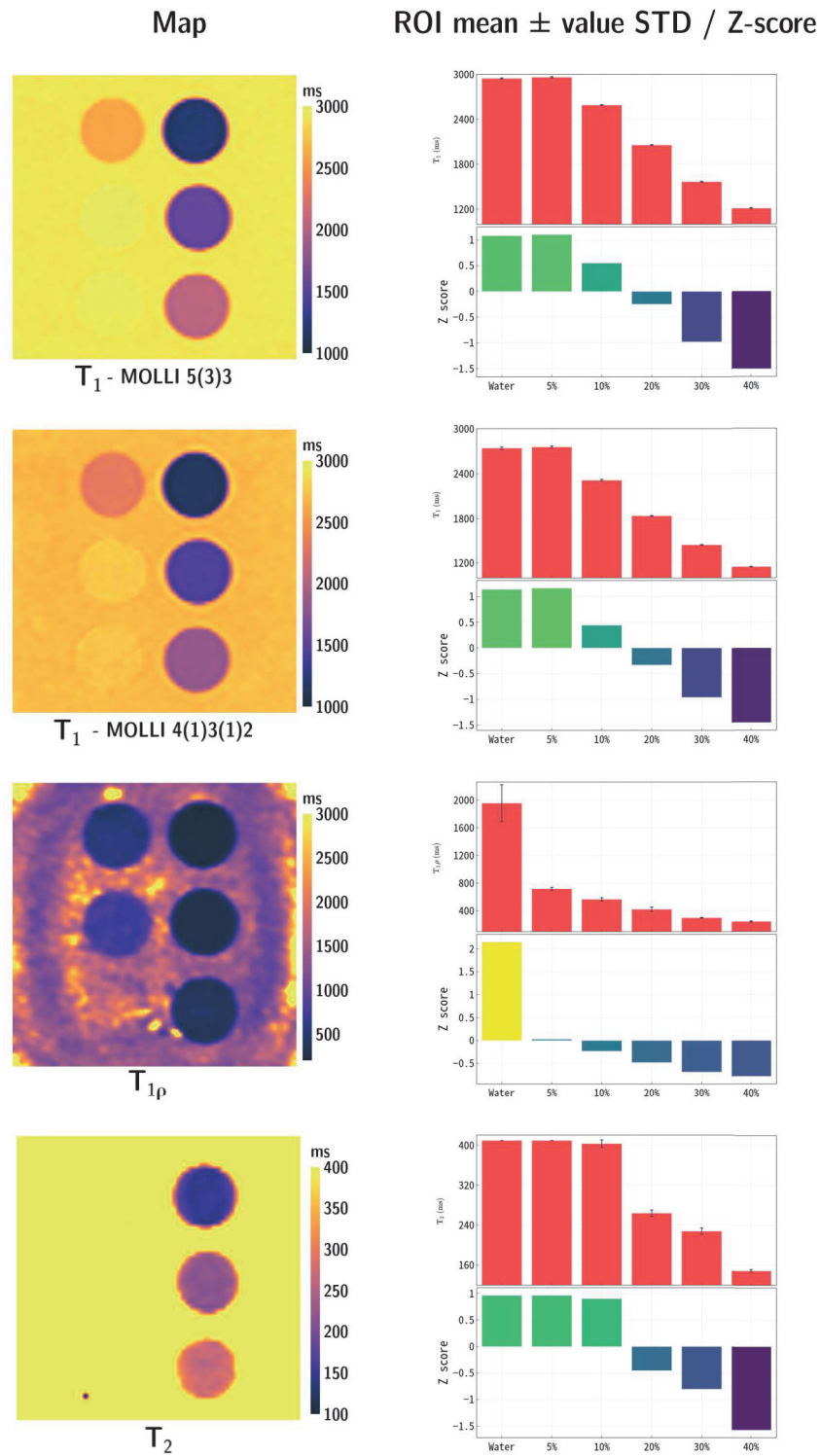


Figure 5.2: Exemplar T_1 , T_2 and $T_{1\rho}$ parametric maps calculated from collagen powder (type I and III) / water solutions. Figures present the ROI mean values \pm standard deviation across tubes and respective z-score.

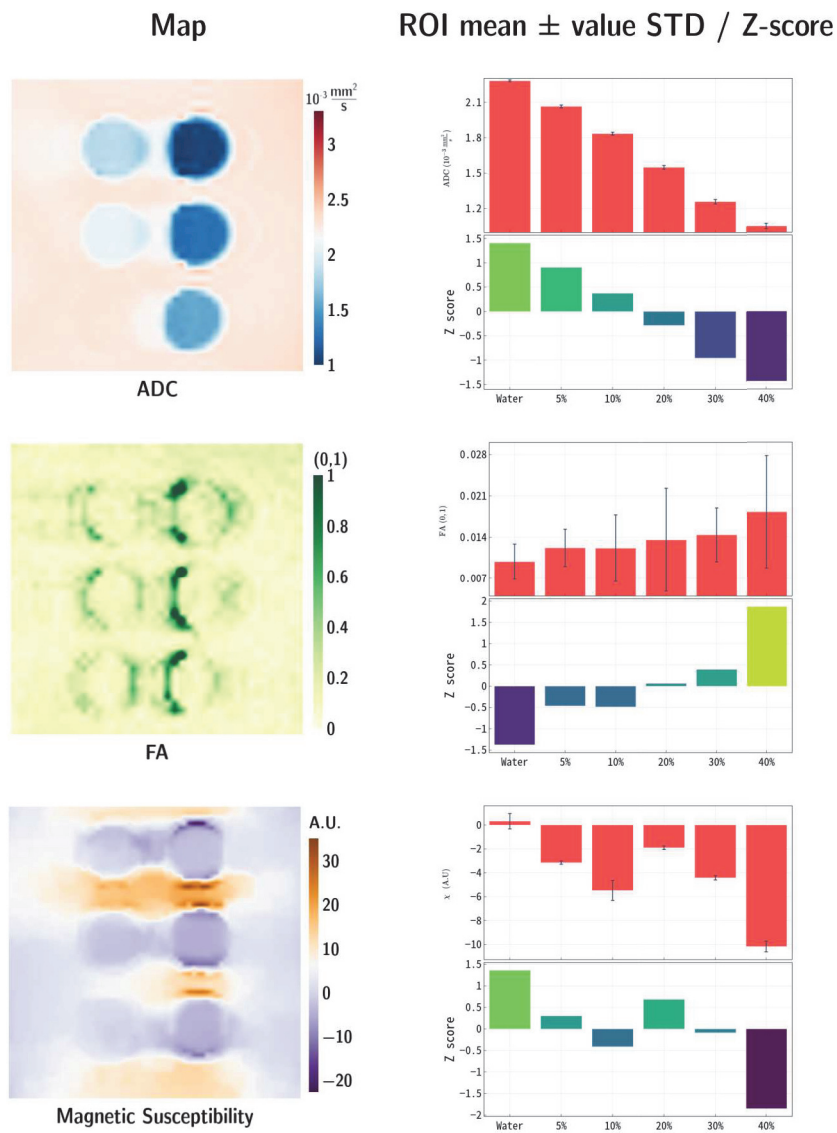


Figure 5.3: Exemplar ADC, FA and magnetic susceptibility (χ) parametric maps calculated from collagen powder (type I and III) / water solutions. Figures present the ROI mean values \pm standard deviation across tubes and respective z-score.

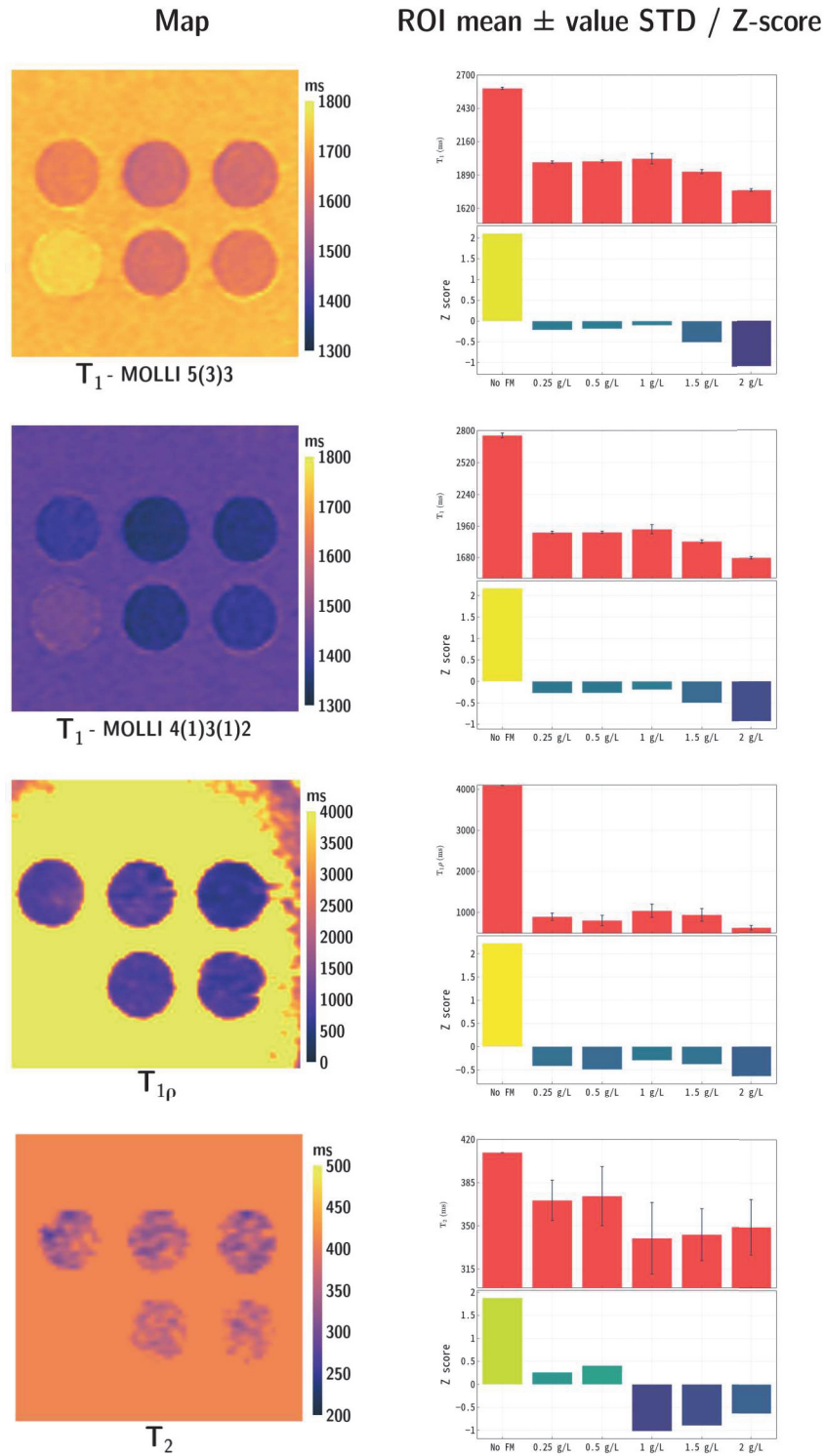


Figure 5.4: Exemplar T_1 , T_2 and $T_{1\rho}$ parametric maps calculated from collagen (type I)/gelatin fibrillar matrices. Figures present the ROI mean values \pm standard deviation across tubes and respective z -score.

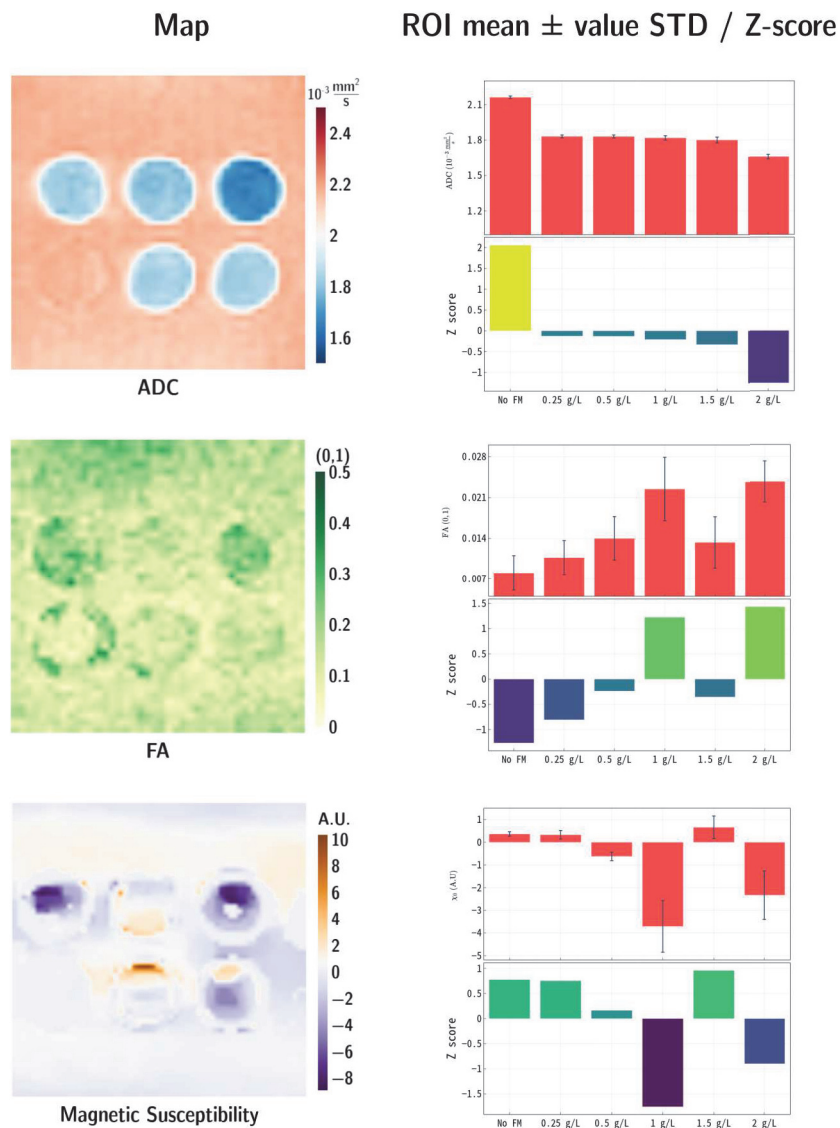


Figure 5.5: Exemplar ADC, FA and magnetic susceptibility (χ) parametric maps calculated from collagen (type I)/gelatin fibrillar matrices. Figures present the ROI mean values \pm standard deviation across tubes and respective z-score.

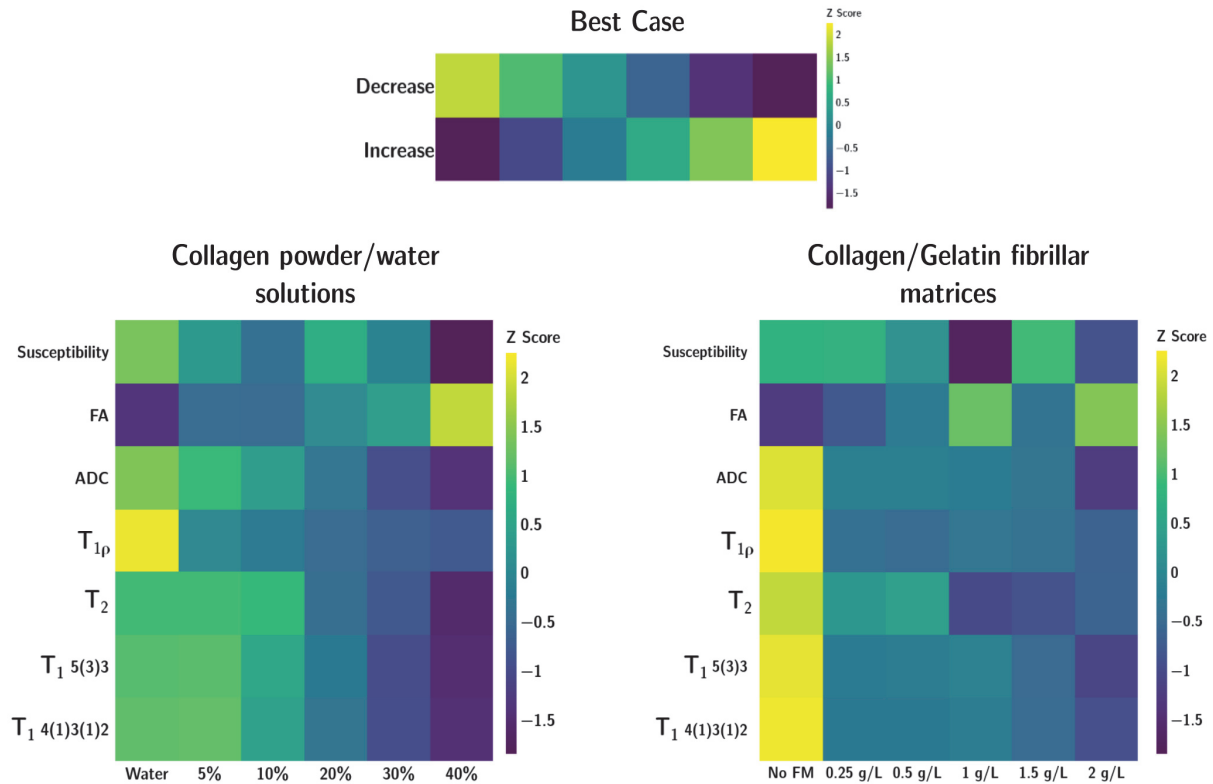


Figure 5.6: MRI parametric z -score maps. The figure presents the best case in which the z -score is equally dispersed across the entire range from -1.85σ to 2.4σ

5.3 Discussion

ADC behaviour is consistent with previous *in vivo* studies in which ADC decreases in fibrotic tissue. Each row on the Z -score map provides the degree of precision in measuring different concentrations of collagen. The results of this study suggest that diffusion imaging is able to differentiate collagen concentrations generating specific contrast on the ADC map for aqueous solutions as well as collagen/gelatin fibrillar matrices.

Negative susceptibility confirms the diamagnetic property of collagen. The z -score and FA map do not present a clear difference between collagen concentrations. The phantom lack of anisotropic microstructure can lead to this behaviour in aqueous solutions. However, in fibrillar matrices, anisotropy increases with increasing collagen concentration because of the anisotropy of fibrillar structure. The significant difference in ADC mean value for each tube enables high contrast across collagen concentrations. In the case of $T_{1\rho}$, the difference is not significant to create high contrast across collagen concentrations.

5.4 Conclusion

The results provide convincing evidence that apparent diffusion coefficient (ADC) is the parameter that guarantees the most precise differentiation of collagen concentrations in aqueous solutions. A multi-parametric approach allows to define an MRI signature based on magnetic susceptibility, diffusion and $T_{1\rho}$ parameters which might be useful to identify different clusters related to different types of fibrosis (diffuse, reactive, infiltrative, focal). A multi-parametric approach would enable a better understanding of MRI biomarkers in

Conclusion

the assessment of myocardial fibrosis, specially for the quantification of collagen in the cardiac tissue.

Chapter 6

Diffusion Tensor Imaging: post-processing workflow, imaging sequences benchmarking and clinical transfer

Diffusion tensor imaging (DTI) is an emerging contrast agent-free technique which has been used to assess diffuse fibrosis in failing hearts with a histological validation [87] as well as on patients with hypertrophic cardiomyopathy [88], [90]. The results presented in Chapter 5 showed that ADC is sensitive to the collagen concentration and therefore, this measurement provides the best characterisation across different concentrations. In this chapter, two studies are presented: a multicentre phantom imaging experiment for assessing the repeatability and reproducibility of diffusion parameters using state-of-the-art pulse sequences for cardiac DTI; and a preliminary in vivo analysis of the variability of ADC across age groups.

6.1 Imaging sequences benchmarking

The benchmarking of Cardiac DTI imaging sequences is the result of three-years collaboration with Dr. Irvin Teh and Dr. Jürgen E. Schneider from the Leeds Institute of Cardiovascular and Metabolic Medicine (University of Leeds, United Kingdom) who led this project within the Special Interest Group in Cardiac Diffusion (Society for Cardiovascular Magnetic Resonance). The objective of the study was to investigate the inter- and intra-site variation of DTI across 10 clinical scanners.

The work summarised in this section was published in the following articles and conference abstracts:

- Teh, I., Romero R, W. A., et al., “*Validation of cardiac diffusion tensor imaging sequences: A multicentre test–retest phantom study*”, NMR in Biomedicine 35.6 (2022): e4685.
- Romero R, W. A. et al., “*Exploring DTI Benchmark Databases Through Visual Analytics*”, Computational Diffusion MRI, Springer, Cham, 2021. 291-301.

- Teh I., Romero W., et al., “*Reproducibility of diffusion tensor imaging (DTI) on 12 clinical scanners: Towards validation of cardiac dti sequences*”, in ISMRM 2020.
- Teh I., Romero W., et al., “*Multi-centre evaluation of diffusion tensor imaging (dti) in anisotropic phantom: Towards validation of cardiac dti sequences*”, in SCMR 23rd Annual Scientific Sessions, 2020.

6.1.1 Materials and methods

6.1.1.1 Phantom preparation

The phantom comprised 7×50 ml Falcon tubes filled with polyvinylpyrrolidone (Sigma Aldrich, Dorset, UK) in distilled water in concentrations ranging from 0 - 20%. The tubes were immersed in an ice water bath and given sufficient time to equilibrate to 0°C before scanning imaging (Figure 6.1). The reference diffusivity D_{ref} was measured using an independent non-MR technique; the self-diffusion of water was measured and extrapolated to 0°C using a 2nd order polynomial fit [91].

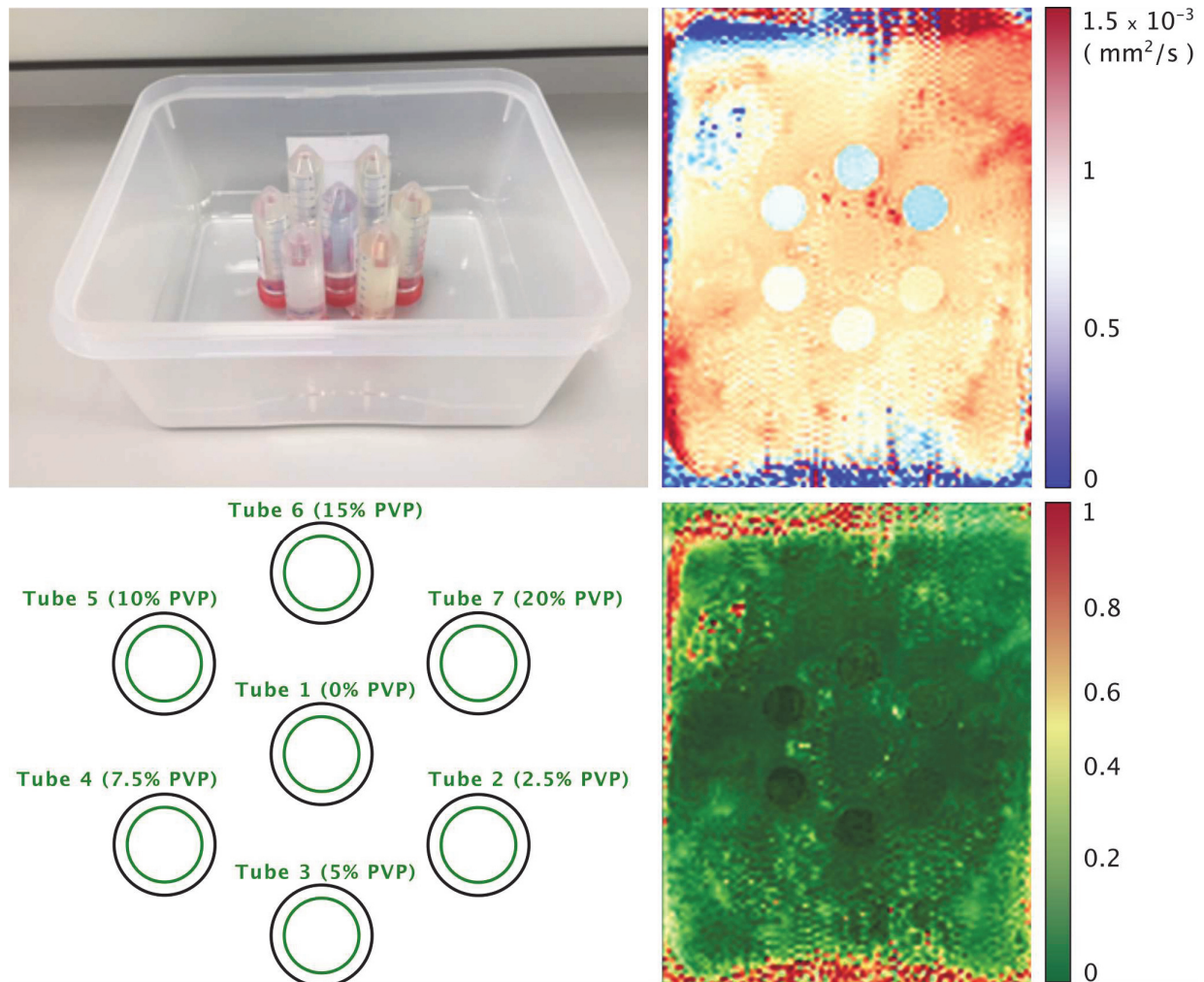


Figure 6.1: Isotropic Phantom, ROI and DAI maps. Photograph of phantom before filling with ice and water (top left); layout of tubes and Regions of Interest (green circles, bottom left); MD and FA maps (top right and bottom right respectively). Background image texture in the MD and FA maps is caused by the ice. Figure reproduced from [92]

6.1.1.2 Data acquisition

The phantom was scanned by each site using product and custom DTI acquisition sequences (Gradient Spin Echo, PGSE; spin echo, SE; and Stimulated Echo Acquisition Mode, STEAM) with parameters matching typical cardiac DTI protocols: TR = 3000 ms, TE = 85 ms, in-plane resolution = 2.5 mm, slices = 3, thickness = gap = 8 mm, blow = $100 \frac{s}{mm^2}$, bhigh = $450 \frac{s}{mm^2}$, number of diffusion directions = 6, bandwidth ~ 3000 Hz, parallel imaging = 2x, and triggered with simulated ECG = 60 bpm. The phantoms are chilled in ice water and imaged at 0 °C. Subsequent scans are performed under the same conditions in a time lapse between 1 and 30 days.

6.1.1.3 Data management, post-processing and analysis

Data storage and management were performed using the Human Heart Project[93], an online platform for heart imaging research. Figure 6.2 describes the main components and data flow implemented for this study.

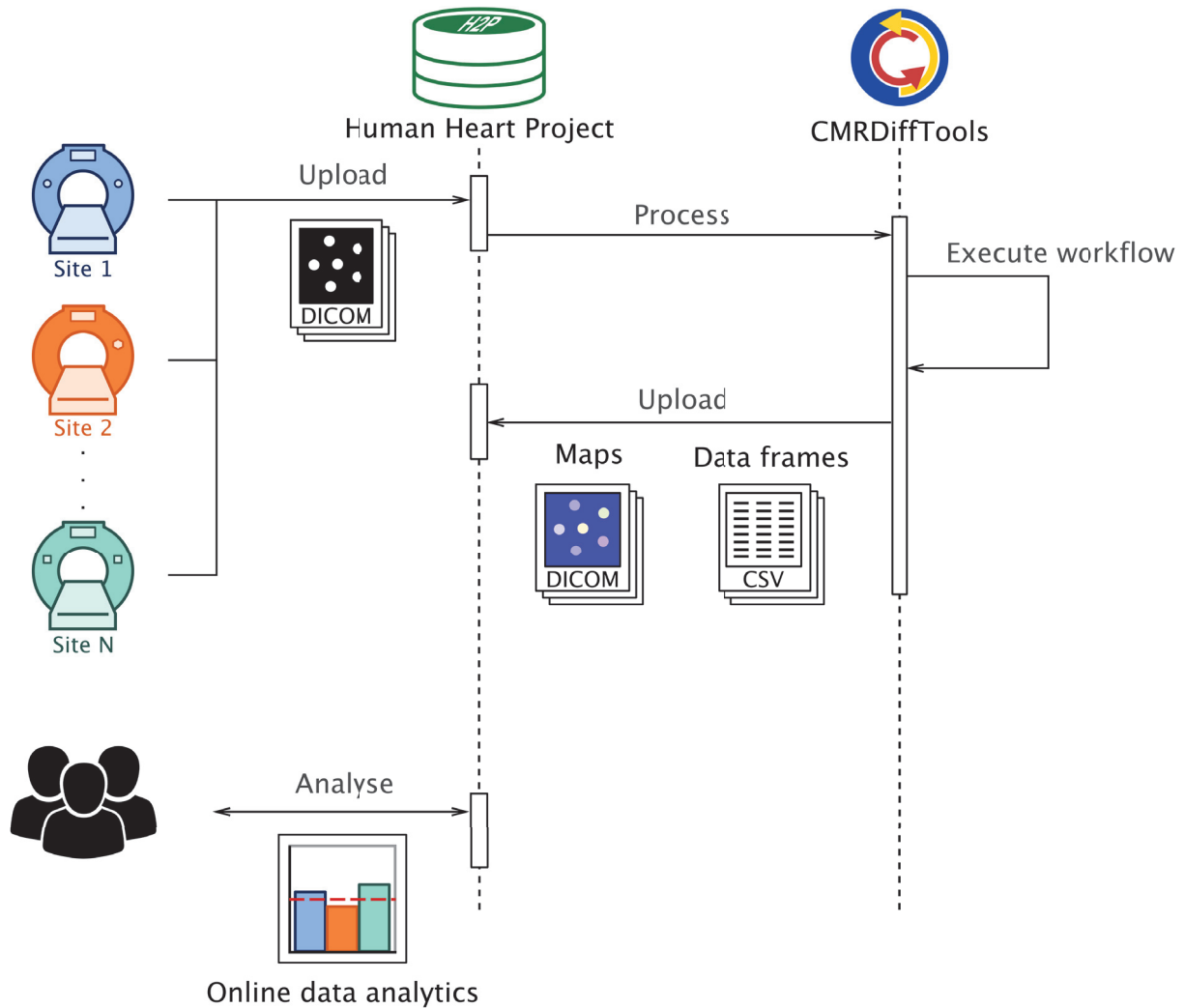


Figure 6.2: Data management and data processing. Main components and data flow.

CMRDiffTools [94] was used for image processing, including automatic tube segmentation, tensor fitting, and calculation of MD and FA (Figure 6.3).

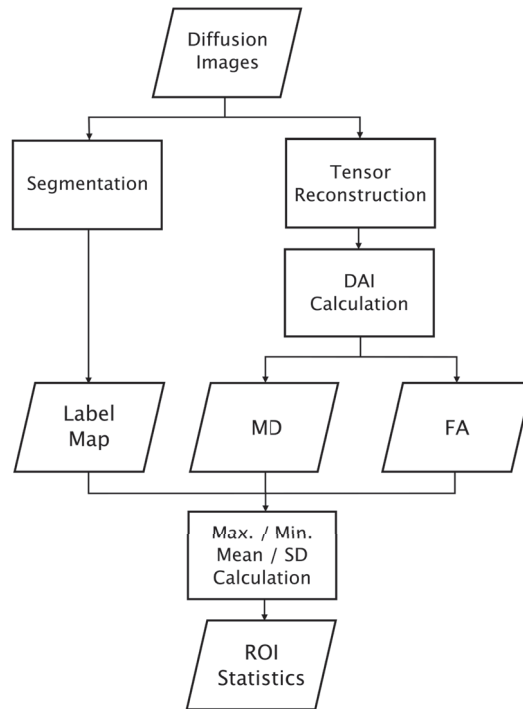


Figure 6.3: Post-Processing workflow.

A visual analytic tool was developed (CMRDiffMonitor [92]) in order to accelerate data analysis and enhance collaborative work. This solution corresponds to the *Online data analytics* process presented in Figure 6.2. CMRDiffMonitor enabled MRI researchers to track and review the variability of diffusion anisotropy indices (ADC, MD, FA) from different image acquisition sequences. The CMRDiffMonitor’s dashboard displays a temporal overview of the data sets (monitoring of the system stability) and the statistical measurements in ROIs on a DAI map (benchmarking of the different imaging sequences and systems) as presented in Figure 6.4.

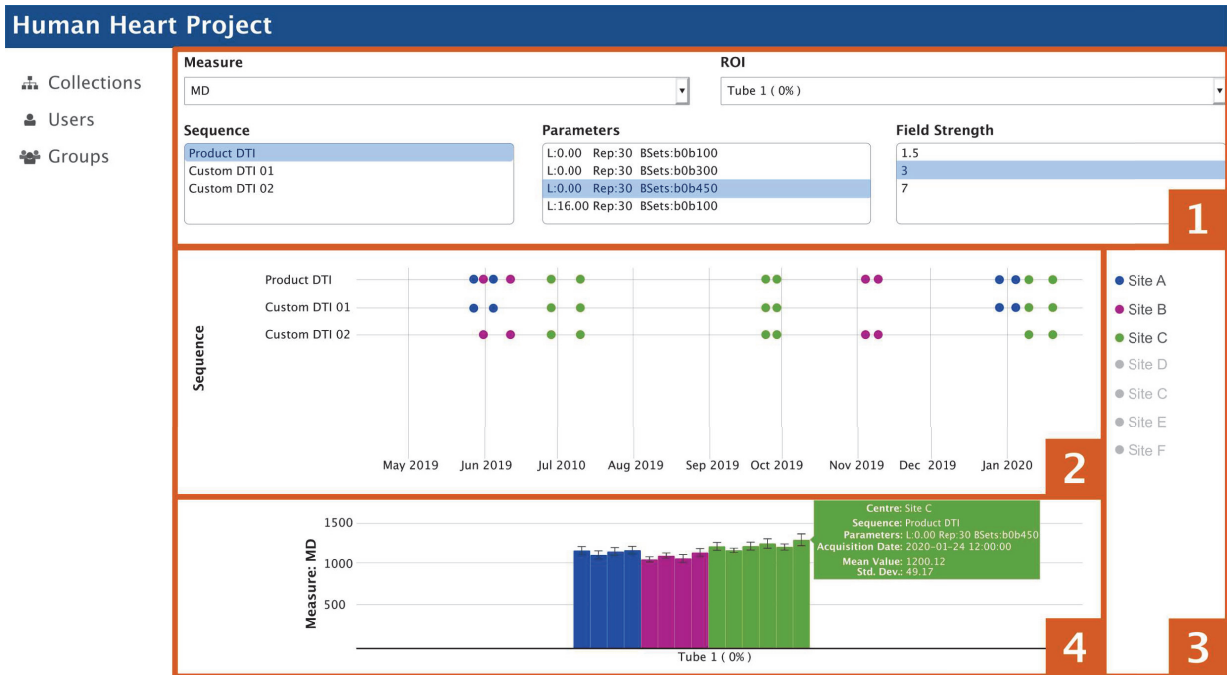


Figure 6.4: Graphical User Interface (GUI) of CMRDiffMonitor. Components: 1 data filters, 2 timeline view, 3 list of sites, and 4 measure view.

6.1.2 Results

MD measurements across tubes between 2 different scans (time delay within 30 days) are shown in Figures 6.5. In tube 1 (0% PVP), the average MDs across all sites and scans 1 and 2 were $1.124 \times 10^{-3} \frac{mm^2}{s}$ (PGSE), $1.130 \times 10^{-3} \frac{mm^2}{s}$ (SE) and $1.113 \times 10^{-3} \frac{mm^2}{s}$ (STEAM). Relative to the reference diffusivity $D_{ref}(H_2O) = 1.113 \times 10^{-3} \frac{mm^2}{s}$, the average MD of tube 1, as measured by PGSE and SE, was overestimated by 1.0% ($p = 0.01$) and 1.5% ($p = 0.01$), respectively, while STEAM provided a result that was accurate to within 0.04% ($p = 0.9$). The SD across ROI in tubes 1-7 increased with PVP concentration, particularly in the STEAM data.

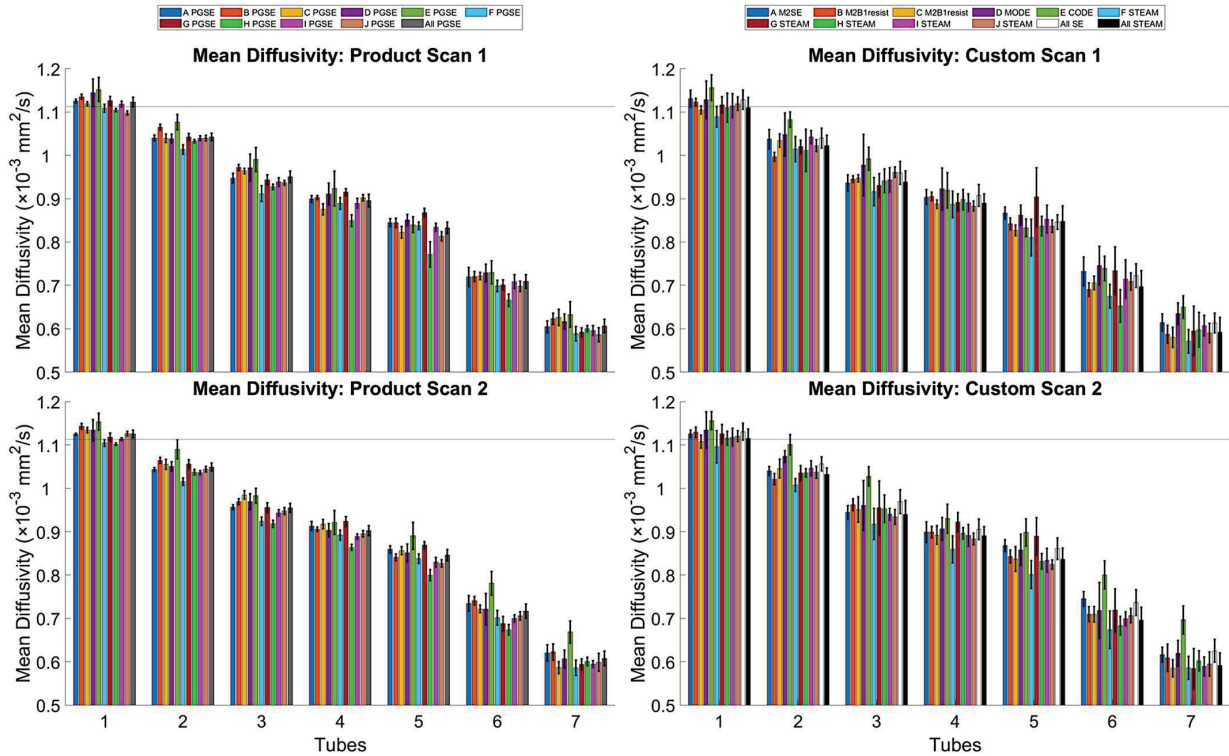


Figure 6.5: Average MD across ROI as a function of PVP concentration. Tensors were reconstructed using $b = (100, 450) \frac{s}{\text{mm}^2}$ data. Tubes 1-7 corresponded to 0%, 2.5%, 5%, 7.5%, 10%, 15% and 20% PVP, respectively. $Mean \pm SD$ across voxels in the ROI. The horizontal black line indicates the reference diffusivity $D_{ref}(H_2O) = 1.113 \times 10^{-3} \frac{\text{mm}^2}{s}$. PVP: polyvinylpyrrolidone, PGSE: Gradient Spin Echo, SE: spin echo, STEAM: Stimulated Echo Acquisition Mode. Figure reproduced from [95]

Bland-Altman plots of MD and FA across 2 different scans (time delay within 30 days) are presented in Figure 6.6. In tube 1, the mean differences of MD were $0.3 \pm 2.3 \times 10^{-5} \frac{\text{mm}^2}{s}$ PGSE, $0.24 \pm 0.95 \times 10^{-5} \frac{\text{mm}^2}{s}$ SE and $0.52 \pm 0.58 \times 10^{-5} \frac{\text{mm}^2}{s}$ in STEAM ($mean \pm 1.96 SD$). mean differences in FA were 0.0006 ± 0.0099 , 0.006 ± 0.018 and -0.012 ± 0.039 respectively.

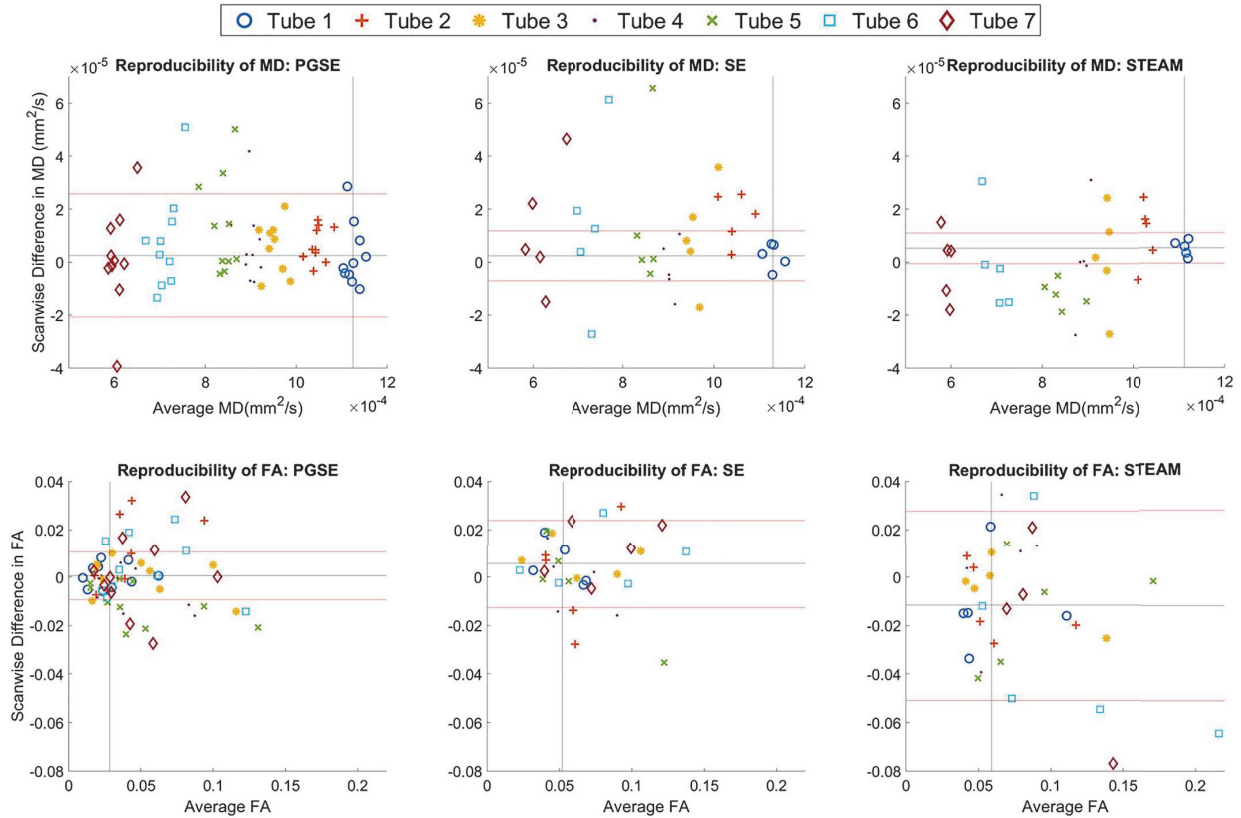


Figure 6.6: Bland-Altman plots of MD and FA across two scans. Data acquired using PGSE (left), SE (middle) and STEAM (right) sequences in tubes 1 to 7 (0%–20% PVP) are colour-coded by increasing PVP concentration. The black and red horizontal lines indicate the mean and ± 1.96 SD values for tube 1, respectively. The black vertical line indicates the average values for tube 1 across sites. PVP: polyvinylpyrrolidone, PGSE: Gradient Spin Echo, SE: spin echo, STEAM: Stimulated Echo Acquisition Mode. Figure reproduced from [95]

6.1.3 Discussion

In this study, a benchmark of cardiac DTI suitable for in vivo imaging was performed. Measurements at isocentre (Tube 1) are consistent with the reference diffusivity of water at 0° C, within $\pm 1.5\%$ percentage of error across sites and sequences. This measurements also consistent with previous results [33, 34, 35] (within $\pm 1\%$) showing good conformance with prescribed experimental conditions. In an isotropic phantom, the FA values should be zero. Non-zero FA measurements are less surprising if eddy currents, imperfect gradient calibration and vibration are considered. Using a static phantom prevents a truth assessment of the heart conditions (impact of motion on the MR signal). Nevertheless, this study demonstrated that cardiac DTI sequences from different centres have excellent agreement as detailed in [95], Appendix 7.

Another interesting outcome from this work was the development and deployment of a visual analytic tool. The multi-centre study provided an opportunity to address the infrastructural developments needed to explore large amounts of data easily and quickly by providing key information in a readily interpretable format. CMRDiffMonitor allows MRI researchers to see, in a concise and accessible way, the current status of the experiment. In a single eye glance, research scientists can:

- Verify protocol compliance by checking time gaps on the **timeline view**.
- Identify anomalies by looking for unusual values on the **measure view**, using the historical registry **timeline view**.
- Compare the outcomes with similar imaging systems from different sites by using the **filters panel** to select: the type of sequence, the b values used to calculate DAI maps (i.e. b0b450, b100b450, b300b450, etc.) and the field strength (1.5T, 3T or 7T).
- Verify and validate a hypothesis. The dashboard summarises the results for all sites.
- Export experiment-specific figures for reporting.

The plug-in integrates simple visualisation techniques to empower research scientists to explore data, analyse and share results. Moreover, the GUI reduces the cognitive load of information, all the image post-processing settings are managed by the back-end components (Girder [96], CMRDiffTools [94], etc.) as well as data sets details, driving the user attention to one task: analyse the outcomes from different imaging systems and cardiac DTI sequences.

This type of application software has potential application in quality assurance protocols such as the T1MES program [97], [98] enabling longitudinal monitoring the stability of MR systems. Based on data acquired on a reference phantom, the application enables MR scientists to verify protocol compliance, identify anomalies and compare imaging sequences across different sites.

6.1.4 Conclusion

This study benchmarked the performance of product PGSE against custom SE and STEAM sequences identifying baseline variation across scanners and sequences as presented in [95], Appendix 7. In the context of this multi-centre study a VA tool was developed (CMRDiff-Monitor) in order to track and review experimental imaging data as presented in [92], Appendix 7.

6.2 Preliminary analysis of the correlation between ADC and age in healthy volunteers

In the ageing heart, the thickening of the collagen-based mesh (increase of collagen deposition in the extracellular matrix, ECM) is a normal process [29], [30]. Consequently, physiological changes in the heart are due to the cardiac muscle stiffness reducing its contractility and optimal deformation, leading to a decrease in the cardiac function. In this direction, the aim of the MARVEL project is to investigate the association between changes in cardiac function and the amount of fibrosis based on novel MRI techniques. In this context, a preliminary analysis was performed in 2019 to determine the ADC variation by age. To ensure the quality and accuracy of the results, a quality control protocol was developed within an application software, deployed on the infrastructure of the main clinical research centre of the study (CHU Saint Étienne).

The work summarised in this section was published in the following articles and conference abstracts:

- Moulin K., Viallon M., Romero W., et al., “*MRI of reperfused acute myocardial infarction edema: ADC quantification versus T1 and T2 mapping*”, Radiology 295.3 (2020): 542-549.
- Romero R, W. A., et al., “*CMRDiffTools: A Processing and Analysis Tool for Cardiac Diffusion MR images*”, in ISMRM 2018.

6.2.1 Materials and methods

6.2.2 Patient population

This prospective study was undertaken in a single tertiary centre (Centre Hospitalier Universitaire de Saint-Étienne). All volunteers fulfilled the following inclusion criteria: More than 18 years old, reduced physical activity (less than 3 sessions endurance sport per week, i.e running), non-smoker and absence of cardiovascular risk factors. In this preliminary study, images from 31 volunteers (19 women) were analysed.

6.2.2.1 Data acquisition

Image acquisition was performed on a SIEMENS Prisma MRI scanner (Siemens, Erlangen, Germany) with an 18 channels cardiac phased-array coil. Imaging parameters are summarised in Table 6.1.

Parameter	Value
Sequence	SE-EPI
TR (<i>ms</i>)	400
TE (<i>ms</i>)	63
FOV (<i>mm</i>)	164 × 200
Image matrix	100 × 82
Pixel resolution (<i>mm</i> ²)	2
Flip angle (<i>deg</i>)	90
Bandwidth (<i>Hz/pixel</i>)	2175
Diffusion gradient directions	12
Averages	5

Table 6.1: DTI imaging parameters within the MARVEL protocol.

6.2.2.2 Data analysis

A post-processing workflow was developed within CMRDiffTools [94]. The workflow includes an affine multi-resolution registration scheme based on mutual information [99], [100] with 3 levels (shrinking factors = 8, 4, 2). Images corresponding to the same diffusion gradient direction were averaged (repetitions) to generate the final data set. Trace, ADC, MD, FA and Helix Angle maps were calculated for each volunteer. Tensor calculation was performed using a linear least-square algorithm [101]. The centre of the Left-Ventricle (LV) required for the Helix Angle calculation was derived from a manual segmentation performed using CMRSegTools [102], [103]

In addition, a quality control protocol was defined in order to avoid under/over estimation of diffusion coefficients caused by motion artefacts. The assessment of motion

correction was based on a LV segmentation performed using CMRSegTools [102], [103]. Image quality measurements (IQM) were calculated before and after performing the maps computation using the quality assessment module within CMRDiffTools [94].

In the assessment of motion correction, pixels are classified in a LV segmentation of two images S_1 and S_2 as: true positive if the pixel is classified as LV myocardium in S_1 and S_2 ; true negative if the pixel is classified as non LV myocardium in S_1 and S_2 ; false positive if the pixel is classified as LV myocardium in S_2 and non LV myocardium in S_1 ; and false negative if pixel is classified as non LV myocardium in S_2 LV myocardium in S_1 . Therefore, four IQM are calculated: the Dice coefficient [104], sensitivity, specificity and Over/Under segmentation [105]. An overlap map was generated as a quantitative index in which it is possible to visualise motion-induced misalignment based on the LV segmentation.

Noise assessment is based on three regions of interest: background noise (BN), signal of reference (SR) and signal of interest (or target signal, ST). The IQM for noise assessment were Signal-to-Noise ratio (SNR), Contrast-to-Noise ratio (CNR) and Contrast are defined by the following equations:

$$SNR = \frac{\mu_{SR}}{\sigma_{BN}} \quad (6.1)$$

$$CNR = \frac{|\mu_{ST} - \mu_{SR}|}{\sigma_{BN}} \quad (6.2)$$

$$Contrast = \frac{|\mu_{ST} - \mu_{SR}|}{\mu_{SR}} \quad (6.3)$$

$$(6.4)$$

where μ is the mean value and σ the standard deviation of each of the ROI (BN, SR and ST).

Manual segmentation of the LV was made by an expert radiologist using CMRSegTools [103] within the Horos DICOM viewer [70]. Mean value and standard deviation in all 6 LV segments reported.

6.2.3 Results

Exemplar results from the image quality assessment are presented in Figure 6.7 (single slice mid short axis, 12 diffusion gradient directions and 5 repetitions).

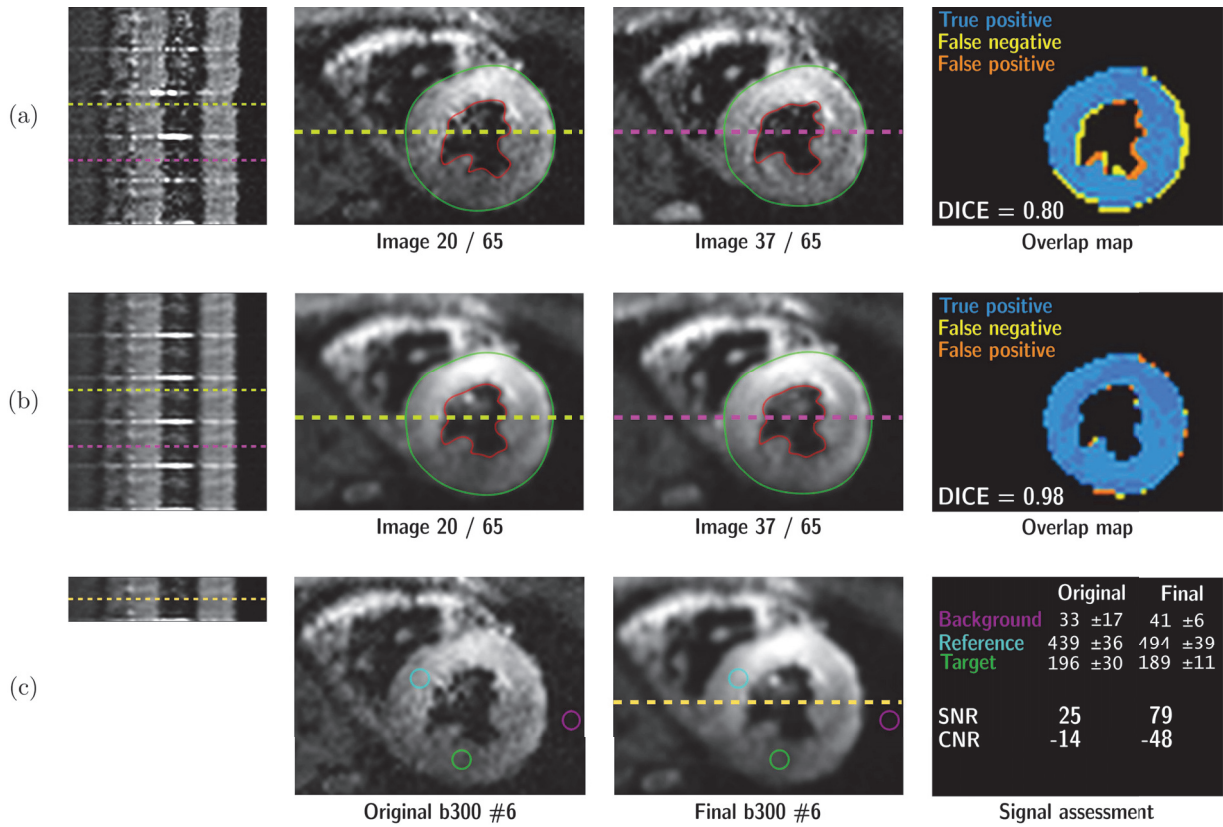


Figure 6.7: Image quality assessment. A qualitative evaluation was performed based on the visualisation of a line profiling across images. (a) Initial quality assessment based on a line profiling across diffusion gradient directions and repetitions (left column) and left ventricle (LV) segmentation (central columns); overlap map (left column) visually outlines the LV misalignment. (b) Quality assessment after motion correction and de-noising. (c) Final data set reduction by using temporal MIP (left column). Signal intensity evaluation between the original magnitude image and the final correction outcome (right column).

The Helix Angle is the best parameter to highlight the inner structure of the myocardium and the impact of motion-induced misalignment. Figure 6.8 shows the difference before and after post-processing on the Helix Angle map and Figure 6.9 on the ADC map.

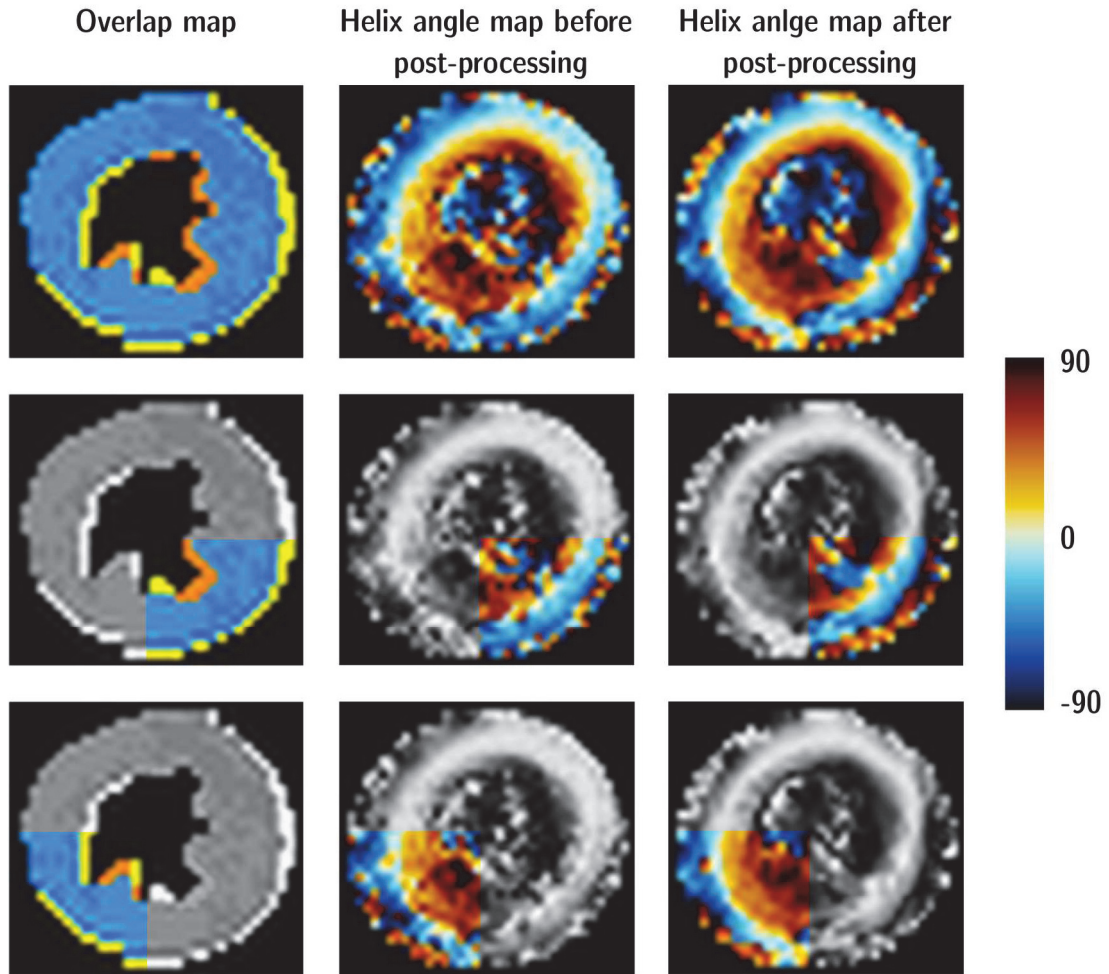


Figure 6.8: Image quality assessment impact on the Helix Angle map. Overlap map (left column) visually outlines and quantifies the LV misalignment. The difference in the helix angle definition is due the correction of the LV alignment as highlighted in the middle and bottom row.

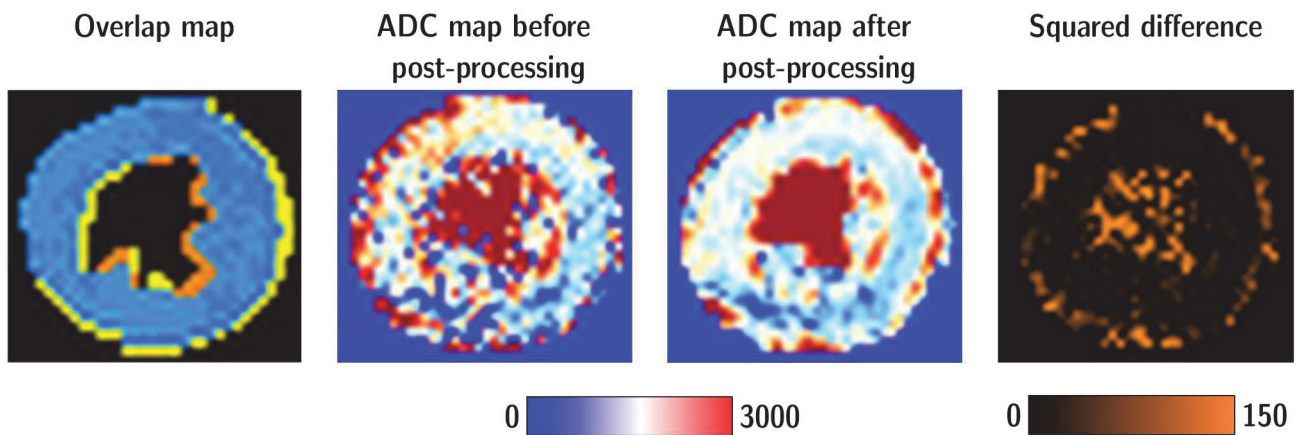


Figure 6.9: Image quality assessment impact on the ADC map. Overlap map (left column) visually outlines and quantifies the LV misalignment. The squared difference between maps is calculated as $\Delta p(i, j) = \sqrt{ADC_{post}(i, j) - ADC_{pre}(i, j)}$. Squared difference highlights the adjustments made based on the overlap map.

An overview of the ADC in the myocardium across age groups is presented in Figure 6.10. Approximately 50% of the population had ADC values ranging between 1.4 and $1.6 \times 10^{-3} \frac{\text{mm}^2}{\text{s}}$. As shown in Figure 6.11, a significant difference in the mean ADC was observed. The mean value in sectors 4 and 6 was slightly high for more than 60% of the population in comparison to segments 1, 2 and 3 (between 1.6 and $1.8 \times 10^{-3} \frac{\text{mm}^2}{\text{s}}$). Correlations between ADC and age were negative and statistically insignificant in all cases. Table 6.2 shows the correlation R-squared value (R^2) between age and the mean ADC for the whole myocardium, and per segment.

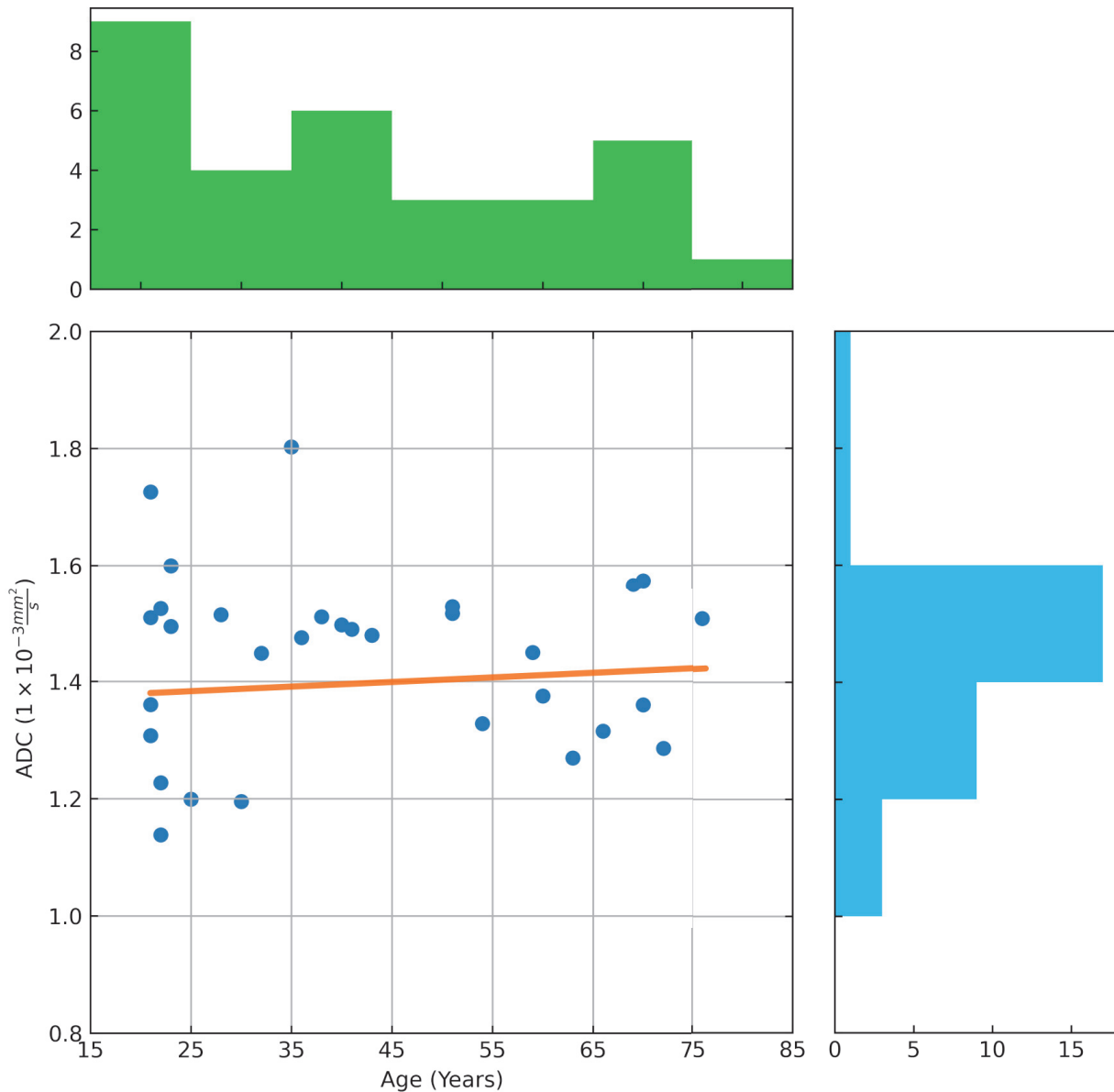


Figure 6.10: ADC values in the myocardium across age. The green and blue histogram describes the age group and ADC values respectively within the population. The orange line is the best-fit linear regression ($R^2 = 3.90 \times 10^{-5}$).

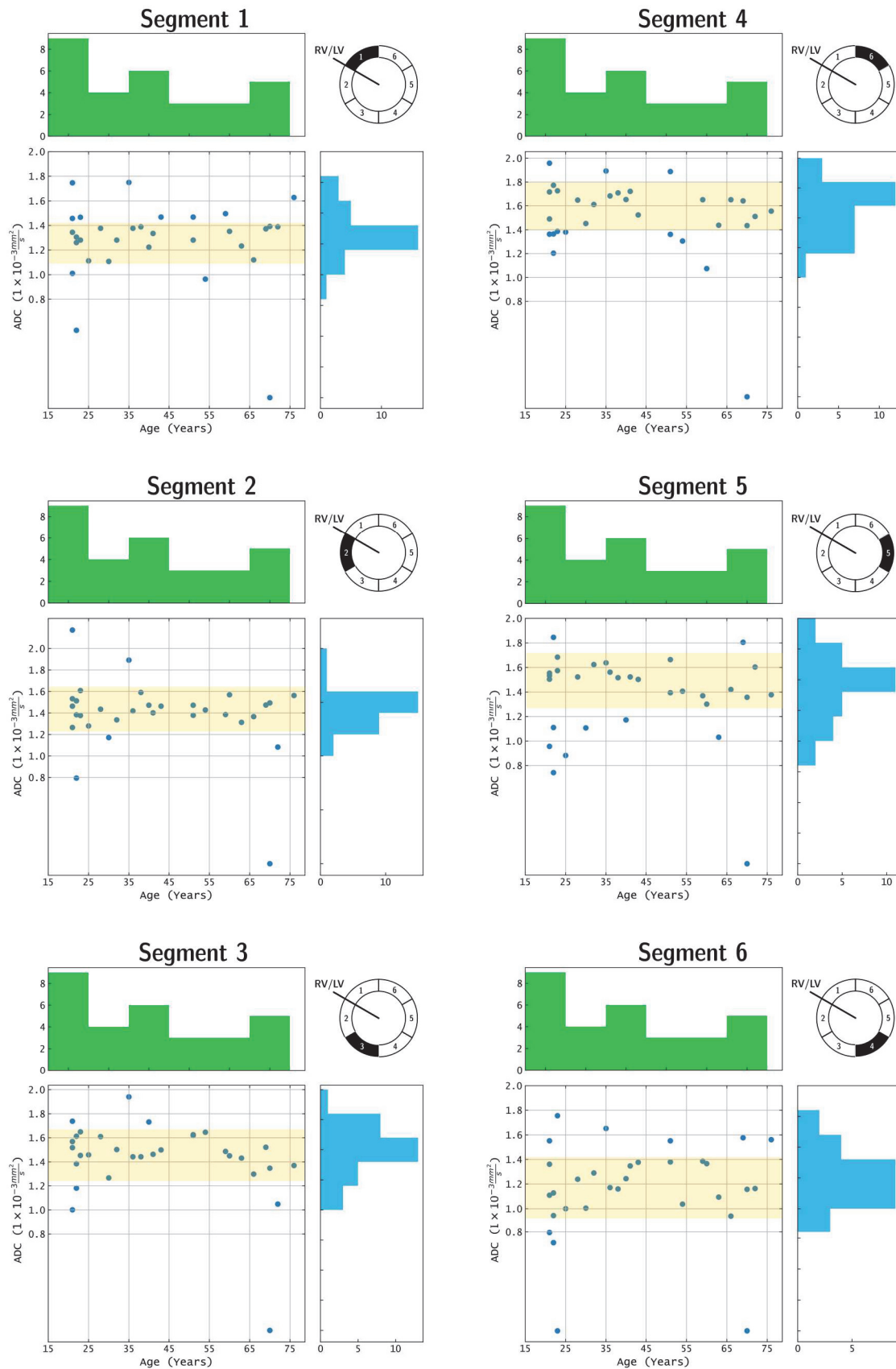


Figure 6.11: ADC mean values across age by segment on the left ventricle. The green and blue histogram describes the age group and ADC mean value respectively within the population. More than 60% of the population (highlighted band) presented a slight difference in segments 4 and 5 in which ADC reach values up to $1.8 \times 10^{-3} \frac{\text{mm}^2}{\text{s}}$ in comparison to segments 1, 2 and 3.

ROI	R^2 Correlation with age
Myocardium	3.90×10^{-5}
Segment 1	0.007
Segment 2	0.058
Segment 3	0.102
Segment 4	0.083
Segment 5	0.012
Segment 6	0.005

Table 6.2: Correlation of ADC with age. Linear regression calculated on the entire population.

6.2.4 Discussion

In this study, a DTI post-processing workflow was implemented in CMRDiffTools [94] enabling research scientist to process and assess large clinical data sets. After post-processing and quality control, DTI data sets were ready for statistical analysis.

The MARVEL data set for the preliminary analysis was limited to 31 volunteers (August 2019). As shown in Table 6.2, there was no correlation found between age and mean ADC values for the entire myocardium or segments. In other words, R^2 provided preliminary evidence against a significant correlation between ADC and age. There is an article in preparation based on the entire population of the study to report *The effect of aging on relaxometry and diffusion parameters in healthy subjects at 3T CMR*.

The post-processing workflow used on the MARVEL data set included to stages: image registration and de-noising. The parameters used in each stage of the workflow were experimentally calibrated. In general, there are two types of registration techniques, those based on rigid transformations (rotations and/or translations) and those that require a more complex transformation (non-rigid or elastic) based on splines interpolation or point set registration [106], [107]. These methods are computationally heavy; consequently they may require a segmentation or landmarks not only to accelerate but also to guide and improve the precision of the correction.

The selection and tuning of the image registration scheme would depend on the quality of the images in terms of alignment and deformation of the structure of interest [108]. Image registration metrics usually rely on segmentation such as DICE similarity coefficient [104] or the analysis of line profiles in the temporal or diffusion gradient dimensions. There is no standard image registration scheme because there are several factors to analyse before selecting the key components of the method (type of transformation, metric, optimiser, landmarks, etc.). However, image registration must be performed before any pixel-wise filter or model fitting. Figure 6.7 illustrates a pre- and post-motion correction assessment based on LV segmentation and line profiling in the diffusion gradient dimension.

Noise reduction strategies exploit the availability of multiple repetitions by using principal components analysis [109]–[111]. Information from spatial and repetition neighborhood windows are included in the PCA analysis. Final results are usually obtained by maximum intensity projection in time PCAtMIP [110]. These methods perform better after image registration to improve accuracy. The most common metrics for noise reduction assessment are SNR and CNR. Figure 6.7 illustrates a pre- and post-noise reduction assessment.

The post-processing workflow implemented CMRDiffTools was used in the study reported by Moulin et al. in [112] which demonstrated that ADC depicts myocardial edema better than T1 and T2 maps.

6.2.5 Conclusion

A DTI post-processing workflow has been implemented within CMRDiffTools in order to provide on-the-job support to ease quality control tasks on large clinical cohorts. The results provide preliminary evidence that ADC could not be useful to assess the increase in collagen deposition across age groups.

Chapter 7

Conclusions

This thesis has addressed important challenges towards a multi-parametric quantitative MRI assessment of myocardial fibrosis. In this direction, the first contribution was to propose collagen/gelatin fibrillar matrices for in vitro experimentation enabling the measurement of the collagen MR signal on samples with fibrillar structure. The experiments conducted in this work explored potential biomarkers such as $T_{1\rho}$ relaxation, diffusion and magnetic susceptibility.

The second contribution was to analyse the reliability of short- T_2^* quantification with an accelerated GA-Based R3D sequence compatible with a clinical setting at 3T. Cardiac imaging sequences rely on compressed sensing techniques in order to reconstruct reliable diagnostic images from data below the Nyquist criterion. Based on numerical experiments, a noise floor was identified such that the MR collagen signal is preserved within the intrinsic noise of images, setting the boundaries of reliability in MR measurements and quantifying the short- T_2^* at 3T. In addition, a set of echo times were selected for a correct temporal sampling. This is an important first step for assessing the implementation of compressed sensing techniques enabling future application in-vivo. Consequently, future studies will have to continue to explore the development of free-breathing ECG-triggered acquisitions.

The third contribution was a comparative multi-parametric analysis based on magnetic susceptibility, diffusion and $T_{1\rho}$. These results enable a better understanding of MRI biomarkers and their relationship. These experiments lead to the following question: can MRI differentiate non-fibrillar from fibrillar structures? According to the experiments and results from this work: the presence of collagen is confirmed by spectroscopy; diamagnetic behaviour is observed with magnetic susceptibility, diffusion decreases and anisotropy increases with increasing collagen concentration in both, non-fibrillar and fibrillar structures; this statement cannot be completely given for aqueous solutions because of the lack of anisotropic microstructure. Consequently, to completely answer this question, an MR parameter to extract geometrical properties must be included such as susceptibility tensor imaging and tractography.

Nowadays, where multi-parametric studies combined with machine learning methods are on the rise, the understanding of MRI biomarkers and their relationship plays a key role in the assessment of new techniques such as physics-informed neural network in which the outcome is the agreement of a multi-dimensional analysis including T_1 , T_2 , T_2^* , $T_{1\rho}$, magnetic susceptibility, diffusion and more to come.

Appendix A

Romero R, W. A., Viallon M. et al., “*CMRSegTools: an open-source software enabling reproducible research in segmentation of acute myocardial infarct in CMR images*”, PloS one 17.9 (2022): e0274491.
<https://doi.org/10.1371/journal.pone.0274491>

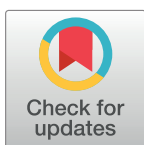
RESEARCH ARTICLE

CMRSegTools: An open-source software enabling reproducible research in segmentation of acute myocardial infarct in CMR images

William A. Romero R.¹, Magalie Viallon^{1*}, Joël Spaltenstein², Lorena Petrusca¹, Olivier Bernard¹, Loïc Belle³, Patrick Clarysse¹, Pierre Croisille¹

1 Univ Lyon, INSA-Lyon, Université Claude Bernard Lyon 1, UJM-Saint Etienne, CNRS, Inserm, CREATIS UMR 5220, U1294, Saint Etienne, France, **2** Spaltenstein Natural Image, Geneva, Switzerland, **3** Department of Cardiology, Centre Hospitalier Annecy-Genevois, Annecy, France

* Magalie.Viallon@creatis.insa-lyon.fr



OPEN ACCESS

Citation: Romero R. WA, Viallon M, Spaltenstein J, Petrusca L, Bernard O, Belle L, et al. (2022) CMRSegTools: An open-source software enabling reproducible research in segmentation of acute myocardial infarct in CMR images. PLoS ONE 17(9): e0274491. <https://doi.org/10.1371/journal.pone.0274491>

Editor: Kumaradevan Punithakumar, University of Alberta, CANADA

Received: March 15, 2022

Accepted: August 29, 2022

Published: September 13, 2022

Peer Review History: PLOS recognizes the benefits of transparency in the peer review process; therefore, we enable the publication of all of the content of peer review and author responses alongside final, published articles. The editorial history of this article is available here: <https://doi.org/10.1371/journal.pone.0274491>

Copyright: © 2022 Romero R. et al. This is an open access article distributed under the terms of the [Creative Commons Attribution License](https://creativecommons.org/licenses/by/4.0/), which permits unrestricted use, distribution, and reproduction in any medium, provided the original author and source are credited.

Data Availability Statement: In vivo images were obtained from the MIMI study (ClinicalTrials.gov Identifier: NCT01360242,217) and are available on

Abstract

In the last decade, a large number of clinical trials have been deployed using Cardiac Magnetic Resonance (CMR) to evaluate cardioprotective strategies aiming at reducing the irreversible myocardial damage at the time of reperfusion. In these studies, segmentation and quantification of myocardial infarct lesion are often performed with a commercial software or an in-house closed-source code development thus creating a barrier for reproducible research. This paper introduces CMRSegTools: an open-source application software designed for the segmentation and quantification of myocardial infarct lesion enabling full access to state-of-the-art segmentation methods and parameters, easy integration of new algorithms and standardised results sharing. This post-processing tool has been implemented as a plug-in for the OsiriX/Horos DICOM viewer leveraging its database management functionalities and user interaction features to provide a bespoke tool for the analysis of cardiac MR images on large clinical cohorts. CMRSegTools includes, among others, user-assisted segmentation of the left-ventricle, semi- and automatic lesion segmentation methods, advanced statistical analysis and visualisation based on the American Heart Association 17-segment model. New segmentation methods can be integrated into the plug-in by developing components based on image processing and visualisation libraries such as ITK and VTK in C++ programming language. CMRSegTools allows the creation of training and testing data sets (labeled features such as lesion, microvascular obstruction and remote ROI) for supervised Machine Learning methods, and enables the comparative assessment of lesion segmentation methods via a single and integrated platform. The plug-in has been successfully used by several CMR imaging studies.

the Human Heart Project (<http://humanheart-project.creatis.insa-lyon.fr>) under research collaboration agreement. The source code is available at <https://github.com/OpenCardiacMRIsoftware/CMRSegTools>.

Funding: This work has been performed within the framework of LABEX PRIMES 372 (ANR-11-LABX-0063) of Université de Lyon, within the program "Investissements d'Avenir" (ANR-11-IDEX-0007) and France Life Imaging (ANR-11-INBS-0006) operated by the French National Research Agency (ANR). The funders had no role in study design, data collection and analysis, decision to publish, or preparation of the manuscript.

Competing interests: The authors have declared that no competing interests exist.

Introduction

Myocardial infarct size is a crucial parameter serving as a surrogate endpoint in clinical studies of new therapeutic interventions after Acute Myocardial Infarction (AMI). Therefore, considerable research engagement has been directed toward the automatic quantification of the infarct size as well as the size of the post-reperfusion no-reflow lesion based on CMR Late Gadolinium Enhanced (LGE) images [1–5]. These studies require reliable post-processing tools for the segmentation and quantification of the myocardial infarct lesion; in general, these tools are reported to be an in-house code development in a numeric computing environment (i.e. MATLAB) or a commercial application software. Not only do these tools restrict reproducibility of the studies but they can also prevent a full understanding of the use of computational methods. Because what is behind the mathematical model (constraints, parameters, etc.) is not clear, it is difficult to provide an objective assessment of lesion segmentation methods. For instance, a recent publication of Wu et al. [5] presents a general review of cardiac scar segmentation methods (including methods for non-LGE images). This review reports quantitative results across publications. The conclusion states the need of a public benchmarking of the methods as a fairer review of their performances. This is a challenge that requires tools for open collaboration in a growing culture focused on advancing methods by reproducible science [6, 7]. The neuroimaging research community is a clear example of this research and development methodology [8, 9].

In the field of Cardiac MRI, there is a gap between open-source software built within the scientific community and commercial applications. The issue is not the availability of computational methods for image processing in open-source packages *per se*, but the fact that these methods are not assembled in a suitable workflow for processing and carrying out statistical analysis on large clinical cohorts. A suitable workflow requires to select the structure of interest (myocardial segmentation), perform a computational method on the data from this structure, and analyse the output based on the American Heart Association (AHA) 17-segment model [10] (commonly named bullseye plot). Although it does not seem complex, it has been apparently embraced only by commercial applications which offer a custom-made workflow for myocardial segmentation and statistical analysis based on the AHA model. To provide an example, Table 1 presents an overview of well-known image processing tools in terms of two requirements for Cardiac MR image analysis: myocardial segmentation and statistical analysis following the standardised AHA 17-segment model. In general, a commercial software is a product designed to be marketed under a utilisation licence. The user must pay for a binary

Table 1. Overview of available post-processing tools. Requirement 1 (R1): myocardial segmentation, requirement 2 (R2): statistical analysis and visualisation following the AHA 17-segment model.

Application Software	Description	R1	R2	Target Platform	Licence
3D Slicer [13]	Subject-specific biomedical image processing and visualisation	No	No	Linux, Windows, macOS	Open-Source, BSD-style
ImageJ [14]	Multi-purpose scientific image processing and visualisation	No	No	Linux, Windows, macOS	Public Domain, BSD-2
MeVisLab [15]	Workflow-based fast-prototyping	No	No	Linux, Windows, macOS	Proprietary, freeware
Medis Suite MR [16]	Cardiac MR image analysis	Yes	Yes	Windows	Commercial
Circle CVI42 [17]	Cardiac MR image analysis	Yes	Yes	Windows, macOS	Commercial
Segment CMR [18]	Cardiac MR image analysis	Yes	Yes	MATLAB on Linux, Windows, macOS	Segment open licence agreement
Caas MR Solutions [19]	Cardiac MR image analysis	Yes	Yes	Windows	Commercial
CMRSegTools	Cardiac MR image analysis	Yes	Yes	macOS	CeCILL

<https://doi.org/10.1371/journal.pone.0274491.t001>

version which must be used as in accordance with the licence directives. There is no access to the source code of the commercial product (closed-source). Freeware software is free of charge but closed-source. In open-source software, the user has access to the source code and the different licences (i.e. BSD, GNU GPL, etc.) provide the rights to copy, modify, redistribute the code, as well as build and release binary versions for commercial purposes [11]. Open-source software promotes open collaboration and research communities have been attracted to this innovation methodology [12]. Overall, open-source image processing software is not closely linked to the CMR concepts and practice. Therefore, a customised computer-based tool such as the one presented in this paper, could provide on-the-job support to ease analysis task performance on large clinical cohorts.

Moreover, a new demand has arisen with the advent of computational methods based on Machine Learning (ML). Using ML, the scientific community is now developing new solutions to solve the long-standing problem of a reliable quantification of infarct lesions. These approaches require annotated data sets which are generated and assessed by standard methods (i.e. signal threshold versus reference mean, full-width at half-maximum, etc.) [4, 5, 20, 21]. Consequently, there is a clear need for a unified reference of computational methods for lesion segmentation. This could be met with a common assessment platform that could easily be used by clinicians, radiologists and MRI researchers.

This paper presents CMRSegTools, a novel application software that allows users to benchmark new lesion segmentation methods as compared to state-of-the-art methods in the field. CMRSegTools, includes customised tools for user-assisted myocardial segmentation; manual, semi- and automatic lesion segmentation which can be used in the generation of training data sets for Machine Learning (ML) strategies. This computer-based tool can be easily deployed on clinical infrastructures, closing the gap between analysis methods and their direct utilisation in clinical trials, as demonstrated in the studies [22–25].

CMRSegTools plug-in

CMRSegTools is an application software specifically designed to ease myocardial segmentation, quantification and tissue characterisation on CMR images. CMRSegTools has been implemented as a plug-in for the widely available commercial OsiriX and open-source Horos DICOM viewers [26, 27] in order to take advantage of usability features and advanced visualisation tools (ROI outline tools, colour look-up tables, pixel interpolation algorithms for display, etc.) as well as the effortless deployment on a clinical or research infrastructure. Fig 1 shows the main components of the plug-in and its integration within the OsiriX/Horos environment.

The user-friendly Graphical User Interface (GUI) empowers the user to: segment the Left-Ventricle (LV); calculate infarct size, Microvascular Obstruction (MVO) lesion size, Endocardial Surface Length (ESL), and Endocardial Surface Area (ESA) amongst others. The real-time feedback updates the GUI with statistical information (number of pixels, minimum and maximum pixel value, mean value, standard deviation, etc.) of the pixels selected by the segmentation along with an interactive histogram. The image of interest is also dynamically updated (Epicardium and Endocardium contours, LV/RV junction landmark, region segments statistics in the 17-segment model, AHA [10]) according to the user interaction (Fig 2). Furthermore, CMRSegTools saves the workspace state, which means that it restores the GUI and image viewer to the state they were in when the plug-in was last used. The source code of the plug-in is available at <https://github.com/OpenCardiacMRISoftware/CMRSegTools>.

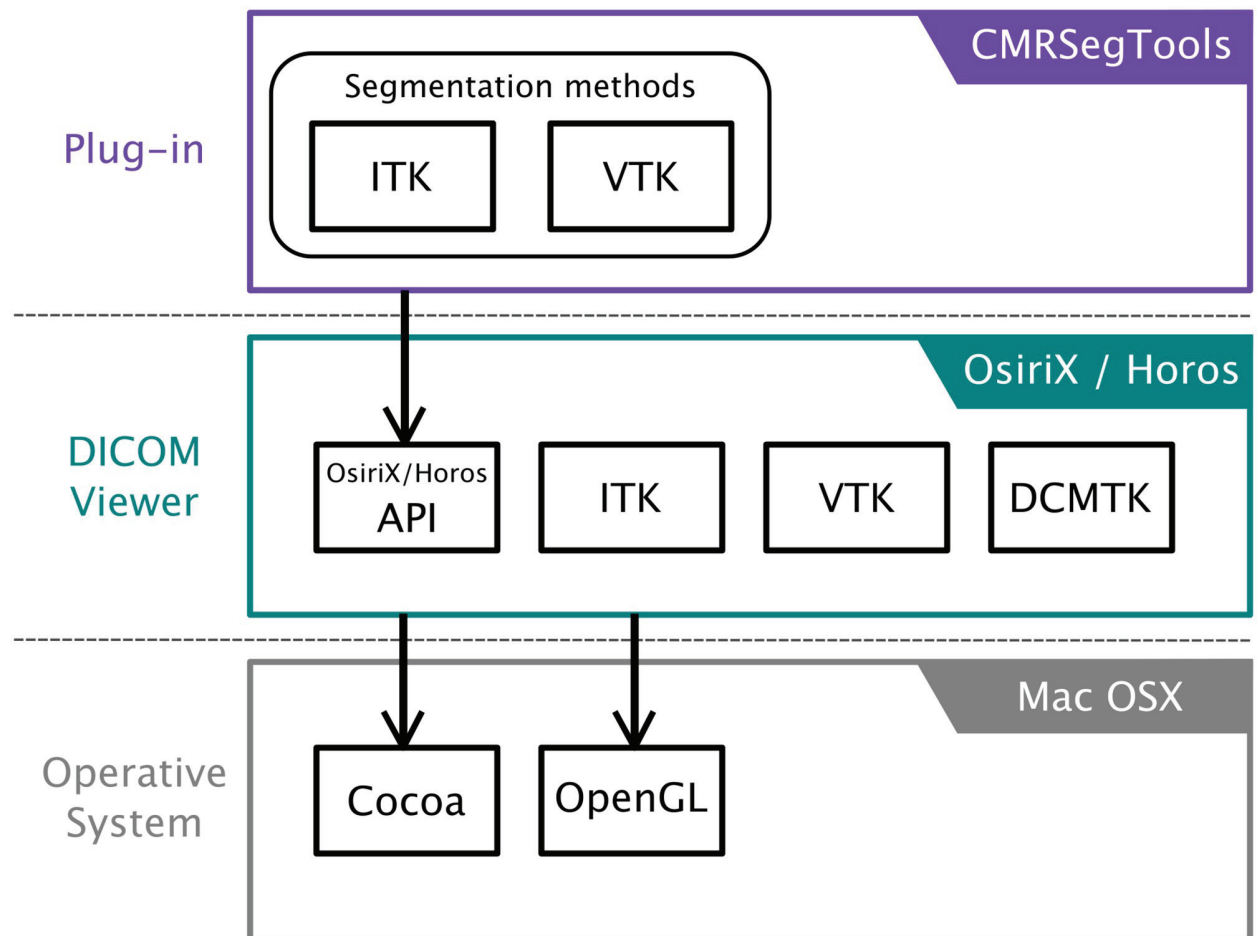


Fig 1. CMRSegTools architecture diagram. The plug-in has access to the DICOM viewer functionalities through the Application Program Interface (API) exposed by OsiriX/Horos. The DICOM viewer runs on MacOS operating system. List of the frameworks and toolkits in each layer: ITK, Insight Toolkit; VTK, Visualisation Toolkit; DCMTK, DICOM Toolkit; Cocoa, Mac OSX Native AP; OpenGL, Computer Graphics API.

<https://doi.org/10.1371/journal.pone.0274491.g001>

Interoperability and extension

The CMRSegTools plug-in is independent of scanner vendor, sequence type and protocol. The OsiriX/Horos framework [26, 27] eliminates common requirements for data access (access to PACS), database management, transformation from the DICOM standard to final post-processing format, and data provenance; requirements which are critical in the development of clinical trials. In addition, the plug-in includes a functionality to import ROI from cvi42 (Circle Cardiovascular Imaging Inc., Calgary, Canada) file format.

This application software has been designed with the CMR lexicon in mind. All graphical elements generated by the plug-in (i.e. segmentation contours, set of pixels corresponding to the lesion, etc.) are tagged with keywords for identification within the OsiriX/Horos runtime environment. This enables the interaction with other plug-ins. For example, a specialised plug-in for myocardial segmentation (i.e. ML-based segmentation [21]) can export the segmentation output with the keywords “*CMRSegTools: Epicardium*” and “*CMRSegTools: Endocardium*” (ROI names can be set by the user in the OsiriX/Horos ROI manager). Therefore, this

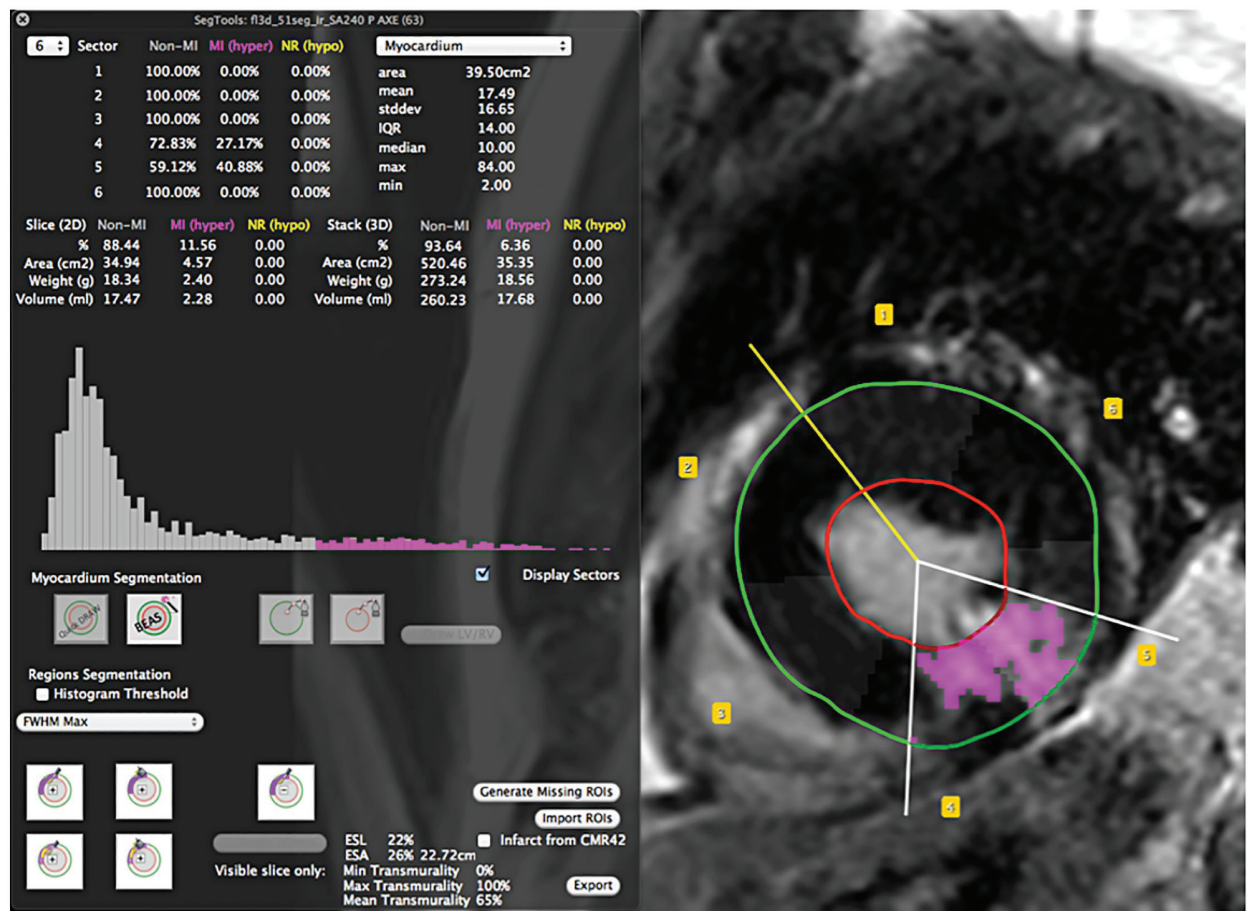


Fig 2. CMRSegTools workspace. The CMRSegTools GUI (left) shows the histogram highlighting the bins matching the lesion segmentation. The user can select the algorithms for the segmentation of the myocardium or some of its regions. The image viewer (right) displays the segmented area in magenta as well as the Epicardium (green) and Endocardium (red) contours, LV/RV junction landmark (yellow segment) and AHA region segments. The LGE image presented was obtained with a 3D IR GRE sequence.

<https://doi.org/10.1371/journal.pone.0274491.g002>

segmentation can be identified by CMRSegTools. Inversely, another plug-in can start working with the CMRSegTools ROIs (“CMRSegTools: Epicardium”, “CMRSegTools: Endocardium”, “CMRSegTools:Remote_stddev”, etc.) by searching for these keywords in the OsiriX/Horos ROI manager.

Statistical results include the number of pixels, minimum and maximum pixel values, mean value, and standard deviation, among others of each ROI (lesion, MVO and remote) per segment, slice and for the entire myocardium. This information can be exported to an Excel file or as a delimited text file (comma-separated values) for a more comprehensive examination over different studies or cohorts of interest using application software for statistical analysis (e.g. pandas [28], R scripts [29] or any statistical package).

The main computational methods are written in C++ using the Insight Segmentation and Registration ToolKit (ITK) [30] and the Visualisation ToolKit (VTK) [31], which grant extensibility and interoperability in terms of new functionalities required, that is new image processing methods.

Myocardial segmentation

The initialisation of the endocardial and epicardial contours is performed in 2 mouse clicks, and then automatically adjusted to the myocardium using the Boundary Enhanced Automated Surface (BEAS) algorithm [32, 33].

BEAS was originally developed for automatic segmentation of 3D cine-loop echocardiographic images to provide an efficient, fast and accurate solution for quantification of the main left ventricular volumetric indices used in clinical routine. In addition, the method was adapted for 3D+time CMR data sets (acquired by a cine steady state free precession sequence, SSFP) and benchmarked against the data sets available from the MICCAI 2009 Cardiac MR Left Ventricle Segmentation Challenge [34]. The benchmark demonstrated the technique to be robust, efficient and fast in terms of accuracy and computational load, which makes the BEAS algorithm suitable for a clinical practice [33].

The contours automatically determined by BEAS can be interactively corrected using OsiriX/Horos ROI edition functionalities such as the repulsor tool. Endocardial and epicardial contours can also be manually outlined. Moreover, the contours can be delineated on the basal, mid-cavity and apical slices and automatically propagated to the intermediate slices.

In order to remove pixels from the segmented myocardium close to the endocardial and epicardial contours, and avoid contamination from partial volume effect between myocardial tissue and blood (in the cavity) or air (at the myocardium to lung interface), an inner (epicardial) and outer (endocardial) offset in millimetres can be optionally set as a parameter of the segmentation method. These parameters can be configured by the user in the plug-in preferences.

Lesion segmentation

Methods for measuring infarct size can be divided into visual assessment, manual planimetry, and voxel-based approaches. Visual assessment scores hyperenhancement on a 5-point grading scale on the AHA 17-segment model [10]. Manual planimetry involves a manual definition of the hyperenhanced regions of interest (ROI) across contiguous short-axis slices in order to calculate the lesion size [10, 35]. Both methods are inherently operator dependent, which makes them time consuming as they rely on a manual process. Consequently, they are unsuitable for clinical routine or the analysis of large cohorts. Voxel-based thresholding techniques start with a comparative measurement of hyperenhanced regions with a remote healthy region set as a reference (Signal Threshold versus Reference Mean, STRM) [36]. Threshold calculation can be based on a statistical measure such as the Full-Width at Half-Maximum (FWHM) [37, 38] or on histogram information as in the case of the Gaussian mixture model (GMM) approaches [39]. Depending on whether the methods require an initialisation parameter to calculate the threshold or not they are classified as semi-automatic or fully automatic. These methods are more time efficient and suitable for large scale processing.

The methods for the segmentation of the hyperenhanced region in CMRSegTools include:

- manual cut-off: the threshold is calculated as $T = \mu + c\sigma$ where μ is the mean of signal intensity in the remote and healthy myocardium and σ its the standard deviation, c is the parameter to set by the user (a positive integer usually between 2 and 10);
- manual histogram-based segmentation: the pixel intensity range is defined by two interactive cursors on the histogram;
- automatic cut-off: the threshold is calculated as $T = \frac{I_{max}}{2}$ where I_{max} is the maximum intensity within the myocardium in the infarct zone (method known in the literature as Full-Width at Half-Maximum, FWHM);

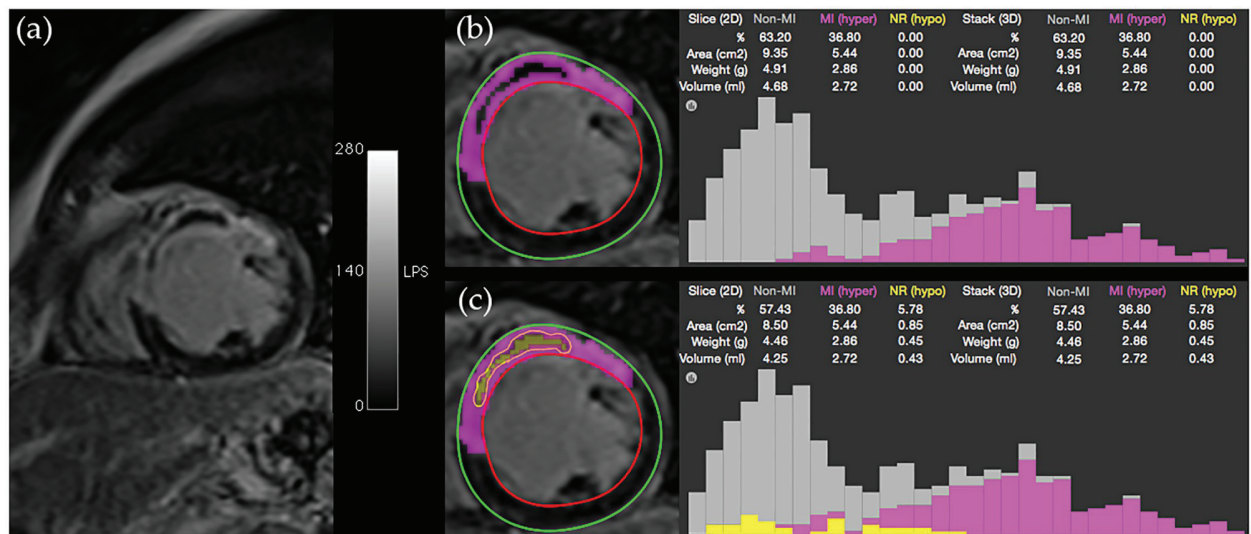


Fig 3. CMRSegTools segmentation output. (a) Image viewer before executing CMRSegTools; (b) Epicardium and endocardium contours from the myocardial segmentation, lesion segmentation (pixels in magenta colour), histogram and quantification statistics without MVO region; (c) Segmented regions, histogram and quantification statistics after defining the MVO region (contour and pixels in yellow colour).

<https://doi.org/10.1371/journal.pone.0274491.g003>

- Gaussian mixture model: the threshold is defined as the intersection of a Rician-Gaussian mixture model fitted on the histogram [39];
- Hsu modified: this method is based on the feature analysis and combined thresholding (FACT) algorithm where an iterative refining process eliminates false-positives based on regional analysis [37];
- hidden Markov random field model with expectation-maximisation (HMRF-EM): this algorithm is founded on the method proposed in [40]. It labels pixels within the myocardium by calculating the set of parameters (mean and standard deviation) of the Probability Density Function (PDF) that defines each label (lesion and remote) [41].

These methods are described in detail in [S1 Appendix](#).

Manual definition of the MVO region

Only Hsu and HMRF-EM methods provide a segmentation of the MVO (or no-reflow) regions. The MVO region can be selected (or edited) manually after segmentation of the infarct by using a pixel selection tool (brush) or region growing functionality. If there is a MVO region, this new class of tissue is automatically added to the infarct size, with corresponding pixels being automatically displayed in yellow (default color on the GUI for highlighting the MVO region). Similarly, if MVO pixels are categorised as false positive and highlighted in yellow by Hsu or HMRF-EM methods, they can be manually removed. MVO size and statistics (number of pixels, minimum and maximum pixel value, mean value, standard deviation, etc.) are calculated (Fig 3).

Transmural extent, endocardial surface length and endocardial surface area

An interactive 2D/3D wiper tool (white segments in Fig 2) allows the user to manually identify the lateral edges of myocardial infarct in order to determine the Endocardial Surface Length

(ESL) of the infarct (in percent of the endocardial contour perimeter) [42]. When multiple slices are evaluated (wipers location is propagated across slices), the Endocardial Surface Area (ESA) is automatically calculated. This functionality also intrinsically allows the user to clean up the segmentation results a posteriori and provides a transmural extent estimation.

Testing data

A series of synthetic images emulating myocardial infarct lesions were generated with arbitrary size, transmural extent, percent Signal Enhancement (%SE) and CNR. In order to test the influence of the noise level on the results, several synthetic levels of noise were computed to reproduce what was previously measured in vivo using various CMR sequences in patients [43]. To achieve a realistic model of the cavity, myocardium, infarct size and shape, and signal intensity in each compartment, the numeric images were built using multi-slice 3D data sets acquired on patients. Synthetic images were generated with a resolution similar to the one used in clinical acquisitions [41].

In vivo images from the MIMI study (ClinicalTrials.gov Identifier: NCT01360242, [44]) were used in this study to validate the plug-in functionalities on real clinical data. The MIMI (Minimalist Immediate Mechanical Intervention) study was a multicentric randomised trial aiming at comparing immediate stenting and 24–48h delayed stenting in patients treated with primary percutaneous coronary intervention (PCI); the MR protocol included T1, T2, T2*, Cine and 3D/2D Late Gadolinium Enhancement (LGE) scans. The data set is available through the Human Heart Project [45] under research collaboration agreement.

Results

The validation of the implemented methods within CMRSegTools includes a functional validation of the myocardial segmentation method; verification of the lesion segmentation output on synthetic data, and an assessment of the automated segmentation functionalities based on a reference made by a radiology expert.

Myocardial contour segmentation with BEAS

An example of the CMRSegTools LV segmentation output is presented in Fig 4. These results show the variation of the segmented contours across different image types (LGE, EGE and cine images) as a consequence of the image contrast difference and myocardial mass.

Although the BEAS algorithm was originally developed for segmentation of echocardiographic images, the method has shown very good performance on images with homogeneous myocardium wall (well-defined ring structure) such as cardiac cine MRI based on balanced SSFP contrast. As this method is based on active contours principle [46, 47], the segmentation is affected by the heterogeneity of the myocardium wall with multiple tissue classes (lesion, MVO and remote healthy pixels). These tissue classes have an impact on the energy function that penalises the deviation to the initial model (LV template presented in Fig 4a and 4d), which means that the user may have to manually correct the LV segmentation contours.

Validation on synthetic data

The numerical phantom generation from real clinical data (2D and 3D) is illustrated in Fig 5 and a performance benchmark across segmentation methods is presented in Fig 6. Fig 6 shows the relative and absolute error in the calculation of the lesion size as a function of the CNR. Absolute relative error is plotted on logarithmic scale to highlight the results of 2-SD, 3-SD and 5-SD for $CNR > 5$. Overall, the accuracy improves as the CNR increases. The

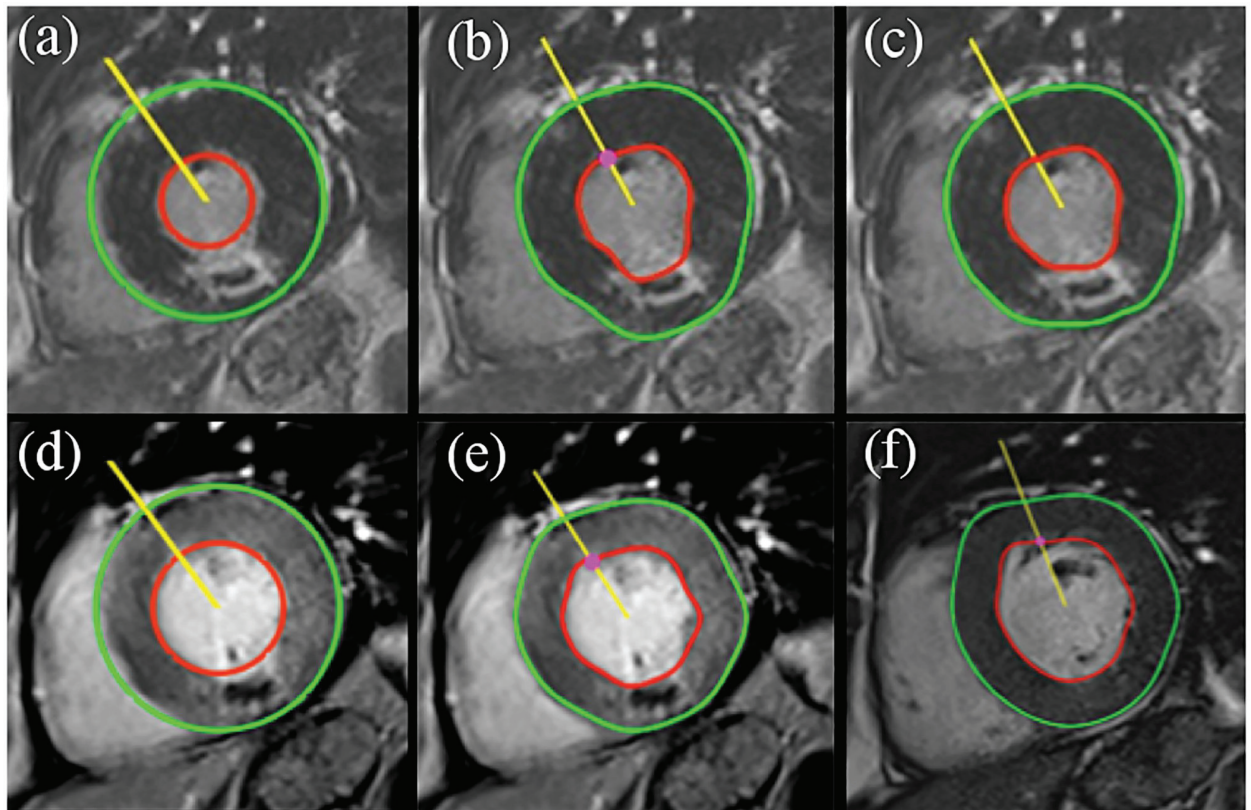


Fig 4. Performance of BEAS segmentation on images with different contrast type. (a) User initialisation on the LGE image; (b) first and (c) second iteration of the automatic segmentation based on (a). (d) User initialisation on the EGE image and (e) segmentation output. (f) Segmentation output on cine bSSFP. All images were taken at the same slice location and from the same patient at different breath-hold scans.

<https://doi.org/10.1371/journal.pone.0274491.g004>

segmentation by STRM (n-SD) methods is strongly determined by the remote region and CNR. Lower CNR ($CNR < 6$) leads to an under-estimation (less pixels categorised as MI) by 2-SD, 3-SD, 5-SD and FWHM Region methods, and to an over-estimation (more pixels categorised as MI) by FWHM Max, GMM, Hsu and HMRF-EM methods. This is due to the incorrect categorisation of the infarct edges or some noisy pixels. On a real image coil sensitivity variation, cardiac motion and partial-volume effects may generate this kind of intermediate SI pixels that may be included within the n-SD constraint or statistical model. However, at lower CNR scenarios, a lower cut-off provides a more accurate infarct segmentation with an error less than 3.8%. Lower CNR impacts the performance of the GMM method reaching about 60% of mean relative error. The best performance corresponds to STRM with 5-SD, FWHM, Hsu and HMRF-EM providing a very low margin of error starting at $CNR > 3$.

Radiology expert segmentation vs automated segmentation methods

An example of the manual segmentation made by an expert radiologist (P.C. with 20 years of experience in cardiovascular imaging) against each one of the methods within CMRSegTools on a patient with MVO is presented in Figs 7 and 8. The relative error between methods output and expert segmentation of a ROI was calculated as $Error_{ROI} = \frac{Area_{ROI}(method) - Area_{ROI}(expert)}{Area_{ROI}(expert)}$

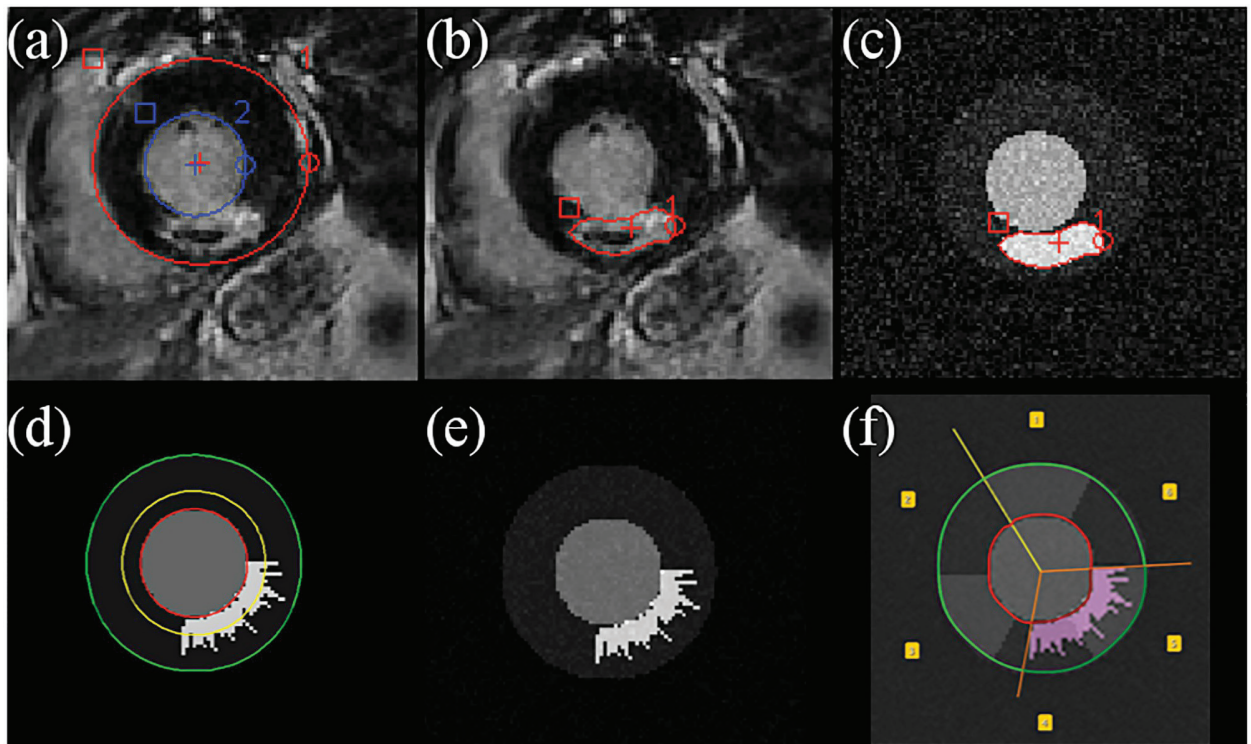


Fig 5. Example of numerical phantom generation (c), (d), (e) and (f) from a real clinical data set (a) and (b). Images were acquired with a 3D-IR-GRE sequence on a patient with a myocardial infarct. (a) Traced endocardial and epicardial contours on one slice (2D), (b) manual lesion segmentation, (c) output synthetic image (2D). The figures (d), (e) and (f) illustrate transmural extent and ESL calculation on a numerically generated infarct with known size and variable transmural extent around a user-defined mean value. (d) Red, green and yellow contours are respectively the endocardial and epicardial borders, and the mean simulated transmural extent; (e) final synthetic image. (f) CMRSegTools segmentation output (HMRF-EM); magenta pixels on the synthetic image correspond to those classified as myocardial infarct on the numerical phantom. The orange wipers delineate the ESL.

<https://doi.org/10.1371/journal.pone.0274491.g005>

Discussion

Although a considerable research has been conducted to develop and assess computational methods for the quantification of lesion size in CMR, to date and to the best of our knowledge, there has been no initiative to provide a unified reference for lesion segmentation methods within a common assessment platform. The baseline of existing publications reporting infarct lesion sizing is usually an offline analysis based on in-house (closed-source) implementations of conventional or, less often, innovative segmentation algorithms. Following this approach it is difficult to make an objective evaluation of existing methods. The assessment would only be performed when a medical device vendor releases the methods in a commercial software product. In this scenario, the benchmarking of computational methods implemented by research groups and commercial solutions is biased by the vendor constraints for the algorithms. Since manufacturers are under regulatory restrictions, the integration of the latest hardware and software on their platforms typically requires long production time, often resulting in regrettable delays in early testing of new, advanced and potentially valuable algorithms. CMRSegTools is therefore a contribution to enable reproducible research by assembling the most used methods for infarct segmentation in a suitable workflow executed in a single and widely available environment: Osirix/Horos DICOM viewers. This platform was chosen because it provides an Application Programming Interface (API) that grants access to the data management, user interaction and visualisation functionalities. It was also chosen because it has an open-source

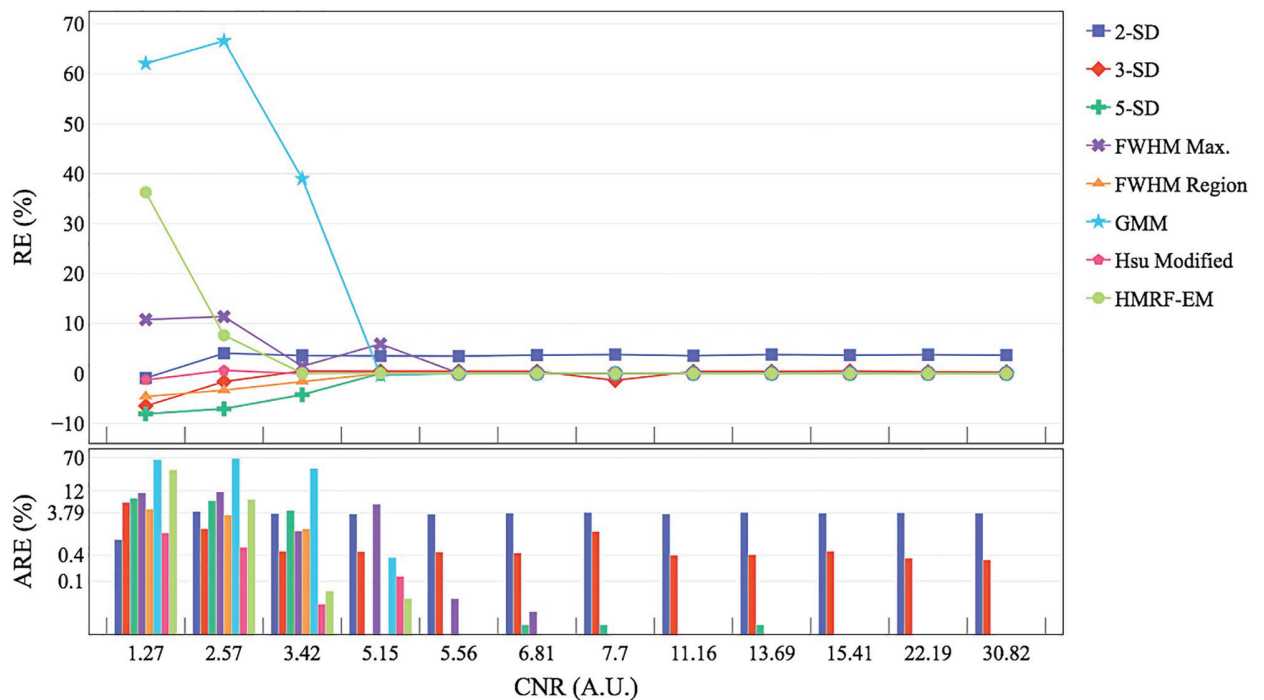


Fig 6. Performance of the lesion segmentation methods across different Contrast-to-Noise Ratio (CNR) scenarios. The curves show the relative error (RE) and bars the absolute relative error (ARE, logarithmic scale) for each segmentation method. The CNR was calculated as the ratio between the SI difference of the infarct and healthy myocardium over the standard deviation of the SI in the myocardium.

<https://doi.org/10.1371/journal.pone.0274491.g006>

licence. However, OsiriX/Horos is a macOS-only software, which limits its deployment on platforms based on a different operating system.

One of the contributions to the infarct segmentation workflow is the implementation of a semi-automatic method for the LV segmentation based on active contours [32, 33]. The BEAS algorithm utilises a LV template provided by the user in order to automatically fit the template to the epicardium and endocardium boundaries. Although the outcome of the BEAS segmentation may be affected by the different tissue classes in the myocardial wall, this functionality enhances automation capabilities for clinical routine or the analysis of large cohorts as demonstrated in [33]. A reliable segmentation of the myocardium is important as the edge of the endocardium may constitute up to 50% of the infarct perimeter; this means that a wrong determination of the endocardial infarct border is a large source of variability in final infarct size measurements. At present, there are no automated algorithms that can reliably distinguish the bright LV cavity from the bright endocardial border of the infarct. This challenge is being addressed by new segmentation methods (including non-LGE images) based on ML [5, 21, 48, 49].

To validate the correspondence between the mathematical model (S1 Appendix) and the code implementation, the correctness of the computational methods has been verified with synthetic data. This also allowed the benchmarking of infarct segmentation methods (Fig 6) on synthetic data. The main lesson emerging from the analysis is that STRM (n -SD) methods with $n < 5$ and GMM are easily influenced by CNR. At lower CNR conditions the outcomes from these methods are unreliable, making them unsuitable for real clinical conditions. When $CNR > 5$, 2-SD and 3-SD are insensible to CNR. The HMRF-EM has shown a good

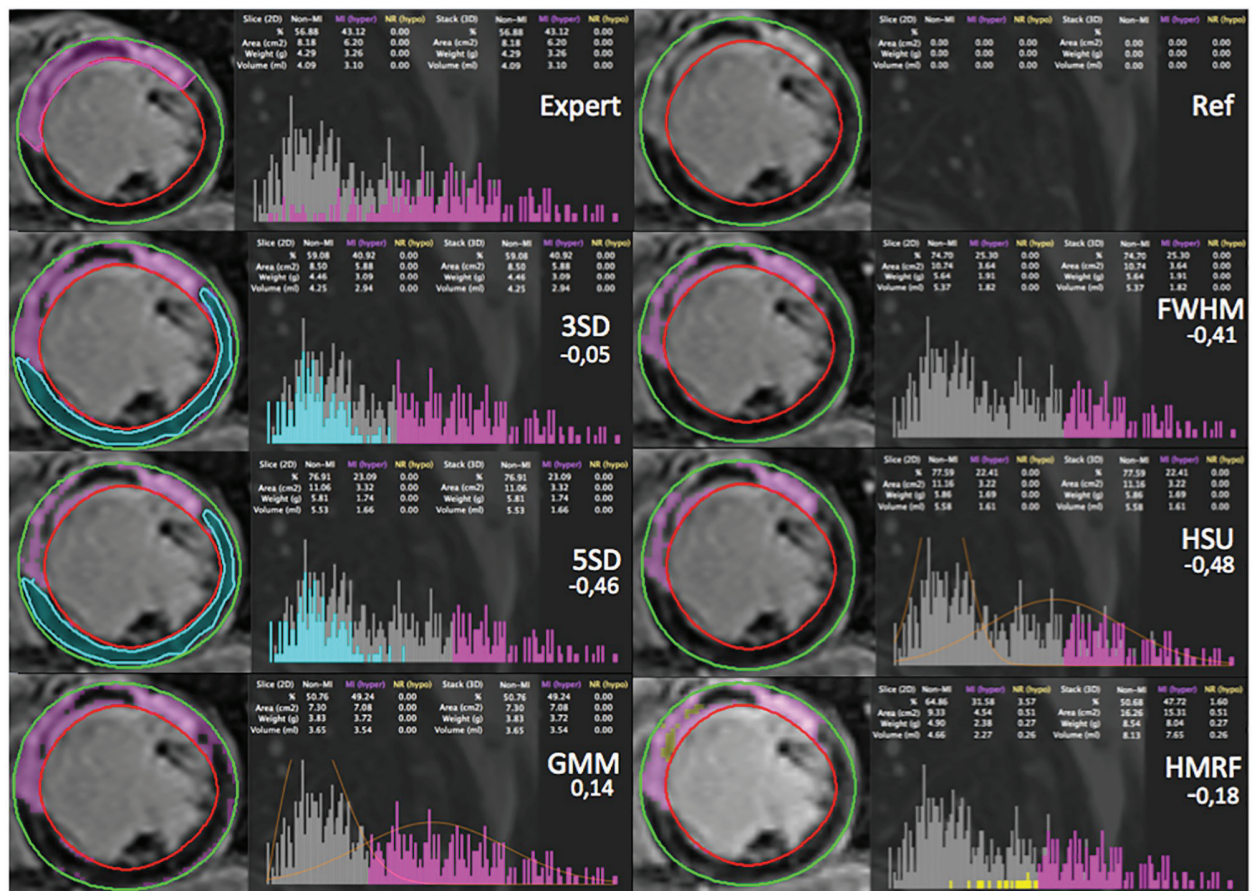


Fig 7. Comparison between the manual segmentation made by an expert (without the definition of the MVO region), and the segmentation made by each of the methods within CMRSegTools. For each segmentation, the figure shows: epicardium (green) and endocardium (red) contours from the myocardial segmentation, lesion segmentation (magenta), remote healthy myocardium (turquoise), no-reflow region by HMRP (yellow), histogram, quantification statistics and relative error.

<https://doi.org/10.1371/journal.pone.0274491.g007>

performance in most of the different scenarios ($CNR > 3$). A comparison between expert and automated segmentation methods is presented in Figs 7 and 8 as an example of the output of the current version. CMRSegTools has been tested and used successfully in several studies [22–25].

An extended assessment or benchmarking of infarct segmentation methods is beyond the scope of this paper. The goal is to provide a computer-based tool which includes well-known lesion segmentation methods (S1 Appendix) in order to empower research scientists to reproduce results and assess comparatively new methods. In this direction, CMRSegTools source code has been released under the CeCILL licence (a French free software license compatible with GPL) that grants users the right to copy, modify, and distribute new versions of the plug-in.

Machine learning approaches for SI classification would require reference data that can be applied to a learning process [50]. With CMRSegTools, it is possible to generate labeled features (infarct, MVO and remote ROIs) extracted from the data and the expected quantification based on reference segmentation methods. These specific features are the main input of supervised learning approaches. As shown in Figs 7 and 8, outcomes from ML methods can be easily

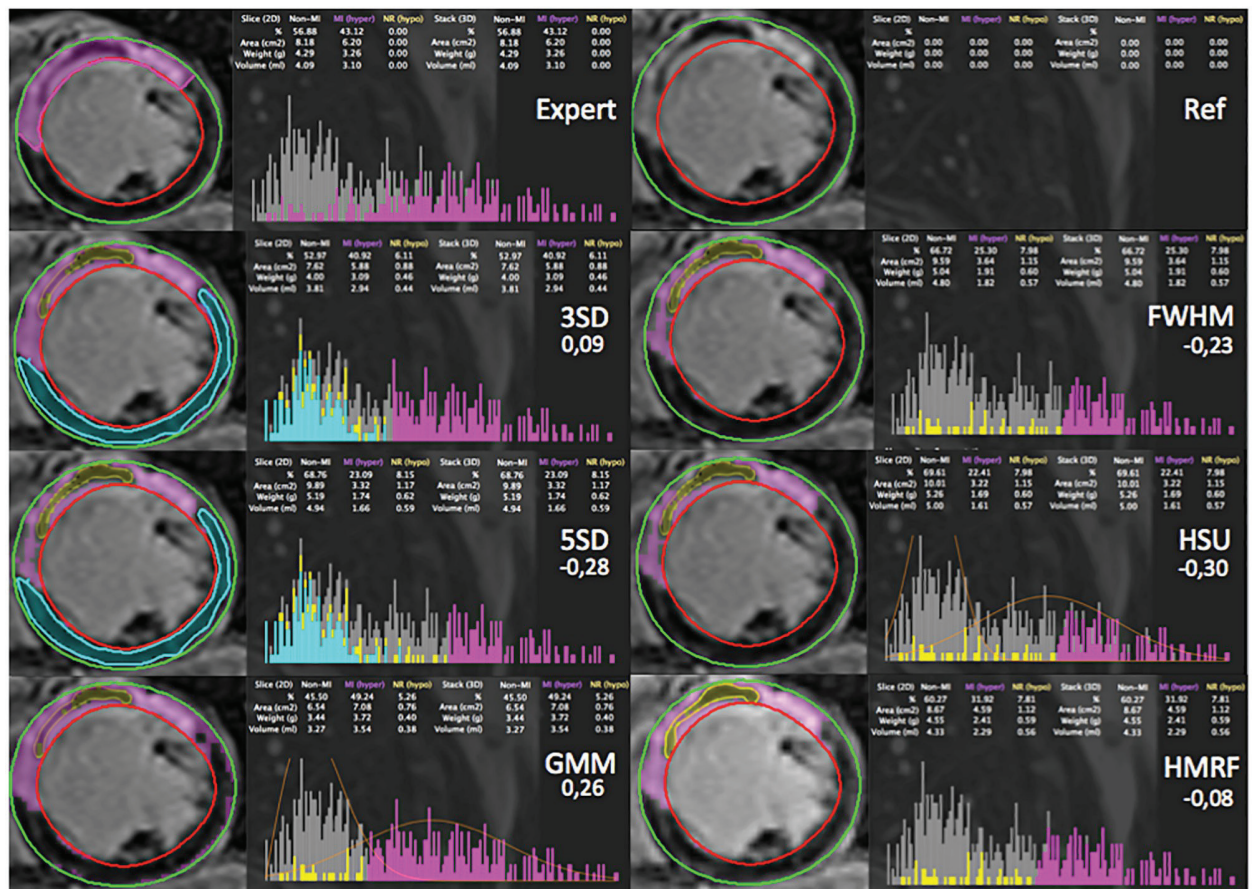


Fig 8. Comparison between the manual segmentation made by an expert (including a manual definition of the MVO region), and the segmentation made by each of the methods within CMRSegTools. For each segmentation, the figure shows: epicardium (green) and endocardium (red) contours from the myocardial segmentation, lesion segmentation (magenta), remote healthy myocardium (turquoise), no-reflow region (yellow), histogram, quantification statistics and relative error.

<https://doi.org/10.1371/journal.pone.0274491.g008>

compared to manual, semi- or full-automated state-of-the-art methods. Additionally, errors performed by ML methods may be labeled as well in order to improve the accuracy, specially in strategies involving active learning.

The analysis scenario presented in this paper (methods benchmarking and expert vs computational methods assessment) can be replicated by research scientists working in CMR on their own data or by downloading the testing data used for this work from the Human Heart Project [45]. This is particularly interesting as it allows reproducible research in this field.

Conclusions

CMRSegTools is an application software for the comparative assessment of infarct segmentation methods applied to CMR images via a single and integrated platform (widely available Osirix and Horos DICOM viewers). This helps to improve the reproducibility of post-processing methods in clinical studies. This application software works on native DICOM images; the OsiriX/Horos functionalities enable direct connection to PACS making the plug-in independent of scanner vendor, imaging sequence and protocol. Interoperability functionalities allow

importing data from external software such as ROI created in other application software (e.g. cvi42). New segmentation methods can be easily integrated into the plug-in by developing components based on well-known image processing and visualisation libraries such as ITK and VTK in C++ programming language. By using CMRSegTools, it is possible to create training and testing data sets that can be used in Machine Learning approaches. In addition, statistical measurements can be exported for further examination in specialised data analysis tools.

Supporting information

S1 Appendix. Lesion segmentation methods in CMRSegTools.
(PDF)

Acknowledgments

The authors would like to thank Alessandro Volz, M.Sc. (Medical imaging software developer. Bellinzona, Switzerland.) for his valuable contributions to this project.

Author Contributions

Conceptualization: Magalie Viallon, Pierre Croisille.

Data curation: Magalie Viallon, Loïc Belle, Pierre Croisille.

Formal analysis: Magalie Viallon.

Funding acquisition: Loïc Belle, Pierre Croisille.

Methodology: Magalie Viallon, Patrick Clarysse, Pierre Croisille.

Software: William A. Romero R., Joël Spaltenstein, Olivier Bernard.

Validation: William A. Romero R., Magalie Viallon, Joël Spaltenstein, Lorena Petrusca, Olivier Bernard, Loïc Belle, Patrick Clarysse, Pierre Croisille.

Writing – original draft: William A. Romero R., Magalie Viallon.

Writing – review & editing: William A. Romero R., Magalie Viallon, Joël Spaltenstein, Lorena Petrusca, Olivier Bernard, Loïc Belle, Patrick Clarysse, Pierre Croisille.

References

1. Kim HW, Farzaneh-Far A, Kim RJ. Cardiovascular magnetic resonance in patients with myocardial infarction: current and emerging applications. *Journal of the American College of Cardiology*. 2009; 55(1):1–16. <https://doi.org/10.1016/j.jacc.2009.06.059> PMID: 20117357
2. Kim RJ, Wu E, Rafael A, Chen EL, Parker MA, Simonetti O, et al. The use of contrast-enhanced magnetic resonance imaging to identify reversible myocardial dysfunction. *New England Journal of Medicine*. 2000; 343(20):1445–1453. <https://doi.org/10.1056/NEJM200011163432003> PMID: 11078769
3. Kim RJ, Shah DJ, Judd RM. How we perform delayed enhancement imaging: HOW I DO. . . . *Journal of cardiovascular magnetic resonance*. 2003; 5(3):505–514. <https://doi.org/10.1081/JCMR-120022267> PMID: 12882082
4. Karim R, Bhagirath P, Claus P, Housden RJ, Chen Z, Karimghaloo Z, et al. Evaluation of state-of-the-art segmentation algorithms for left ventricle infarct from late Gadolinium enhancement MR images. *Medical image analysis*. 2016; 30:95–107. <https://doi.org/10.1016/j.media.2016.01.004> PMID: 26891066
5. Wu Y, Tang Z, Li B, Firmin D, Yang G. Recent Advances in Fibrosis and Scar Segmentation From Cardiac MRI: A State-of-the-Art Review and Future Perspectives. *Frontiers in Physiology*. 2021; 12. <https://doi.org/10.3389/fphys.2021.709230> PMID: 34413789

6. Nosek BA, Alter G, Banks GC, Borsboom D, Bowman SD, Breckler SJ, et al. Promoting an open research culture. *Science*. 2015; 348(6242):1422–1425. <https://doi.org/10.1126/science.aab2374> PMID: [26113702](https://pubmed.ncbi.nlm.nih.gov/26113702/)
7. Donoho DL. An invitation to reproducible computational research. *Biostatistics*. 2010; 11(3):385–388. <https://doi.org/10.1093/biostatistics/kxq028> PMID: [20538873](https://pubmed.ncbi.nlm.nih.gov/20538873/)
8. Nichols TE, Das S, Eickhoff SB, Evans AC, Glatard T, Hanke M, et al. Best practices in data analysis and sharing in neuroimaging using MRI. *Nature neuroscience*. 2017; 20(3):299–303. <https://doi.org/10.1038/nn.4500> PMID: [28230846](https://pubmed.ncbi.nlm.nih.gov/28230846/)
9. Eglén SJ, Marwick B, Halchenko YO, Hanke M, Sufi S, Gleeson P, et al. Toward standard practices for sharing computer code and programs in neuroscience. *Nature neuroscience*. 2017; 20(6):770–773. <https://doi.org/10.1038/nn.4550> PMID: [28542156](https://pubmed.ncbi.nlm.nih.gov/28542156/)
10. on Myocardial Segmentation AHA/AHA, for Cardiac Imaging: R, Cerqueira MD, Weissman NJ, Dilsizian V, Jacobs AK, et al. Standardized myocardial segmentation and nomenclature for tomographic imaging of the heart: a statement for healthcare professionals from the Cardiac Imaging Committee of the Council on Clinical Cardiology of the American Heart Association. *Circulation*. 2002; 105(4):539–542. <https://doi.org/10.1161/hc0402.102975>
11. Guadamuz A. Free and open source software. *LAW AND THE INTERNET*, 3rd Ed, Edwards L, Waelde C, eds, Oxford: Hart. 2009;.
12. Levine SS, Prietula MJ. Open collaboration for innovation: Principles and performance. *Organization Science*. 2014; 25(5):1414–1433. <https://doi.org/10.1287/orsc.2013.0872>
13. Fedorov A, Beichel R, Kalpathy-Cramer J, Finet J, Fillion-Robin JC, Pujol S, et al. 3D Slicer as an image computing platform for the Quantitative Imaging Network. *Magnetic resonance imaging*. 2012; 30(9):1323–1341. <https://doi.org/10.1016/j.mri.2012.05.001> PMID: [22770690](https://pubmed.ncbi.nlm.nih.gov/22770690/)
14. Schneider CA, Rasband WS, Eliceiri KW. NIH Image to ImageJ: 25 years of image analysis. *Nature methods*. 2012; 9(7):671–675. <https://doi.org/10.1038/nmeth.2089> PMID: [22930834](https://pubmed.ncbi.nlm.nih.gov/22930834/)
15. Koenig M, Spindler W, Rexilius J, Jomier J, Link F, Peitgen HO. Embedding VTK and ITK into a visual programming and rapid prototyping platform. In: *Medical Imaging 2006: Visualization, Image-Guided Procedures, and Display*. vol. 6141. International Society for Optics and Photonics; 2006. p. 61412O.
16. Medis Suite MR, Medis Medical Imaging Systems BV, Leiden, The Netherlands;. <https://medisimaging.com/medis-suite-mr>.
17. cvi42 for Cardiovascular MRI, Circle Cardiovascular Imaging Inc., Calgary, Canada;. <https://www.circlecvi.com/cvi42/cardiac-mri>.
18. Heiberg E, Sjögren J, Ugander M, Carlsson M, Engblom H, Arheden H. Design and validation of Segment-freely available software for cardiovascular image analysis. *BMC medical imaging*. 2010; 10(1):1–13. <https://doi.org/10.1186/1471-2342-10-1> PMID: [20064248](https://pubmed.ncbi.nlm.nih.gov/20064248/)
19. CAAS MR Solutions, Pie Medical Imaging, Maastricht, The Netherlands;. <https://www.piemedicalimaging.com/product/mr-solutions>.
20. Ranschaert ER, Morozov S, Algra PR. Artificial intelligence in medical imaging: opportunities, applications and risks. Springer; 2019.
21. Chen C, Qin C, Qiu H, Tarroni G, Duan J, Bai W, et al. Deep learning for cardiac image segmentation: a review. *Frontiers in Cardiovascular Medicine*. 2020; 7:25. <https://doi.org/10.3389/fcvm.2020.00025> PMID: [32195270](https://pubmed.ncbi.nlm.nih.gov/32195270/)
22. Bernelin H, Mewton N, Si-Mohamed S, Croisille P, Rioufol G, Bonnefoy-Cudraz E, et al. Neprilysin levels at the acute phase of ST-elevation myocardial infarction. *Clinical Cardiology*. 2019; 42(1):32–38. <https://doi.org/10.1002/clc.23090> PMID: [30284298](https://pubmed.ncbi.nlm.nih.gov/30284298/)
23. Paccalet A, Crola Da Silva C, Mechtouff L, Amaz C, Varillon Y, De Bourguignon C, et al. Serum Soluble Tumor Necrosis Factor Receptors 1 and 2 Are Early Prognosis Markers After ST-Segment Elevation Myocardial Infarction. *Frontiers in pharmacology*. 2021; p. 2083. <https://doi.org/10.3389/fphar.2021.656928> PMID: [34539391](https://pubmed.ncbi.nlm.nih.gov/34539391/)
24. Hayek A, Paccalet A, Mechtouff L, Da Silva CC, Ivanov F, Falque H, et al. Kinetics and prognostic value of soluble VCAM-1 in ST-segment elevation myocardial infarction patients. *Immunity, inflammation and disease*. 2021; 9(2):493–501. <https://doi.org/10.1002/iid3.409> PMID: [33559404](https://pubmed.ncbi.nlm.nih.gov/33559404/)
25. Zeilinger MG, Kunze KP, Munoz C, Neji R, Schmidt M, Croisille P, et al. Non-rigid motion-corrected free-breathing 3D myocardial Dixon LGE imaging in a clinical setting. *European Radiology*. 2022; 32. <https://doi.org/10.1007/s00330-022-08560-6> PMID: [35184220](https://pubmed.ncbi.nlm.nih.gov/35184220/)
26. Rosset A, Spadola L, Ratib O. OsiriX: an open-source software for navigating in multidimensional DICOM images. *Journal of digital imaging*. 2004; 17(3):205–216. <https://doi.org/10.1007/s10278-004-1014-6> PMID: [15534753](https://pubmed.ncbi.nlm.nih.gov/15534753/)
27. Horos, free and open source code software (FOSS) program;. <http://Horosproject.org>.

28. Wes McKinney. Data Structures for Statistical Computing in Python. In: Stéfan van der Walt, Jarrod Millman, editors. Proceedings of the 9th Python in Science Conference; 2010. p. 56–61.
29. R Core Team. R: A Language and Environment for Statistical Computing; 2018. Available from: <https://www.R-project.org/>.
30. McCormick MM, Liu X, Ibanez L, Jomier J, Marion C. ITK: enabling reproducible research and open science. *Frontiers in neuroinformatics*. 2014; 8:13. <https://doi.org/10.3389/fninf.2014.00013> PMID: 24600387
31. Schroeder W, Martin KM, Lorensen WE. The visualization toolkit an object-oriented approach to 3D graphics. Prentice-Hall, Inc.; 1998.
32. Barbosa D, Pedrosa J, Heyde B, Dietenbeck T, Friboulet D, Bernard O, et al. heartBEATS: A hybrid energy approach for real-time B-spline explicit active tracking of surfaces. *Computerized Medical Imaging and Graphics*. 2017; 62:26–33. <https://doi.org/10.1016/j.compmedimag.2017.07.004> PMID: 28784271
33. Queirós S, Barbosa D, Heyde B, Morais P, Vilaça JL, Friboulet D, et al. Fast automatic myocardial segmentation in 4D cine CMR datasets. *Medical image analysis*. 2014; 18(7):1115–1131. <https://doi.org/10.1016/j.media.2014.06.001> PMID: 25042098
34. Radau P, Lu Y, Connelly K, Paul G, Dick A, Wright G. Evaluation framework for algorithms segmenting short axis cardiac MRI. The MIDAS Journal-Cardiac MR Left Ventricle Segmentation Challenge. 2009; 49.
35. Mewton N, Revel D, Bonnefoy E, Ovize M, Croisille P. Comparison of visual scoring and quantitative planimetry methods for estimation of global infarct size on delayed enhanced cardiac MRI and validation with myocardial enzymes. *European journal of radiology*. 2011; 78(1):87–92. <https://doi.org/10.1016/j.ejrad.2009.09.027> PMID: 19962260
36. Bondarenko O, Beek AM, Hofman MB, Kühl HP, Twisk JW, Van Dockum WG, et al. Standardizing the definition of hyperenhancement in the quantitative assessment of infarct size and myocardial viability using delayed contrast-enhanced CMR. *Journal of Cardiovascular Magnetic Resonance*. 2005; 7(2):481–485. <https://doi.org/10.1081/JCMR-200053623> PMID: 15881532
37. Hsu LY, Natanzon A, Kellman P, Hirsch GA, Aletras AH, Arai AE. Quantitative myocardial infarction on delayed enhancement MRI. Part I: Animal validation of an automated feature analysis and combined thresholding infarct sizing algorithm. *Journal of Magnetic Resonance Imaging: An Official Journal of the International Society for Magnetic Resonance in Medicine*. 2006; 23(3):298–308. <https://doi.org/10.1002/jmri.20496> PMID: 16450367
38. Hsu LY, Ingkanisom WP, Kellman P, Aletras AH, Arai AE. Quantitative myocardial infarction on delayed enhancement MRI. Part II: Clinical application of an automated feature analysis and combined thresholding infarct sizing algorithm. *Journal of Magnetic Resonance Imaging: An Official Journal of the International Society for Magnetic Resonance in Medicine*. 2006; 23(3):309–314. <https://doi.org/10.1002/jmri.20495> PMID: 16450368
39. Friman O, Hennemuth A, Peitgen H. A Rician-Gaussian mixture model for segmenting delayed enhancement MRI images. In: Proc. 16th Sci. Meeting Int. Soc. Magn. Reson. Med.(ISMRM'08); 2008. p. 1040.
40. Zhang Y, Brady M, Smith S. Segmentation of brain MR images through a hidden Markov random field model and the expectation-maximization algorithm. *IEEE Transactions on Medical Imaging*. 2001; 20(1):45–57. <https://doi.org/10.1109/42.906424> PMID: 11293691
41. Viallon M, Spaltenstein J, de Bourguignon C, Vandroux C, Ammor A, Romero W, et al. Automated quantification of myocardial infarction using a hidden Markov random field model and the EM algorithm. In: International Conference on Functional Imaging and Modeling of the Heart. Springer; 2015. p. 256–264.
42. Ibanez B, Aletras AH, Arai AE, Arheden H, Bax J, Berry C, et al. Cardiac MRI endpoints in myocardial infarction experimental and clinical trials: JACC scientific expert panel. *Journal of the American College of Cardiology*. 2019; 74(2):238–256. <https://doi.org/10.1016/j.jacc.2019.05.024> PMID: 31296297
43. Viallon M, Jacquier A, Rotaru C, Delattre BM, Mewton N, Vincent F, et al. Head-to-head comparison of eight late gadolinium-enhanced cardiac MR (LGE CMR) sequences at 1.5 tesla: From bench to bedside. *Journal of magnetic resonance imaging*. 2011; 34(6):1374–1387. <https://doi.org/10.1002/jmri.22783> PMID: 21972032
44. Belle L, Motreff P, Mangin L, Rangé G, Marcaggi X, Marie A, et al. Comparison of Immediate With Delayed Stenting Using the Minimalist Immediate Mechanical Intervention Approach in Acute ST-Segment–Elevation Myocardial Infarction: The MIMI Study. *Circulation: Cardiovascular Interventions*. 2016; 9(3):e003388. <https://doi.org/10.1161/CIRCINTERVENTIONS.115.003388> PMID: 26957418
45. The Human Heart Project; <http://humanheart-project.creatis.insa-lyon.fr/>.


46. Kass M, Witkin A, Terzopoulos D. Snakes: Active contour models. *International journal of computer vision*. 1988; 1(4):321–331. <https://doi.org/10.1007/BF00133570>
47. Caselles V, Catté F, Coll T, Dibos F. A geometric model for active contours in image processing. *Numerische mathematik*. 1993; 66(1):1–31. <https://doi.org/10.1007/BF01385685>
48. Xu C, Xu L, Gao Z, Zhao S, Zhang H, Zhang Y, et al. Direct delineation of myocardial infarction without contrast agents using a joint motion feature learning architecture. *Medical image analysis*. 2018; 50: 82–94. <https://doi.org/10.1016/j.media.2018.09.001> PMID: 30227385
49. Guo S, Xu L, Feng C, Xiong H, Gao Z, Zhang H. Multi-level semantic adaptation for few-shot segmentation on cardiac image sequences. *Medical Image Analysis*. 2021; 73:102170. <https://doi.org/10.1016/j.media.2021.102170> PMID: 34380105
50. Maes F, Robben D, Vandermeulen D, Suetens P. The role of medical image computing and machine learning in healthcare. In: *Artificial Intelligence in Medical Imaging*. Springer; 2019. p. 9–23.

Appendix B

Teh, I., Romero R, W. A., et al., “*Validation of cardiac diffusion tensor imaging sequences: A multicentre test–retest phantom study*”, *NMR in Biomedicine* 35.6 (2022): e4685.
<https://doi.org/10.1002/nbm.4685>

RESEARCH ARTICLE

Validation of cardiac diffusion tensor imaging sequences: A multicentre test–retest phantom study

Irvin Teh¹  | William A. Romero R.²  | Jordan Boyle³ | Jaume Coll-Font⁴  |
 Erica Dall'Armellina¹  | Daniel B. Ennis^{5,6}  | Pedro F. Ferreira^{7,8}  |
 Prateek Kalra⁹ | Arunark Kolipaka⁹ | Sebastian Kozerke¹⁰  | David Lohr¹¹  |
 François-Pierre Mongeon¹² | Kévin Moulin⁶  | Christopher Nguyen⁴  |
 Sonia Nielles-Vallespin^{7,8} | Brian Raterman⁹ | Laura M. Schreiber¹¹  |
 Andrew D. Scott^{7,8}  | David E. Sosnovik⁴  | Christian T. Stoeck¹⁰  |
 Cyril Tous¹³  | Elizabeth M. Tunnicliffe^{14,15}  | Andreas M. Weng¹⁶  |
 Pierre Croisille²  | Magalie Viallon²  | Jürgen E. Schneider¹ 

¹Leeds Institute of Cardiovascular and Metabolic Medicine, University of Leeds, Leeds, UK

²Univ Lyon, INSA-Lyon, Université Claude Bernard Lyon 1, UJM-Saint Etienne, CNRS, Inserm, CREATIS UMR 5220, U1294, F-42023, Saint Etienne, France

³School of Mechanical Engineering, University of Leeds, Leeds, UK

⁴Cardiovascular Research Center and A. A. Martinos Center for Biomedical Imaging, Massachusetts General Hospital and Harvard Medical School, Boston, Massachusetts, USA

⁵Division of Radiology, VA Palo Alto Health Care System, Palo Alto, California, USA

⁶Department of Radiology, Stanford University, Stanford, California, USA

⁷Cardiovascular Magnetic Resonance Unit, The Royal Brompton and Harefield NHS Foundation Trust, London, UK

⁸National Heart and Lung Institute, Imperial College London, London, UK

⁹Department of Radiology, The Ohio State University Wexner Medical Center, Columbus, Ohio, USA

¹⁰Institute for Biomedical Engineering, University and ETH Zurich, Zurich, Switzerland

¹¹Department of Cardiovascular Imaging, Comprehensive Heart Failure Center, Würzburg, Germany

¹²Division of Non-invasive Cardiology, Montreal Heart Institute, Montreal, Canada

¹³Department of Radiology, Radiation-Oncology and Nuclear Medicine and Institute of Biomedical Engineering, Université de Montréal, Montréal, Canada

¹⁴Radcliffe Department of Medicine, University of Oxford, Oxford, UK

¹⁵Oxford NIHR Biomedical Research Centre, Oxford, UK

¹⁶Department of Diagnostic and Interventional Radiology, University Hospital Würzburg, Würzburg, Germany

Correspondence

Irvin Teh, University of Leeds, LICAMM, Worsley Building, Room 8.49j, Clarendon Way, Leeds, LS2 9NL, UK.
 Email: i.teh@leeds.ac.uk

Cardiac diffusion tensor imaging (DTI) is an emerging technique for the in vivo characterisation of myocardial microstructure, and there is a growing need for its validation and standardisation. We sought to establish the accuracy, precision, repeatability and reproducibility of state-of-the-art pulse sequences for cardiac DTI among

Abbreviations used: ADC, apparent diffusion coefficient; CODE, convex optimised diffusion encoding; CV, coefficient of variation; DTI, diffusion tensor imaging; DW, diffusion-weighted; DWI, diffusion-weighted imaging; EPI, echo planar imaging; FA, fractional anisotropy; HCM, hypertrophic cardiomyopathy; M2B1resist, M2SE with improved robustness to B₁ inhomogeneities; M2SE, second-order motion-compensated spin echo; MD, mean diffusivity; MODE, motion-compensated optimised diffusion encoding; PGSE, pulsed gradient spin echo; PVP, polyvinylpyrrolidone; RMSD, root mean squared difference; ROI, region of interest; SD, standard deviation; SE, spin echo; SNR, signal-to-noise ratio; STEAM, stimulated echo acquisition mode.

This is an open access article under the terms of the [Creative Commons Attribution](https://creativecommons.org/licenses/by/4.0/) License, which permits use, distribution and reproduction in any medium, provided the original work is properly cited.

© 2021 The Authors. *NMR in Biomedicine* published by John Wiley & Sons Ltd.

Funding information

British Heart Foundation, Grant/Award Numbers: PG/19/1/34076, SI/14/1/30718, FS/13/71/30378, PG/17/28/32943, RG/19/1/34160; German Ministry of Education and Research (BMBF), Grant/Award Number: 01EO1504; Swiss National Science Foundation, Grant/Award Number: PZ00P2_174144; National Institutes of Health (NIH), Grant/Award Numbers: R21-EB024701, R01-HL151704, R01-HL135242, R01-HL124096, R01-HL131823, R01-H131975, R01-HL141563; Oxford NIHR Biomedical Research Centre

10 centres internationally. Phantoms comprising 0%–20% polyvinylpyrrolidone (PVP) were scanned with DTI using a product pulsed gradient spin echo (PGSE; $N = 10$ sites) sequence, and a custom motion-compensated spin echo (SE; $N = 5$) or stimulated echo acquisition mode (STEAM; $N = 5$) sequence suitable for cardiac DTI in vivo. A second identical scan was performed 1–9 days later, and the data were analysed centrally. The average mean diffusivities (MDs) in 0% PVP were (1.124, 1.130, 1.113) $\times 10^{-3}$ mm^2/s for PGSE, SE and STEAM, respectively, and accurate to within 1.5% of reference data from the literature. The coefficients of variation in MDs across sites were 2.6%, 3.1% and 2.1% for PGSE, SE and STEAM, respectively, and were similar to previous studies using only PGSE. Reproducibility in MD was excellent, with mean differences in PGSE, SE and STEAM of (0.3 \pm 2.3, 0.24 \pm 0.95, 0.52 \pm 0.58) $\times 10^{-5}$ mm^2/s (mean \pm 1.96 SD). We show that custom sequences for cardiac DTI provide accurate, precise, repeatable and reproducible measurements. Further work in anisotropic and/or deforming phantoms is warranted.

KEYWORDS

cardiac DTI, isotropic phantom, multicentre, polyvinylpyrrolidone, pulse sequence validation, reproducibility

1 | INTRODUCTION

Diffusion tensor imaging (DTI) is an emerging noninvasive and contrast agent-free method for the characterisation of cardiac microstructure. It provides measurements, such as mean diffusivity (MD) and fractional anisotropy (FA), that are sensitive to the diffusion of water molecules, and therefore local tissue structure. Increased MD, for example, corresponded well to late gadolinium-enhanced segments in myocardial infarction,^{1,2} while decreased FA can reflect cardiomyocyte disarray and increased extracellular volume in hypertrophic cardiomyopathy (HCM).³ Changes in MD and FA have also been associated with a range of conditions including myocardial infarction,^{4,5} hypertrophy,⁶ athlete's heart,⁷ fibrosis,⁸ amyloidosis⁹ and dilated cardiomyopathy.^{10,11}

Despite recent advances, several major challenges need to be addressed to facilitate integration of DTI in clinical routine. The first is the uncertainty in choice of pulse sequence. As a result of cardiac motion, methods for motion compensation have had to be developed. These can be classed into two broad approaches, both employing cardiac triggering for synchronising to the cardiac cycle, and a single-shot echo planar imaging (EPI) readout for reduced motion sensitivity. The first method is based on stimulated echo acquisition mode (STEAM)¹² with monopolar¹³ diffusion gradient waveforms. The second method is based on spin echo (SE) with motion-compensated diffusion gradient waveforms.¹⁴ The most widely used SE implementation involves up to second-order motion compensation, rendering the sequence insensitive to constant velocity and acceleration. Second-order motion-compensated spin echo (M2SE) can be achieved with a range of methods, including asymmetric bipolar waveforms,¹⁵ symmetric tripolar waveforms with improved robustness to B_1 inhomogeneities (M2B1resist)¹⁶ and numerically optimised waveforms convex optimised diffusion encoding (CODE)¹⁷ and motion-compensated optimised diffusion encoding (MODE)¹⁸ with reduced echo times. Two studies compared the performance of STEAM and M2SE. One reported more than twofold higher signal-to-noise ratio (SNR) efficiency in M2SE compared with STEAM,¹⁹ while the other, performed on a system with standard clinical gradients, observed that STEAM was more robust over a range of cardiac phases.²⁰

The second challenge is the known sensitivity of diffusion MRI, not just to tissue properties, but also to acquisition parameters. Fitting of a tensor to diffusion-weighted (DW) data ignores non-Gaussian diffusion effects²¹ stemming from the multiple compartments and barriers present within the complex cell microenvironment, leading to measures of apparent diffusivity that are sensitive to parameters such as pulse sequences,^{19,20} diffusion times²² and b-value.²³ Furthermore, DTI relies on low SNR DW images, leading to errors in measured parameters,^{24,25} and sensitivity to image resolution and SNR.²⁶ The low SNR necessitates larger voxel sizes that enhance partial volume and residual motion artefacts,²⁷ while the rapid switching of diffusion gradient waveforms may enhance eddy current effects.²⁷ Additionally, early STEAM studies erroneously ascribed b-values of 0 s/mm^2 to the non-DW data during the reconstruction, leading to bias in MD, even within one sequence type.^{28,29} Consequently, studies in the myocardium of healthy volunteers have reported a wide range of MD (0.87 $\times 10^{-3}$ to 1.72 $\times 10^{-3}$ mm^2/s) and FA (0.29 to 0.61).^{19,20,30,31} This hampers comparison of data between sites and studies, and a standardised protocol is needed for comparison of absolute values.

The third challenge is the need to establish reproducibility of DTI parameters within and across sites. One intrasite study in healthy volunteers using a STEAM-EPI sequence showed no significant differences in myocardial MD and FA acquired at two time points.²⁸ Another single-site study in patients with HCM³² reported coefficients of variation (CVs) of myocardial MD and FA across two time points of 19% and 7.2%, respectively. Intersite reproducibility is typically measured by scanning standardised subjects and substrates, such as travelling volunteers and phantoms, respectively, at multiple sites. Such studies have been performed most widely in the context of brain imaging, and have reported good reproducibility in MD and FA across up to 11 sites, with intersite CV_{MD} in brain ranging from 1.6% to 5.4% and CV_{FA} ranging from 2.0% to 4.5%.^{33–35} One cardiac DTI study involving healthy volunteers at two sites reported myocardial CV_{MD} and CV_{FA} of up to 7% and 6%, respectively.²⁹

While volunteers are key to assessing the real-world performance of DTI, phantoms are more cost-effective for larger scale studies, offer longer term stability and allow for customisation of features for isolation of sources of variation in the data. Isotropic phantoms, for example, ice water³³ or aqueous solutions of polyvinylpyrrolidone (PVP)^{34,36,37} or nickel chloride and sodium chloride,³⁵ provide a homogeneous substrate with known MD, while biomimetic phantoms simulating cardiac microstructure³⁸ additionally permit reproducible measurements of FA. While such anisotropic phantoms could facilitate more realistic evaluation of anisotropy, these remain generally unavailable. Moreover, isotropic phantoms have a unique advantage, in that there exist gold standard reference measurements of diffusivity in the case of water, and corroborating MD values in the literature in the case of PVP.

In this multicentre study, we sought to establish the accuracy, precision, repeatability and reproducibility of state-of-the-art pulse sequences for cardiac DTI among 10 centres internationally. We employed a standardized, custom-built, temperature-controlled PVP phantom to permit baseline evaluation of MD and FA, as well as intrasite and intersite reproducibility in a homogeneous, isotropic substrate with known diffusivity, and acquired data using a product noncardiac DTI pulse sequence to serve as a reference.

2 | MATERIALS AND METHODS

Ten sites participated in the study (one Philips 1.5-T scanner, nine Siemens 3-T scanners). Phantoms were produced at a single site and shipped to participating sites. Data were acquired using a standardised protocol prescribing both product and custom DTI sequences. A second scan was performed from 1–9 days following the first scan. Data were uploaded to a central server, and analysed by a single site using a standardised processing pipeline.

2.1 | Phantom preparation

The phantom comprised 7 × 50-ml Falcon tubes filled with PVP (Sigma Aldrich, Dorset, UK) in distilled water in concentrations ranging from 0% to 20%. The tubes were positioned vertically in an outer container using a laser-cut plastic holder. Prior to imaging, the tubes were immersed in an ice-water bath and given sufficient time to equilibrate to 0°C (Figure 1). The phantoms were placed at the isocentre in identical orientation.

2.2 | Data acquisition

To verify consistent temperature, a fast diffusion-weighted imaging (DWI) scout scan was performed using the product sequence (i.e. pulsed gradient spin echo [PGSE] with single-shot EPI readout). The mean apparent diffusion coefficient (ADC) was measured in a region of interest (ROI) in

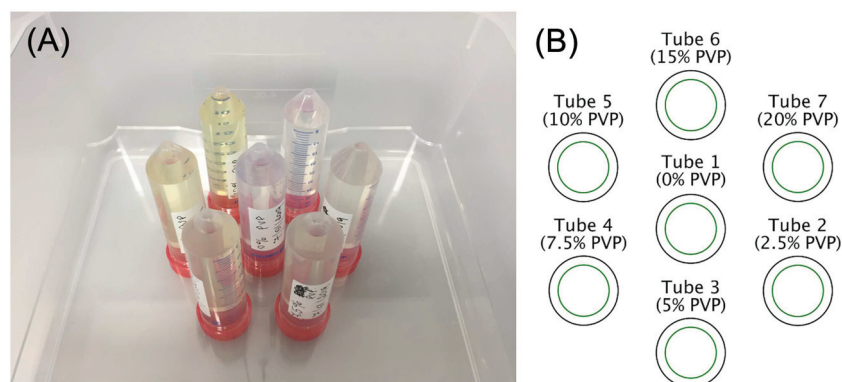


FIGURE 1 Phantom design. (A) Photograph of phantom prior to filling with ice-water bath. (B) Key for identifying tubes with different concentrations of polyvinylpyrrolidone (PVP)

the central tube. The scout scan was repeated at 10-min intervals, until the mean ADCs across two consecutive scans were within 3% agreement. Sites performed experiments using the product PGSE sequence¹³ and a custom DTI sequence of their choice optimised for cardiac-specific applications. The scan parameters for the product sequence were TR/TE = 3000/85 ms, coronal view, field of view (FOV) = 300 × 230 mm, in-plane resolution = 2.5 mm, slice thickness = 8 mm, gap = 8 mm, slices = 3, bandwidth ~ 3000 Hz, parallel imaging acceleration = 2x, ECG-triggered with simulated heart rate = 60 beats per min. Specified parameters such as TE and resolution were fairly conservative, to ensure that all sites could meet the sequence specifications in the presence of different hardware capabilities. To ensure consistency in diffusion schemes across different scanners, the following diffusion schemes were specified: (i) DWI scout scan: non-DW images = 1, diffusion vectors (3) = [1 0 0; 0 1 0; 0 0 1], $b = 450 \text{ s/mm}^2$, repetitions = 3, acquisition time ~36 s; (ii) DTI scan: non-DW images = 1, diffusion vectors³⁹ (6) = [0.5257 0.8507 0; 0.5257-0.8507 0; 0 0.5257 0.8507; 0.5257-0.8507 0 0.5257; -0.8507 0 0.5257], $b = 100, 300, 450 \text{ s/mm}^2$, repetitions = 30, acquisition time ~29 min. Each site performed imaging with one custom sequence of their preference, including spin echo-based sequences with up to second-order motion compensation (M2SE, CODE, MODE, M2B1resist) and STEAM (Figure 2). The relevant acquisition parameters can be found in Table 1 and the supporting information.

2.3 | Data analysis

Image reconstruction was performed on the scanners using standard vendor reconstruction software. Data storage and management were performed using the Human Heart Project, an online platform for heart imaging research.^{40,41} Data were analysed centrally using open source Matlab

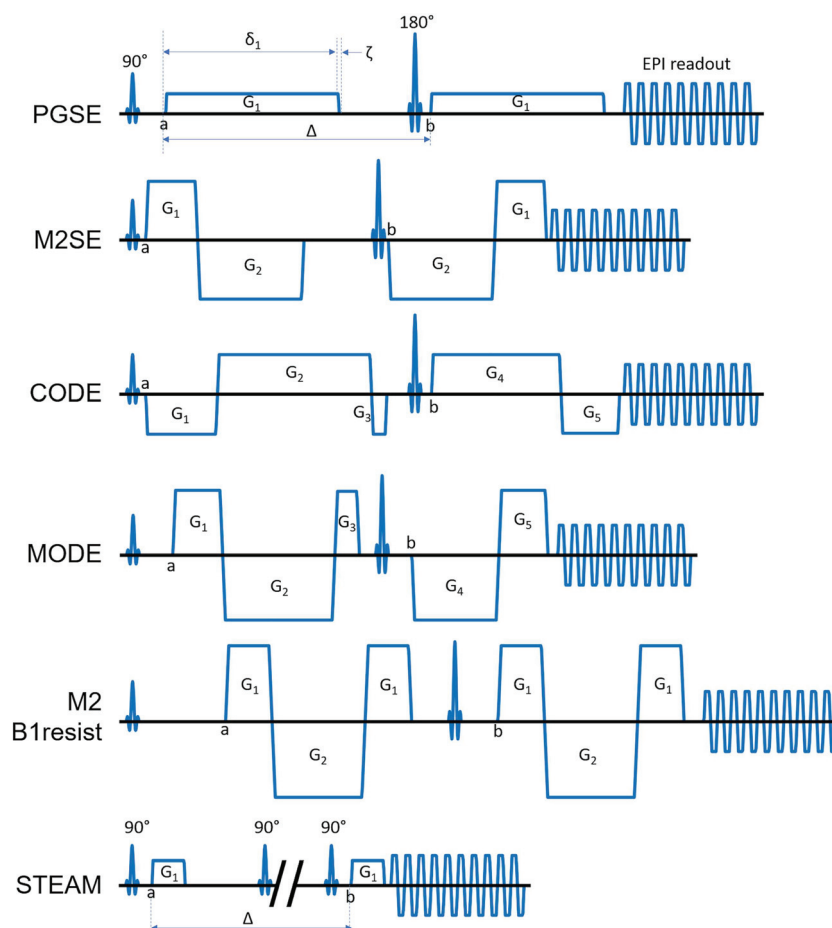


FIGURE 2 Schematic pulse sequence diagrams describing the diffusion waveforms used. These include the pulsed gradient spin echo (PGSE) product sequence and custom sequences as follows: motion-compensated spin echo (M2SE), convex optimised diffusion encoding (CODE), motion-compensated optimised diffusion encoding (MODE), motion-compensated symmetric spin echo (M2B1resist) and stimulated echo acquisition mode (STEAM). All custom spin echo sequences were motion-compensated up to the second order, and all sequences used a single-shot echo planar imaging readout. For clarity, preparation pulses, navigators, crushers and spoilers are not shown. Gradient waveform parameters, including diffusion gradient duration (δ_n) for each unique gradient lobe, time ($b - a$), slew time (ζ) and diffusion time (Δ) where applicable, are given in Table 1. δ_n was measured from the start of each unique gradient lobe (G_n) to the end of its plateau. Pulse sequences are not shown to scale

TABLE 1 Relevant hardware and custom sequence parameters

Hardware		Pulse sequence (custom)													
Site	B_0 (T)	Scanner	G_{max} (mT/m)	Max slew rate (T/m/s)	Gradient coil	RF coil	Pulse sequence	TR (ms)	TE (ms)	Diffusion duration, $\delta_1 \dots \delta_n$ (ms)	Time (b - a) (ms)	Slew time, ζ (ms)	Grad Amp, $G_1 \dots G_n$ (mT/m)	b-value for non-DW (b_{low} : s/mm ²)	Crushers during DW scans
A	3	Prisma	80	200	XR	32Ch body + 18Ch spine	M2SE	3000	74	7.8/16	36	1.6	59	5	N
B	3	Prisma	80	200	XR	32Ch body + 18Ch spine	M2 B1resist	3000	97	7.0/14	41	1.0	76	2	Y
C	3	Prisma	80	200	XR	32Ch body + 18Ch spine	M2 B1resist	3000	97	7.0/14	41	1.0	76	2	Y
D	3	Prisma	80	200	XR	32Ch body + 18Ch spine	MODE	3000	75	7.3/17/3.7/13/7.2	36	1.4	65/ -65/66/ -65/65	0	Y
E	3	Skyra	45	200	XQ	32Ch body + 18Ch spine	CODE	3000	85	11/23/2.3/22/11	42	0.7	-40/40/ -40/40/ -39	5	N
F	3	Vida	60	200	XT	18Ch body + 18Ch spine	STEAM	2000	35	5.4	1000	0.9	15	42	N
G	3	Skyra	45	200	XQ	18Ch body + 32Ch spine	STEAM	2000	35	4.9	1003	1	16	76	N
H	1.5	Achieva	80/40	100/200	QD	32Ch cardiac (16/16 anterior/posterior)	STEAM	6000	37	4.0	1000	0.21	20	39	N
I	3	Prisma	80	200	XR	18Ch body + 32Ch spine	STEAM	2000	34	4.0	1000	1.5	20	20	N
J	3	Prisma Fit	80	200	XR	32Ch body + 18Ch spine	STEAM	2000	24	2.8	998	0.4	28	16	N

Note: The timings and amplitudes of diffusion gradient waveforms ($b = 450$ s/mm²) are stated with reference to the schematic pulse sequence diagrams given in Figure 2. In the case of PGSE and STEAM, time (b - a) corresponds to the diffusion time, Δ .

Abbreviations: CODE, convex optimised diffusion encoding; M2B1resist, M2SE with improved robustness to B_1 inhomogeneities; M2SE, second-order motion-compensated spin echo; MODE, motion-compensated optimised diffusion encoding; PGSE, pulsed gradient spin echo; STEAM, stimulated echo acquisition mode.

code (<https://github.com/vigente/gerardus>). The first step was semiautomatic tube segmentation, where tube centres were defined manually, and ROIs generated up to a fixed radius from the tube centres. Tensors were fit directly to the data using linear least squares, using all image repetitions without prior averaging. MD and FA were calculated as follows (Equations 1 and 2, respectively).

$$MD = \frac{\lambda_1 + \lambda_2 + \lambda_3}{3} \quad (1)$$

$$FA = \frac{1}{\sqrt{2}} \sqrt{\frac{(\lambda_1 - \lambda_2)^2 + (\lambda_1 - \lambda_3)^2 + (\lambda_2 - \lambda_3)^2}{\lambda_1^2 + \lambda_2^2 + \lambda_3^2}}, \quad (2)$$

where λ_1 , λ_2 and λ_3 are the principal eigenvalues of the diffusion tensor. To obtain the reference diffusivity of water (D_{ref}), the self-diffusion of water, as measured using an independent non-MR technique, was extrapolated to 0°C using a second-order polynomial fit.⁴² To assess the effect of b-values and rationalise an appropriate choice of b-values, average values of MD and FA across an ROI in tube 1 using data acquired with different b-value combinations are reported. Root mean squared differences (RMSDs) between scans 1 and 2 were assessed. MD and FA across ROIs in all tubes were reported using data from all repetitions, and also expressed as a time course reconstructed from subsampled single repetitions. The reference diffusivity for water was defined as $D_{ref}(\text{H}_2\text{O}) = 1.113 \times 10^{-3} \text{ mm}^2/\text{s}$ at 0°C extrapolated from Mills.⁴²

To calculate drift, the MD and FA across repetitions were first smoothed with a sliding window of five repetitions. Drift was determined by the difference between final and initial values. The stability of MD and FA measurements across repetitions were expressed in terms of the standard deviation (SD) across repetitions. As the non-DW data had variable b-values, image SNR was calculated based on the $b = 100 \text{ s}/\text{mm}^2$ images averaged across six DW directions: $\text{SNR} = \text{mean}/\text{SD}$ over repetitions.⁴³

Accuracy in MD in each tube and site was expressed as⁴⁴:

$$\text{Accuracy, } \partial_{j,k} = \frac{\overline{MD}_{j,k} - \overline{MD}_{ref,j}}{\overline{MD}_{ref,j}} \times 100\%, \quad (3)$$

where \overline{MD} is averaged across each ROI and both scans. The reference \overline{MD}_{ref} is the MD measured by PGSE averaged across each ROI, and all sites and both scans. j and k are the tube and site indexes.

Precision in MD in each tube and site was expressed in terms of⁴⁵:

$$\text{Coefficient of variation, } CV(\text{ROI})_{j,k} = \frac{[\sigma(\text{MD}_i)]_{j,k}}{[\mu(\text{MD}_i)]_{j,k}} \times 100\%, \quad (4)$$

where σ is the SD of MD and μ is the mean MD across each ROI in scan 1. i , j and k are the voxel, tube and site indexes, respectively.

Intrasite repeatability was assessed by Bland–Altman plots, with mean differences and 95% limits of agreement reported.

Intersite reproducibility was assessed in terms of:

$$\text{Coefficient of variation, } CV_{k,l,m} = \frac{\sigma(\overline{MD}_{k,l,m})}{\mu(\overline{MD}_{k,l,m})} \times 100\%, \quad (5)$$

where σ is the SD of MD and μ is the mean MD across each variable separately, \overline{MD} is averaged across each ROI and both scans. k is the site index (1, 2, ... 10), l is the sequence index (1:PGSE, 2:SE, 3:STEAM), m is the scan index (1, 2). We report the interscan, intersite (PGSE, SE, STEAM), intersequence (PGSE vs. SE, PGSE vs. STEAM) and intersite/sequence CV (SE vs. STEAM).

2.4 | Statistical analysis

Differences in MD with respect to D_{ref} were assessed by one-sample t-tests. Shapiro–Wilk tests were performed to test for normality in the accuracy of MD. Wilcoxon rank-sum tests were performed in each tube to determine the significance of differences between the medians of each sequence with respect to other sequences. The Bland–Altman results were analysed by pairwise comparisons of mean differences between PGSE, SE and STEAM, using two-sample t-tests with unequal variances. A significance level of $p = 0.05$ was used. To compare statistical distributions of the reproducibility of MD and FA, bootstrapped histograms were calculated by sampling the differences in MD and FA between scans 1000 times with replacement. Medians and 95% confidence intervals are reported. Histograms with nonoverlapping 95% CIs were deemed to be significantly different from one another.

3 | RESULTS

3.1 | Data quality

All sites acquired DTI data at two time points. The custom sequence acquisitions were split evenly into two groups, SE ($N = 5$) and STEAM ($N = 5$). While the product sequence acquisitions were standardised apart from small scanner variations in diffusion gradient duration (25.6 ± 2.9 ms) and diffusion time (39.9 ± 3.5 ms; mean \pm SD across sites), there was greater variation across the custom sequence acquisitions. The main difference was that of all those sites that acquired STEAM data, only one site (site H) was able to acquire three slices of data as stipulated in the protocol, by slice interleaving and using $TR = 6000$ ms. To maintain consistent scan time, 15 repetitions were used in the analysis. The other four sites were unable to acquire multislice data in an interleaved fashion because of implementation limitations, and therefore only acquired single-slice data. As $TR = 2000$ ms was used, 45 repetitions were acquired to match scan times (sites F, G and I), although one site acquired 30 repetitions (site J). In the custom SE data, 30 repetitions were acquired with $TR = 3000$ ms, matching the product sequence. There were, however, instances in the custom SE data where not all 30 repetitions were available for all DW directions: 27 (site A, scan 1), 29 (site A, scan 2) and 28 (site E, scan 2) repetitions. Where a given repetition did not include all required DW directions, that repetition was excluded from analysis. In one site (site H), the data were exported at a reconstructed in-plane resolution of 0.94×0.94 mm, and had to be resampled to the nominal 2.5×2.5 mm resolution. Variations in parameters such as TR, TE and diffusion gradient timings are given in Table 1.

Figure 3 shows representative MD and FA maps in a single slice acquired at scan 1, using both product and custom sequences. Qualitatively, the maps were of good quality within the tubes. By contrast, the data in the surrounding ice-water bath were highly variable, and some voxels were masked out by the scanner reconstruction (site F). Gibb's ringing (all sites), geometric distortions (site G) and SENSE unfolding artefacts (site H) were observed.

3.2 | Mean diffusivity

The dependence of MD on b-values in the DTI reconstruction is illustrated in Figure 4. The results show that MD calculated from the product sequence data was relatively stable at $(1.120 \pm 0.022) \times 10^{-3}$ mm²/s across all b-value combinations. By contrast, greater sensitivity to b-value combinations was observed in MODE and STEAM custom sequences with MD = $(1.61 \pm 0.73, 1.06 \pm 0.13) \times 10^{-3}$ mm²/s across b-value combinations, respectively. The RMSDs of MD between scans 1 and 2 in the custom sequence data were $(0.214, 0.078, 0.048, 0.010, 0.005, 0.010, 0.012) \times 10^{-3}$ mm²/s across the b-value combinations $b_{low}, 100$; $b_{low}, 300$; $b_{low}, 450$; 100, 300; 100, 450; 300, 450; and $b_{low}, 100, 300, 450$, respectively. The lowest RMSD for MD was found using the combination of $b = 100$ and 450 s/mm², and this was therefore used for subsequent analysis. As phantom was isotropic, we focus on MD; corresponding FA measurements can be found in the supporting information.

Figure 5 depicts the MD averaged over ROIs within each tube. In tube 1 (0% PVP), the average MDs across all sites and scans 1 and 2 were $(1.124, 1.130, 1.113) \times 10^{-3}$ mm²/s for PGSE, SE and STEAM, respectively. Relative to the reference diffusivity of H₂O at 0°C of

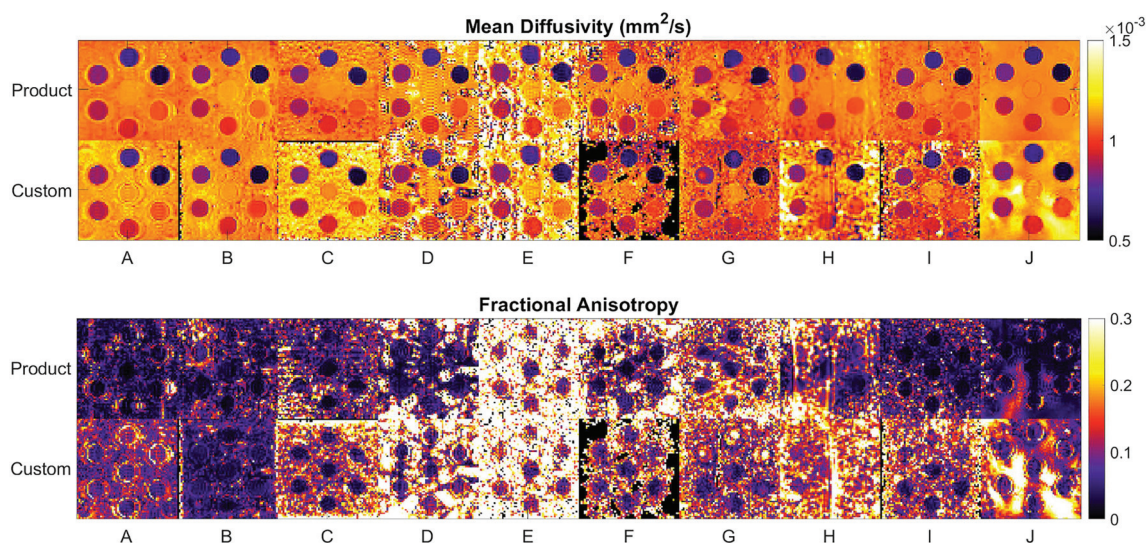


FIGURE 3 Mosaic of mean diffusivity (MD; top) and fractional anisotropy (FA; bottom) maps. Single-slice data are shown and were acquired using product (top) and custom sequences (bottom) at scan 1

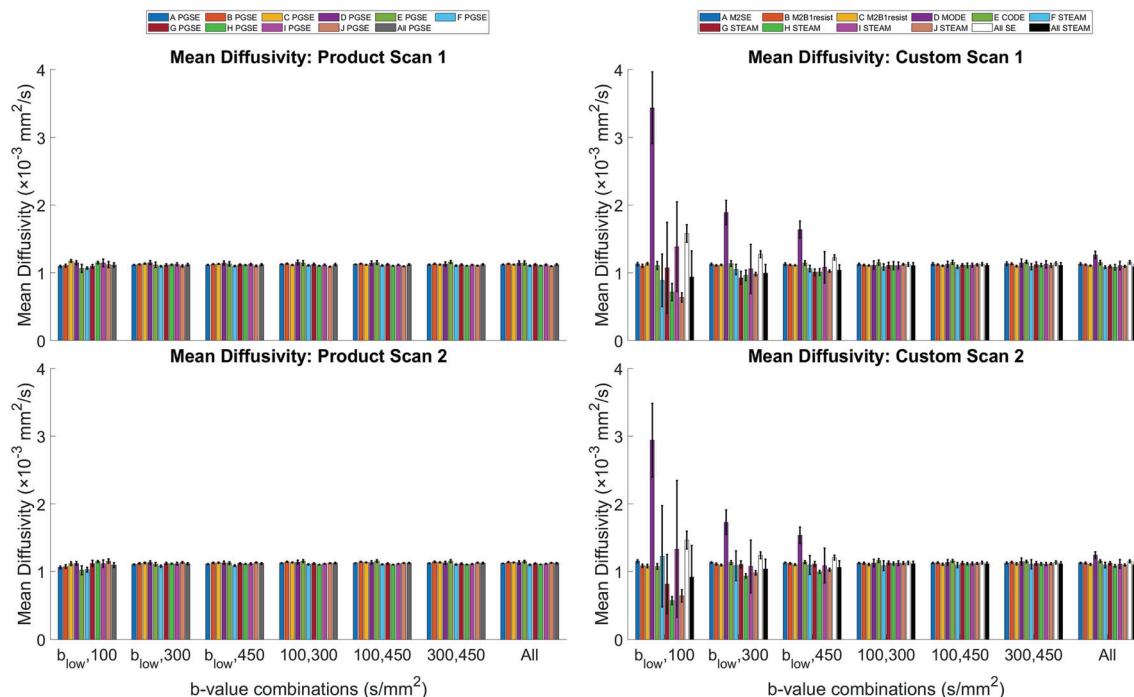


FIGURE 4 Sensitivity of mean diffusivity (MD) to b-values used in the diffusion tensor imaging (DTI) reconstruction. Average MD in tube 1 (0% polyvinylpyrrolidone) across sites, two time points, product (left) and custom sequence data (right) and b-value combinations. Mean \pm SD across voxels in the region of interest. Average values for pulsed gradient spin echo (PGSE), spin echo (SE) and stimulated echo acquisition mode (STEAM) are given by grey, white and black bars, respectively. The b-values of nondiffusion-weighted data are denoted by b_{low} , and ranged from 0 to 76 s/mm^2 across sites (Table 1). MD and FA reconstructed using pairs of b-values that include b_{low} are generally further from expected values and less reproducible across scans. The combination of $b = (100, 450) s/mm^2$ was considered in subsequent analysis

$1.113 \times 10^{-3} mm^2/s$, the average MD of tube 1, as measured by PGSE and SE, was overestimated by 1.0% ($p = 0.01$) and 1.5% ($p = 0.01$), respectively, while STEAM provided a result that was accurate to within 0.04% ($p = 0.9$). The SD across ROIs in tubes 1–7 increased with PVP concentration, particularly in the STEAM data. Summary values of MD and FA grouped by pulse sequence are presented in Table 2, alongside literature values where available.

3.3 | Accuracy

The accuracy of MD relative to the average MD measured across sites is presented in Figure 6. The null hypothesis that samples were normally distributed was rejected in three cases (STEAM tube 1, SE tube 3 and PGSE tube 7). Median accuracies between sequences were not significantly different, except for PGSE tube 2 versus STEAM tube 2 ($p < 0.05$). Within pulse sequences and between tubes, there were no significant differences in median accuracies.

3.4 | Precision

The precision of MD across pairs of sequences and tubes show that SE has significantly higher median CV than PGSE in three tubes, whereas STEAM has significantly higher median CV than PGSE in six tubes (Figure 7). There were clear differences as well when comparing medians between pairs of tubes, with precision worsening with increasing tube number (i.e. PVP concentration).

3.5 | Intrascan stability

Figure 8 shows the SNR of the $b = 100 s/mm^2$ data in a single repetition. In tube 1, the average SNRs across scans 1 and 2 were 23.3, 19.9 and 20.8 in PGSE, SE and STEAM, respectively, whereas in tube 7, the corresponding average SNRs were 44.1, 41.8 and 31.2. The stability of measurements across repetitions is reported in the supporting information.

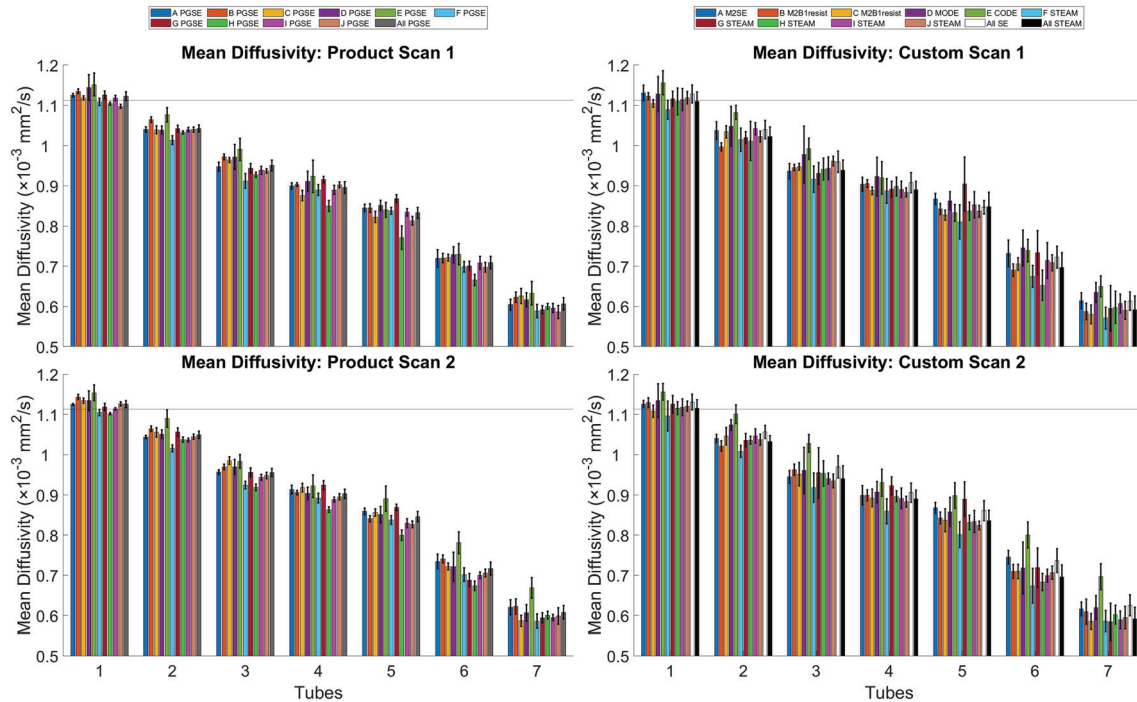


FIGURE 5 Average mean diffusivity (MD) across regions of interest (ROIs) as a function of polyvinylpyrrolidone (PVP) concentration. Tensors were reconstructed using $b = (100, 450)$ s/mm² data. Tubes 1–7 corresponded to 0%, 2.5%, 5%, 7.5%, 10%, 15% and 20% PVP, respectively. Mean \pm SD across voxels in the ROI. The horizontal black line indicates the reference diffusivity (H_2O at $0^\circ C$) = $1.113 \times 10^{-3} \text{ mm}^2/\text{s}$

3.6 | Intrasite repeatability

Bland–Altman plots of MD and FA across two scans are presented in Figure 9. In tube 1, the mean differences of MD in PGSE, SE and STEAM were $(0.3 \pm 2.3, 0.24 \pm 0.95, 0.52 \pm 0.58) \times 10^{-5} \text{ mm}^2/\text{s}$, respectively (mean \pm 1.96 SD). The corresponding mean differences in FA were $0.0006 \pm 0.0099, 0.006 \pm 0.018$ and -0.012 ± 0.039 . The differences between pulse sequences, as observed in the mean differences of MD and FA, were not significant at $p = 0.05$. Linear regression of difference by average values of MD and FA showed low proportional bias, with R^2 of 0.16 or less in all cases. Figure 10 summarises the bootstrapped scan-wise mean differences in MD and FA, grouped by pulse sequence. On average and across tubes, the greatest median scan-wise difference in MD of $0.96 \times 10^{-5} \text{ mm}^2/\text{s}$ was seen in the SE data, whereas STEAM exhibited the greatest median scan-wise difference in FA of -0.012 . Table S1 compares the mean difference averaged across all tubes across sites. The lowest absolute mean differences in MD and FA in the custom sequence data were seen in sites A and D, respectively.

Overall, STEAM yielded more accurate MD than SE at the isocentre ($p = 0.02$), while MD and FA across repetitions were more stable in SE compared with STEAM ($p < 0.001$). Although SE tended to higher reproducibility in MD and FA than STEAM, these were not significant at $p = 0.05$.

3.7 | Intersite reproducibility

The average CV_{MD} was evaluated across scans, sites (PGSE, SE and STEAM separately) and sequence pairs (PGSE vs. SE, PGSE vs. STEAM and SE vs. STEAM). The results were: $CV_{MD(\text{scans})} = 1.0\%$, $CV_{MD(\text{sites, PGSE})} = 2.6\%$, $CV_{MD(\text{sites, SE})} = 3.1\%$, $CV_{MD(\text{sites, STEAM})} = 2.1\%$, $CV_{MD(\text{sequences, PGSE vs SE})} = 1.2\%$, $CV_{MD(\text{sequences, PGSE vs. STEAM})} = 1.6\%$ and $CV_{MD(\text{sequences, SE vs. STEAM})} = 2.6\%$ (Figure 11). Within the intersite grouping, there were no significant differences in median CV between different sequences. Within the intersequence grouping, median CV in SE versus STEAM was significantly higher than both PGSE versus SE and PGSE versus STEAM.

4 | DISCUSSION

In this study, we compared several state-of-the-art methods suitable for in vivo cardiac DTI alongside conventional PGSE data. The results at the isocentre (i.e. tube 1) showed that, averaged across sites, PGSE, SE and STEAM yielded accurate MD, agreeing with the reference diffusivity of

TABLE 2 Mean diffusivity (MD) and fractional anisotropy (FA) across regions of interest in tubes 1–7 by sequence

Tube	[PVP] (%)	MD ($\times 10^{-3}$ mm ² /s)				FA			
		PGSE	SE	STEAM	Literature	PGSE	SE	STEAM	Literature
1	0	1.124 ± 0.017	1.13 ± 0.017 [†]	1.113 ± 0.011*	1.115 ± 0.033, ²⁹ 1.123 ± 0.023, ³⁰ 1.12 ± 0.01 ³⁴	0.028 ± 0.016	0.052 ± 0.016*	0.059 ± 0.030*	0.037 ± 0.010 ²⁹
2	2.5	1.046 ± 0.018	1.048 ± 0.030	1.027 ± 0.014*	1.05 ± 0.02 ³⁴	0.036 ± 0.023	0.059 ± 0.023*	0.064 ± 0.031*	
3	5	0.953 ± 0.023	0.964 ± 0.028 [†]	0.939 ± 0.015	0.98 ± 0.02 ³⁴	0.049 ± 0.034	0.065 ± 0.032	0.069 ± 0.038	
4	7.5	0.899 ± 0.020	0.907 ± 0.014 [†]	0.890 ± 0.016		0.042 ± 0.024	0.060 ± 0.021*	0.066 ± 0.023*	
5	10	0.839 ± 0.026	0.854 ± 0.022	0.842 ± 0.032	0.850 ± 0.024, ³⁰ 0.85 ± 0.01 ³⁴	0.049 ± 0.036	0.062 ± 0.034	0.090 ± 0.047*	
6	15	0.713 ± 0.025	0.729 ± 0.031 [†]	0.697 ± 0.015	0.71 ± 0.01 ³⁴	0.052 ± 0.032	0.078 ± 0.042	0.113 ± 0.066*	
7	20	0.607 ± 0.021	0.619 ± 0.035 [†]	0.592 ± 0.010*	0.607 ± 0.019, ³⁰ 0.59 ± 0.02 ³⁴	0.048 ± 0.028	0.078 ± 0.032*	0.123 ± 0.067*	

Note: MD and FA given as mean ± SD across sites and time points. Values from the literature using PGSE at a single time point are given for matching PVP concentrations and temperature. Significant differences at $p < 0.05$ (i) in SE and STEAM with respect to PGSE are denoted by *, and (ii) in SE with respect to STEAM by †.

Abbreviations: PGSE, pulsed gradient spin echo; PVP, polyvinylpyrrolidone; SE, spin echo; STEAM, stimulated echo acquisition mode.

water at 0°C to within 1.5% or less. Moreover, the MDs in the PGSE, SE and STEAM data were within ±1% of averaged literature values,^{33,34,37} suggesting good conformance with prescribed experimental conditions. The diffusivity of PVP depends on the concentration, temperature and length of polymer chains, and an independently measured ground truth is unavailable. We therefore used the MD acquired using PGSE averaged across sites and scans as a reference for assessing accuracy in PVP with different concentrations: these values were in good agreement with the literature (Table 2).

The expected value of FA in an isotropic phantom is zero. However, factors including noise, imperfect gradient calibration, eddy currents, and convection and vibration within the phantom could in principle contribute to nonzero FA. Both SE and STEAM had lower SNRs than PGSE, which could have resulted in the higher FA in the custom sequences. We chose not to report CV_{FA} because the expected FA in isotropic media is zero, which leads to unstable CV_{FA} that is biased by the measured FA. For instance, poor gradient calibration would lead to a higher FA, and therefore artificially lower CV_{FA} . Vibration and convection were not deemed to be major issues due to the good accuracy of MD.

CV (ROI) in MD and FA across sites was lowest in PGSE and highest in STEAM. In an isotropic liquid phantom, the underlying substrate is expected to be homogeneous. Reasons that could increase CV (ROI) include noise and image artefacts. From Figure 3, Gibb's ringing can be seen in all datasets due to the hard edges of the phantom. Additional artefacts are visible in the STEAM data (sites G and H), potentially increasing the CV (ROI). Furthermore, as the tube number and PVP concentration increased, we observed that the mean FA and CV (ROI) in MD and FA were increasingly elevated, particularly in STEAM. This may be associated with (i) effects of concomitant fields away from the isocentre (site E), (ii) localised image artefacts in tubes 5, 6 and 7 possibly caused by vibration (site G), and (iii) the increased effect of Gibb's ringing in the tubes with higher PVP concentrations due to the increased differential in DW image intensities relative to the surrounding ice-water bath.

In cardiac DTI, DW data with finite, low b -values are often used instead of non-DW data to suppress the effects of microvascular perfusion.²³ There was no perfusion in the phantom, and therefore MD and FA would be expected to be relatively insensitive to the b -value combinations used, insofar as perfusion is concerned. This was generally the case for PGSE data. Greater deviations were seen when custom DTI data were reconstructed from b -value pairs that included non-DW data. See b_{low} in Table 1 for corresponding b -values. Deviations from the expected values of MD and FA were particularly striking in MODE and STEAM data. With MODE, high MD was seen whenever the b_{low} data were used. This was due to a shading artefact seen in the DW data, but not in the non-DW data, therefore resulting in a positive bias in MD when the non-DW data were included in the reconstruction. The shading artefact was potentially due to residual concomitant gradient field effects, and this was reflected in higher regional heterogeneity compared with other SE data. In STEAM, the value of b_{low} can be substantial due to the effect of crushers and long diffusion times. The diffusion contrast between b_{low} and $b_{high} = 100$ s/mm² can therefore be insufficient for reliable estimation of MD and FA. This is a general result of the increased effects of noise as the range of b -values used for reconstruction are reduced, for instance, resulting in a positive bias in FA. As b_{high} increased to 450 s/mm², the errors were reduced. Where combinations of $b = (100, 300), (100, 450)$ and $(300, 450)$

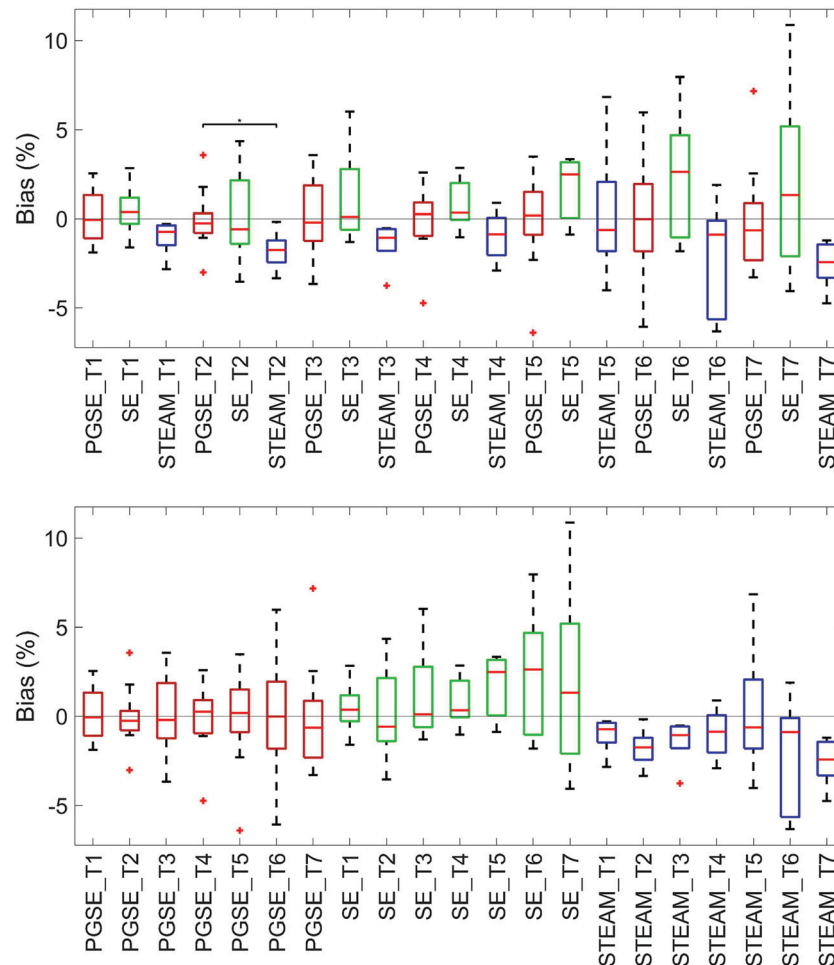


FIGURE 6 Accuracy in mean diffusivity (MD) measurements. Accuracy of MD relative to the reference MD was reported across pulse sequences and tubes (T). The reference MD in each tube was determined by the mean MD across sites and scans. Data from scans 1 and 2 were first averaged. Wilcoxon rank-sum tests were performed between pairs of sequences (pulsed gradient spin echo [PGSE] vs. spin echo [SE]; SE vs. stimulated echo acquisition mode [STEAM]; PGSE vs. STEAM) for each separate tube, and between pairs of tubes for each separate sequence; $*p < 0.05$). Differences in median accuracy between tubes within the same sequence were not significant at $p < 0.05$. Data were sorted by sequences-tubes (top) and tubes-sequences (bottom) for clarity

s/mm^2 were used, the MD and FA were qualitatively indistinguishable. However, we found that the combination of $b = (100, 450) s/mm^2$ yielded the best reproducibility in MD between scans 1 and 2, and this was consistent with typical b -values used in the literature.^{19,22}

The SNRs in the $b = 100 s/mm^2$ images at the isocentre were comparable between SE and STEAM. The SNR generally increased with PVP concentration as the mean signal intensity was less attenuated by diffusion-weighting. Away from the isocentre in tube 7, the image SNRs in PGSE and SE were 41% and 34% higher than that in STEAM, which may have arisen from image artefacts as described (sites G and H). Furthermore, in four instances of STEAM, only a single slice was acquired due to limitations in implementation. In these cases, reduced FOV was used, which involved excitation slice-selection gradients that were orthogonal to subsequent slice-selection gradients. As a result, acquisition of multiple slices while maintaining constant acquisition time would necessitate a reduction in the number of repetitions proportional to the number of slices (site H). By implementing a slab-tilted reduced FOV imaging method that is compatible with multislice imaging, this enabled site H to extend the TR to 6 s, rather than the 2 s used by the other STEAM sites, which recovers some of the SNR efficiency lost by using the STEAM technique. This motivates a shift from standard slab-perpendicular methods towards better methods of reduced FOV imaging, such as slab-tilted methods. We note that image SNR does not fully reflect the stability of measurements, as it does not take into account higher b -value data and associated potential issues. For instance, among the STEAM acquisitions, lower SNR was found alongside lower CV in MD and FA (site H).

The mean differences in MD in tube 1 across scans were relatively small at 0.22%, 0.21% and 0.47% in PGSE, SE and STEAM, respectively, expressed as a percentage of the respective average MD. The 95% limits of agreement were higher at $\pm 0.84\%$ in SE compared with $\pm 0.52\%$ in the

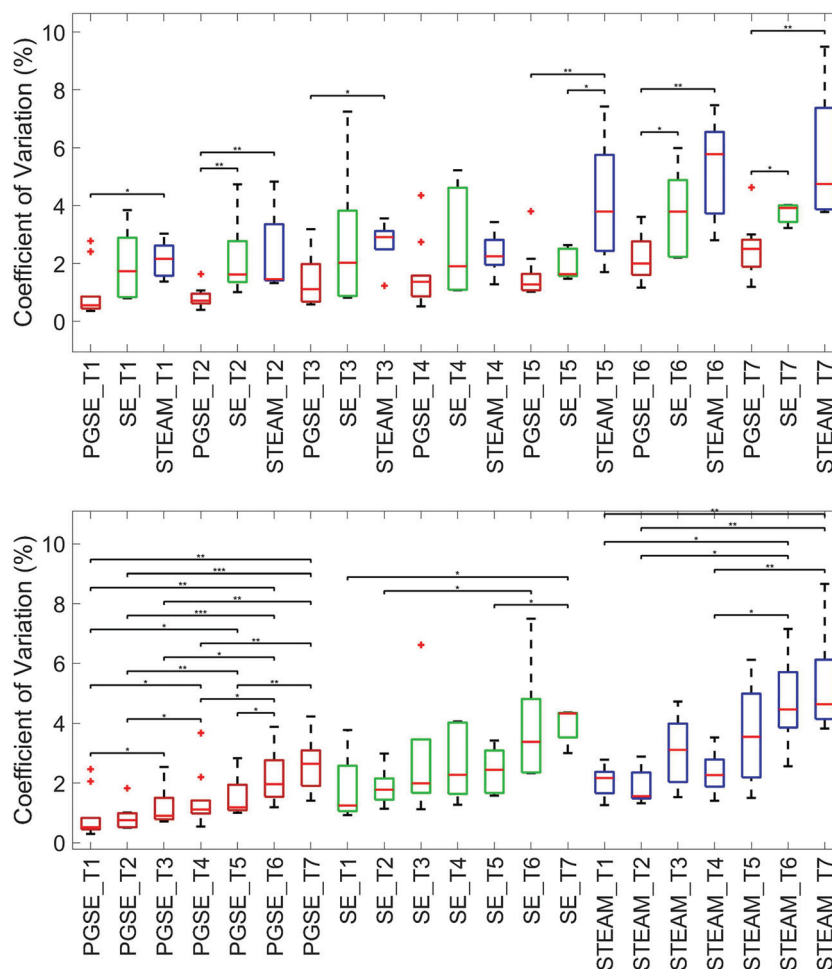


FIGURE 7 Precision in mean diffusivity (MD) measurements. Precision of MD was reported across pulse sequences and tubes (T). Wilcoxon rank-sum tests were performed between pairs of sequences and tubes; * $p < 0.05$, ** $p < 0.01$, *** $p < 0.001$. In several tubes, precision was poorer in spin echo (SE) and stimulated echo acquisition mode (STEAM) compared with pulsed gradient spin echo (PGSE). There was a clear dependence of precision on tube number. Data were sorted by sequences-tubes (top) and tubes-sequences (bottom) for clarity

STEAM data. For FA, both the absolute mean difference and 95% limits of agreement were lower in SE (0.006 ± 0.018) compared with STEAM (-0.012 ± 0.039). The MD data suggest that there was good reproducibility across the different classes of sequences. That the reproducibility with respect to FA was poorer could be due to the intrinsically low FA and lack of underlying microstructure.

Intrasite repeatability was superior to intersite and intersequence reproducibility, as measured in terms of CV_{MD} . This is consistent with the literature. Intersite reproducibility ranging from 2.1% (STEAM) to 3.1% (SE) was similar to other studies using PGSE alone,^{33,34} where values ranged from 2.1% to 3%. We also observed that intersite reproducibility was marginally poorer than intersequence reproducibility. The CV in all cases was low compared with CV in vivo,²⁹ as the phantoms were static, isotropic and consistently fabricated. We would anticipate greater variation between sites and sequences, with added phantom complexity simulating anisotropy and/or motion.

While we consider the various SE sequences collectively, it is worth noting that each of the four SE sequences used have their specific characteristics. Despite having the longest TE, the M2B1resist sequence had the lowest FA, regional heterogeneity in MD and FA, and SD_{MD} and SD_{FA} across repetitions, and highest SNR among custom sequences. Owing to the symmetric design of the diffusion gradients, the sequence, along with M2SE, is inherently more robust to concomitant fields. Furthermore, as the zeroth and first gradient moments are nulled prior to the refocusing pulse, its insensitivity to motion with constant velocity is less dependent on the refocusing pulse being close to 180° compared with other custom SE sequences.⁴⁶ However, the additional gradient lobes relative to M2SE, and the need for crushers due to the nulling of zeroth gradient moments before the refocusing pulse, extend the minimum TE. M2SE and MODE yielded the best interscan reproducibility in MD and FA, respectively. While shorter TE are feasible with CODE and MODE compared with M2SE and M2B1resist, the former two sequences are sensitive to spatially varying concomitant fields due to the asymmetry of diffusion gradient waveforms about the refocusing pulse, and corrections are

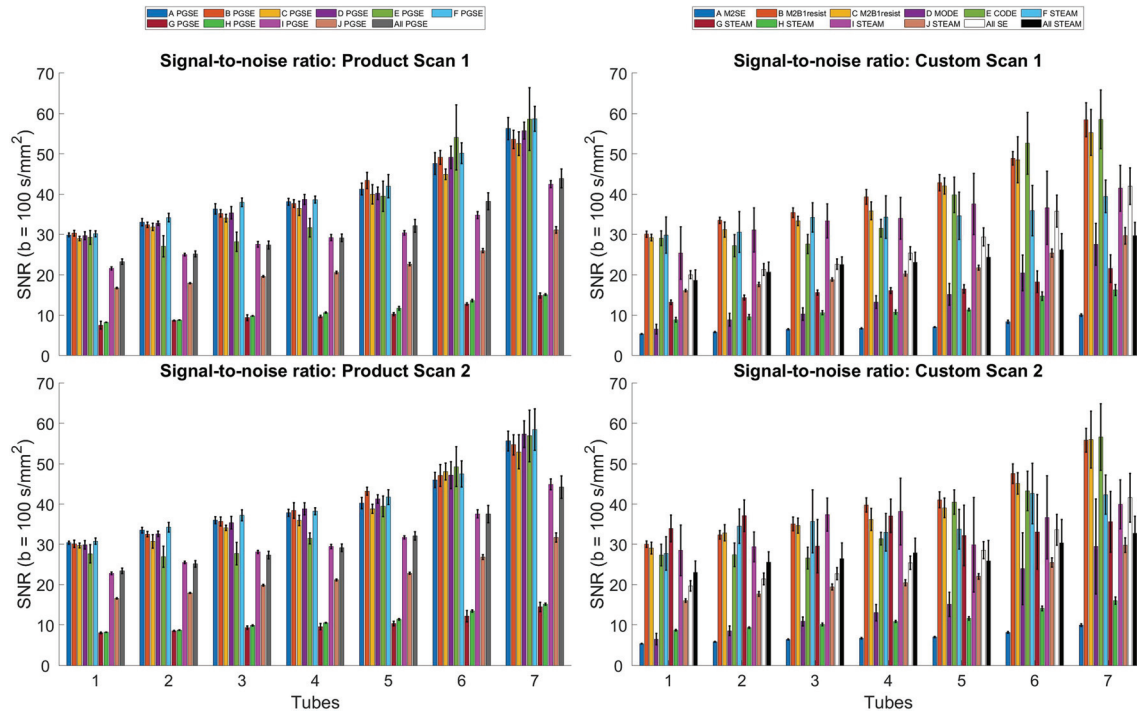


FIGURE 8 Signal-to-noise ratio (SNR) of $b = 100 \text{ s/mm}^2$ images. SNR was highest in the pulsed gradient spin echo (PGSE) data: 23.3 and 44.1 in tubes 1 and 7, respectively. Relative to PGSE, SNRs (spin echo [SE]) in tubes 1 and 7 were 85.1% and 94.8%, respectively, while SNRs (stimulated echo acquisition mode [STEAM]) were 89.4% and 70.8%, respectively. Mean \pm SD across voxels in the region of interest

employed to mitigate image artefacts arising from concomitant fields. As the custom SE group data include data acquired with four different SE sequences, the within-group variation would be expected to decrease were a single sequence used.

The current work provides a promising basis for future clinical studies. While other quantitative CMR techniques have arguably been hampered by methods that differ even in phantoms and are very sensitive to readout parameters,⁴⁷ here we demonstrate that a wide range of sequences from different centres have excellent agreement in a simple phantom. Clinically, the availability of multiple sequences for cardiac DTI offers sites the flexibility to choose the sequence to suit the pathology of interest and hardware configuration available. SE, for instance, yields higher SNR efficiency but requires higher performance gradient systems. STEAM, on the other hand, is able to acquire data over a wider range of cardiac phases, but requires breath-holding, which may be difficult in some patient cohorts. While the comparison of cardiac DTI sequences remains an active area of research, there may be a clinical case for both classes of sequences.

There are several limitations of using a static isotropic phantom for quantifying the performance of cardiac DTI sequences. First, the phantom lacks motion. This prevents the assessment of the quality of motion compensation in the custom sequences, where inadequate motion compensation is a primary reason for rejected images, elevated MD and failed scans. Incorrect triggering could be difficult to identify from the static phantom images. Second, the phantom lacks anisotropic microstructure, leading to an expected FA of zero. This results in non-Gaussian distribution of errors in FA, and enhancement in the errors when expressed as a percentage. Third, the phantom substrate is liquid and therefore could be prone to scanner vibration and thermal convection, which in turn could increase MD, although this was not observed to be a major issue. This effect may be more pronounced in STEAM, where diffusion times are an order of magnitude longer. Fourth, the T_1 and T_2 relaxation times of the liquid substrate are different compared with that found in the heart,^{37,48} with $T_{1,\text{H}_2\text{O}@0^\circ\text{C}} = 1525 \text{ ms}$, $T_{2,\text{H}_2\text{O}@0^\circ\text{C}} = 1472 \text{ ms}$, $T_{1,20\%\text{PVP}@0^\circ\text{C}} = 753 \text{ ms}$, $T_{2,20\%\text{PVP}@0^\circ\text{C}} = 623 \text{ ms}$, $T_{1,\text{Heart in vivo}} = 1184 \text{ ms}$ and $T_{2,\text{Heart in vivo}} = 52 \text{ ms}$, as measured at 3 T. This translates to higher SNR in the phantom relative to heart, and sequences with longer TE such as custom SE, would suffer greater SNR penalties in vivo. Adjusting for T_1 and T_2 in the in vivo setting relative to iced water, the signal in SE would be expected to decrease by 73% to 82%, while the signal in the STEAM data would decrease by 29% to 49% based on TR and TE in the custom sequences. This would lead to a theoretical 2.7x increase in signal in STEAM relative to SE in tube 1. In 20% PVP, the relative theoretical improvement in signal in STEAM over SE would be 2.4x.

Despite its shortcomings, the use of a static, isotropic phantom is an important first step for assessing custom sequence performance in a multicentre study, as it allows a baseline assessment of parameters in the absence of additional variables associated with tissue microstructure and motion. The phantom was robust and consistent, having been manufactured centrally, and stable over time, permitting repeated scanning with negligible change in substrate. The use of the ice-water bath permitted accurate temperature control, which is important, as

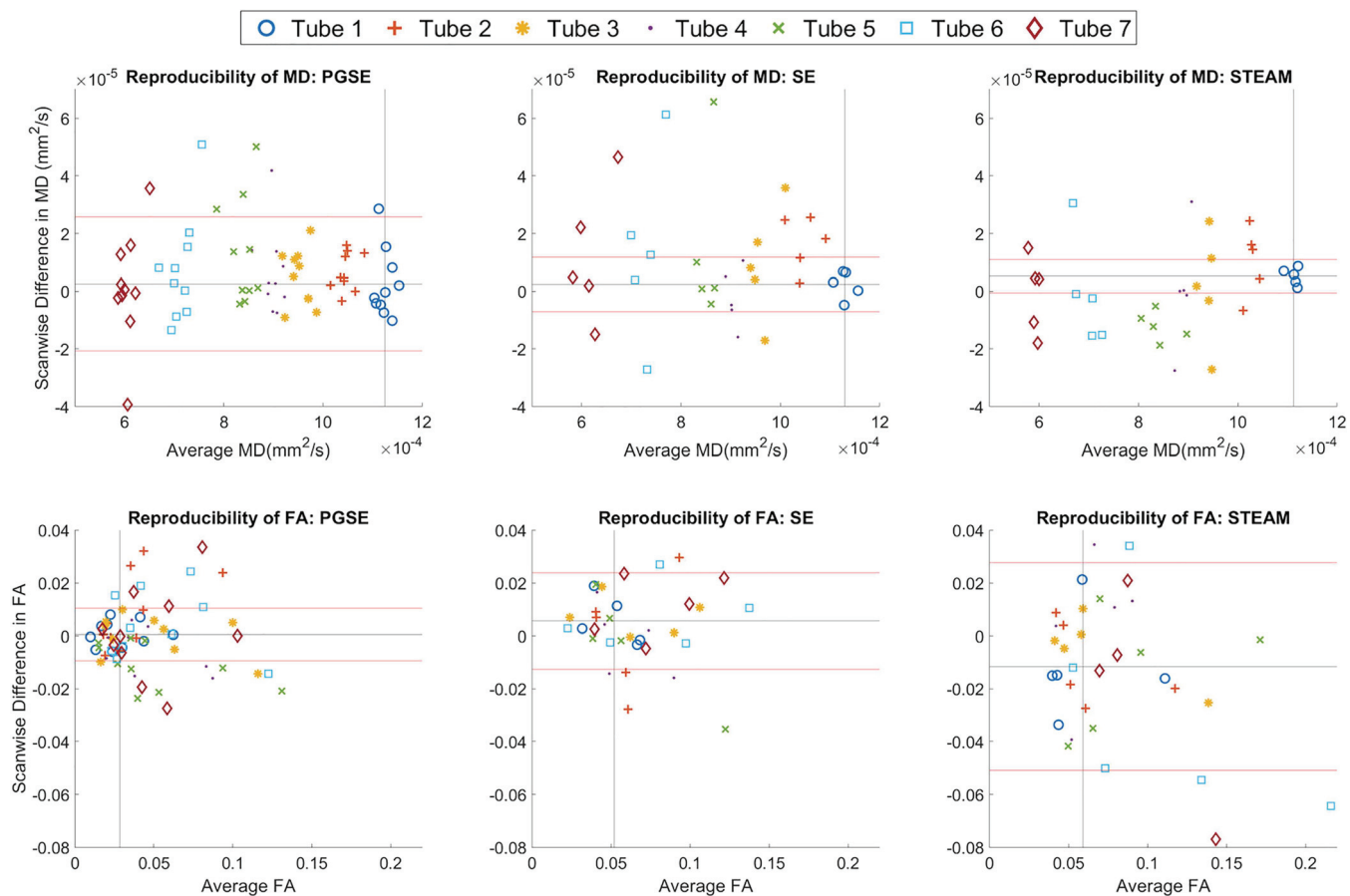


FIGURE 9 Bland–Altman plots of mean diffusivity (MD) and fractional anisotropy (FA) across two scans (scan 2 – scan 1). Data acquired using pulsed gradient spin echo (PGSE; left), spin echo (SE; middle) and stimulated echo acquisition mode (STEAM; right) sequences in tubes 1 to 7 (0%–20% polyvinylpyrrolidone [PVP]) are colour-coded by increasing PVP concentration. The black and red horizontal lines indicate the mean and ± 1.96 SD values for tube 1, respectively. The black vertical line indicates the average values for tube 1 across sites

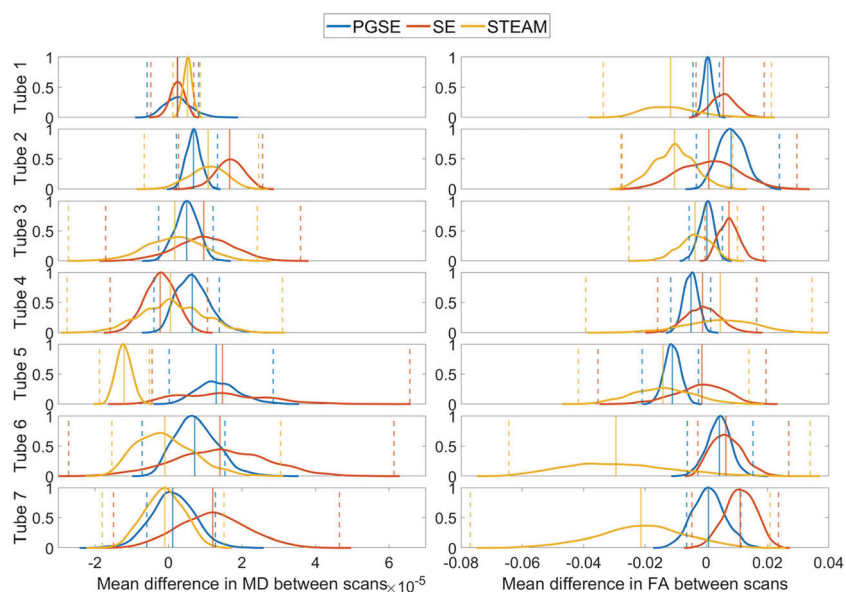


FIGURE 10 Bootstrapped normalised histograms of mean differences in mean diffusivity (MD) and fractional anisotropy (FA) between scans. Median and 95% confidence intervals (CIs) are given by vertical solid and dashed lines. The MD difference in stimulated echo acquisition mode (STEAM) was significantly lower than that of pulsed gradient spin echo (PGSE) and spin echo (SE) in tube 5. All other differences in reproducibility between sequences were not significant

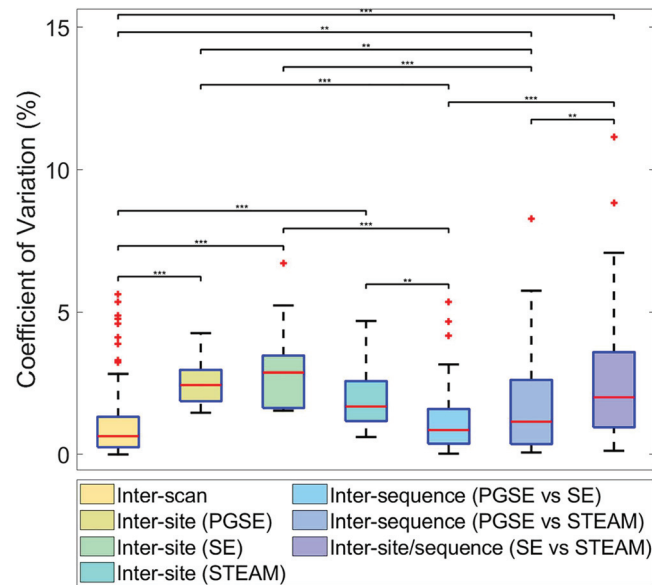


FIGURE 11 Reproducibility of mean diffusivity (MD) across scans, sites and sequences. Coefficients of variation in MD across scans, sites and sequences. Wilcoxon rank-sum tests were performed pairwise between groups; ** $p < 0.01$, *** $p < 0.001$. PGSE, pulsed gradient spin echo; SE, spin echo; STEAM, stimulated echo acquisition mode

every 1°C increase in temperature at 0°C leads to an ~5% increase in diffusivity. More elaborate systems for monitoring and maintaining accurate temperature are feasible, but would be costly to implement. In this ice-water phantom, the maximum MD achievable was $\sim 1.1 \times 10^{-3} \text{ mm}^2/\text{s}$ in water. This was in the middle of the range of MDs measured in the heart in vivo with SE and STEAM (0.87×10^{-3} to $1.72 \times 10^{-3} \text{ mm}^2/\text{s}$), and attributable to the low temperature. To simulate higher MD, a higher temperature would be needed. At 35°C, water would have too high an MD ($3.0 \times 10^{-3} \text{ mm}^2/\text{s}$). Instead, PVP solutions with concentrations (20% to 40%) would cover an appropriate MD range (0.9×10^{-3} to $1.8 \times 10^{-3} \text{ mm}^2/\text{s}$), based on a previous study.⁴⁹ Crucially, there exist gold standard, independent reference measurements of MD in water over a range of temperatures, and corroborating values of MD in temperature-controlled PVP phantoms in the literature.

5 | CONCLUSIONS

In summary, we have validated the accuracy, precision, repeatability and reproducibility of state-of-the-art custom sequences for in vivo cardiac DTI. This study benchmarks the performance of custom SE and STEAM against product PGSE sequences, and identifies baseline variation across sites, scanners and sequences. Some areas of inconsistency in the measurements have been highlighted, which warrant further methodological refinement. Future work includes the development of more sophisticated phantoms with more physiological relaxation times, diffusion anisotropy and motion characteristics. This would add further insight into the robustness and behaviour of cardiac DTI sequences, and the availability of appropriate phantoms will be key to facilitating quality assurance protocols. Quantitative validation of pulse sequences in phantoms represents an important step towards rationalising pulse sequences, and will contribute to protocol harmonisation and the establishment of cardiac DTI in the clinical setting.

ACKNOWLEDGMENTS

This study was supported by the British Heart Foundation (grant nos PG/19/1/34076, SI/14/1/30718, FS/13/71/30378, PG/17/28/32943 and RG/19/1/34160), the German Ministry of Education and Research (BMBF; grant no. 01EO1504), the Swiss National Science Foundation (grant no. PZ00P2_174144), National Institutes of Health (grant nos R21-EB024701, R01-HL151704, R01-HL135242, R01-HL124096, R01-HL131823, R01-H131975 and R01-HL141563) and the Oxford NIHR Biomedical Research Centre.

CONFLICT OF INTEREST

Royal Brompton Hospital has research collaboration agreements with Siemens AG Medical Solutions.

AUTHOR CONTRIBUTIONS

Study conception (AS, CTS, DBE, IT, JES, MV), study coordination and drafting of manuscript (IT); phantom design and build (IT, JB); data acquisition (AS, BR, CN, CT, CTS, DL, EMT, IT, JCF, KM, PK, MV); data analysis (IT, WR); study design and planning, and manuscript review (all). All the authors have approved the submitted version and any substantially modified version that involves each author's contribution to the study, and have agreed both to be personally accountable for their own contributions and to ensure that questions related to the accuracy or integrity of any part of the work are appropriately investigated, resolved, and the resolution documented in the literature.

DATA AVAILABILITY STATEMENT

The datasets generated from the current study are available on the Human Heart Project repository <https://humanheart-project.creatis.insa-lyon.fr/MultiCentreEvaluationCDTI.html>.

ORCID

Irvin Teh  <https://orcid.org/0000-0002-6705-3129>
William A. Romero R.  <https://orcid.org/0000-0001-7312-6745>
Jaume Coll-Font  <https://orcid.org/0000-0001-9341-6838>
Erica Dall'Armellina  <https://orcid.org/0000-0002-2165-7154>
Daniel B. Ennis  <https://orcid.org/0000-0001-7435-1311>
Pedro F. Ferreira  <https://orcid.org/0000-0002-0436-3496>
Sebastian Kozerke  <https://orcid.org/0000-0003-3725-8884>
David Lohr  <https://orcid.org/0000-0002-6509-3776>
Kévin Moulin  <https://orcid.org/0000-0002-9188-6403>
Christopher Nguyen  <https://orcid.org/0000-0003-1475-2329>
Laura M. Schreiber  <https://orcid.org/0000-0002-8827-1838>
Andrew D. Scott  <https://orcid.org/0000-0001-7656-3123>
David E. Sosnovik  <https://orcid.org/0000-0002-6486-7434>
Christian T. Stoeck  <https://orcid.org/0000-0001-8670-0929>
Cyril Tous  <https://orcid.org/0000-0003-2664-5272>
Elizabeth M. Tunnicliffe  <https://orcid.org/0000-0002-6945-5201>
Andreas M. Weng  <https://orcid.org/0000-0001-8943-3539>
Pierre Croisille  <https://orcid.org/0000-0003-4019-3460>
Magalie Viallon  <https://orcid.org/0000-0001-9118-0438>
Jürgen E. Schneider  <https://orcid.org/0000-0003-0999-5684>

REFERENCES

1. Nguyen C, Fan Z, Xie Y, et al. In vivo contrast free chronic myocardial infarction characterization using diffusion-weighted cardiovascular magnetic resonance. *J Cardiovasc Magn Reson*. 2014;16:68.
2. Mekkaoui C, Jackowski MP, Kostis WJ, et al. Myocardial scar delineation using diffusion tensor magnetic resonance tractography. *J Am Heart Assoc*. 2018;7(3):e007834.
3. Ariga R, Tunnicliffe EM, Manohar SG, et al. Identification of myocardial disarray in patients with hypertrophic cardiomyopathy and ventricular arrhythmias. *J Am Coll Cardiol*. 2019;73(20):2493-2502.
4. Wu MT, Tseng WY, Su MY, et al. Diffusion tensor magnetic resonance imaging mapping the fiber architecture remodeling in human myocardium after infarction: correlation with viability and wall motion. *Circulation*. 2006;114(10):1036-1045.
5. Moulin K, Viallon M, Romero W, et al. MRI of reperfused acute myocardial infarction edema: ADC quantification versus T1 and T2 mapping. *Radiology*. 2020;295(3):542-549.
6. Tseng WYI, Dou JG, Reese TG, Wedeen VJ. Imaging myocardial fiber disarray and intramural strain hypokinesis in hypertrophic cardiomyopathy with MRI. *J Magn Reson Imaging*. 2006;23(1):1-8.
7. Das A, Chowdhary A, Kelly C, et al. Insight into myocardial microstructure of athletes and hypertrophic cardiomyopathy patients using diffusion tensor imaging. *J Magn Reson Imaging*. 2020;53(1):73-82.
8. Nguyen C, Lu MJ, Fan ZY, et al. Contrast-free detection of myocardial fibrosis in hypertrophic cardiomyopathy patients with diffusion-weighted cardiovascular magnetic resonance. *J Cardiovasc Magn Reson*. 2015;17(1):107.
9. Gotschy A, von Deuster C, van Gorkum RJH, et al. Characterizing cardiac involvement in amyloidosis using cardiovascular magnetic resonance diffusion tensor imaging. *J Cardiovasc Magn Reson*. 2019;21(1):56.
10. Abdullah OM, Drakos SG, Diakos NA, et al. Characterization of diffuse fibrosis in the failing human heart via diffusion tensor imaging and quantitative histological validation. *NMR Biomed*. 2014;27(11):1378-1386.
11. von Deuster C, Sammut E, Asner L, et al. Studying dynamic myofiber aggregate reorientation in dilated cardiomyopathy using in vivo magnetic resonance diffusion tensor imaging. *Circ Cardiovasc Imaging*. 2016;9(10):e005018.
12. Edelman RR, Gaa J, Wedeen VJ, et al. In vivo measurement of water diffusion in the human heart. *Magn Reson Med*. 1994;32(3):423-428.

13. Stejskal EO, Tanner JE. Spin diffusion measurements: spin echoes in the presence of a time-dependent field gradient. *J Chem Phys.* 1965;42(1):288-292.
14. Gamper U, Boesiger P, Kozerke S. Diffusion imaging of the in vivo heart using spin echoes—considerations on bulk motion sensitivity. *Magn Reson Med.* 2007;57(2):331-337.
15. Stoeck CT, von Deuster C, Genet M, Atkinson D, Kozerke S. Second-order motion-compensated spin echo diffusion tensor imaging of the human heart. *Magn Reson Med.* 2016;75(4):1669-1676.
16. Ma S, Nguyen CT, Christodoulou AG, et al. Accelerated cardiac diffusion tensor imaging using joint low-rank and sparsity constraints. *IEEE Trans Biomed Eng.* 2018;65(10):2219-2230.
17. Aliotta E, Wu HH, Ennis DB. Convex optimized diffusion encoding (CODE) gradient waveforms for minimum echo time and bulk motion-compensated diffusion-weighted MRI. *Magn Reson Med.* 2016;77(2):717-729.
18. Majeed W, Kalra P, Kolipaka A. Motion Compensated, Optimized Diffusion Encoding (MODE) Gradient Waveforms. In: *Paper presented at: Proceedings of the 26th Annual Meeting of ISMRM, Paris, France; 2018.*
19. von Deuster C, Stoeck CT, Genet M, Atkinson D, Kozerke S. Spin echo versus stimulated echo diffusion tensor imaging of the in vivo human heart. *Magn Reson Med.* 2016;76(3):862-872.
20. Scott AD, Nielles-Vallespin S, Ferreira PF, et al. An in-vivo comparison of stimulated-echo and motion compensated spin-echo sequences for 3 T diffusion tensor cardiovascular magnetic resonance at multiple cardiac phases. *J Cardiovasc Magn Reson.* 2018;20(1):1.
21. McClymont D, Teh I, Carruth E, et al. Evaluation of non-Gaussian diffusion in cardiac MRI. *Magn Reson Med.* 2017;78(3):1174-1186.
22. Lasic S, Szczepankiewicz F, Dall'Armellina E, et al. Motion-compensated b-tensor encoding for in vivo cardiac diffusion-weighted imaging. *NMR Biomed.* 2020;33(2):e4213.
23. Scott AD, Ferreira PF, Nielles-Vallespin S, et al. Optimal diffusion weighting for in vivo cardiac diffusion tensor imaging. *Magn Reson Med.* 2015;74(2):420-430.
24. Jones DK, Basser PJ. "Squashing peanuts and smashing pumpkins": how noise distorts diffusion-weighted MR data. *Magn Reson Med.* 2004;52(5):979-993.
25. Gahm JK, Kindlmann G, Ennis DB. The effects of noise over the complete space of diffusion tensor shape. *Med Image Anal.* 2014;18(1):197-210.
26. McClymont D, Teh I, Schneider JE. The impact of signal-to-noise ratio, diffusion-weighted directions and image resolution in cardiac diffusion tensor imaging - insights from the ex-vivo rat heart. *J Cardiovasc Magn Reson.* 2017;19(1):90.
27. Stoeck CT, von Deuster C, van Gorkum RJH, Kozerke S. Motion and eddy current-induced signal dephasing in in vivo cardiac DTI. *Magn Reson Med.* 2020;84(1):277-288.
28. Nielles-Vallespin S, Mekkaoui C, Gatehouse P, et al. In vivo diffusion tensor MRI of the human heart: reproducibility of breath-hold and navigator-based approaches. *Magn Reson Med.* 2013;70(2):454-465.
29. Tunncliffe EM, Scott AD, Ferreira P, et al. Intercentre reproducibility of cardiac apparent diffusion coefficient and fractional anisotropy in healthy volunteers. *J Cardiovasc Magn Reson.* 2014;16(1):31.
30. Moulin K, Croisille P, Feiweier T, et al. In vivo free-breathing DTI and IVIM of the whole human heart using a real-time slice-followed SE-EPI navigator-based sequence: A reproducibility study in healthy volunteers. *Magn Reson Med.* 2016;76(1):70-82.
31. Stoeck CT, Kalinowska A, von Deuster C, et al. Dual-phase cardiac diffusion tensor imaging with strain correction. *PLoS ONE.* 2014;9(9):e107159.
32. McGill LA, Ismail TF, Nielles-Vallespin S, et al. Reproducibility of in-vivo diffusion tensor cardiovascular magnetic resonance in hypertrophic cardiomyopathy. *J Cardiovasc Magn Reson.* 2012;14:86.
33. Grech-Sollars M, Hales PW, Miyazaki K, et al. Multi-centre reproducibility of diffusion MRI parameters for clinical sequences in the brain. *NMR Biomed.* 2015;28(4):468-485.
34. Palacios EM, Martin AJ, Boss MA, et al. Toward precision and reproducibility of diffusion tensor imaging: a multicenter diffusion phantom and traveling volunteer study. *Am J Neuroradiol.* 2017;38(3):537-545.
35. Prohl AK, Scherrer B, Tomas-Fernandez X, et al. Reproducibility of structural and diffusion tensor imaging in the TACERN multi-center study. *Front Integr Neurosci.* 2019;13:24
36. Pierpaoli C, Sarlls J, Nevo U, Basser PJ, Horkay F. Polyvinylpyrrolidone (PVP) water solutions as isotropic phantoms for diffusion MRI studies. In: *Proceedings of the 17th Annual Meeting of ISMRM, Honolulu, USA; 2009.*
37. Jerome NP, Papoutsaki MV, Orton MR, et al. Development of a temperature-controlled phantom for magnetic resonance quality assurance of diffusion, dynamic, and relaxometry measurements. *Med Phys.* 2016;43(6):2998-3007.
38. Teh I, Zhou FL, Cristinacce PLH, Parker GJM, Schneider JE. Biomimetic phantom for cardiac diffusion MRI. *J Magn Reson Imaging.* 2016;43(3):594-600.
39. Szczepankiewicz F, Hoge S, Westin CF. Linear, planar and spherical tensor-valued diffusion MRI data by free waveform encoding in healthy brain, water, oil and liquid crystals. *Data Brief.* 2019;25:104208.
40. Romero W, Viallon M, Froeling M, et al. CMRDifTools: A Processing and Analysis Tool for Cardiac Diffusion MR images. In: *Paper presented at: Proc Int Soc Magn Reson Med.* Paris, France; 2018.
41. CREATIS The Human Heart Project, 2020. Accessed January 17, 2022. <https://humanheart-project.creatis.insa-lyon.fr/>
42. Mills R. Self-diffusion in normal and heavy-water in range 1-45 degrees. *J Phys Chem.* 1973;77(5):685-688.
43. Dietrich O, Raya JG, Reeder SB, Reiser MF, Schoenberg SO. Measurement of signal-to-noise ratios in MR images: influence of multichannel coils, parallel imaging, and reconstruction filters. *J Magn Reson Imaging.* 2007;26(2):375-385.
44. Zhu T, Hu R, Qiu X, et al. Quantification of accuracy and precision of multi-center DTI measurements: a diffusion phantom and human brain study. *NeuroImage.* 2011;56(3):1398-1411.
45. Farrell JA, Landman BA, Jones CK, et al. Effects of signal-to-noise ratio on the accuracy and reproducibility of diffusion tensor imaging-derived fractional anisotropy, mean diffusivity, and principal eigenvector measurements at 1.5 T. *J Magn Reson Imaging.* 2007;26(3):756-767.
46. Nguyen C, Fan Z, Xie Y, et al. In vivo diffusion-tensor MRI of the human heart on a 3 tesla clinical scanner: An optimized second order (M2) motion compensated diffusion-preparation approach. *Magn Reson Med.* 2016;76(5):1354-1363.
47. Kellman P, Hansen MS. T1-mapping in the heart: accuracy and precision. *J Cardiovasc Magn Reson.* 2014;16:2.

48. Granitz M, Motloch LJ, Granitz C, et al. Comparison of native myocardial T1 and T2 mapping at 1.5T and 3T in healthy volunteers: reference values and clinical implications. *Wien Klin Wochenschr*. 2019;131(7-8):143-155.
49. Wagner F, Laun FB, Kuder TA, et al. Temperature and concentration calibration of aqueous polyvinylpyrrolidone (PVP) solutions for isotropic diffusion MRI phantoms. *PLoS ONE*. 2017;12(6):e0179276.

SUPPORTING INFORMATION

Additional supporting information may be found in the online version of the article at the publisher's website.

How to cite this article: Teh I, Romero R, WA, Boyle J, et al. Validation of cardiac diffusion tensor imaging sequences: A multicentre test-retest phantom study. *NMR in Biomedicine*. 2022;35(6):e4685. doi:[10.1002/nbm.4685](https://doi.org/10.1002/nbm.4685)

Appendix C

Romero R, W. A. et al., “*Exploring DTI Benchmark Databases Through Visual Analytics*”, Computational Diffusion MRI, Springer, Cham, 2021. 291-301.

<https://doi.org/10.1007/978-3-030-73018-523>

Exploring DTI Benchmark Databases Through Visual Analytics

William A. Romero R.^{1,2}, Daniel Althviz Moré³, Irvin Teh⁴, Jürgen E. Schneider⁴, Magalie Viallon¹, and Pierre Croisille¹

¹ Université de Lyon, UJM-Saint-Etienne, INSA, CNRS UMR 5520, INSERM U1206, CREATIS, F-42023, Saint Etienne, France

² Siemens Healthcare SAS, Saint-Denis, France

{William.Romero, Magalie.Viallon, Pierre.Croisille}@creatis.insa-lyon.fr

³ Systems and Computing Engineering Department, Universidad de los Andes, Bogotá, Colombia

d.althviz10@uniandes.edu.co

⁴ Leeds Institute of Cardiovascular and Metabolic Medicine, University of Leeds, Leeds, UK

{I.Teh, J.E.Schneider}@leeds.ac.uk

Abstract. Diffusion MRI studies include tests on standardised phantoms and measurements on the output images to assess and benchmark the imaging system. These tests are an essential methodological step to guarantee the reproducibility of measurement outcomes. However, in longitudinal and multi-centre studies, analysis tasks become more complex with the increase in the sources and volume of data, as well as the parameters of interest. To manage this complexity, Visual Analytics (VA) allows researchers to explore large amounts of data easily and quickly by providing key information in a readily interpretable format and reducing the cognitive load of information. This paper presents CMRDiffMonitor, a VA tool for monitoring and benchmarking Diffusion Tensor Imaging (DTI) databases developed in the context of a multi-centre MRI project. Through an interactive dashboard, CMRDiffMonitor enables users to capture a snapshot of the study which includes: a temporal overview of the data sets (monitoring of the system stability across sites) and statistical measurements in Regions of Interest on Diffusion Anisotropy Indices (benchmarking of the different imaging sequences and systems).

Keywords: Visual Analytics · MRI Benchmark Databases · Cardiac Diffusion Tensor Imaging.

1 Introduction

Clinical research involves multi-centre studies with the objective to evaluate MRI protocols on a large number of patients and imaging systems, and consequently demonstrate the utility of the developed tools. Therefore, ensuring the stability of the systems involved [14] enables the evaluation (intra- and inter-centre) of reliable and reproducible results. Moreover, Quality Assurance (QA) protocols

include tests on a standardised phantom and measurements on the output images to identify the causes of failure and the potential corrective actions [22, 7].

The scenario of a multi-centre study relies on the capacity to manage and process data. As it is well-discussed by Burmeister et al., data collection and processing are the first stages of the workflow [6]. Research scientists need to extract meaningful information, find interesting insights and make correlations; in this direction, data analysis tools must not only extract parameters, but also ease the way to explore, report and share results. In this scenario, Visual Analytics (VA) techniques have the potential to enhance data exploration based on interactive visualisation. Consequently, research scientists may benefit from having a graphical representation to verify protocol compliance, identify anomalies, and validate imaging sequence outcomes across different systems and time-points in a concise and accessible way.

This paper describes CMRDiffMonitor, a VA tool for monitoring and benchmarking *in vitro* Diffusion MRI databases in order to enhance the ability to track, review and assess image acquisition sequences in longitudinal and multi-centre studies. CMRDiffMonitor is the result of an incremental development cycle in the context of a multi-centre study of cardiac diffusion MR sequences in an isotropic phantom. The tool has enabled participant researchers to streamline the analysis task as well as to report partial results of the research project as presented in [26, 27]

The next section gives an overview of the technological context and similar approaches. The subsequent sections describe in detail the problem domain and the system architecture in which the tool has been deployed. The paper concludes with a description of how the tool supports analysis tasks on *in vitro* DTI databases.

2 Related Work

The advent of data management solutions, workflow engines, and online interactive visualisation applications has led to the implementation of specialised databases and platforms such as the Cardiac Atlas Project [12], OpenNeuro [21], and Brainlife.io [5], to mention but a few. Bearing in mind the idea of reproducible computational research [11], research communities in Biomedical Sciences and Engineering have been contributing with exemplar infrastructures and technologies [10, 8, 4] in order to:

- collect, standardise and share data,
- execute complex computational methods (workflows) on different computing resources (grid, supercomputer, GPU-based cluster, etc.),
- manage workflows outputs or data formatting (new utilisable data), and
- provide online data visualisation.

Following these ideas, the Human Heart Project [1] has been implemented to provide access to medical databases and computer-based tools in order to share data easily, test computational methods and enhance collaboration in the

research community of cardiovascular imaging. The back-end infrastructure of this solution is based on Girder [18], a web-based data management platform, and the Virtual Imaging Platform (VIP) [13, 3], a scientific gateway for medical simulation and image data analysis.

DTI benchmark databases are used in the context of the harmonisation of imaging sequences [25–27]; a standard reference object (phantom) is used to assess and benchmark the performance of an MRI scanner. Understanding how images are produced by a set of parameters and conditions enables MRI and medical researchers to calibrate the imaging system as well as identify sources of variability and corrective actions. In the case of a multi-centre evaluation [25–27], the benchmark database allows the assessment of imaging sequences (product and custom-made) and scanner’s stability (acquisitions over time, intra-scanner analysis), and highlight the factors that may influence reliable and predictable results across the different imaging systems (inter-scanner analysis).

Several approaches to automatic data processing and visualisation are presented by every single platform publication [10, 8, 4]. The work presented by Davids et al. [9] provides insights into automatic processing of phantom measurements, based on the quality parameters recommended by the American College of Radiology accreditation [22]. However, there is no discussion about interactive visualisation tools for the interpretation of the results or traceability of data. One such solution, outlined by Burmeister et al. [6], describes in detail the design guidelines in the development of a platform for data preprocessing, cohort exploration and result reporting. In spite of the cohort-driven nature of the solution, there are valuable and practical lessons about the implementation of VA tools for data stratification, hypothesis testing and data analysis.

In addition, a Quality Control (QC) system of neuroimaging data can be found in [17]. This solution has been implemented to calculate QC metrics for various modality images (sMRI, fMRI, DTI or CT), report image QC rating and visual assessment performed by users. A general overview of the user interaction follows: data selection (project, modality, data set, image, status, etc), QC Settings (i.e. metric threshold) and visual inspection. To this extent, the system provides an evaluation of data sets to users. Therefore, users know the quality of the data they are using for analysing or as input in image processing workflows. In contrast to this work, CMRDiffMonitor is a domain and data specific tool focused on a multi-centre study of cardiac DTI sequences in an isotropic phantom. There is no data quality ranking or visual assessment by users.

3 Use Case

The main motivation to implement CMRDiffMonitor comes from a multi-centre study (11 geographically dispersed research sites) to investigate intra- and inter-site variation in DTI parameters in an isotropic phantom [2].

The experimental protocol is set up to scan a standardised phantom (7 tubes filled with 0 - 20% polyvinylpyrrolidone [20], figure 1) using product and custom DTI acquisition sequences with parameters matching typical cardiac DTI pro-

ocols: TR = 3000 ms, TE = 85 ms, in-plane resolution = 2.5 mm, slices = 3, thickness = gap = 8 mm, blow = $100 \frac{s}{mm^2}$, bhigh = $450 \frac{s}{mm^2}$, number of diffusion directions = 6, bandwidth ~ 3000 Hz, parallel imaging = 2x, and triggered with simulated ECG = 60 bpm. The phantoms are chilled in ice water and imaged at 0°C . Subsequent scans are performed under the same conditions in a time lapse between 1 and 30 days.

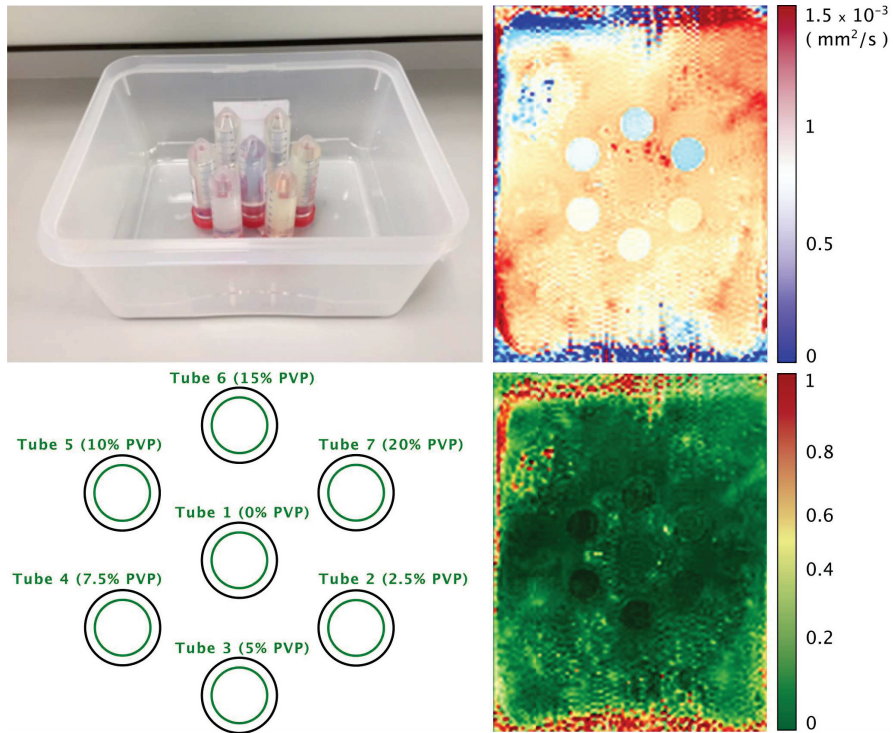


Fig. 1. Isotropic Phantom, ROI and DAI maps. Photograph of phantom before filling with ice and water (top left); layout of tubes and Regions of Interest (green circles, bottom left); MD and FA maps (top right and bottom right respectively). Background image texture in the MD and FA maps is caused by the ice.

MRI researchers have become increasingly interested in the utilisation of interactive visualisation tools to accelerate data analysis and enhance collaborative work. This research project brought attention to Visual Analytics as a tool to track and review the variability of Diffusion Anisotropy Indices (DAI) from different image acquisition sequences across participant sites in time. The goal was to explore simple VA techniques to provide the full picture of the multi-centre study. Therefore, the project established the following requirements:

- R1.** Collect and organise DICOM data sets from each site.

- R2.** Process data sets to calculate DAI maps: Mean Diffusivity (MD) and Fractional anisotropy (FA).
- R3.** Segment DAI maps and calculate statistics (minimum, maximum, mean, standard deviation, etc.) in the Regions of Interest (ROI).
- R4.** Export DAI/ROI statistics in CSV format.
- R5.** Display a timeline of the data set uploads of each site.
- R6.** Display statistical results by filtering sites, DAI, ROI, acquisition sequence and parameters.

The baseline of the solution is the Human Heart Project infrastructure. Requirement R1 is managed by the Girder platform [18] which provides user authentication and data management functionalities. Requirements R2, R3 and R4 are managed by CMRDiffTools [23]. Figure 2 outlines the main components, workload process and data flow. Figure 3 presents the image processing workflow performed by CMRDiffTools.

Dynamic graphics (requirements R5 and R6) were requested in order to basically provide two points of view of the original data (series of 2D MR images): first, the temporal dimension of data sets; and second, the statistical measurements on the DAI maps. The temporal dimension would give researchers the capacity to evaluate the imaging system stability (monitor), while statistical measurements would quantitatively assess the reproducibility across the different scanners (benchmarking). The next section presents the VA tool developed to address requirements R5 and R6.

4 Implementation

To fulfil requirements R5 and R6, a plug-in for the Girder platform [18] has been developed using Plotly [15], and open-source graphing library. The plug-in is fed with the statistical reports (CSV files, R4) in order to display a dashboard composed of 4 interactive areas (Figure 4):

1. The **filters panel** is a dynamic interface where the user can select filter conditions: DAI measure, ROI, acquisition sequence, acquisition parameters and field strength.
2. **Timeline view** shows the performed acquisitions (per acquisition sequence) over the course of time.
3. **Sites panel** lists all the sites in the study. The user can select the sites of interest.
4. **Measure view** displays the DAI value across the different sites for a selected ROI.

The Measure view is interactively updated according to the user selection on the filters panel, timeline view and sites panel. The user interaction follows the “Visual Information Seeking Mantra: overview first, zoom and filter, then details-on-demand” [24] in order to provide an effortless pathway to extract information. As an example of details-on-demand features, the mouse over action

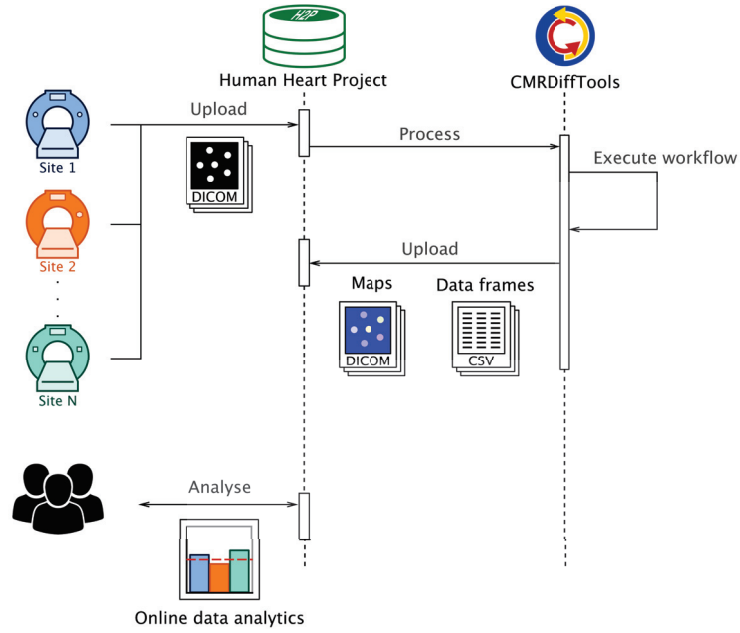


Fig. 2. Sequence diagram: main components and data flow.

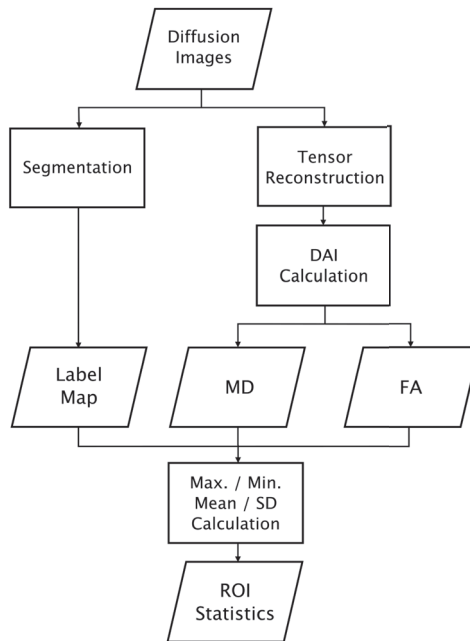


Fig. 3. Image processing workflow.

displays details of the data according to the view. For instance, the mouse pointer over a bar on the measure view will display: centre, sequence name, sequence parameters, acquisition date, mean value, and standard deviation.

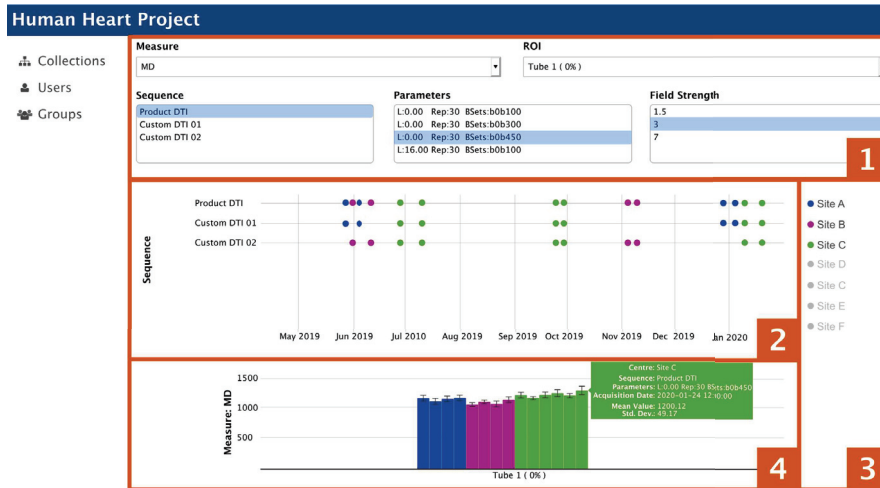


Fig. 4. Graphical User Interface (GUI) of the Girder plug-in. Components: 1 data filters, 2 timeline view, 3 list of sites, and 4 measure view.

5 Discussion

According to Keim et al. [16], "Visual analytics combines automated analysis techniques with interactive visualisations for an effective understanding, reasoning and decision making on the basis of very large and complex data sets". The developed VA tool, CMRDiffMonitor, allows MRI researchers to see, in a concise and accessible way, the current status of the experiment. In a single eye glance, research scientists can:

- Verify protocol compliance by checking time gaps on the **timeline view**.
- Identify anomalies by looking for unusual values on the **measure view**, using the historical registry **timeline view**.
- Compare the outcomes with similar imaging systems from different sites by using the **filters panel** to select: the type of sequence, the b values used to calculate DAI maps (i.e. b0b450, b100b450, b300b450, etc.) and the field strength (1.5T, 3T or 7T).
- Verify and validate a hypothesis. The dashboard summarises the results for all sites.
- Export experiment-specific figures for reporting.

The plug-in integrates simple visualisation techniques to empower research scientists to explore data, analyse and share results. Moreover, the GUI reduces the cognitive load of information, all the image post-processing settings are managed by the back-end components (Girder, CMRDiffTools, etc.) as well as data sets details, driving the user attention to one task: analyse the outcomes from different imaging systems and cardiac DTI sequences.

As an example of reporting, representative MD across tubes between 2 different scans (time delay within 30 days) are shown in figure 5. At 0% PVP, the average MD (mean \pm standard deviation across scanners) between scans were $(1.149 \pm 0.032) \times 10^{-3} \frac{mm^2}{s}$ and $(1.159 \pm 0.049) \times 10^{-3} \frac{mm^2}{s}$ respectively, while the coefficient of variation at Scan 1 was $1.9 \pm 1.4\%$. Ground truth diffusivity D_{ref} (H_2O), corresponding to 0% PVP, extrapolated from [19] was $1.113 \times 10^{-3} \frac{mm^2}{s}$.

Partial results of the analysis of product DTI sequences have been reported in [26, 27].

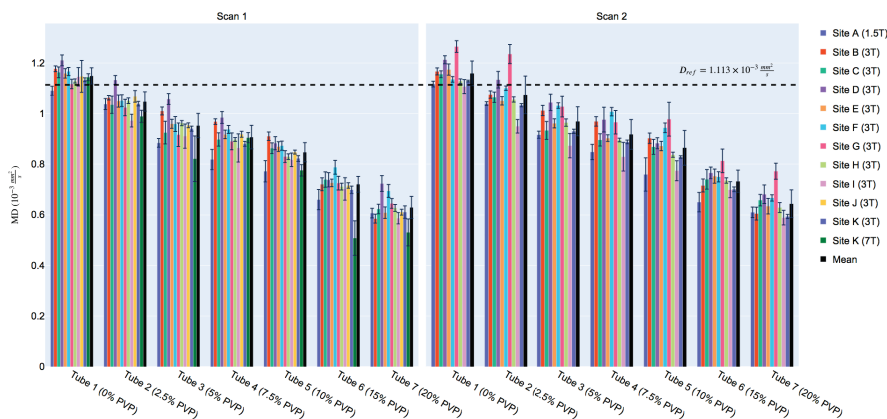


Fig. 5. MD across sites and tubes between two different scans (mean \pm standard deviation across ROI). Figure reproduced from [27]

The current plug-in version is the result of a first development cycle. Indeed, improvements and new functionalities will be implemented according to the development of the project. Nonetheless, lessons learnt may help towards future projects supported by the Human Heart Project.

6 Conclusions and Future Work

DTI benchmark databases are used in the context of the imaging sequence harmonisation as well as QA protocols. A standard reference object (phantom) is used to assess and benchmark the performance of an MRI scanner. Understanding how images are produced by a set of parameters and conditions enables

MRI and medical researchers to calibrate the imaging system as well as identify sources of variability. VA tools can streamline the analysis of extensive data sets of in vitro MR images through interactive data exploration in order to filter and display parameters of interest in an easily interpretable format.

In the context of a multi-centre study to investigate the inter- and intra-site variation of cardiac DTI sequences, CMRDiffMonitor, VA tool has been developed. This solution enables MRI researchers to track and review the variability of DAI from different image acquisition sequences. The CMRDiffMonitor’s dashboard displays a temporal overview of the data sets (monitoring of the system stability) and the statistical measurements in ROIs on a DAI map (benchmarking of the different imaging sequences and systems). Future work will focus on the visualisation of the source image (DAI map) based on the user selection over a statistical measurement.

Acknowledgements. This work was performed within the framework of the RHU MARVELOUS (ANR-16-RHUS-0009) of l’Université Claude Bernard Lyon 1 (UCBL), within the program ”Investissements d’Avenir” operated by the French National Research Agency (ANR). This study was supported by the British Heart Foundation (PG/19/1/34076). The authors acknowledge the contributions of the members of the SCMR diffusion working group as they provided data for the multi-centre study: Erica Dall’Armellina (Leeds Institute of Cardiovascular and Metabolic Medicine, University of Leeds, Leeds, UK), Daniel Ennis (Department of Radiology, VA Palo Alto Health Care System, Palo Alto, USA), Pedro F. Ferreira, Andrew Scott, Sonia NIELLES-Vallespin (Royal Brompton Hospital and Imperial College, London, UK), Prateek Kalra, Arunark Kolipaka (Department of Radiology, The Ohio State University Wexner Medical Center, Columbus, USA), Sebastian Kozerke, Christian T. Stoeck (Institute for Biomedical Engineering, University and ETH Zurich, Zurich, Switzerland), David Lohr, Laura M. Schreiber (Department of Cardiovascular Imaging, Comprehensive Heart Failure Center, Würzburg, Germany), Kevin Moulin (Stanford University, Stanford, USA), Christopher Nguyen, David Sosnovik (Massachusetts General Hospital and Harvard Medical School, Boston, USA), Beau Pontre (Department of Anatomy and Medical Imaging, The University of Auckland, Auckland, New Zealand), Cyril Tous (Department of Radiology, Radiation-Oncology and Nuclear Medicine and Institute of Biomedical Engineering, Université de Montréal, Montréal, Canada), Elizabeth Tunnicliffe (University of Oxford, Oxford, UK), Vicky Wang (San Francisco Veteran Affairs Medical Center, San Francisco, USA), Andreas M. Weng (Department of Diagnostic and Interventional Radiology, University Hospital Würzburg, Würzburg, Germany), and Alistair Young (Department of Biomedical Engineering, King’s College London, London, UK).

References

1. The human heart project. <http://humanheart-project.creatis.insa-lyon.fr/> (Accessed March 17, 2020)

2. Multi-centre evaluation of cardiac dti sequences. <http://humanheart-project.creatis.insa-lyon.fr/MultiCentreEvaluationCDTI.html> (Accessed March 17, 2020)
3. The virtual imaging platform. <http://vip.creatis.insa-lyon.fr/> (Accessed March 17, 2020)
4. Afgan, E., Baker, D., Batut, B., Van Den Beek, M., Bouvier, D., Čech, M., Chilton, J., Clements, D., Coraor, N., Grüning, B.A., et al.: The galaxy platform for accessible, reproducible and collaborative biomedical analyses: 2018 update. *Nucleic acids research* **46**(W1), W537–W544 (2018)
5. Avesani, P., McPherson, B., Hayashi, S., Caiafa, C.F., Henschel, R., Garyfallidis, E., Kitchell, L., Bullock, D., Patterson, A., Olivetti, E., et al.: The open diffusion data derivatives, brain data upcycling via integrated publishing of derivatives and reproducible open cloud services. *Scientific data* **6**(1), 1–13 (2019)
6. Burmeister, J., Bernard, J., May, T., Kohlhammer, J.: Self-service data preprocessing and cohort analysis for medical researchers. In: 2019 IEEE Workshop on Visual Analytics in Healthcare (VAHC). pp. 17–24. IEEE (2019)
7. Chen, C.C., Wan, Y.L., Wai, Y.Y., Liu, H.L.: Quality assurance of clinical mri scanners using acr mri phantom: preliminary results. *Journal of digital imaging* **17**(4), 279–284 (2004)
8. Das, S., Glatard, T., Rogers, C., Saigle, J., Paiva, S., MacIntyre, L., Safi-Harab, M., Rousseau, M.E., Stirling, J., Khalili-Mahani, N., et al.: Cyberinfrastructure for open science at the montreal neurological institute. *Frontiers in neuroinformatics* **10**, 53 (2017)
9. Davids, M., Zöllner, F.G., Ruttorf, M., Nees, F., Flor, H., Schumann, G., Schad, L.R., Consortium, I., et al.: Fully-automated quality assurance in multi-center studies using mri phantom measurements. *Magnetic resonance imaging* **32**(6), 771–780 (2014)
10. Dinov, I.D., Petrosyan, P., Liu, Z., Eggert, P., Hobel, S., Vespa, P., Woo Moon, S., Van Horn, J.D., Franco, J., Toga, A.W.: High-throughput neuroimaging-genetics computational infrastructure. *Frontiers in neuroinformatics* **8**, 41 (2014)
11. Donoho, D.L.: An invitation to reproducible computational research. *Biostatistics* **11**(3), 385–388 (2010)
12. Fonseca, C.G., Backhaus, M., Bluemke, D.A., Britten, R.D., Chung, J.D., Cowan, B.R., Dinov, I.D., Finn, J.P., Hunter, P.J., Kadish, A.H., et al.: The cardiac atlas project—an imaging database for computational modeling and statistical atlases of the heart. *Bioinformatics* **27**(16), 2288–2295 (2011)
13. Glatard, T., Lartizien, C., Gibaud, B., Da Silva, R.F., Forestier, G., Cervenansky, F., Alessandrini, M., Benoit-Cattin, H., Bernard, O., Camarasu-Pop, S., et al.: A virtual imaging platform for multi-modality medical image simulation. *IEEE Transactions on Medical Imaging* **32**(1), 110–118 (2012)
14. Ihalainen, T.M., Lönnroth, N.T., Peltonen, J.I., Uusi-Simola, J.K., Timonen, M.H., Kuusela, L.J., Savolainen, S.E., Sipilä, O.E.: Mri quality assurance using the acr phantom in a multi-unit imaging center. *Acta oncologica* **50**(6), 966–972 (2011)
15. Inc., P.T.: Collaborative data science. <https://plot.ly> (Accessed March 17, 2020)
16. Keim, D., Kohlhammer, J., Ellis, G., Mansmann, F.: Mastering the information age: solving problems with visual analytics (2010)
17. Kim, H., Irimia, A., Hobel, S.M., Esquivel Castelo-Blanco, R.I., Duffy, B., Zhao, L., Crawford, K.L., Liew, S.L., Clark, K., Law, M., et al.: Loni qc system: a semi-automated, web-based and freely-available environment for the comprehensive quality control of neuroimaging data. *Frontiers in neuroinformatics* **13**, 60 (2019)

18. Kitware: Girder: a data management platform. <https://girder.readthedocs.io/> (Accessed March 17, 2020)
19. Mills, R.: Self-diffusion in normal and heavy water in the range 1-45. deg. *The Journal of Physical Chemistry* **77**(5), 685–688 (1973)
20. Pierpaoli, C., Sarlls, J., Nevo, U., Basser, P., Horkay, F.: Polyvinylpyrrolidone (pvp) water solutions as isotropic phantoms for diffusion mri studies. In: ISMRM. vol. 17, p. 1414 (2009)
21. Poldrack, R.A., Barch, D.M., Mitchell, J., Wager, T., Wagner, A.D., Devlin, J.T., Cumba, C., Koyejo, O., Milham, M.: Toward open sharing of task-based fmri data: the openfmri project. *Frontiers in neuroinformatics* **7**, 12 (2013)
22. of Radiology, A.C., et al.: Phantom test guidance for the acr mri accreditation program. Reston, Va: ACR (1998)
23. Romero R., W.A., Viallon, M., Froeling, M., Stoeck, C., Kozerke, S., Tunncliffe, E., Scott, A., Ferreira, P., Aliotta, E., Ennis, D., Moulin, K., Croisille, P.: CM-RDiffTools: A Processing and Analysis Tool for Cardiac Diffusion MR images. In: ISMRM (2018)
24. Shneiderman, B.: The eyes have it: A task by data type taxonomy for information visualizations. In: Proceedings 1996 IEEE symposium on visual languages. pp. 336–343. IEEE (1996)
25. Tax, C.M., Grussu, F., Kaden, E., Ning, L., Rudrapatna, U., Evans, C.J., St-Jean, S., Leemans, A., Koppers, S., Merhof, D., et al.: Cross-scanner and cross-protocol diffusion mri data harmonisation: A benchmark database and evaluation of algorithms. *NeuroImage* **195**, 285–299 (2019)
26. Teh, I., Romero, W., et al.: Multi-centre evaluation of diffusion tensor imaging (dti) in an isotropic phantom: Towards validation of cardiac dti sequences. In: SCMR 23rd Annual Scientific Sessions (2020)
27. Teh, I., Romero, W., et al.: Reproducibility of diffusion tensor imaging (dti) on 12 clinical scanners: Towards validation of cardiac dti sequences. In: ISMRM (2020)

Bibliography

- [1] N. Mewton, C. Y. Liu, P. Croisille, D. Bluemke, and J. A. Lima, “Assessment of myocardial fibrosis with cardiovascular magnetic resonance,” *Journal of the American College of Cardiology*, vol. 57, no. 8, pp. 891–903, 2011.
- [2] S. de Jong, J. J. Zwanenburg, F. Visser, R. van der Nagel, H. V. van Rijen, M. A. Vos, J. M. de Bakker, and P. R. Lijten, “Direct detection of myocardial fibrosis by mri,” *Journal of molecular and cellular cardiology*, vol. 51, no. 6, pp. 974–979, 2011.
- [3] B. J. van Nierop, N. A. Bax, J. L. Nelissen, F. Arslan, A. G. Motaal, L. de Graaf, J. J. Zwanenburg, P. R. Lijten, K. Nicolay, and G. J. Strijkers, “Assessment of myocardial fibrosis in mice using a t2*-weighted 3d radial magnetic resonance imaging sequence,” *PloS one*, vol. 10, no. 6, e0129899, 2015.
- [4] A. G. Siu, A. Ramadeen, X. Hu, L. Morikawa, L. Zhang, J. Y. Lau, G. Liu, M. Pop, K. A. Connelly, P. Dorian, *et al.*, “Characterization of the ultrashort-te (ute) mr collagen signal,” *NMR in Biomedicine*, vol. 28, no. 10, pp. 1236–1244, 2015.
- [5] E. CA Araujo, N Azzabou, A Vignaud, G Guillot, and P. Carlier, “Quantitative ultrashort te imaging of the short-t2 components in skeletal muscle using an extended echo-subtraction method,” *Magnetic resonance in medicine*, vol. 78, no. 3, pp. 997–1008, 2017.
- [6] C. Olchowy, K. Cebulski, M. Łasecki, R. Chaber, A. Olchowy, K. Kałwak, and U. Zaleska-Dorobisz, “The presence of the gadolinium-based contrast agent depositions in the brain and symptoms of gadolinium neurotoxicity-a systematic review,” *PloS one*, vol. 12, no. 2, e0171704, 2017.
- [7] T. J. Fraum, D. R. Ludwig, M. R. Bashir, and K. J. Fowler, “Gadolinium-based contrast agents: A comprehensive risk assessment,” *Journal of Magnetic Resonance Imaging*, vol. 46, no. 2, pp. 338–353, 2017.
- [8] J. Garcia, S. Z. Liu, and A. Y. Louie, “Biological effects of mri contrast agents: Gadolinium retention, potential mechanisms and a role for phosphorus,” *Philosophical Transactions of the Royal Society A: Mathematical, Physical and Engineering Sciences*, vol. 375, no. 2107, p. 20170180, 2017.
- [9] D. G. Nishimura, *Principles of magnetic resonance imaging*. Stanford University, 1996.
- [10] P. C. Lauterbur, “Image formation by induced local interactions: Examples employing nuclear magnetic resonance,” *nature*, vol. 242, no. 5394, pp. 190–191, 1973.
- [11] M. Bernstein, K. King, X. Zhou, *et al.*, “Advanced pulse sequence techniques,” *Handbook of pulse sequence*. San Diego: Elsevier, pp. 802–96, 2004.
- [12] S. Foucart and H. Rauhut, *A mathematical introduction to compressive sensing*. New York: Birkhäuser/Springer, 2013, p. 625, ISBN: 978-0-8176-4948-7.

- [13] M. Lustig, D. Donoho, and J. M. Pauly, “Sparse mri: The application of compressed sensing for rapid mr imaging,” *Magnetic Resonance in Medicine: An Official Journal of the International Society for Magnetic Resonance in Medicine*, vol. 58, no. 6, pp. 1182–1195, 2007.
- [14] C. Roy, A. Slimani, C. de Meester, M. Amzulescu, A. Pasquet, D. Vancraeynest, J.-L. Vanoverschelde, A.-C. Pouleur, and B. L. Gerber, “Age and sex corrected normal reference values of t1, t2 t2* and ecv in healthy subjects at 3t cmr,” *Journal of Cardiovascular Magnetic Resonance*, vol. 19, no. 1, pp. 1–12, 2017.
- [15] J. E. Holmes and G. M. Bydder, “Mr imaging with ultrashort te (ute) pulse sequences: Basic principles,” *Radiography*, vol. 11, no. 3, pp. 163–174, 2005.
- [16] D. J. Tyler, M. D. Robson, R. M. Henkelman, I. R. Young, and G. M. Bydder, “Magnetic resonance imaging with ultrashort te (ute) pulse sequences: Technical considerations,” *Journal of Magnetic Resonance Imaging: An Official Journal of the International Society for Magnetic Resonance in Medicine*, vol. 25, no. 2, pp. 279–289, 2007.
- [17] C. F. Chan, N. G. Keenan, S. Nielles-Vallespin, P. Gatehouse, M. N. Sheppard, J. J. Boyle, D. J. Pennell, and D. N. Firmin, “Ultra-short echo time cardiovascular magnetic resonance of atherosclerotic carotid plaque,” *Journal of Cardiovascular Magnetic Resonance*, vol. 12, no. 1, pp. 1–8, 2010.
- [18] J. F. Schenck, “The role of magnetic susceptibility in magnetic resonance imaging: Mri magnetic compatibility of the first and second kinds,” *Medical physics*, vol. 23, no. 6, pp. 815–850, 1996.
- [19] B. F. Moon, S. K. Iyer, E. Hwuang, M. P. Solomon, A. T. Hall, R. Kumar, N. J. Josselyn, E. M. Higbee-Dempsey, A. Tsourkas, A. Imai, *et al.*, “Iron imaging in myocardial infarction reperfusion injury,” *Nature communications*, vol. 11, no. 1, pp. 1–14, 2020.
- [20] S. Buch, S. Liu, Y. Ye, Y.-C. N. Cheng, J. Neelavalli, and E. M. Haacke, “Susceptibility mapping of air, bone, and calcium in the head,” *Magnetic resonance in medicine*, vol. 73, no. 6, pp. 2185–2194, 2015.
- [21] A. Deistung, F. Schweser, B. Wiestler, M. Abello, M. Roethke, F. Sahm, W. Wick, A. M. Nagel, S. Heiland, H.-P. Schlemmer, *et al.*, “Quantitative susceptibility mapping differentiates between blood depositions and calcifications in patients with glioblastoma,” *PloS one*, vol. 8, no. 3, e57924, 2013.
- [22] A. Deistung, F. Schweser, and J. R. Reichenbach, “Overview of quantitative susceptibility mapping,” *NMR in Biomedicine*, vol. 30, no. 4, e3569, 2017.
- [23] A. Martino and R. Damadian, “Improved discrimination of normal and malignant tissue using 1h nmr relaxation time measurements at 2.18 mhz,” *Physiological chemistry and physics and medical NMR*, vol. 16, no. 1, pp. 49–55, 1984.
- [24] A. Einstein, “Über die von der molekularkinetischen theorie der wärme geforderte bewegung von in ruhenden flüssigkeiten suspendierten teilchen,” *Annalen der physik*, vol. 4, 1905.
- [25] I. Teh, “Cardiac diffusion mri,” in *Protocols and Methodologies in Basic Science and Clinical Cardiac MRI*, Springer, 2018, pp. 55–109.

- [26] E. O. Stejskal and J. E. Tanner, “Spin diffusion measurements: Spin echoes in the presence of a time-dependent field gradient,” *The journal of chemical physics*, vol. 42, no. 1, pp. 288–292, 1965.
- [27] P. B. Kingsley, “Introduction to diffusion tensor imaging mathematics: Part i. tensors, rotations, and eigenvectors,” *Concepts in Magnetic Resonance Part A*, vol. 28, no. 2, pp. 101–122, 2006.
- [28] —, “Introduction to diffusion tensor imaging mathematics: Part ii. anisotropy, diffusion-weighting factors, and gradient encoding schemes,” *Concepts in Magnetic Resonance Part A*, vol. 28, no. 2, pp. 123–154, 2006.
- [29] A. Biernacka and N. G. Frangogiannis, “Aging and cardiac fibrosis,” *Aging and disease*, vol. 2, no. 2, p. 158, 2011.
- [30] L. Lu, J. Guo, Y. Hua, K. Huang, R. Magaye, J. Cornell, D. J. Kelly, C. Reid, D. Liew, Y. Zhou, *et al.*, “Cardiac fibrosis in the ageing heart: Contributors and mechanisms,” *Clinical and Experimental Pharmacology and Physiology*, vol. 44, pp. 55–63, 2017.
- [31] B. Ambale-Venkatesh and J. A. Lima, “Cardiac mri: A central prognostic tool in myocardial fibrosis,” *Nature Reviews Cardiology*, vol. 12, no. 1, p. 18, 2015.
- [32] T. Pezel, M. Viallon, P. Croisille, L. Sebbag, T. Bochaton, J. Garot, J. A. Lima, and N. Mewton, “Imaging interstitial fibrosis, left ventricular remodeling, and function in stage a and b heart failure,” *Cardiovascular Imaging*, vol. 14, no. 5, pp. 1038–1052, 2021.
- [33] V. O. Puntmann, E. Peker, Y Chandrashekhara, and E. Nagel, “T1 mapping in characterizing myocardial disease: A comprehensive review,” *Circulation research*, vol. 119, no. 2, pp. 277–299, 2016.
- [34] P. Haaf, P. Garg, D. R. Messroghli, D. A. Broadbent, J. P. Greenwood, and S. Plein, “Cardiac t1 mapping and extracellular volume (ecv) in clinical practice: A comprehensive review,” *Journal of Cardiovascular Magnetic Resonance*, vol. 18, no. 1, pp. 1–12, 2017.
- [35] P. Kellman, J. R. Wilson, H. Xue, M. Ugander, and A. E. Arai, “Extracellular volume fraction mapping in the myocardium, part 1: Evaluation of an automated method,” *Journal of Cardiovascular Magnetic Resonance*, vol. 14, no. 1, pp. 1–11, 2012.
- [36] P. Kellman, J. R. Wilson, H. Xue, W. P. Bandettini, S. M. Shanbhag, K. M. Druey, M. Ugander, and A. E. Arai, “Extracellular volume fraction mapping in the myocardium, part 2: Initial clinical experience,” *Journal of Cardiovascular Magnetic Resonance*, vol. 14, no. 1, pp. 1–8, 2012.
- [37] A. Fischer, P. Martirosian, T. Benkert, and F. Schick, “Spatially resolved free-induction decay spectroscopy using a 3d ultra-short echo time multi-echo imaging sequence with systematic echo shifting and compensation of b0 field drifts,” *Magnetic Resonance in Medicine*, vol. 87, no. 5, pp. 2099–2110, 2022.
- [38] B. J. Bielajew, J. C. Hu, and K. A. Athanasiou, “Collagen: Quantification, biomechanics and role of minor subtypes in cartilage,” *Nature Reviews Materials*, vol. 5, no. 10, pp. 730–747, 2020.

- [39] M. Baues, A. Dasgupta, J. Ehling, J. Prakash, P. Boor, F. Tacke, F. Kiessling, and T. Lammers, “Fibrosis imaging: Current concepts and future directions,” *Advanced drug delivery reviews*, vol. 121, pp. 9–26, 2017.
- [40] Y.-J. Ma, E. Y. Chang, G. M. Bydder, and J. Du, “Can ultrashort-te (ute) mri sequences on a 3-t clinical scanner detect signal directly from collagen protons: Freeze-dry and d2o exchange studies of cortical bone and achilles tendon specimens,” *NMR in Biomedicine*, vol. 29, no. 7, pp. 912–917, 2016.
- [41] M. A. Horn and A. W. Trafford, “Aging and the cardiac collagen matrix: Novel mediators of fibrotic remodelling,” *Journal of molecular and cellular cardiology*, vol. 93, pp. 175–185, 2016.
- [42] J. Bella and D. J. S. Hulmes, “Fibrillar collagens,” in *Fibrous Proteins: Structures and Mechanisms*, D. A. Parry and J. M. Squire, Eds. Cham: Springer International Publishing, 2017, pp. 457–490, ISBN: 978-3-319-49674-0. DOI: 10.1007/978-3-319-49674-0_14. [Online]. Available: https://doi.org/10.1007/978-3-319-49674-0_14.
- [43] K. Okuyama and T. Kawaguchi, “Molecular and fibrillar structures of collagen,” *Kobunshi Ronbunshu*, vol. 67, no. 4, 2010.
- [44] F. Portier, C. Teulon, A. Nowacka-Perrin, F. Guenneau, M.-C. Schanne-Klein, and G. Mosser, “Stabilization of collagen fibrils by gelatin addition: A study of collagen/gelatin dense phases,” *Langmuir*, vol. 33, no. 45, pp. 12916–12925, 2017.
- [45] Y. Ohyabu, S. Yunoki, H. Hatayama, and Y. Teranishi, “Fabrication of high-density collagen fibril matrix gels by renaturation of triple-helix collagen from gelatin,” *International journal of biological macromolecules*, vol. 62, pp. 296–303, 2013.
- [46] A. Kafak-Hachulska, A. Samoson, and W. Kolodziejcki, “¹H MAS and ¹H → ³¹P CP/MAS NMR study of human bone mineral,” *Calcified Tissue International*, vol. 73, no. 5, pp. 476–486, 2003.
- [47] C. Wittig and R. Szulcek, “Extracellular matrix protein ratios in the human heart and vessels: How to distinguish pathological from physiological changes?” *Frontiers in Physiology*, vol. 12, 2021.
- [48] V. Jellus and P. Speiper, *Ute 3d imaging with ultrashort echo times - applications guide*, SIEMENS AG - Healthcare, 2010.
- [49] E. B. Saff and A. B. Kuijlaars, “Distributing many points on a sphere,” *The mathematical intelligencer*, vol. 19, no. 1, pp. 5–11, 1997.
- [50] R. W. Chan, E. A. Ramsay, C. H. Cunningham, and D. B. Plewes, “Temporal stability of adaptive 3d radial mri using multidimensional golden means,” *Magnetic Resonance in Medicine: An Official Journal of the International Society for Magnetic Resonance in Medicine*, vol. 61, no. 2, pp. 354–363, 2009.
- [51] Z. Zhou, F. Han, L. Yan, D. J. Wang, and P. Hu, “Golden-ratio rotated stack-of-stars acquisition for improved volumetric mri,” *Magnetic resonance in medicine*, vol. 78, no. 6, pp. 2290–2298, 2017.
- [52] M. Uecker, F. Ong, J. I. Tamir, D. Bahri, P. Virtue, J. Y. Cheng, T. Zhang, and M. Lustig, “Berkeley advanced reconstruction toolbox,” in *Proc. Intl. Soc. Mag. Reson. Med.*, vol. 23, 2015.

- [53] J. I. Tamir, F. Ong, J. Y. Cheng, M. Uecker, and M. Lustig, “Generalized magnetic resonance image reconstruction using the berkeley advanced reconstruction toolbox,” in *ISMRM Workshop on Data Sampling & Image Reconstruction, Sedona, AZ*, 2016.
- [54] (2021). “The berkeley advanced reconstruction toolbox (bart),” [Online]. Available: <https://mrirecon.github.io/bart/> (visited on 01/22/2021).
- [55] M. Uecker, P. Virtue, S. S. Vasanawala, and M. Lustig, “Espirit reconstruction using soft sense,” in *Proceedings of the 21st Annual Meeting ISMRM*, vol. 21, 2013, p. 127.
- [56] Z. Wang, A. C. Bovik, H. R. Sheikh, and E. P. Simoncelli, “Image quality assessment: From error visibility to structural similarity,” *IEEE transactions on image processing*, vol. 13, no. 4, pp. 600–612, 2004.
- [57] L. Feng, L. Axel, H. Chandarana, K. T. Block, D. K. Sodickson, and R. Otazo, “Xd-grasp: Golden-angle radial mri with reconstruction of extra motion-state dimensions using compressed sensing,” *Magnetic resonance in medicine*, vol. 75, no. 2, pp. 775–788, 2016.
- [58] L. Feng, S. Coppo, D. Piccini, J. Yerly, R. P. Lim, P. G. Masci, M. Stuber, D. K. Sodickson, and R. Otazo, “5d whole-heart sparse mri,” *Magnetic resonance in medicine*, vol. 79, no. 2, pp. 826–838, 2018.
- [59] P. Ehses, N. Seiberlich, D. Ma, F. A. Breuer, P. M. Jakob, M. A. Griswold, and V. Gulani, “Ir truefisp with a golden-ratio-based radial readout: Fast quantification of t1, t2, and proton density,” *Magnetic resonance in medicine*, vol. 69, no. 1, pp. 71–81, 2013.
- [60] B. Sharif, R. Dharmakumar, R. Arsanjani, L. Thomson, C. N. Bairey Merz, D. S. Berman, and D. Li, “Non-ecg-gated myocardial perfusion mri using continuous magnetization-driven radial sampling,” *Magnetic resonance in medicine*, vol. 72, no. 6, pp. 1620–1628, 2014.
- [61] A. Fyrdahl, J. G. Ramos, M. J. Eriksson, K. Caidahl, M. Ugander, and A. Sigfridsson, “Sector-wise golden-angle phase contrast with high temporal resolution for evaluation of left ventricular diastolic dysfunction,” *Magnetic Resonance in Medicine*, vol. 83, no. 4, pp. 1310–1321, 2020.
- [62] S. Winkelmann, T. Schaeffter, T. Koehler, H. Eggers, and O. Doessel, “An optimal radial profile order based on the golden ratio for time-resolved mri,” *IEEE transactions on medical imaging*, vol. 26, no. 1, pp. 68–76, 2006.
- [63] A. G. Siu and G. A. Wright, *System and method for detection of collagen using magnetic resonance imaging*, US Patent 10,307,076, 2019.
- [64] K. G. Hollingsworth, “Reducing acquisition time in clinical mri by data under-sampling and compressed sensing reconstruction,” *Physics in Medicine & Biology*, vol. 60, no. 21, R297, 2015.
- [65] L. Feng, R. Grimm, K. T. Block, H. Chandarana, S. Kim, J. Xu, L. Axel, D. K. Sodickson, and R. Otazo, “Golden-angle radial sparse parallel mri: Combination of compressed sensing, parallel imaging, and golden-angle radial sampling for fast and flexible dynamic volumetric mri,” *Magnetic resonance in medicine*, vol. 72, no. 3, pp. 707–717, 2014.

- [66] R.-M. Menchón-Lara, F. Simmross-Wattenberg, P. Casaseca-de-la Higuera, M. Martín-Fernández, and C. Alberola-López, “Reconstruction techniques for cardiac cine mri,” *Insights into imaging*, vol. 10, no. 1, pp. 1–16, 2019.
- [67] A. Bustin, N. Fuin, R. M. Botnar, and C. Prieto, “From compressed-sensing to artificial intelligence-based cardiac mri reconstruction,” *Frontiers in cardiovascular medicine*, vol. 7, p. 17, 2020.
- [68] J. C. Ye, “Compressed sensing mri: A review from signal processing perspective,” *BMC Biomedical Engineering*, vol. 1, no. 1, pp. 1–17, 2019.
- [69] M. Aminghafari, N. Cheze, and J.-M. Poggi, “Multivariate denoising using wavelets and principal component analysis,” *Computational Statistics & Data Analysis*, vol. 50, no. 9, pp. 2381–2398, 2006.
- [70] *Horos, free and open source code software (foss) program*, <http://Horosproject.org>.
- [71] J. Du, E. Diaz, M. Carl, W. Bae, C. B. Chung, and G. M. Bydder, “Ultrashort echo time imaging with bicomponent analysis,” *Magnetic resonance in medicine*, vol. 67, no. 3, pp. 645–649, 2012.
- [72] S. Aja-Fernández and G. Vegas-Sánchez-Ferrero, “Noise filtering in mri,” in *Statistical Analysis of Noise in MRI*, Springer, 2016, pp. 89–119.
- [73] Y. Feng, T. He, M. Feng, J.-P. Carpenter, A. Greiser, X. Xin, W. Chen, D. J. Pennell, G.-Z. Yang, and D. N. Firmin, “Improved pixel-by-pixel mri r2* relaxometry by nonlocal means,” *Magnetic resonance in medicine*, vol. 72, no. 1, pp. 260–268, 2014.
- [74] A. M. Segura, O. Frazier, and L. M. Buja, “Fibrosis and heart failure,” *Heart failure reviews*, vol. 19, no. 2, pp. 173–185, 2014.
- [75] M. A. Rossi, “Connective tissue skeleton in the normal left ventricle and in hypertensive left ventricular hypertrophy and chronic chagasic myocarditis,” *Medical science monitor: international medical journal of experimental and clinical research*, vol. 7, no. 4, pp. 820–832, 2001.
- [76] A. S. Flett, M. P. Hayward, M. T. Ashworth, M. S. Hansen, A. M. Taylor, P. M. Elliott, C. McGregor, and J. C. Moon, “Equilibrium contrast cardiovascular magnetic resonance for the measurement of diffuse myocardial fibrosis: Preliminary validation in humans,” *Circulation*, vol. 122, no. 2, pp. 138–144, 2010.
- [77] Y. Wang and T. Liu, “Quantitative susceptibility mapping (qsm): Decoding mri data for a tissue magnetic biomarker,” *Magnetic resonance in medicine*, vol. 73, no. 1, pp. 82–101, 2015.
- [78] E. M. Haacke, S. Liu, S. Buch, W. Zheng, D. Wu, and Y. Ye, “Quantitative susceptibility mapping: Current status and future directions,” *Magnetic resonance imaging*, vol. 33, no. 1, pp. 1–25, 2015.
- [79] Y. Kee, Z. Liu, L. Zhou, A. Dimov, J. Cho, L. De Rochefort, J. K. Seo, and Y. Wang, “Quantitative susceptibility mapping (qsm) algorithms: Mathematical rationale and computational implementations,” *IEEE Transactions on Biomedical Engineering*, vol. 64, no. 11, pp. 2531–2545, 2017.
- [80] S. Mazzucchi, D. Frosini, M. Costagli, E. Del Prete, G. Donatelli, P. Cecchi, G. Migaleddu, U. Bonuccelli, R. Ceravolo, and M. Cosottini, “Quantitative susceptibility mapping in atypical parkinsonisms,” *NeuroImage: Clinical*, vol. 24, p. 101999, 2019.

- [81] M. Keuken, P.-L. Bazin, K Backhouse, S Beekhuizen, L Himmer, A Kandola, J. Lafeber, L Prochazkova, A Trutti, A Schäfer, *et al.*, “Effects of aging on t_1 and t_2^* , and qsm mri values in the subcortex,” *Brain Structure and Function*, vol. 222, no. 6, pp. 2487–2505, 2017.
- [82] Y. Wen, T. D. Nguyen, Z. Liu, P. Spincemaille, D. Zhou, A. Dimov, Y. Kee, K. Deh, J. Kim, J. W. Weinsaft, *et al.*, “Cardiac quantitative susceptibility mapping (qsm) for heart chamber oxygenation,” *Magnetic resonance in medicine*, vol. 79, no. 3, pp. 1545–1552, 2018.
- [83] Y. Wen, J. W. Weinsaft, T. D. Nguyen, Z. Liu, E. M. Horn, H. Singh, J. Kochav, S. Eskreis-Winkler, K. Deh, J. Kim, *et al.*, “Free breathing three-dimensional cardiac quantitative susceptibility mapping for differential cardiac chamber blood oxygenation—initial validation in patients with cardiovascular disease inclusive of direct comparison to invasive catheterization,” *Journal of Cardiovascular Magnetic Resonance*, vol. 21, no. 1, pp. 1–13, 2019.
- [84] W. R. Witschey, J. J. Pilla, G. Ferrari, K. Koomalsingh, M. Haris, R. Hinmon, G. Zsido, J. H. Gorman III, R. C. Gorman, and R. Reddy, “Rotating frame spin lattice relaxation in a swine model of chronic, left ventricular myocardial infarction,” *Magnetic resonance in medicine*, vol. 64, no. 5, pp. 1453–1460, 2010.
- [85] Y. Han, T. Liimatainen, R. C. Gorman, and W. R. Witschey, “Assessing myocardial disease using $T_1\rho$ mri,” *Current cardiovascular imaging reports*, vol. 7, no. 2, p. 9248, 2014.
- [86] C. Wang, J. Zheng, J. Sun, Y. Wang, R. Xia, Q. Yin, W. Chen, Z. Xu, J. Liao, B. Zhang, *et al.*, “Endogenous contrast $T_1\rho$ cardiac magnetic resonance for myocardial fibrosis in hypertrophic cardiomyopathy patients,” *Journal of cardiology*, vol. 66, no. 6, pp. 520–526, 2015.
- [87] O. M. Abdullah, S. G. Drakos, N. A. Diakos, O. Wever-Pinzon, A. G. Kfoury, J. Stehlik, C. H. Selzman, B. B. Reid, K. Brunisholz, D. R. Verma, *et al.*, “Characterization of diffuse fibrosis in the failing human heart via diffusion tensor imaging and quantitative histological validation,” *NMR in Biomedicine*, vol. 27, no. 11, pp. 1378–1386, 2014.
- [88] R. Wu, D.-A. An, R.-Y. Shi, B.-h. Chen, M. Jiang, A. Bacyinski, T.-T. Han, J. Hu, J.-R. Xu, and L.-M. Wu, “Myocardial fibrosis evaluated by diffusion-weighted imaging and its relationship to 3d contractile function in patients with hypertrophic cardiomyopathy,” *Journal of Magnetic Resonance Imaging*, vol. 48, no. 4, pp. 1139–1146, 2018.
- [89] T. Winkler, P. Martirosian, E. Schleicher, T. Benkert, and F. Schick, “Behavior of the signal components of collagen solutions in vitro using ute-mri and mrs sequences,” in *ISMRM 27th annual meeting and exhibition. Montreal: sn*, vol. 2258, 2019.
- [90] C. Nguyen, M. Lu, Z. Fan, X. Bi, P. Kellman, S. Zhao, and D. Li, “Contrast-free detection of myocardial fibrosis in hypertrophic cardiomyopathy patients with diffusion-weighted cardiovascular magnetic resonance,” *Journal of Cardiovascular Magnetic Resonance*, vol. 17, no. 1, pp. 1–7, 2015.
- [91] R Mills, “Self-diffusion in normal and heavy water in the range 1-45. deg.,” *The Journal of Physical Chemistry*, vol. 77, no. 5, pp. 685–688, 1973.

Bibliography

- [92] W. A. Romero R, D. Althviz Moré, I. Teh, J. E Schneider, M. Viallon, and P. Croisille, “Exploring dti benchmark databases through visual analytics,” in *Computational Diffusion MRI*, Springer, 2021, pp. 291–301.
- [93] (2021). “The human heart project,” [Online]. Available: <http://humanheart-project.creatis.insa-lyon.fr/> (visited on 01/22/2021).
- [94] W. A. Romero R., M. Viallon, M. Froeling, C. Stoeck, S. Kozerke, E. Tunnicliffe, A. Scott, P. Ferreira, E. Aliotta, D. Ennis, K. Moulin, and P. Croisille, “CMRDiffTools: A Processing and Analysis Tool for Cardiac Diffusion MR images,” in *Proceedings of the 26th Annual Meeting of the International Society for Magnetic Resonance in Medicine*, 2018.
- [95] I. Teh, W. A. Romero R, J. Boyle, J. Coll-Font, E. Dall’Armellina, D. B. Ennis, P. F. Ferreira, P. Kalra, A. Kolipaka, S. Kozerke, *et al.*, “Validation of cardiac diffusion tensor imaging sequences: A multicentre test-retest phantom study,” *NMR in Biomedicine*, vol. 35, no. 6, e4685, 2022.
- [96] Kitware, *Girder: A data management platform*, <https://girder.readthedocs.io/>, 2022.
- [97] G. Captur, P. Gatehouse, K. E. Keenan, F. G. Heslinga, R. Bruehl, M. Prothmann, M. J. Graves, R. J. Eames, C. Torlasco, G. Benedetti, *et al.*, “A medical device-grade t1 and ecv phantom for global t1 mapping quality assurance—the t1 mapping and ecv standardization in cardiovascular magnetic resonance (t1mes) program,” *Journal of cardiovascular magnetic resonance*, vol. 18, no. 1, pp. 1–20, 2016.
- [98] G. Captur, A. Bhandari, R. Brühl, B. Ittermann, K. E. Keenan, Y. Yang, R. J. Eames, G. Benedetti, C. Torlasco, L. Ricketts, *et al.*, “T1 mapping performance and measurement repeatability: Results from the multi-national t1 mapping standardization phantom program (t1mes),” *Journal of Cardiovascular Magnetic Resonance*, vol. 22, no. 1, pp. 1–17, 2020.
- [99] P. Thévenaz and M. Unser, “Optimization of mutual information for multiresolution image registration,” *IEEE transactions on image processing*, vol. 9, no. 12, pp. 2083–2099, 2000.
- [100] D. Mattes, D. R. Haynor, H. Vesselle, T. K. Lewellen, and W. Eubank, “Pet-ct image registration in the chest using free-form deformations,” *IEEE transactions on medical imaging*, vol. 22, no. 1, pp. 120–128, 2003.
- [101] C. Westin and S. Maier, “A dual tensor basis solution to the stejskal-tanner equations for dtmri,” in *Proceedings of International Society for Magnetic Resonance in Medicine*, 2002.
- [102] M. Viallon, J. Spaltenstein, C. de Bourguignon, C. Vandroux, O. Bernard, L. Belle, P. Clarysse, and P. Croisille, “Cmrsegtools: An osirix plugin for myocardial infarct sizing on de-cmr images,” *Journal of Cardiovascular Magnetic Resonance*, vol. 16, no. 1, pp. 1–3, 2014.
- [103] W. A. Romero R, M. Viallon, J. Spaltenstein, L. Petrusca, O. Bernard, L. Belle, P. Clarysse, and P. Croisille, “Cmrsegtools: An open-source software enabling reproducible research in segmentation of acute myocardial infarct in cmr images,” *Plos one*, vol. 17, no. 9, e0274491, 2022.
- [104] L. R. Dice, “Measures of the amount of ecologic association between species,” *Ecology*, vol. 26, no. 3, pp. 297–302, 1945.

Bibliography

- [105] C. Wachinger and P. Golland, “Atlas-based under-segmentation,” in *International Conference on Medical Image Computing and Computer-Assisted Intervention*, Springer, 2014, pp. 315–322.
- [106] J. Kybic and M. Unser, “Fast parametric elastic image registration,” *IEEE transactions on image processing*, vol. 12, no. 11, pp. 1427–1442, 2003.
- [107] D. Rueckert and P. Aljabar, “Non-rigid registration using free-form deformations,” in *Handbook of Biomedical Imaging*, Springer, 2015, pp. 277–294.
- [108] I. Mekkaoui, K. Moulin, P. Croisille, J. Pousin, and M. Viallon, “Quantifying the effect of tissue deformation on diffusion-weighted mri: A mathematical model and an efficient simulation framework applied to cardiac diffusion imaging,” *Physics in Medicine & Biology*, vol. 61, no. 15, p. 5662, 2016.
- [109] J. Veraart, D. S. Novikov, D. Christiaens, B. Ades-Aron, J. Sijbers, and E. Fieremans, “Denoising of diffusion mri using random matrix theory,” *Neuroimage*, vol. 142, pp. 394–406, 2016.
- [110] V. Pai, S Rapacchi, P Kellman, P Croisille, and H. Wen, “Pcatmip: Enhancing signal intensity in diffusion-weighted magnetic resonance imaging,” *Magnetic Resonance in Medicine*, vol. 65, no. 6, pp. 1611–1619, 2011.
- [111] J. V. Manjón, P. Coupé, L. Concha, A. Buades, D. L. Collins, and M. Robles, “Diffusion weighted image denoising using overcomplete local pca,” *PloS one*, vol. 8, no. 9, e73021, 2013.
- [112] K. Moulin, M. Viallon, W. Romero R., A. Chazot, N. Mewton, K. Isaaz, and P. Croisille, “Mri of reperfused acute myocardial infarction edema: Adc quantification versus t1 and t2 mapping,” *Radiology*, vol. 295, no. 3, pp. 542–549, 2020.